MICROBEAM ANALYSIS SOCIETY

PROCEEDINGS

TENTH ANNUAL CONFERENCE

AUGUST 11-15, 1975

MGM HOTEL

LAS VEGAS, NEVADA

Additional copies of these and previous
Proceedings may be obtained from:

Dr. J. I. Goldstein
Metallurgy and Materials Science Department
Leheigh University
Bethlehem, Pennsylvania 18015

TENTH ANNUAL CONFERENCE

of the

MICROBEAM ANALYSIS SOCIETY

August II - 15, 1975

MGM HOTEL

Las Vegas, Nevada

PREFACE

This meeting again brings the MAS and EMSA together in a joint effort at combining our programs and broadening our horizons. It is hoped that such efforts will be of benefit to the members of both societies and the many exhibitors.

Meetings such as this one do not organize themselves but are the result of considerable effort by the members of the various committees. Paul Lublin and John Colby had major roles in the organization of the meeting. Eric Lifshin was responsible for the program and Don Beaman for the publication of the Proceedings. Bob Bils of EMSA contributed much of his expertise and time. We all hope that you have found our efforts worthwhile.

Art Chodos
General Chairman

TENTH NATIONAL CONFERENCE COMMITTEE

Arthur Chodos, General Chairman
California Institute of Technology
Pasadena, California

Paul Lublin
General Telephone and Electronic
Waltham, Massachusetts

John Colby
Bell Telephone Labs
Allentown, Labs

Eric Lifshin, Program Chairman
General Electric Corporate Research & Development
Schenectady, New York

William Kane
Corning Glass Research and Development Labs
Corning, New York

Don Beaman, Publications
Dow Chemical Company
Midland, Michigan

Dave Kyser, Photographic Exhibit
International Business Machines
San Jose, California

Lavern Birks, Awards
Naval Research Laboratory
Washington, D.C.

Norma Chodos, Hospitality

INVITED SPEAKERS

D.R. Beaman
The Dow Chemical Company
Midland, Michigan

A.N. Broers
IBM Thomas J. Watson Research Center
Yorktown Heights, New York

C.A. Evans, Jr.
University of Illinois
Urbana, Illinois

R.H. Geiss
IBM Research Laboratory
San Jose, California

K.F.J. Heinrich
National Bureau of Standards
Washington, D.C.

C. Lechene
Harvard Medical School
Boston, Massachusetts

J. Mayer
California Institute of Technology
Pasadena, California

R.E. Ogilvie
Massachusetts Institute of Technology
Cambridge, Massachusetts

W. Reuter
IBM Research Center
Yorktown Heights, New York

R. Shimizu
Osaka University
Osaka, Japan

D.A. Shirley
University of California
Berkeley, California

E.W. White
Pennsylvania State University
University Park, Pennsylvania

SUSTAINING MEMBERS -- 1975

A.E.I. SCIENTIFIC APPARATUS, INC.
Elmsford, New York

ADVANCED METALS RESEARCH CORPORATION
Bedford, Massachusetts

APPLIED RESEARCH LABORATORIES
Sunland, California

BABCOCK & WILCOX RESEARCH CENTER
Alliance, Ohio

CAMBRIDGE INSTRUMENT CO., INC.
Ossining, New York

CAMECA INSTRUMENTS, INC.
Elmsford, New York

EDAX INTERNATIONAL INC.
Prairie View, Illinois

ETEC CORPORATION
Hayward, California

HI-REL LABORATORIES
San Marino, California

INTERNATIONAL SCIENTIFIC INSTRUMENTS, INC.
Mountain View, California

JEOL U.S.A.
Medford, Massachusetts

KEVEX CORPORATION
Burlingame, California

McCRONE ASSOCIATES
Chicago, Illinois

3M COMPANY
St. Paul, Minnesota

NUCLEAR SEMICONDUCTOR
Menlo Park, California

ORTEC INC.
Oak Ridge, Tennessee

PERKIN-ELMER/HITACHI
Palo Alto, California

PHYSICAL ELECTRONICS IND., INC.
Eden Prairie, Minnesota

PRINCETON GAMMA-TECH, INC.
Princeton, New Jersey

Q.B.I. INTERNATIONAL
San Francisco, California

CHARLES M. TAYLOR CO.
Stanford, California

TRACOR NORTHERN
Middleton, Wisconsin

VARIAN ASSOCIATES
Palo Alto, California

ANNUAL AWARDS MADE BY THE
MICROBEAM ANALYSIS SOCIETY

This award of $300 was established in 1973 to honor the memory of Dr. Victor Macres, one of the pioneers of electron probe analysis, a dedicated teacher, and a competitive instrument manufacturer. The award is given for the best instrumentation paper presented at the annual meeting. In 1974 the award was made to E. Chatfield and V. Nielsen.

JEOL AWARD

The Japan Electron Optics Laboratory Corporation sponsors this award of $300 but it is administered by the Microbeam Analysis Society. The award is given for an outstanding student paper presented at the annual MAS meeting. In 1974 the JEOLCO award was given to L. Parobek.

CORNING AWARD

In 1974 the Corning Glass Company established an award of $300 to the most outstanding contributed paper presented at the annual MAS meeting. The award is administered by the MAS. The 1974 award was shared by J. Brown and L. Parobek with A. Armigliato, P. Bergamini, L. Morettini and with D. Newbury, H. Yakowitz and R. Myklebust.

THE MAS STUDENT SUPPORT PROGRAM

The encouragement of student participation at the annual meeting is an important objective of the MAS as it was for EPASA which preceeded MAS. The registration fee is reduced for student attendees, of course, but the Student Support Program is specifically pointed towards soliciting the presentation of research papers by students at the annual meeting. In addition to being good training for the students, such presentations often bring refreshing new views of theoretical as well as experimental aspects of probe analysis.

The guidelines for the support program are simple:

1. The paper must be co-authored by a bona fide student and his or her professor.

2. It must be of a quality to be accepted by the program committee.

3. It must be presented at the meeting by the student.

4. The professor is asked to attest to the kind and amount of contribution made by the student to each facet of the work presented.

Travel support for the student is furnished by MAS to ensure that his or her attendance will not be an undue financial burden to either the student or the university. The amount of travel support will generally cover round trip economy fare plus partial coverage of food and lodging.

In addition to the student travel support the MAS administers the annual JEOLCO award for an outstanding student presentation (see accompanying description of the MAS Awards).

NATIONAL OFFICERS -- 1975

President

J.W. Colby
Bell Laboratories

President-Elect

E. Lifshin
General Electric Corporate Research & Development

Past President

P. Lublin
GTE Laboratories, Inc.

Secretary

M.A. Giles
Princeton Applied Research Laboratory

Treasurer

D.R. Beaman
The Dow Chemical Company

Members At Large

O.C. Wells
IBM Thomas J. Watson Research Center

E.W. White
Pennsylvania State University

D.F. Kyser
IBM Research Division

MICROBEAM ANALYSIS SOCIETY

COMMITTEES 1975

AWARDS COMMITTEE (all awards - student, Macres, photo exhibit)

    L.S. Birks - Chairman
    O. Wells   G. Judd   J. Tabock
    J. Colby   K. Heinrich
    J. Coleman   J. Bomback
    J. Woodhouse   D. Beaman

MEMBERSHIP   M.A. Giles - Chairman
                              G. Fisher (Public Relations &
                                         Membership Drives)

SUSTAINING MEMBERSHIP   D. Beaman - Chairman
                              J. Tabock

LEGAL   P. Lublin - Chairman
                              M.A. Giles

STANDARDS   A. Chodos - Chairman
                              D. Beaman
                              J. Bomback

EMPLOYMENT SERVICES   J. Woodhouse - Chairman

FUTURE MEETING SITES   P. Lublin - Chairman
                              J. Colby
                              A. Chodos
                              D. O'Boyle

SECTION LIAISON (speakers tour, section support)

                              J. Colby - Chairman
                              D. Wittry
                              Chairmen of local sections

INTERNATIONAL USERS LIAISON   E. Lifshin - Chairman

EDUCATIONAL   G. White - Chairman
                              D. Beaman
                              D. Brown
                              J. Goldstein
                              J. Woodhouse

PUBLICATIONS   J. Goldstein - Chairman

CERTIFICATES & SCROLLS   D. Kyser - Chairman

MEETING ANNOUNCEMENT

ELEVENTH ANNUAL CONFERENCE OF THE MICROBEAM ANALYSIS SOCIETY

Location: Fontainbleau Hotel
                   Miami Beach, Florida

Date: August 8-13, 1976

For information concerning this meeting, please contact:

Dr. William Kane   Dr. Paul Lublin
Research & Development Laboratories   GTE Laboratories
Corning Glass Works   40 Sylvan Road
Corning, New York 14830   Waltham, Massachusetts   02154
(256)974-3363   (617)890-8460

The technical sessions will include invited and contributed
papers on all aspects of electron probe analysis, energy dis-
persive spectrometry, scanning electron microscopy, secondary
ion mass analysis, Auger electron spectroscopy, ion scattering
spectrometry, electron spectroscopy chemical analysis, soft
x-ray emission, instrumentation, computer control and data
reduction, and applications.

Contributed papers are welcome and instructions to authors will
be provided through meeting announcements and the MicroNews.

TWELFTH ANNUAL CONFERENCE OF THE MICROBEAM ANALYSIS SOCIETY

                   AND THE EIGHTH INTERNATIONAL CONFERENCE ON
                   X-RAY OPTICS AND MICROANALYSIS

Location: Sheraton Boston Hotel
                   Boston, Massachusetts

Date: August 18-26, 1977

For information concerning this meeting, please contact:

Dr. R.E. Ogilvie   Dr. D. Wittry
Massachusetts Institute of Tech-   Department of Materials Science
nology   & Electrical Engineering
Cambridge, Massachusetts   University of Southern California
                                          Los Angeles, California   90007
(617)253-1000   (213)746-2510

PROGRAM

TENTH ANNUAL CONFERENCE

OF THE

MICROBEAM ANALYSIS SOCIETY

MONDAY 11 AUGUST 1975

TUTORIAL SESSION

Rialto 1 and 2

P. Lublin, Chairman

	8:30 AM	Registration
	9:45 AM	Introductory Remarks by J. Colby, President, MAS

TUTORIAL LECTURES

T1	10:00 AM	"Principles of Electron Probe Microanalysis" R.E. Ogilvie, Massachusetts Institute of Technology
T2	11:00 AM	"The Use of a Multi-Technique Approach to the Characterization of Surfaces and Thin Films" D.A. Evans, Jr., University of Illinois
	12:00 PM	LUNCH
W1	2:00 PM	Workshop I - "Optimizing Scanning Electron Microscope Images" E. White, Pennsylvania State University
W2	3:00 PM	Workshop II - "Procedures for Collecting and Evaluating Quantitative Data" D. Beaman, Dow Chemical Company

TUESDAY 12 AUGUST 1975

SESSION I - X-RAY MEASUREMENT AND QUANTITATIVE ANALYSIS

Rialto 1 and 2

D. Wittry, Chairman

	8:30 AM	Registration
	8:55 AM	Introduction of MAS Officers
1	9:00 AM	INVITED PAPER: "Fluorescence Excited by the Continuum and the Accuracy of Electron Probe Microanalysis" K.F. Heinrich, National Bureau of Standards

2	9:30 AM	"Monte Carlo Calculation of Electron Backscatter Yield from Thin Films on Thick Substrates" D.F. Kyser, IBM Research Division
3	9:45 AM	"Cross Sections for Ionization of Inner-Shell Electrons by Electron Impact" C.J. Powell, National Bureau of Standards
4	10:00 AM	"Theoretical Performance of Blazed Gratings at Grazing Incidence" D.B. Wittry, University of Southern California and K. Tsutsumi, University of Osaka Prefecture
5	10:15 AM	"Behaviors of Electrons in a Deep Region of Metallic Target" G. Shinoda, Rigaku-Denki Company, M. Takahashi, Japan Women's University
	10:30 AM	INTERMISSION
6	10:45 AM	"Improvement in X-ray Spatial Resolution at Phase Boundaries" J.I. Goldstein and E. Randich, Lehigh University
7	11:00 AM	"A Simple Correction for Backscattering from Inclined Samples" J.C. Russ, EDAX International, Inc.
8	11:15 AM	"Evaluation of Instrumental and Physical Limitations Encountered in the Study of Two Phase Structures" R.B. Bolon and M.D. McConnell, General Electric Corporate Research and Development
9	11:30 AM	"The Minimization of Size and Geometric Effects in the Quantitative Analysis of Microparticles with Electron Beam Instruments" J.T. Armstrong and P.R. Buseck, Arizona State University
10	11:45 AM	"The Effects of Variations in Specimen Height and Orientation of the Spectrometer Rowland Circle on Measured X-ray Intensities" D. File, H. Walker, R. Lewis, Cameca Instruments
	12:00 PM	LUNCH

TUESDAY 12 AUGUST 1975

SESSION II - SCANNING ELECTRON MICROSCOPY

Joint MAS-EMSA Session

Rialto 1 and 2

O. Wells, Chairman

11   2:00 PM   INVITED PAPER: "Scanning Electron Microscopy of
                 Bacteriophage" A.N. Broers, IBM Thomas J. Watson
                 Research Center, B.J. Panessa and J.F. Gennaro,
                 New York University

12   2:30 PM   "Microanalysis by Electron Spectroscopy of Inner-
                 Shell Excitations" V.E. Cosslett and R.D. Leapman,
                 Cavendish Laboratory

13   2:45 PM   "Observation of Dynamic Deformation of Stereoscopic
                 SEM" E.J. Chatfield and V.H. Nielson, Ontario
                 Research Foundation

14   3:00 PM   "High Contrast Observation of Magnetic Domain with
                 High Voltage SEM" R. Shimizu and T. Ikuta, Osaka
                 University, M. Kinoshita and T. Murayama, Tokyo
                 Shibaura Electric Company, Ltd. and H. Nishizawa
                 and T. Yamamoto, Japan Electron Optics Lab. Co., Ltd.

15   3:15 PM   "Experimental Method for Measuring Source Size in
                 the SEM" O.C. Wells, IBM

      3:30 PM   INTERMISSION

16   3:45 PM   "An Analytical Scanning Transmission Electron
                 Microscope" H. von Harrach, C.E. Lyman, A.R. Walker,
                 D.C. Joy and G.R. Booker, University of Oxford

17   4:00 PM   "An Improved Specimen Mount for Scanning Electron
                 Microscopy" M.K. Lamvik and S.D. Lin, Enrico Fermi
                 Institute, University of Chicago

18   4:15 PM   "A Simple Transmission Stage for a Scanning Electron
                 Microscope" P.S.D. Lin and M.K. Lamvik, Enrico Fermi
                 Institute, University of Chicago

      4:30 PM   END SESSION

WEDNESDAY 13 AUGUST 1975

SESSION III - ENERGY DISPERSIVE ANALYSIS

Joint MAS-EMSA Session

Rialto 1 and 2

E. Lifshin, Chairman

19   9:00 AM   INVITED PAPER: Quantitative X-ray Energy Dispersive
                   Analysis with the Transmission Electron Microscope"
                   R.H. Geiss and T.C. Huang, IBM Research Laboratory

20   9:30 AM   "Frame B: An On-line Correction Procedure for
                   Quantitative Electron Probe Microanalysis with a
                   Si(Li) Detector" C.E. Fiori, R.L. Myklebust,
                   K.F.J. Heinrich and H. Yakowitz, National Bureau
                   of Standards

21   9:45 AM   "An Approach to Fully Quantitative Energy Disper-
                   sive Electron Microprobe Analysis" D.G.W. Smith,
                   University of Alberta

22   10:00 AM   "A Computer Program for Spectrum Analysis"
                   R.M. Keyser, D.M. Bartell and R.S. Moneymaker,
                   Ortec, Incorporated

23   10:15 AM   "Quantitative Analysis with Energy Dispersive
                   Detector System" M.F. Ciccarelli, R.B. Bolon and
                   E. Lifshin, General Electric Corporate Research
                   and Development

        10:30 AM   INTERMISSION

24   10:45 AM   "Least Squares Peak Fitting Within the ZAF Iteration
                   Loops" C. Maggiore and M. Foster, Princeton Gamma Tech

25   11:00 AM   "The High Counting Rate Limits on Analytical Pre-
                   cision Due to Deadtime Losses" D.A. Gedcke, Ortec
                   Incorporated

26   11:15 AM   "On the Use of A Variable Geometry Proportional
                   Counter for X-rays Microanalysis of Light Elements
                   with an Electron Microscope" A. Armigliato and
                   G.G. Bentini, CNR-LAMEL, Bologna, ITALY and
                   P. Bergamini, CISE, Milano, ITALY.

27 11:30 AM "Electron Beam Microanalysis of Environmental Samples Using a High Resolution Scanning Electron Microscope with an Energy Dispersive X-ray Analyzer (SEMI-EDXRA)" M.M. Reddy, New York State Department of Health

28 11:45 AM "Sample Mass Determination from Compton Scattering Using an X-ray Probe Energy Dispersive Analyzer" H.L. Cox, Jr. and P.S. Ong, The University of Texas System Cancer Center

   12:00 PM MAS Awards Luncheon

   3:00 PM Business Meeting - Rialto 1 and 2

THURSDAY 14 AUGUST 1975

SESSION IV-A MATERIALS APPLICATIONS

Rialto 1

G. Plant, Chairman

29 9:00 AM "Quantitative Microprobe X-ray Analysis and X-ray Imaging Techniques of Boron-Beryllium Compounds" D.D. McCoy, W.F. Morris and R.G. Gutmacher, University of California

30 9:15 AM "Microprobe Technique for Determining the Thickness of Ag_2S Films as a Function of Sulfur Vapor Pressure at Saturation and Below" G. DiGiacomo, IBM System Product Division

31 9:30 AM "Ambiguities in the Identification of Asbestos Fibers in Liquids" D.R. Beaman, Dow Chemical Company and D.M. File, Cameca Instruments, Inc.

32 9:45 AM "Electron Microprobe Whole Rock Analysis of 20mg Samples" R. Brown and O. Mullins, Jr., Lockheed Electronics Company

33 10:00 AM "Microscopic Investigations of Coal Fly Ash Particles" J.E. Baker, C.A. Evans, A. Loh and D.F.S. Natusch, University of Illinois

34	10:15 AM	"Applications of Quantitative Electron Beam Analysis of Microparticles in Air Pollution Research" J.T. Armstrong and P.R. Buseck, Arizona State University
	10:30 AM	INTERMISSION
35	10:45 AM	"Improvements in Rapid Multi-Element Analysis Using a Matrix of Concentration Dependent Correction Coefficients" J.W. Leitner, Applied Research Laboratories
36	11:00 AM	"Analysis of Phase Separation in Tl-As-Se Glass" M.J. Mitchell, IBM at SP Division, S. Narasimhan, IBM at Research Division and M.I. deRojas, Signetics Corporation
37	11:15 AM	"Quantitative Analysis of Zeolites Using an Energy Dispersive System" I.M. Steele,J.V. Smith, J.J. Pluth and T.N. Solberg, University of Chicago
38	11:30 AM	"Electron Microprobe-Derived Soft X-ray Spectral Parameters; Their Use in Chemical Bonding Studies of Iron Minerals" C.G. Dodd, Warner-Lambert Company and P.H. Ribbe, Virginia Polytechnic Institute and State University
39	11:45 AM	"Quantitative Analysis and Phase Identification of Refractory Inclusions in Glasses by Energy Dispersive X-ray Analysis" R.G. Craig and J.P. Sullivan, Jr., GTE Sylvania, Incorporated
	12:00 PM	LUNCH

THURSDAY 14 AUGUST 1975

SESSION IV-B BIOLOGICAL APPLICATIONS

Rialto 2

J. Coleman, Chairman

40	8:45 AM	INVITED PAPER: "Applications of Electron Microprobe Analysis in Physiology" C. Lechene, Harvard Medical School
41	9:15 AM	"Quantitative Electron Probe Analysis of Ultra-Thin Biological Sections" H. Shuman and A.P. Somlyo, University of Pennsylvania Medical Center

42	9:30 AM	"An Electron Probe Study of Elemental Distribution in the Rat Pituitary" G.R. Merriam, F. Naftolin and C. Lechene, Harvard Medical School
43	9:45 AM	"Scanning, Transmission and Electron Probe Analysis of the Cat Tapetum" C.E. Turnbill, NASA-Ames Research Center
44	10:00 AM	"Electron Probe Analysis and Ultrastructure of Cultured, Freeze-Dried Vascular Smooth Muscle" R.E. Garfield and A.P. Somlyo, Presbyterian-University of Pennsylvania Medical Center
45	10:15 AM	"A Simple Transmitted Electron Detector (TED) for Thin Biological Samples" J.R. Coleman, S. Davis, B. Halloran and P. Moran, University of Rochester School of Medicine and Dentistry
	10:30 AM	INTERMISSION
46	10:45 AM	"Microanalysis of Zinc in Injured Myocardia" R. Yarom, Hebrew University, Hadassah Medical School, Jerusalem, Israel, P.D. Peters and T.A. Hall, Cavendish Laboratory, Cambridge, England
47	11:00 AM	"Electron Probe Analysis of the Effect of Para-thyroid Hormone on Inorganic Ions in the Rat Kidney" E.H. Abraham, R.R. Warner and C.P. Lechene, Harvard Medical School
48	11:15 AM	"Microanalysis of Crystals in Biological Tissue" S. Siew, R.K. Matta and M. Johnson, University of Pittsburgh School of Medicine and the Monte-fiore Hospital
49	11:30 AM	"Perspective in Electron Microprobe Analysis of Biological Samples Kept Frozen" C. Lechene, T. Strank and R. Warner, Harvard Medical School and C. Conty, Cameca Instruments, Inc.
50	11:45 AM	"Energy Dispersive X-ray Analysis of Picoliter Samples of Physiological Fluids" P.M. Quinton, University of California
51	12:00 PM	"SEM Characterization of Respirable Dust in Situ in Lung Tissue Using Ashing and Digestion Tech-niques" P.B. DeNee, J.L. Abraham, USPHS ALFORD, NIOSH and E.R. Walker, W.V. University Medical Center

SESSION V - INSTRUMENTATION, AUTOMATION AND SOFTWARE

Rialto 1 and 2

W. Kane, Chairman

52   2:00 PM   "Measurement of Surface Voltages Using the Voltage Dependence of X-ray Intensities" C.J. Wu and D.B. Wittry, University of Southern California

53   2:15 PM   "Practical Applications of Automated Microprobe Analysis" W.T. Hatfield, R.B. Bolon and E. Lifshin, General Electric Corporate Research and Development

54   2:30 PM   "Automated Characterization of Particulates and Inclusions" M.F. Hoover, E.W. White, J. Lebjedzik and G.G. Johnson, Penn State University

55   2:45 PM   "Reproducibility and Operator Bias in a Computer-Controlled System for Quantitative Electron Microprobe Analysis" D.E. Champion, A.L. Albee and A.A. Chodos, California Institute of Technology

56   3:00 PM   "A Minicomputer Based Multi-Instrument Automation System" E.M. Butler and A.K. Agrawal, Gould Laboratory for Electrical and Electronic Research

57   3:15 PM   "Experimental APL Programming for Quantitative Electron Microprobe Analysis" H.R. MacQueen, IBM SPE East Fishkill and R. Lasky, IBM Endicott

       3:30 PM   INTERMISSION

58   3:45 PM   "Comparative Performance of the X-ray Probe and Frieda" P.S. Ong and H.L. Cox, Jr., The University of Texas System Cancer Center, H.D. Anderson Hospital and Tumor Institute.

59   4:00 PM   "SEM and SIMS: A Unique Combination for Surface Characterization" J.A. Leys and J.T. McKinney, 3M Central Research Laboratories

60   4:15 PM   "A Pretreatment Method for SEM-EPMA Specimen Surface: An Instrument Combining Ion-Plating, Ion-Etching and Vacuum Evaporation and its Applications" H. Soezima and T. Araki, Shimadzu Seisakusho Ltd.

61	4:30 PM	" 'Content Map' and 'Content Profile' as Applications of Automated Electron Probe Microanalyzer" K. Okumura and T. Soya, Geological Survey of Japan and H. Ohyi, JEOL Ltd.
62	4:45 PM	"Integrated Microanalysis System for the Modern Laboratory" B. Kenossey and J. Leitner, Applied Research Laboratories
63	5:00 PM	"A New Transmission Electron Microscope Accessory for an SEM/Electron Probe Microanalyzer" C. Conty and D. Colliaux, Cameca Instruments, Inc.
64	5:15 PM	"Adaption of the Combination SEM/Electron Probe to the Investigation of Biological Specimens" C. Conty and R. Lewis, Cameca Instruments, Inc.

FRIDAY 15 AUGUST 1975

SESSION V - SURFACE ANALYSIS

R. Ogilvie, Chairman

65	9:00 AM	INVITED PAPER: "Electron Spectroscopy for Chemical Analysis" D.A. Shirley, University of California
66	9:30 AM	INVITED PAPER: "Ion Induced X-ray Spectroscopy" W. Reuter, IBM Research Laboratories
	10:00 AM	INTERMISSION
67	10:15 AM	INVITED PAPER: "Nuclear Backscattering Techniques" J. Mayer, California Institute of Technology
68	10:45 AM	"Surface Characterization of Heteroepitaxial (0001) CdS Films" H.E. Mishmash, 3M Company
69	11:00 AM	"Digital Processing of Auger Data" J.B. Bindell and J.W. Colby, Bell Telephone Labs, Inc.
70	11:15 AM	"Combined X-ray Photoelectron (XPS) and Auger Electron (AES) Spectroscopic Studies, Principles and Applications" A. Barrie, F.J. Street and P. Swift, AEI Scientific Apparatus Ltd., Manchester, England and W.A. Wolstenholme, AEI Scientific Apparatus Inc., Elmsford, New York
	11:30 AM	LUNCH

FRIDAY 15 AUGUST 1975

SESSION VI - SURFACE ANALYSIS

Rialto 1 and 2

J. Colby, Chairman

71   1:30 PM   INVITED PAPER: "Monte Carlo Calculation Techniques Applied to Ion Microprobe Analysis" R. Shimizu, Osaka University

72   2:00 PM   "Quantitative Impurity Analysis by Secondary Ion Mass Spectrometry -- Principles; Measurements in GaP" M. Lim, Western Electric Company

73   2:15 PM   "Effects of Sample Surface on Ion Microprobe Analysis of PtRhW Alloys" E.A. Hakkila, J.M. Hansel and W.B. Hutchinson, University of California

        2:30 PM   INTERMISSION

74   2:45 PM   "The Application of Peak Stripping to Problems in Ion Probe Microanalysis" J.R. Hinthorne and R.L. Conrad, Hasler Research Center, Applied Research Laboratories

75   3:00 PM   "Ion Microprobe Analysis for Niobium Hydride in Hydrogen-Embrittled Niobium" P. Williams and C.A. Evans, Jr., M.L. Grossbeck and H.K. Birnbaum, University of Illinois

76   3:15 PM   "A Quadrupole Instrument for Investigations of Electron and Ion Beam Interactions with Solids" J.C. Potosky and D.B. Wittry, University of Southern California

77   3:30 PM   "Performance Evaluation of a Cesium Positive Ion Source for Secondary Ion Mass Spectrometry" H.A. Storms, K.F. Brown and J.D. Stein, General Electric Company, Vallecitos Nuclear Center

78   3:45 PM   "Surface Associations of Toxic Elements in Airborne Particulates: An Ion Microprobe Study" R.W. Linton and D.F.S. Natusch, School of Chemical Sciences and P. Williams and C.A. Evans, Jr., Materials Research Laboratory, University of Illinois

79   4:00 PM   "Qualitative Depth Profile Analysis of Metal Hydride Films, Using an Ion Microprobe Mass Analyzer" W.G. Perkins and J.A. Foesch, Sandia Laboratories

        4:15 PM   LATE BREAKING EVENTS

Fluorescence Excited by the Continuum
and the Accuracy of Electron Probe Microanalysis

Kurt F. J. Heinrich
Institute for Materials Research
National Bureau of Standards
Washington, D. C. 20234

Abstract

After the elimination of the most obvious sources of
error in the conventional correction procedure [1], progress
has been slow in the residual error treatment due to the
simultaneous effects of various sources of uncertainty such
as the primary absorption correction, the electron decelera-
tion, the ionization efficiency, the backscattered losses
and the effects of continuum fluorescence. Unless these
effects are unraveled, the correction scheme cannot be
improved, and partial explanation of the failures of cor-
rection schemes are therefore suspect.

At present, the intensity of fluorescence produced
by continuum excitation can be determined with reasonable
accuracy. Notwithstanding, this mode of excitation is
ignored in most procedures for data reduction (such as
FRAME) — due to the relatively extensive calculations
required for its prediction. It is therefore necessary
to consider the following questions:

1. How can this emission be accurately calculated?

2. How large are the effects of continuum fluorescence
and on which parameters do they depend?

3. What is the effect of continuum fluorescence on
the generated and emitted x-ray intensities, on the x-ray
absorption factors, and on the spatial resolution?

4. Is a simplification of the correction calculation
possible and advisable?

IB

5.   Under which circumstances can the calculation of continuum fluorescence be omitted?

Some of these questions have been discussed by us at a previous opportunity [1].   With previously reported procedures, certain simplifications were made which are now, with the increased availability of large computers, unnecessary.   The following simplifications have been used:

1.   the x-ray mass absorption coefficients are supposed to vary as the third power of the wavelength [2,3],

2.   the distribution in depth of the continuum generation is neglected [2], or

3.   the fluorescence due to continuous radiation traveling in an upward direction is not computed [3]

4.   the variations in the "constant" of Kramers' equation (4) is neglected

5.   the anisotropy of generation of the continuum is neglected.

The procedure embodied in COR includes an accurate calculation of absorption coefficients, and the variation of Kramers' constant with atomic number can be taken into account through the permanent data file.   The distribution in depth of continuum is now better documented through experiments with solid-state as well as with wavelength x-ray spectrometers [4,5].   In particular, the work of Fiori et al. indicates that an expression similar to that for the depth distribution of characteristic generation is a good approximation [5].   Therefore, a more rigorous treatment of the continuum correction can now be used in COR.

Tests with the COR model indicate that the relative generated intensity of continuum fluorescence in pure elements is mainly a function of the critical excitation potential of the respective line, and, to a minor degree,

of operating voltage (figure 1). Due to the greater depth of emission of indirect radiation, the relative emergent intensity of continuum fluorescence, I_c'/I_p', is always lower than the generated intensity. However, the effects of the x-ray emergent angles are not very marked (figure 2).
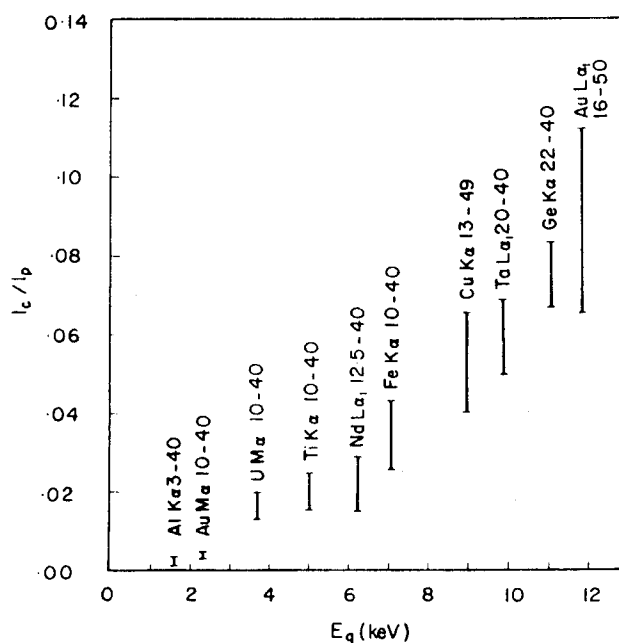
Figure 1. Relative generated intensity of continuum fluorescence for various elements, lines and electron energies (indicated, in keV, after the line notation). Bars indicate the range from lowest (bottom) to highest (top) electron energy. Horizontal scale: critical excitation voltage of the line.
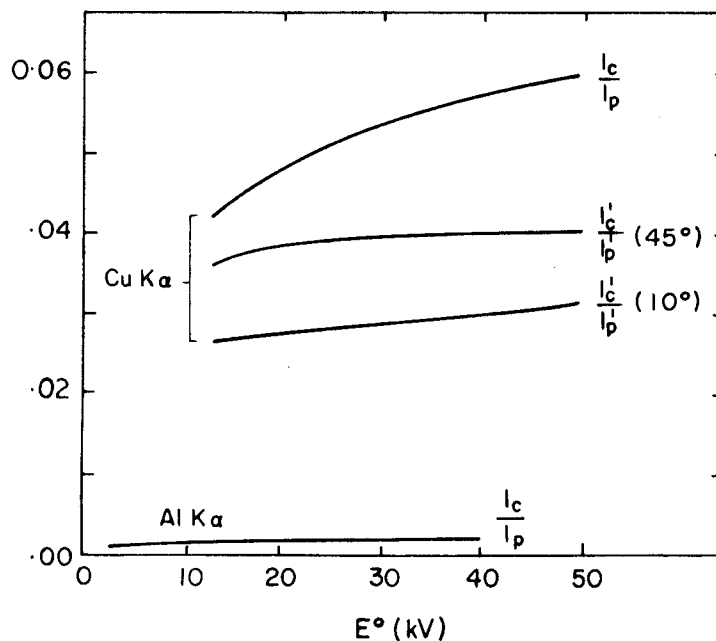
Figure 2. Relative generated (I_c/I_p) and emergent
(I_c'/I_p') intensities of continuum fluor-
escence. E^o = operating potential. The
angles denoted for emergent intensities
are x-ray emergence angles.

In multi-element targets the relative intensity of emergent
continuum fluorescence depends mainly on the mass absorption
coefficients for the continuous radiation. Since the continuum
fluorescence increases with decreasing absorption in the
target, it increases rapidly with decreasing atomic number
of the target. However, since the absorption of the target
changes abruptly at the absorption edges, their effect on
the continuum correction is important.

The refinements of Kramers' equation only improve
marginally the overall quality of analysis because their
effects are of the same order of magnitude as uncertainties
in other corrections. A minor but significant effect can
be caused by the uncertainties in the fluorescent yield
and, for L lines, also in the Coster-Kronig coefficients.
The use of L lines of elements of atomic number above 70
can result in significant continuum fluorescence and
should be discouraged since good results, with low line-
to-background ratios and negligible fluorescence contri-
bution, can be obtained with M lines. The region in which
significant effects (>0.5 weight percent) may be unavoidable
is in K lines of elements of atomic numbers between 25 and
30, for which the corresponding L lines may be too soft for
routine analysis. According to these results, the omission
of the correction will not cause serious problems in
quantitation provided that the use of short-wavelength
lines is avoided where possible. The use of simplified
models may also be admissible, but it does not carry promise
of significant advantages since the most tedious feature
of fluorescence due to the continuum, namely separate
integration of regions between absorption edges, cannot
be avoided.

A serious consequence of continuum fluorescence is
the concomitant loss of spatial resolution. When large
concentration gradients occur, particularly in targets
of low mean atomic number, serious misinterpretations
can occur.

The accurate correction for the continuum fluorescence
effect in the experimental determination of primary absorp-
tion was particularly useful. After the effects of continuum
fluorescence were compensated, a very simple equation for the
primary absorption factor could be proven to be applicable
to all elements and lines.

References

[1] Myklebust, R. L., Yakowitz, H. and Heinrich, K. F. J.,
     Proc. 5th National Conf. EPASA, New York, paper 11
     (1970).

[2] Hénoc, J. in NBS Special Publication 298, Heinrich,
     K. F. J., ed., p. 197, National Bureau of Standards,
     Washington, D. C. 20234 (1968).

[3] Springer, G., Jb. Miner. Abh. 106, 241 (1967).

[4] Rao-Sahib, T. S. and Wittry, D. B., Proc. 6th Inter-
     national Cong. on X-ray Optics and Microanalysis,
     Tokyo (1972).

[5] Fiori, C. E., Myklebust, R. L., Heinrich, K. F. J. and
     Yakowitz, H., Prediction of Continuum Intensity in
     Energy-Dispersive X-ray Microanalysis, submitted to
     Analytical Chemistry.

MONTE CARLO CALCULATION OF ELECTRON BACKSCATTER YIELD
FROM THIN FILMS ON THICK SUBSTRATES

David F. Kyser
IBM Research Division
San Jose, California 95193

Monte Carlo simulation of electron scattering and energy loss in a thin film - thick substrate target has been utilized to calculate the total electron backscatter yield η. The Monte Carlo model is the same as that used previously [1] for calculation of x-ray emission in quantitative electron probe microanalysis. The model includes electron backscattering from the substrate, as well as from within the film. This single-scattering Monte Carlo simulation contains experimental variables such as incident electron beam energy E_0 and angle α , film thickness t and composition, and substrate composition.

Tables 1 and 2 show specific results calculated for the extreme cases of Al film - Au substrate and Au film - Al substrate with $\alpha = 0°$ to the surface normal These results agree with the magnitude and weak energy-dependence of η for <u>thick</u> Al which has been observed with "composite" targets [2], but is less successful for the weak but opposite energy dependence of η observed for <u>thick</u> Au [2,3]. However, the <u>average</u> value for η (Au) is in good agreement with the experimental data. The wrong energy-dependence for η (Au) is due to the failure of the Born approximation in the Bethe energy loss equation with decreasing E_0 and high atomic number Z targets such as Au. For each calculation shown in Tables 1 and 2, 10^4 incident electrons were simulated to provide a calculated standard deviation of 1% (relative) in η due to statistical fluctuations inherent in the Monte Carlo procedure.

Comparison of these Monte Carlo results with experimental data on thin films of Al/Au substrate and Au/Al substrate [4,5] has been made. However this experimental data was obtained with the use of bias grids placed between the target and the collecting electrodes. No corrections were made for secondary electron emission and

backscattering from these grids. Hence this data for the films is in error, and also does not agree with the data for thick samples obtained from "composite" targets without a grid [2,3]. The Monte Carlo calculations in Tables 1 and 2 are in good agreement with the latter data from thick targets, and show a smooth transition from η (substrate material) to η (film material) as the film thickness is increased from 0 to ∞ at constant E_0.

For the case of a Au film - Al substrate in Table 2, the dependence of η (calculated) versus t (film) is <u>linear</u> for t $\leq$ 250Å (10kV), t $\leq$ 1,000Å (20kV), and t $\leq$ 2,000Å (30kV). This suggests a new technique for measuring film thickness, in an SEM or electron microprobe, utilizing a single measurement of electron backscatter yield. For the case of Al film - Au substrate there is not a large range of linear dependence, but the calculations in Table 1 could still be used to measure an unknown Al film thickness. Such a techique relies upon a large difference between $\bar{Z}$ (film) and $\bar{Z}$ (substrate) for maximum sensitivity, but can accomodate elements which are common to both the film and substrate in multi-element targets. The latter case cannot be treated easily with x-ray emission measurements when the film thickness is small compared to the electron range. The special case of a free-standing thin film can be easily simulated by elimination of the substrate or assigning a very low $\bar{Z}$ to the substrate. Monte Carlo calculations for this case are in progress and will be compared with existing experimental data [6] in a separate publication.

1. D. F. Kyser and K. Murata, IBM J. Res. Dev.<u>18</u>, 352 (1974).

2. K. F. J. Heinrich, <u>Proc. 4th Int. Conf. on X-ray Optics and Microanalysis</u> (Hermann, Paris, 1966), p. 159.

3. H. E. Bishop, ibid., p. 153

4. J. E. Holliday and E. J. Sternglass, J. Appl. Phys. <u>30</u>, 1428(1959).

5. N. G. Nakhodkin, A. A. Ostroukhov, and V. A. Romanovskii, Sov. Phys. - Sol. St. <u>4</u>, 1112 (1962).

6. V. E. Cosslett and R. N. Thomas, Brit. J. Appl. Phys. <u>16</u>, 779 (1965).

2C

TABLE 1

ELECTRON BACKSCATTER YIELD FOR Al FILM - Au SUBSTRATE

$E_O = 10kV$		$E_O = 20kV$		$E_O = 30kV$	
t_{Al} (Å)	η	t_{Al} (Å)	η	t_{Al} (Å)	η
0	.520	0	.497	0	.482
500	.505	500	.488	----	----
1,000	.467	---	----	----	----
1,500	.422	---	----	----	----
2,000	.372	2,000	.478	2,000	.477
3,000	.256	---	----	----	----
4,000	.179	---	----	----	----
5,000	.161	5,000	.410	5,000	.451
10,000	.161	10,000	.256	10,000	.405
		15,000	.156	15,000	.333
		20,000	.149	20,000	.258
		∞	.152	∞	.154

TABLE 2

ELECTRON BACKSCATTER YIELD FOR Au FILM - Al SUBSTRATE

$E_O = 10kV$		$E_O = 20kV$		$E_O = 30kV$	
t_{Au} (Å)	η	t_{Au} (Å)	η	t_{Au} (Å)	η
0	.161	0	.152	0	.154
125	.264	125	.182	125	.166
250	.363	---	----	---	----
500	.490	500	.265	500	.195
1,000	.520	1,000	.390	1,000	.257
		1,500	.457	1,500	.312
		2,000	.489	2,000	.360
		∞	.497	∞	.482

CROSS SECTIONS FOR IONIZATION OF

INNER-SHELL ELECTRONS BY ELECTRON IMPACT*

C. J. Powell

National Bureau of Standards, Washington, D.C. 20234

A survey has been made of available theoretical and experimental cross-section data for the ionization of inner-shell electrons by electron impact in the energy range of interest to electron probe microanalysis and to Auger-electron spectroscopy. The data base is unfortunately limited so of necessity the discussion is limited to K-shell and L-shell ionization of light atoms.

Calculated, semiempirical and experimental cross-section data have been intercompared graphically and through fits to the linearized Bethe equation for inner-shell ionization (the Fano plot).[1] Almost all of the data can be satisfactorily fitted over the range $4 \lesssim U_{n\ell} \lesssim 30$ and values can be obtained of the "effective" Bethe parameters $b_{n\ell}$ and $c_{n\ell}$.[†] Values of the parameter $b_{n\ell}$ have also been derived from photoabsorption data and were found to be consistent with the ionization data if account was taken of the distribution of differential oscillator strength with respect to excitation energy and the consequent expected variation of $b_{n\ell}$ with incident electron energy. The derived "effective" Bethe parameters should not therefore be used outside the range of each fit.

Experimental values of $Q_K E_K^2$ appeared to lie on a common curve when plotted as a function of U_K. These values agreed quite well with the theoretical results of Rudge and Schwartz[2] for $5 < U_K < 26$ and the results of McGuire.[3] It therefore appears that values of Q_K for light atoms can be obtained by appropriate scaling. A greater spread existed in the plot of calculated and measured values of $Q_{L_{23}} E_{L_{23}}^2$ as a function of $U_{L_{23}}$ than for the case of K-shell ionization. There did appear to be variation in the magnitude of $Q_{L_{23}}^2$ as a function of Z (for a given value of $U_{L_{23}}$) but the magnitude of the variation was hard to establish on account of discordant data. Modest agreement was found, however,

between the experimental results of Vrakking and Meyer[4] and of Christofzik[5] and the calculations of McGuire.[3]

The derived effective values of b_K and c_K from fits to experimental values of Q_K were found to be in the ranges 0.88 to 0.97 and 0.62 and 0.79, respectively (based on data for C, N, O, Ne and Al). The corresponding derived values of $b_{L_{23}}$ and $c_{L_{23}}$ were in the ranges 0.38 to 0.91 and 0.55 to 0.85, respectively[3] (based on data for P, S, Cl and Ar). These values of $b_{n\ell}$ are appreciably higher while the values of $c_{n\ell}$ are appreciably lower than those recommended many years ago by Mott and Massey[6] (on account of the distribution of oscillator strength mentioned above). The recent calculations and measurements show that inner-shell ionization cross sections are appreciably (40 to 50%) higher than those calculated with the Mott and Massey parameters.

1. M. Inokuti, Rev. Mod. Phys. 43, 297 (1971).

2. M.R.H. Rudge and S. B. Schwartz, Proc. Phys. Soc. (London) 88, 563 (1966).

3. E. J. McGuire, J. de Phys. C4, 37 (1971); Phys. Rev. A3, 267 (1971); private communication.

4. J. J. Vrakking and F. Meyer, Phys. Rev. A9, 1932 (1974).

5. H.-J. Christofzik, Diplom-Thesis, University of Münster (1972).

6. N. F. Mott and H.S.W. Massey, The Theory of Atomic Collisions (Oxford University Press, second edition, 1949), pp. 243-244.

† The Bethe expression for the cross section, per atom, for ionization of the $n\ell$ shell is

$$Q_{n\ell} = \frac{6.51 \times 10^{-14}}{E\, E_{n\ell}}\; Z_{n\ell}\; b_{n\ell}\; \ell n\left[\frac{c_{n\ell}\, E}{E_{n\ell}}\right]\; cm^2$$

where $Z_{n\ell}$ is the number of electrons in the $n\ell$ shell and the energies E and $E_{n\ell}$ are expressed in eV.

THEORETICAL PERFORMANCE OF BLAZED GRATINGS AT GRAZING INCIDENCE

D. B. Wittry

Department of Materials Science
and Electrical Engineering
University of Southern California
Los Angeles, California 90007

and

Kenjiro Tsutsumi

College of Engineering
University of Osaka Prefecture
Sakai, Osaka, Japan

The problem of diffraction of x-rays by a blazed grating at grazing incidence was studied by assuming that the usual approach to calculating the intensity of x-rays diffracted by crystals will give approximately the dependence of the relative efficiency on various parameters such as angle of incidence, wavelength and blaze angle. This approach involves using the diffraction condition:

$$n\lambda = d(\cos \theta_i - \cos \theta_r) \tag{1}$$

and the form factor of the grating defined by:

$$|F|^2 = \mathrm{Re}[\int_{x_m}^{d} e^{(2\pi i\delta)/\lambda}(\Delta I_1/I_1)]^2 \tag{2}$$

In which θ_i and θ_r are the grazing angles of incidence and reflection
x_m and d are the x coordinates of the points where the incident rays strike the lowest and highest parts of a single groove (measured in the plane of the grating).
$(2\pi\delta)/\lambda$ is the phase shift for rays scattered by a point on the grating surface at distance x from the x coordinate of the highest point of the adjacent groove.
$\Delta I_1/I_1$ is the fraction of the energy incident per unit time on a single groove that strikes the region between x and x + dx.

For conventional use of a grating (rays incident toward the uphill side of the grooves):

$$\Delta I_1/I_1 = dx/(d-x_m) \tag{3}$$

and

$$x_m = d\Delta\theta/(\theta_i + \Delta\theta) \tag{4}$$

where $\Delta\theta$ is the blaze angle.

Using the approximation that θ_i, $\Delta\theta$ and θ_r are all small, the form factor for an ideal linear groove profile is found to be:

$$|F|^2 = [A(d - x_m)/d]^{-2} \sin^2[A(d - x_m)/d] \qquad (5)$$

where $A = \pi[n - \Delta\theta(\theta_i + \theta_r)(d/\lambda)]$ \qquad (6)

and $\theta_r = [(2n\lambda)/d + \theta_i^2]^{\frac{1}{2}}$ \qquad (7)

The results for a typical case are shown in Figure 1. For convenience, the wavelengths are given in terms of λ/λ_B where λ_B is the wavelength for maximum intensity in the first order. This is the blaze wavelength given in the small angle approximation by:

$$\lambda_B = 2d\Delta\theta(\theta_i + \Delta\theta) \qquad (8)$$

The results of Eq. (4) and Figure 1 indicate the relative intensity that should appear in different orders since the intensity in different orders should be directly proportional to the form factor. Thus, it can be seen that the blazed grating should concentrate radiation in a given order for the grazing incidence case, just as it does in the more familiar case of non-grazing incidence and longer wavelengths.

The absolute reflection efficiencies will involve other considerations in addition to the form factor, the most important being the variation of the reflection coefficient of soft x-rays from a plane surface with angle of incidence. For typical cases of gratings used in soft x-ray spectrometers, $d/\lambda \approx 100$ so it should be possible to take account of varying reflectance by a simple multiplying factor.

Experimental results reported in the literature[1-3] tend to confirm the results given in Eq. (4) and Figure 1 provided d is not too small (i.e. for d = 16,666 Å corresponding to 600 lines/mm). For smaller d values, it is often found that the blaze wavelength obtained experimentally does not agree with the value predicted by Eq. (8).[4] Also, it is sometimes found that the intensity in the zero order is highest.[4] These discrepancies between theory and experiment can be understood if it is assumed that the grating does not have a linear profile. In fact, because the blaze wavelength shifts to smaller values when d is reduced, small deviations from a linear groove profile are important. This may be seen by considering the blaze condition as shown in Figure 2. When the blaze condition is satisfied, the diffraction condition is the same as Bragg's law for diffraction by crystals, namely

$$n\lambda = 2d'(\sin \theta_i') \text{ with } \theta_i' = \theta_r' \qquad (9)$$

$$\approx 2d\Delta\theta \, \theta_i' \, .$$

Thus deviations from a linear groove profile of the order of the blaze wavelength will be important. For example, if the values of d, $\Delta\theta$, and θ_i predict a blaze wavelength of about 20 Å, the deviation from a linear groove profile can be no more than about 7 atomic diameters (based on the atomic radius of Al). Hence, it will be difficult to achieve the theoretically predicted performance at short wavelengths with blazed gratings fabricated by the usual procedures of ruling and replicating.

REFERENCES

1. A. P. Lukirskii and E. P. Savinov, Opt. Spectrosk, Eng. Trans. 14 (1963), 142.

2. J. B. Nicholson and M. F. Hassler, Advances in X-ray Analysis, 9 (1966), 420.

3. G. Date, Y. Nakajima, Y. Ohmori, T. Shiraiwa and N. Fujino, Proc. Int. Cont. X-ray Optics and Microanalysis, ed. G. Shinoda, K. Kohra and T. Ichinokawa (Univ. Tokoyo Press, 1972), p. 233.

4. Private communication: E. Lowen, Analytical Systems Division, Bausch and Lomb, Rochester, N. Y. 14625.
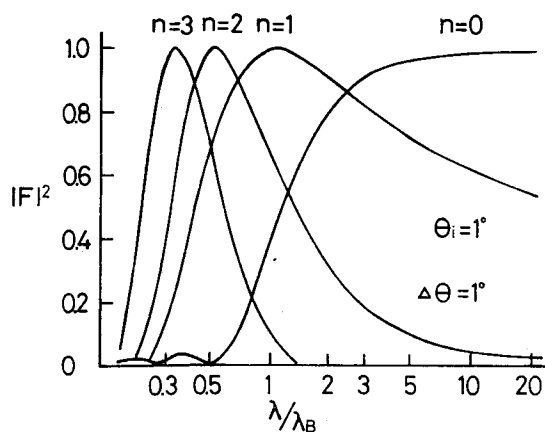
Fig. 1 Form Factor $|F|_n^2$ vs normalized wavelength λ/λ_B.
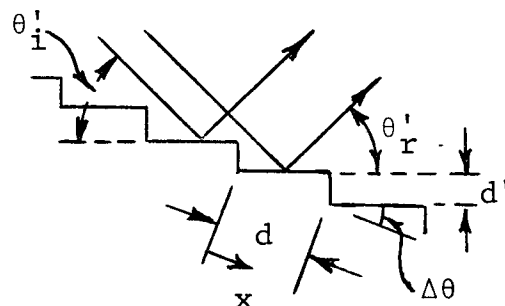
Fig. 2 Diffraction at the blaze condition.

BEHAVIORS OF ELECTRONS IN A DEEP REGION OF METALLIC TARGET

G. Shinoda
S. Nishigaki and Y. Yasuno
Rigaku-Denki Co., Haijima, Tokyo, 196 Japan

M. Takahashi
Japan Women's University, Bunkyo-ku, Tokyo, 112 Japan

Usually radiation damage due to electrons is investigated using high energy electrons.   However, radiation damage would be expected by much lower energy electrons.   It is believed that the range of such low energy electron is small. It is true, but according to the Monte Carlo calculation of behaviors of electrons ia a specimen some of electrons,   though they are very few percent, take nearly straight paths and penetrate considerable depths beyond the range of electrons. For such calculation Bethe law of energy loss is used.   However, it concerns on the average electrons and does not on individual electrons.   Therefore among many electrons there would be an electron whose energy loss is very small and cosequently it can keep its energy and momentum until a considerable depth. Probobility of such case would be very small but if we use very much electrons we can expect significant radiation damage even in a deep region of the specimen.

Figure 1 is a sectional view of a copper alloy containing 1.8% beryllium bombarded by 10^{25} electrons/cm^2 with accelerating voltage of 35 kV.   Until a depth of 500 μm significant radiation damage, disintegration of crystal grains and precipitation of intermetallic compounds, has been observed.   This means that the action of electron beam has dual faces, i.e. mechanical action like cold work and a thermal-like effect approaching to the equilibrium state.   The latter would be liable to be conceived as an effect of temperature rise, however the surface temperature did not exceed 300° C, while the structure and physical properties correspond to those annealed at a temperature higher than 600° C.   Details have been already reported on the Moscow Conference on X-ray Optics and Micro-analysis, last year.

The same behaviors were observed in copper-tin and copper-zinc alloys and already published[1]

In the case of front surface of aluminum we can observe remarkable zone refining action of electron beam.   Similar phenomenon was observed in a copper-tin alloy.   At the rear surface, i.e. cooling water side, even in a target of 3 mm thickness, remarkable electrolytic etching action due to sub-excitation energy electron has been observed.   From the broadening of etch pattern the manner of lateral diffusion of low energy electrons would be postulated.

Next problem is the determination of electron dose which is necessary to give rise to such damage effect.   For this purpose a chill cast copper alloy containing 15% tin has been used.   With 5 x 10^{23} electrons/cm^2 some change of

dendritic structure as shown in Fig. 2 has been observed in the depth of 50 um below the surface. Also formation of twins due to mechanical action of electrons has been observed. Similar change of dendrite has been found in the depth 100 μm for 10^{25} electrons/cm^2.

In the case of copper-beryllium alloy the effect of electron bombardment near the surface of the specimen corresponds to the temperature rise of more than 300° C, the surface temperature being 300° C. Therefore, in the case of copper-tin alloy the structure should correspond to that of 600° C annealing. This corresponds to the beginning of disappearance of dendritic structures.

----

(1)   G. Shinoda and M. Takahashi ; Japan Women's Univ. J., No. 17
(1972) 217.

Fig. 1.   Sectional view of copper-1.8% beryllium alloy after electron bombardment of 1.5 mA, 350 hrs, 35 kV, target area being 0.1 x 1 mm   x 20.
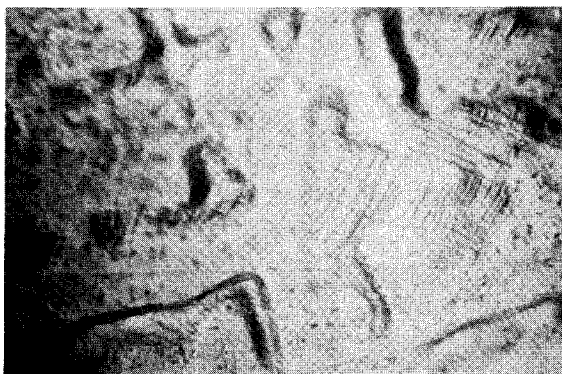
Fig. 2.   Copper-15% tin alloy after bombardment of 5 x 10^{23} electrons/cm^2.   50 μm below the surface.   x 2000.

Improvement in X-ray Spatial Resolution at Phase Boundaries

J. I. Goldstein and E. Randich

Department of Metallurgy and Materials Science

Lehigh University, Bethlehem, Pa.   18017

The volume in which primary X-rays are produced is much larger than the size of the focused beam in solid samples. For analysis of solid samples, the X-ray beam diameter is usually of the order of 1-2 μm. When steep concentration profiles are encountered, such as at a phase boundary, the finite volume for which X-rays are excited in a solid sample causes the true concentration profile to appear "smeared." If a discontinuity in composition occurs, for example at a phase boundary, it is impossible to obtain the compositions at the interface. The concentration profile which is measured is the mathematical convolution of the probe function and the true concentration profile. It is therefore of interest to improve the X-ray spatial resolution at these phase boundaries.

A method has been developed by Gilmour[1-2] in which a convoluted calculated profile is obtained which can be compared to measured probe data at phase boundaries. In this method the lateral or spatial distribution of the emitted characteristic X-ray line being investigated must be obtained experimentally. The X-ray spatial distribution is assumed Gaussian and is described by a probe function $f(x)$ with an appropriate parameter d. Before convolution the true concentration profile must be calculated. The convoluted profile is obtained mathematically by translating the X-ray probe function across the calculated concentration profile.

Figure 1 illustrates the use of the convolution process. A 4.1 wt% Ni, 2.1 wt% P, 93.8 wt% Fe alloy was cooled from 900°C to 685°C at 5×10^{-4}°C/sec. The Ni compositional gradients for phosphide (Ph, $(FeNi)_3P$) growth in ferrite (α) were calculated using a ternary growth model developed by Randich and Goldstein.[3] The values C_{Ni}' (Ph) and C_{Ni}' (α) represent the calculated phase boundary interface compositions in Ph and α. The convoluted profile was obtained using a probe parameter d of 0.65 μm measured with probe operating conditions of 20 kv and 0.05 μA. A measured Ni profile

for the small 10.5 μm wide phosphide agrees very well with the convoluted calculated profile.

A more direct method of improving X-ray spatial resolution is to obtain a smaller X-ray beam diameter. Special transmission electron microscope (TEM) instruments have now been developed in which X-ray analysis can be performed on selected submicron areas in the thin foil samples used for microscopy. These thin foil samples are <2000Å in thickness. The first instrument developed to perform this type of analysis is called EMMA (Electron Microscope Micro Analyzer) and was first described by Duncumb.[4] In the EMMA-4 instrument,[5] another condenser lens is introduced into the electron optical column above the specimen and serves to reduce the size of the TEM electron beam impinging on the sample to about 1500Å. The 100 kv incident beam is not enlarged by scattering (elastic and inelastic) as it passes through the thin specimen due to the relatively large mean free path of the 100 kv electrons. Therefore X-rays are generated from a region essentially the same diameter as the electron beam. This X-ray spatial resolution is an order of magnitude better than that obtained with standard thick samples.

The X-rays produced in the EMMA analysis are measured with a solid state detector allowing rather low beam currents and small spot sizes to be produced. Figure 2 shows two Ni concentration profiles taken across an α (ferrite)-γ (austenite) interface of the Edmonton meteorite using an EMMA instrument at the University of Manchester, England. The instrument uses a conventional W filament and the operating conditions were 100 kv, 4×10^{-9}A beam current and a 1500Å electron beam spot size. The Fe and Ni Kα X-ray data were reduced to chemical composition by the method of Cliff and Lorimer.[6]

A comparison of the EMMA data to that taken with an ARL microprobe, operated at 20 kv, 0.05 μA specimen current on a different α/γ interface in a solid specimen of the Edmonton iron meteorite can be made using Figure 3. The increased X-ray spatial resolution is evident. The EMMA instrument is the first of a new generation of TEM instruments in which submicron X-ray analysis can be performed. The use of smaller beam diameters, higher brightness guns and X-ray energy dispersive detectors placed at positions to optimize X-ray counting should enable one to obtain an X-ray spatial resolution of ≤200Å.

References

(1) J. B. Gilmour, "The Role of Manganese in the Formation of Pro-
eutectoid Ferrite," Ph.D. Thesis, McMaster University (1970).

(2) J. B. Gilmour, G. R. Purdy and J. S. Kirkaldy, Met. Trans., 3,
(1972) p. 3213.

(3) E. Randich and J. I. Goldstein, "Non-Isothermal Finite Diffusion-
Controlled Growth in Ternary Systems," submitted to Met. Trans. (1975).

(4) P. Duncumb, in "The Electron Microprobe," ed. T. O. McKinley,
K. F. J. Heinrich and D. B. Wittry, (1966) p. 490.

(5) J. A. Chandler, in "Proceedings of the Sixth International Conference
on X-ray Optics and Microanalysis," ed. G. Shinoda, K. Kohra and
T. Ichinokawa, (1972) p. 323.

(6) G. Cliff and G. W. Lorimer, "The Quantitative Analysis of Thin
Specimens," in press, J. Microscopy (1975).
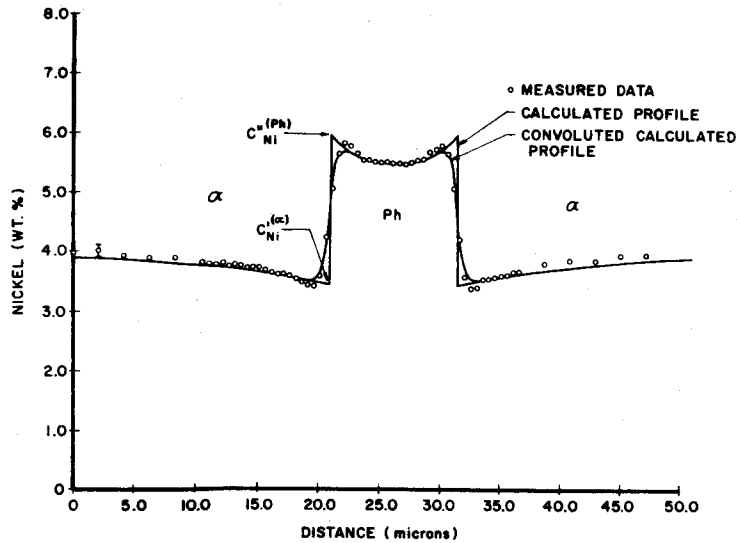
Figure 1: Comparison of convoluted calculated
Ni profile and measured electron probe data from
a phosphide grown during cooling of a 4.1% Ni,
2.1% P, 93.8% Fe alloy.
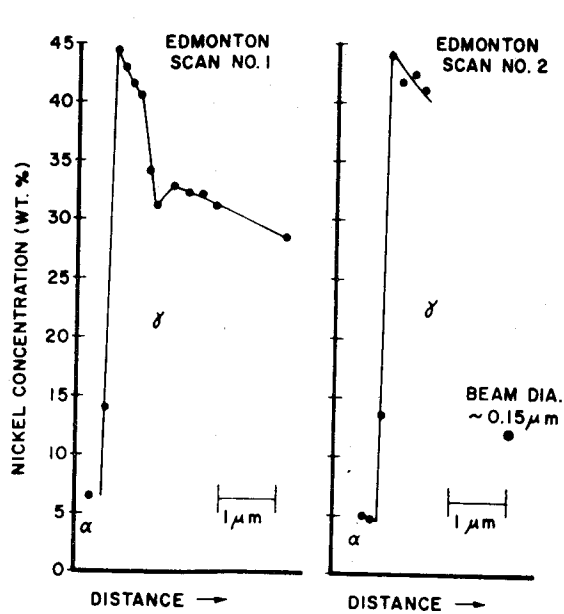
Figure 2: Ni concentration profiles
taken with EMMA across the α/γ interface
of the Edmonton iron meteorite.
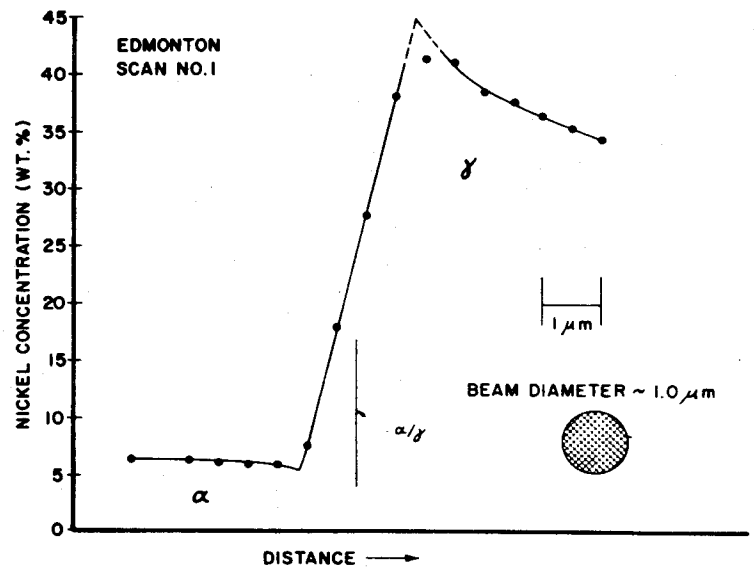
Figure 3: Electron microprobe scan
across an α/γ boundary in the Edmonton
iron meteorite. The X-ray source size
is ~1.0 μm. Compare to Figure 2.

A SIMPLE CORRECTION FOR BACKSCATTERING FROM INCLINED SAMPLES

J. C. Russ
EDAX International, Inc.
P.O. Box 135
Prairie View, Illinois   60069

With the use of the SEM as a microprobe, using either wavelength - or energy-dispersive spectrometers, the sample surface is frequently not perpendicular to the electron beam. Most quantitative correction methods allow the use of an "effective takeoff angle" given by cosec $\Psi_{effective}$ = sin Φ cosec Ψ_{actual} where Φ is the actual angle between the specimen surface and electron beam axis (90^0 for normal incidence). This corrects the absorption path length for the specimen geometry, and has given adequate results in many cases in which a constant instrument geometry is employed.

In many SEM applications, however, the specimen geometry varies from sample to sample, and furthermore may be different for standards and unknown. In the latter case the Z-A-F type of model can still be used by evaluating the terms for the standard at its actual geometry, but an additional correction must be made to R, the effective current or backscatter correction factor. The models presently used for R express it as a function of overvoltage Uo and atomic number Z.

We have derived a crudely simple yet apparently effective model to relate R in the perpendicular case to that for a tilted sample. Using the spherical model of Archard and Mulvey, we assume the electrons penetrate without energy loss to a characteristic depth x and then diffuse outward in all directions producing x-rays as they go. To relate the depth x to the effective current factor R we further assume that the electron stopping power in the matrix is independent of energy, which means that the remaining electron energy decreases linearily with ζ, the distance from the center of the sphere.

Figure 1 shows the resulting model. The portion of the unit sphere protruding from the surface represents the fraction of incident energy that escapes from the sample due to backscattering, and can be calculated as follows. Since the remaining electron energy is proportional to 1-ζ, the total energy in the sphere is

$$\int_0^1 4\pi\zeta^2 (1-\zeta)d\zeta = \frac{\pi}{3}$$

and the energy in the protruding segment is

$$\int_x^1 2\pi\zeta (\zeta-x) \cdot (1-\zeta)d\zeta = \pi (\frac{1}{6} - \frac{x}{3} + \frac{x^3}{3} - \frac{x^4}{3})$$

the effective current factor R is

$$R = 1.0 - \frac{energy\ in\ segment}{total\ energy} = \frac{1}{2} + x - x^3 + \frac{x^4}{2}$$

For an inclined surface (Figure 2) the original penetration depth is the same but the distance of protrusion is changed and y = x cos S where the tilt angle S is 90^0 - Φ. The ratio of $R_{inclined}$/R_{normal} thus becomes independent of the fictitious x variable.

7B

These calculations yield a family of curves for $R_{inclined}$ versus R_{normal} as shown in Figure 3. Reed's[2] data points for 45^0 show reasonable agreement. Practical use in quantitative analysis using standards and unknowns tilted by up to 60^0 relative to each other has not shown any significant or systematic discrepancy that can be attributed to the model.

References

1. G.D. Archard and T. Mulvey, Proc. Symposium on X-Ray Optics and Microanalysis, Stanford, 1962, Academic Press, New York, 1963, p. 393.

2. S.J.B. Reed, J. Phys. D, Appl. Phys., 4, 1971, p. 1910-1912.
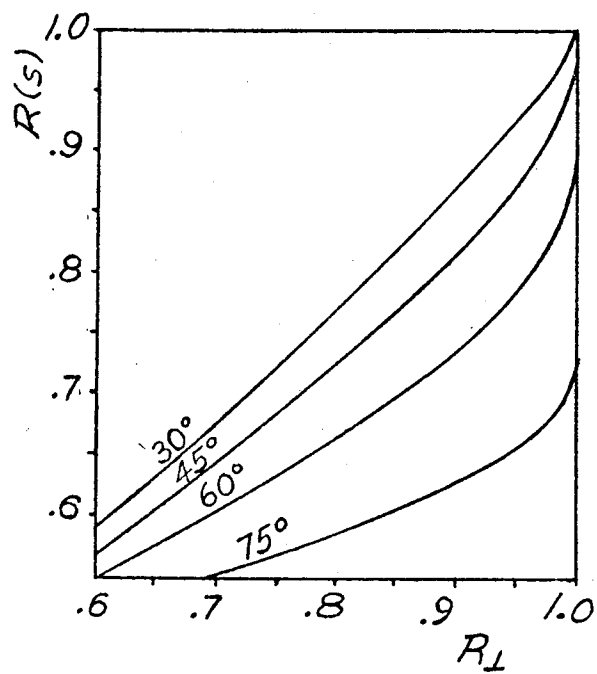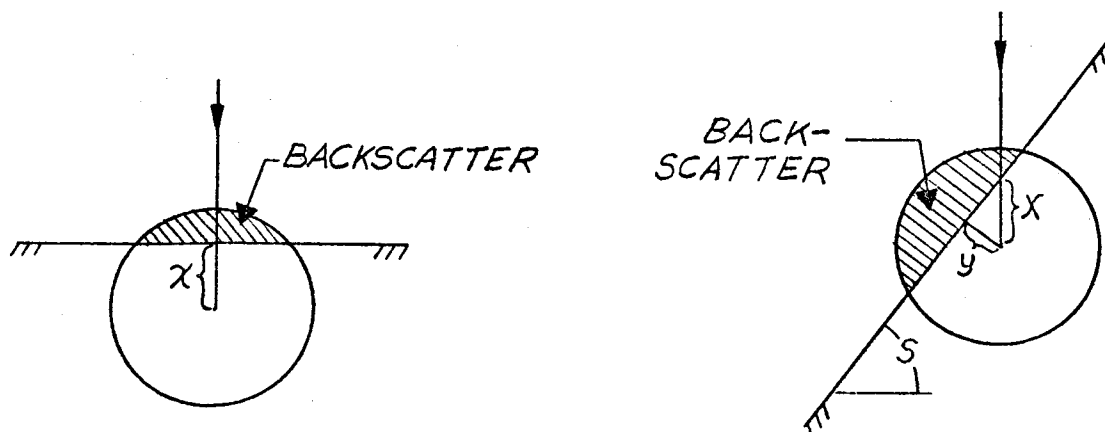
BACKSCATTER

BACK-
SCATTER

EVALUATION OF INSTRUMENTAL AND PHYSICAL LIMITATIONS ENCOUNTERED IN THE STUDY OF TWO PHASE STRUCTURES

R.B. Bolon and M.D. McConnell
General Electric Corporate Research & Development

Microprobe analysis of small inclusions and multi-phase structures is frequently complicated by effects not generally accounted for in conventional correction procedures. It is well known that errors can originate from the generation and detection of unwanted x-rays from either instrumental and/or sample related phenomena[1]. Potential causes include: electron beam "tails", fluorescence by the final aperture[2], back scattered electrons, beam penetration and spreading, sample smearing and characteristic or continuum fluorescence of adjacent phases.

Frequently such problems can be minimized by the judicious use of masking, shielding and collimation, by choosing optimum operating conditions and by analyzing only the largest regions representing specific phases of interest. Unfortunately, the latter option is not always satisfactory in which case the analyst must determine the relative magnitudes of possible errors. This paper presents an experimental study which utilizes well characterized two phase structures for evaluation purposes.

REFERENCES

1. R.B. Bolon and E. Lifshin, Scanning Electron Microscopy/1973, (ed.) O. Johari, IIT Research Institute, Chicago, Illinois, 1973, pp. 285-292.
2. J. Geller, JEOL Newsletter, 2, No. 3, April 1975.

THE MINIMIZATION OF SIZE AND GEOMETRIC EFFECTS IN THE QUANTITATIVE ANALYSIS OF MICROPARTICLES WITH ELECTRON BEAM INSTRUMENTS

John T. Armstrong, Department of Chemistry
Peter R. Buseck, Departments of Chemistry and Geology
Arizona State University, Tempe, Arizona 85281

In order to perform quantitative analyses on microparticles with electron beam instruments, it is necessary to account for the effects of the samples' small sizes and irregular shapes on x-ray production and absorption. We have described theoretical correction procedures which account for these effects and permit routine, accurate ($\pm <8\%$ relative) quantitative analyses of unpolished microparticles with use of conventional thick, polished materials as standards (1,2). In this paper we will discuss the use of these procedures to determine the best experimental conditions for analyzing particles.

The ratio of intensities of an element (A) in a particle to that in a standard can be expressed by the general equation:

$$\frac{I_{A,ptc}}{I_{A,std}} = \frac{C_{A,ptc}}{C_{A,std}} \cdot \frac{R_{A,ptc}S_{A,std}}{R_{A,std}S_{A,ptc}} \cdot \frac{1 + r_{f,A,ptc}}{1 + r_{f,A,std}} \cdot$$

$$\left[\frac{\int_{\rho z=0}^{\zeta} \frac{1}{a} \int_{\rho y=\alpha_1(\rho z)}^{\alpha_2(\rho z)} \int_{\rho x=\beta_1(\rho y,\rho z)}^{\beta_2(\rho y,\rho z)} \phi'(\rho x,\rho y,\rho z,D) \; e^{-\mu g(\rho x,\rho y,\rho z,D,\psi)} d(\rho x)d(\rho y)d(\rho z)}{\int_{\rho z=0}^{\infty} \phi(\rho z) \; d(\rho z)} \right]_{A,ptc}$$

$$\Bigg/ \left[\frac{\int_{\rho z=0}^{\infty} \phi(\rho z) \; e^{-\mu \csc\psi \, \rho z} \; d(\rho z)}{\int_{\rho z=0}^{\infty} \phi(\rho z) \; d(\rho z)} \right]_{A,std}$$

where: ζ = limit of excited electron penetration in a particle,
   a = area of the portion of the electron beam that is striking the particle,
   $\phi'(\rho x, \rho y, \rho z, D)$ = the relative production of primary x-rays as a function of position in the particle,
   $g(\rho x, \rho y, \rho z, D)$ = the x-ray path length in the direction of the detector as a function of position in the particle,
   $\alpha_{1,2}(\rho z)$, $\beta_{1,2}(\rho y, \rho z)$ = functions expressing the geometric limits of the particle.

$(r_{f,A,ptc}$, the particle fluorescence correction, can be a complex hexa-integral function, and is generally ignored or set equal to that in a thick, flat material.)

We have derived expressions for $\phi'(\rho x, \rho y, \rho z, D)$, $g(\rho x, \rho y, \rho z, D, \psi)$ and the limits of integration for a variety of idealized particle geometries. The geometries chosen correspond to the range of shape effects experimentally observed for particles. Utilizing these equations, it is possible to determine the effects of particle geometry on intensity ratios of particle to standard, k_A, and on their ratios for two elements, $R_{A/B} = k_A/k_B$. These simulations compare well with experimentally determined values (see Figure 1).

In particle analyses, the diameter of the particle can be accurately measured by visual observation through the optical system of an electron microprobe or in an SEM image. The particle shape, thickness, and density can be approximated less accurately. The accuracy of a quantitative analysis of a microparticle depends upon the accuracy of these measurements.

In order to increase the inherent accuracy of microbeam analyses of microparticles, it is advantageous to find experimental conditions which result in a minimum variation of $R_{A/B}$ values for changes in particle mass diameter (ρD), mass thickness (ρT), and shape. Three factors affect the degree of size and geometric dependence: (1) the sample composition, (2) ψ, the spectrometer take-off angle, and (3) E_o, the electron beam accelerating potential. The first two factors are fixed by the sample to be analyzed and the instrument to be used. The accelerating potential, however, can be readily modified to minimize particle geometry effects.

Utilizing our correction procedures, we have simulated $R_{A/B}$ values for a variety of shapes, sizes, and thicknesses, using a variety of sample compositions, instrument take-off angles, and accelerating potentials. For convenience in the

simulations, the standards were chosen to be thick, polished materials with the same composition as the samples.

Figures 2-5 show some of the results of our simulations. The curves enclose the range of $R_{A/B}$ values given in the simulations by our geometric models. The effect of varying accelerating potential is shown in Figure 2. At too low an accelerating potential, surface effects predominate and the difference between the intensity ratios predicted for flat topped and non-flat topped particles becomes significant. At too high of an accelerating potential, both thickness and absorption factors increase, resulting in a spread of $R_{A/B}$ values and an increase in the change of $R_{A/B}$ with diameter. At intermediate accelerating potentials, these effects are minimized.

The effect of varying take-off angle is seen in Figure 3. Obviously, while 15 keV is a good accelerating potential for analyzing particles in the Cu-Au system for instruments with quite low take-off angles, it is a very poor potential to use for instruments with high take-off angles. Effectively, the optimum accelerating potential changes with instrument take-off angle. Simulations to determine optimum experimental conditions must therefore be performed for the specific instrument being used.

The effect of varying particle thickness is seen in Figure 4. As can be seen, under the right conditions, the spread in $R_{A/B}$ values due to uncertainty of the particle thickness is not very severe. At too low and too high of an accelerating potential, $R_{A/B}$ can be quite sensitive to particle thickness for particles that are thinner than the effective depths of electron penetration for all the elements being analyzed. Of course, at quite low accelerating potentials, all but the smallest of particles are thicker than the effective depths of penetration.

The effect of varying particle composition is seen in Figure 5. The optimum accelerating potential does not vary much for compounds similar in composition to each other. However, simulations should be performed to determine optimum conditions for materials greatly different in composition (e.g., light element silicates vs. metal alloys vs. heavy metal oxides).

From the above results, it is apparent that optimum accelerating potentials can be used which minimize the effects of particle shape, diameter, and thickness. The value for the best E_o depends upon the general types of samples to be

analyzed, the range of sizes to be studied and the take-off angle of the instrument which is used. In most cases, the optimum accelerating potential is one which is commonly employed in electron beam instruments. By making reasonable compromises, one accelerating potential can be used over a wide range of sample compositions and sizes.

We shall discuss the operating conditions which appear best for the more common commercial electron beam instruments. We shall also briefly discuss the effects of improper sample preparation resulting in substrate interferences, conductivity problems or sample shadowing.

REFERENCES

1. J.T. Armstrong and P.R. Buseck, Abstract, 167th Nat'l. Mtg., Amer. Chem. Soc., Div. of Anal. Chem., Los Angeles, Cal., Apr. 1-5, 1974, pap. 105.
2. J.T. Armstrong and P.R. Buseck, submitted to <u>Anal. Chem.</u>, 1975.
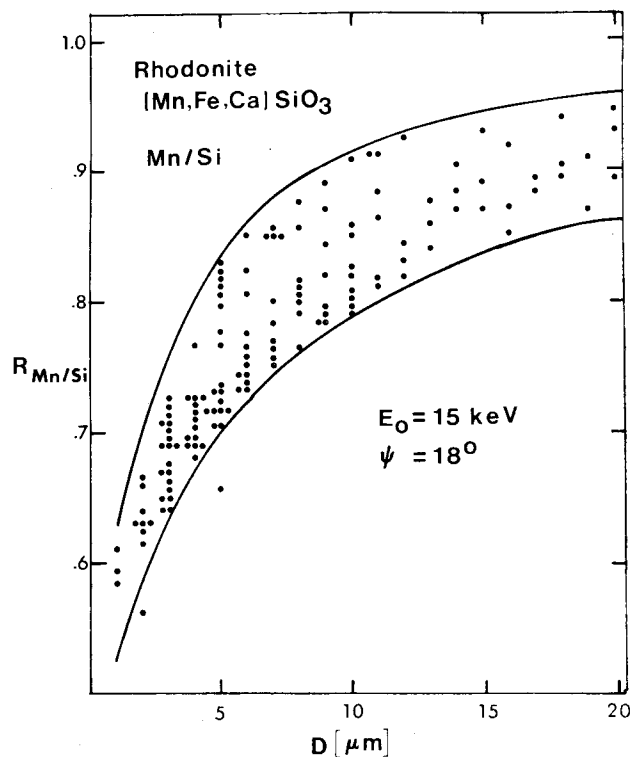
Figure 1. Experimentally determined $R_{Mn/Si}$ intensity ratios vs. diameter for particles of rhodonite [composition: $(Mn_{.65}Fe_{.25}Ca_{.10})$ SiO_3, $\rho = 3.65$ g/cm^3]. The heavy curves enclose the range of $R_{Mn/Si}$ predicted by the particle model simulations (for $T = D$).
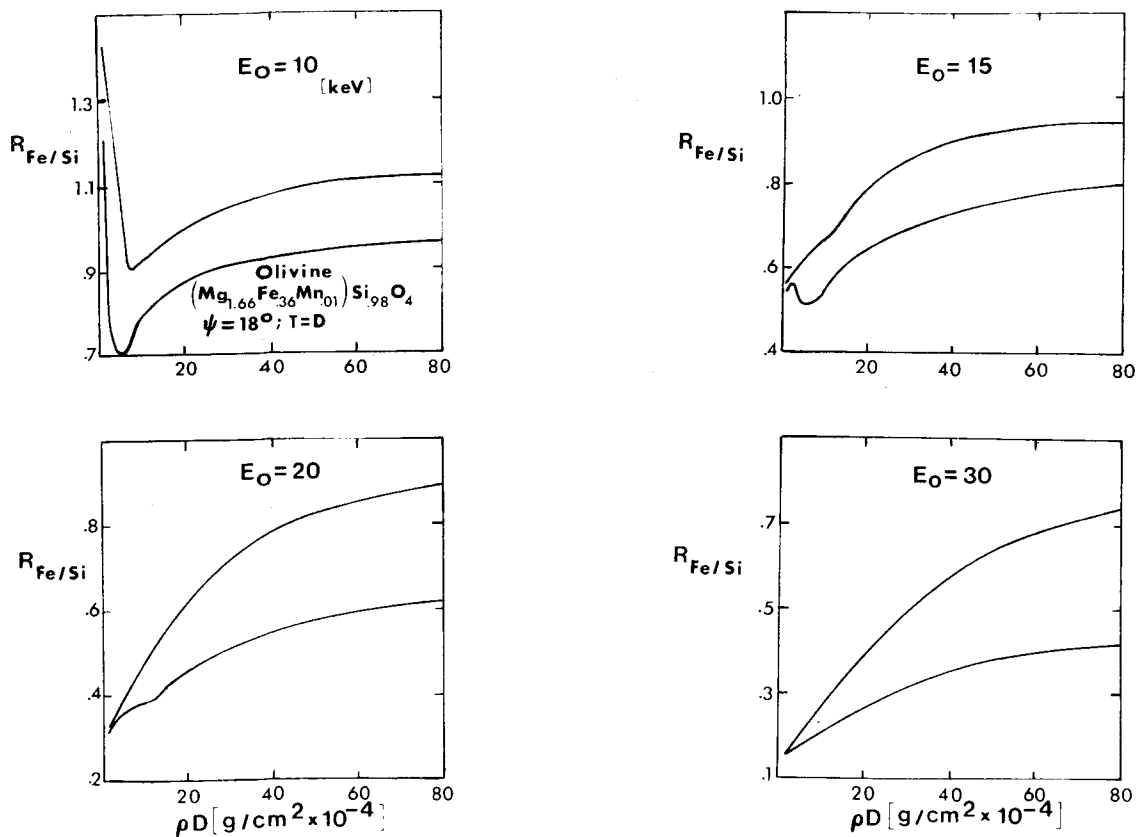
Figure 2. Effect of accelerating potential on $R_{Fe/Si}$.
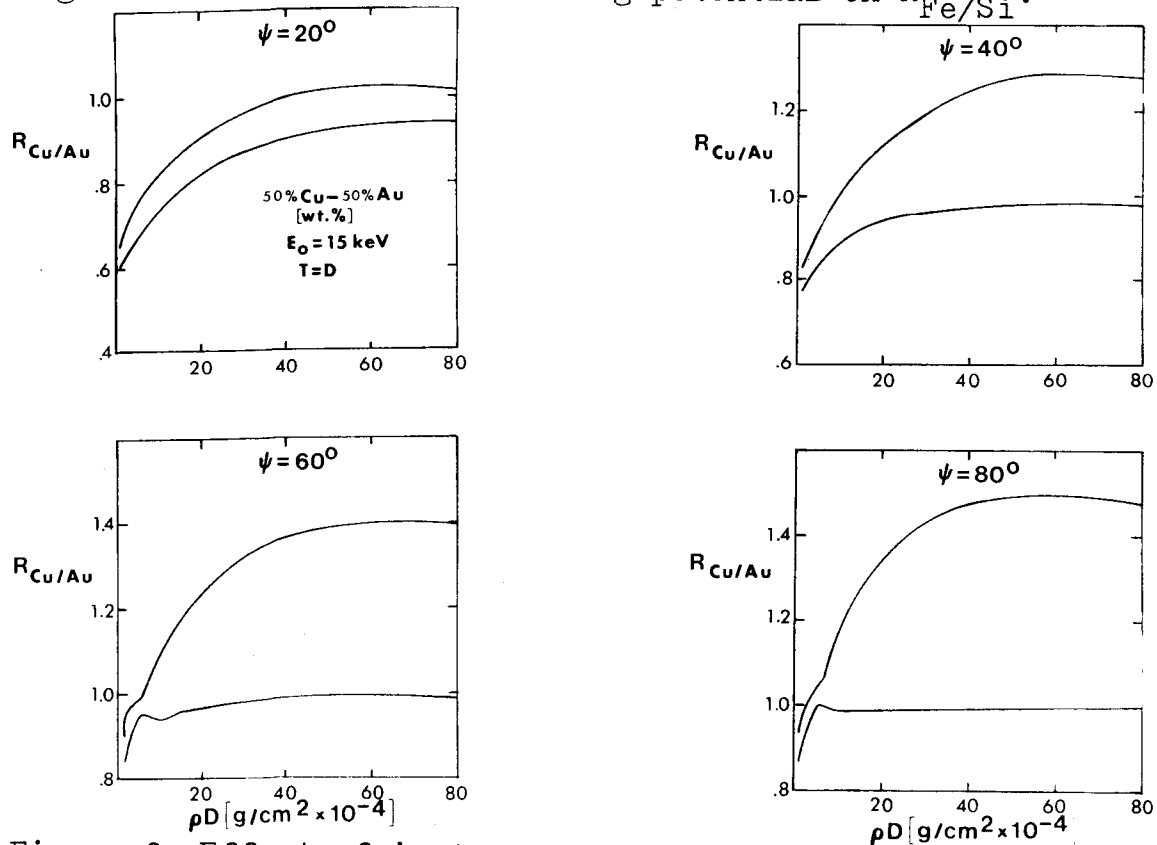
Figure 3. Effect of instrument take-off angle on $R_{Cu/Au}$.
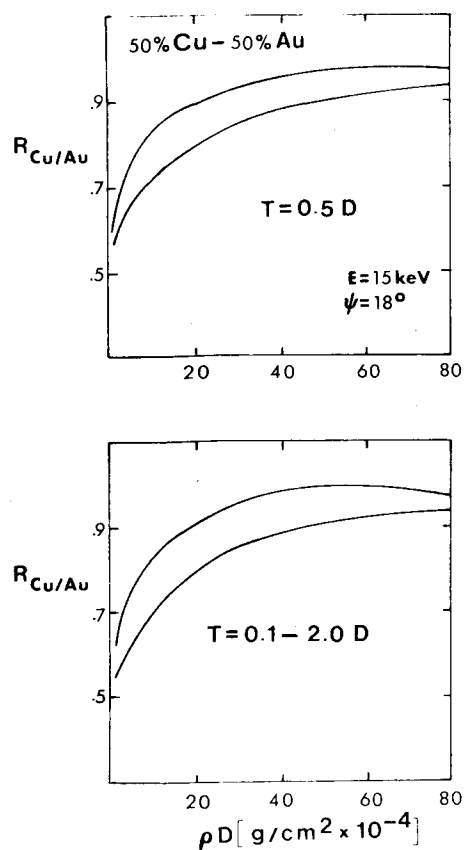
Figure 4. Effect of particle thickness on values of $R_{Cu/Au}$. The upper graph shows simulation results for a fixed thickness of 0.5 x diameter. The lower curve shows results for thicknesses ranging from 0.1 to 2 x diameter.
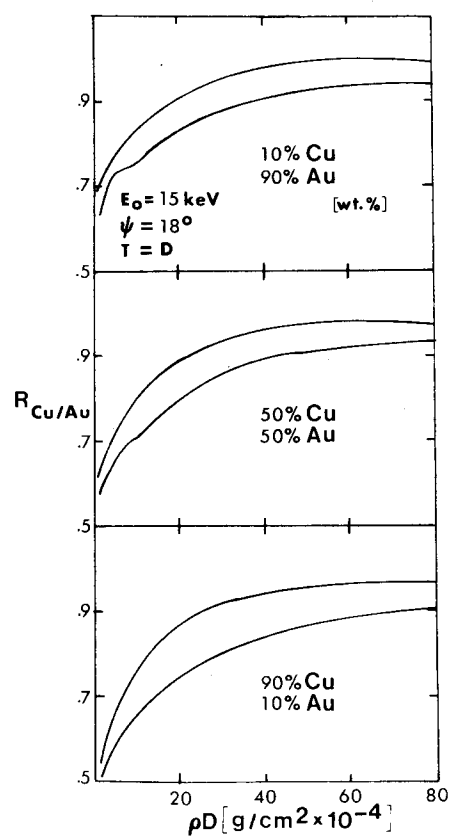
Figure 5. Effect of particle composition on $R_{Cu/Au}$.

THE EFFECTS OF SPECIMEN HEIGHT VARIATIONS ON X-RAY INTENSITIES FROM WAVELENGTH DISPERSIVE SPECTROMETERS MOUNTED VERTICALLY OR OBLIQUELY

H. Walker, D. File and R. Lewis
Cameca Instruments, Inc., Elmsford, New York

Recent developments in scanning electron microscopy and electron probe instrumentation have made it possible to combine both analytical techniques effectively into one instrument with a minimum of compromise in the respective performances of either analytical method. One of the major obstacles in designing this combination instrument was the integration of wavelength dispersive spectrometers suitable for x-ray analysis of the wider range of specimens typically encountered in the SEM. These specimens now range from well polished, flat specimens to unpolished rough specimens such as fracture surfaces. Variations in the specimen surface make quantitative and qualitative (e.g. x-ray mapping) analysis more difficult. A common method of analyzing rough specimens has been to use an energy dispersive spectrometer.

The problems of integrating spectrometers has been effectively overcome on the Cameca MBX combination SEM/electron probe by designing a spectrometer whose Rowland circle can be oriented either normal or inclined to the specimen surface. The more conventional orientation for electron probes is the vertical mounting shown in Figure 1. This orientation offers the most compact arrangement and allows four spectrometers to be mounted on the MBX. Two spectrometers with two crystals in each spectrometer can be used to give full wavelength coverage. This allows different detectors to be used for each spectrometer which are then optimized for the wavelength range covered (e.g. hard or soft radiation). Selecting the detector in this way gives the optimum peak intensities for the respective wavelength ranges. A characteristic of the vertical orientation is that the line focus of the Rowland circle is in the plane of the specimen surface. In the MBX this line is along the Y direction making the spectrometer focussing sensitive to the displacement of the x-ray source along the radius (X direction) or along the column axis (Z direction).

The inclined orientation of the same spectrometer is shown in Figure 2. With this orientation the location of the specimen surface is much less critical because the line focus of the spectrometer is more nearly parallel to the column axis (Z direction). The advantage of this orientation is that specimens with rough irregular surfaces may be accomodated more conveniently.

In order to determine more precisely the differences between the two orientations, two standard wavelength dispersive spectrometers were mounted on a Cameca MBX, one inclined and one vertical as shown in Figures 1 and 2 at a take-off angle of 40°. A polished specimen of pure Fe was placed in light optical focus under the electron beam. Using lithium fluoride as the analyzing crystal, spectral scans were taken across the Fe $K\alpha$ x-ray peak to insure that the resolutions of the two spectrometers were similar. The resolution was found to be approximately 0.0073 Å FWHM for both spectrometers. With both spectrometers peaked on the Fe $K\alpha$ line, the specimen was raised and lowered, and the x-ray intensities measured as a function of displacement from optical focus. Figure 3 is a plot of the results.

In order to retain more than 99% of the x-ray intensity on the vertical spectrometer, it was found necessary to position the specimen within ± 6.5 μm of light optical focus and within ± 3.3 μm to retain more than 99.5% of the x-ray intensity. Locating the specimen surface to this degree of accuracy is accomplished quite easily with the integrated light optics on the MBX which has a depth of focus of 0.7 μm. With the inclined spectrometer the specimen height may be varied ± 1 mm and still retain more than 80% of the original x-ray intensity. To demonstrate graphicaly the large "depth of focus" capability, two 200 mesh Cu TEM grids were placed one above the other as shown in Figure 4. The vertical distance between the two grids was 3 mm. An electron image and an x-ray image of the two over-lapping grids are shown in Figures 5 and 6. As seen in the photos, the "depth of focus" of the spectrometer is quite adequate to map both grids simultaneously. A recent development at Cameca is a system which allows large area x-ray mapping (i.e. areas as large as 1,000μ x 1,000μ) with these spectrometers. Thus, with the combination of the inclined spectrometer and the large area x-ray mapping system, x-ray focus can be maintained over large ranges in the X, Y and Z directions.

It can be concluded that when the inclined spectrometer is used, variations in the specimen height will have much less effect on the precision of the analysis of the specimen. However, the other problems encountered in the analysis of rough specimens, namely variations in the x-ray take-off angle and variations in x-ray absorption, still have to be taken into account.
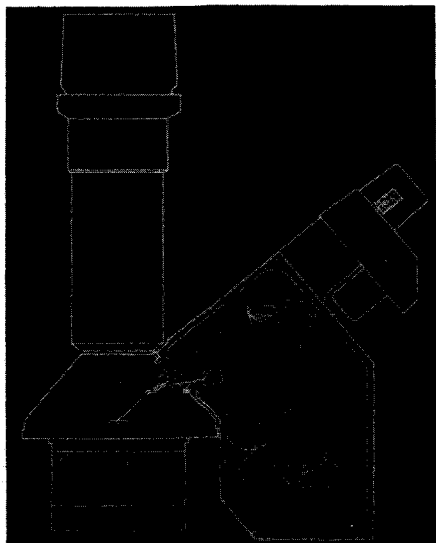
Figure 1
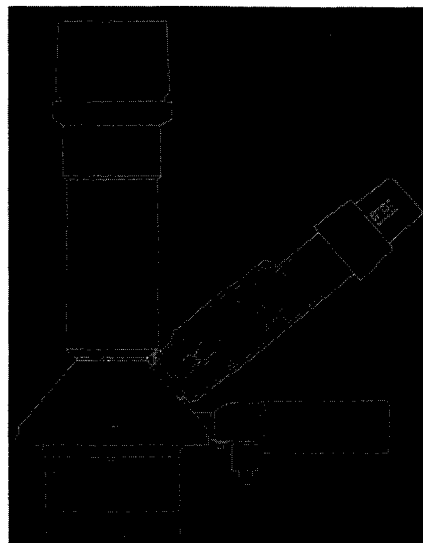
Figure 2
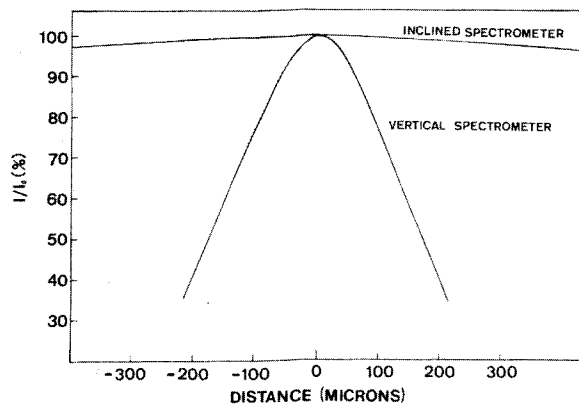
Figure 3
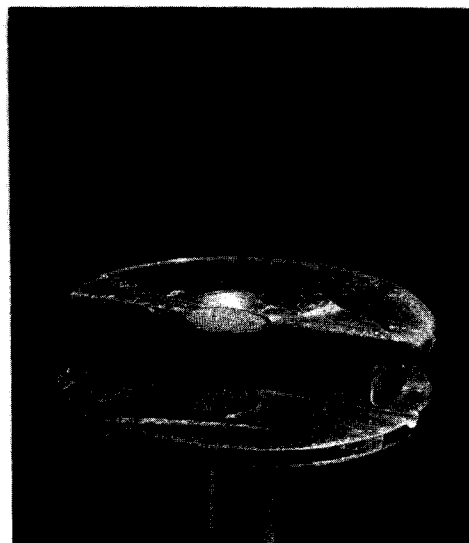
Figure 4

Figure 5
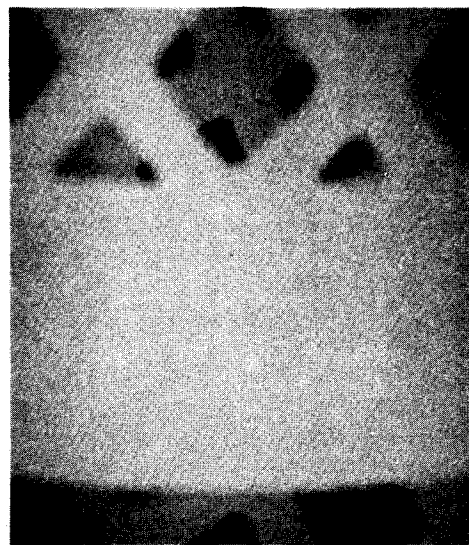
Figure 6

SCANNING ELECTRON MICROSCOPY OF BACTERIOPHAGE

A. N. Broers, IBM Thomas J. Watson Research Center, Yorktown Heights, NY 10598
B. J. Panessa, St. Vincent's Hospital and the Laboratory of Cellular Biology,
        New York University, 100 Washington Square East, New York, NY 10003
J. F. Gennaro, Jr., Laboratory of Cellular Biology, New York University
        100 Washington Square East, New York, New York 10003

Despite its poor resolution as compared with the transmission electron microscope (TEM), the conventional scanning electron microscope (SEM) is a very effective tool in descriptive biology. This is because it can be used to examine bulk samples, thereby avoiding many of the physio-chemical trauma inherent in TEM specimen preparation, and also because the nature of SEM images makes them easier to interpret in 3 dimensions than TEM images. Many critical areas of biology, however, lie beyond the resolution of the conventional SEM, and in these areas the TEM alone has been the only means of examination. It is now possible through the use of a high resolution condenser-objective lens SEM and low-loss imaging, to overcome this limitation and obtain the same resolution in surface SEM images as that obtained when the TEM is used to examine biological samples. The scanning microscope and method used to demonstrate this capability have been described in detail elsewhere.[1] The microscope has a lanthanum hexaboride cathode electron gun and three magnetic lenses each with symmetrical pole-pieces (3 mm diameter bore and 3 mm gap). The sample is placed in the high field region of the condenser-objective lens, and the image is formed by collecting scattered primary electrons from the sample surface. The microscope can also be operated in the scanning transmission mode to obtain images similar in type and in resolution to those obtained in a TEM.

One area of biology which is dependent on high resolution microscopy is the field of virology. In the past, only the TEM could provide the extremely high resolution necessary to visualize viral ultrastructure and viral-host morphology. With this new form of high resolution SEM, we have been able to study bacteriophage morphology, and adsorption of 3C phage and T4-coliphage to their host bacteria, at a resolution an order of magnitude better than the conventional SEM.

Microscope Operating Conditions

All micrographs shown here were obtained at 45 keV. For the low-loss surface mode, the beam current is $1 - 5 \times 10^{-11}$ ampere and the beam diameter is $8 - 10$ Å. The current reaching the detector is $5 \times 10^{-13} - 1 \times 10^{-12}$ ampere and depends upon the sample, the sample shape, the distance of the portion of the sample under examination from the sample edge, the sample inclination to the beam, and the thickness of the sample coating.

The electron detector is a 1 cm diameter quartz light pipe coated with plastic scintillator and 1000 Å of aluminum. It is placed 14 cm below the pole-piece gap. At 4 cm above the detector, there is an aperture plate containing apertures varying in diameter from 20 μ to 1 cm. The 1 cm diameter aperture is used for low-loss surface microscopy, and the smaller apertures are used to eliminate scattered electrons and provide contrast in STEM

IIB

operation. The smaller the aperture, the higher the 'coherence' in the transmission image. For STEM observation of biological samples, an aperture is chosen which has a diameter equal to the diameter of the unscattered beam at the aperture plane. A beam current of about 10^{-12} ampere appears to be a good compromise between adequate S/N ratio, and tolerable sample damage and contamination.

The microscope is pumped with ion pumps and has liquid nitrogen cooled baffles placed close to the sample. This combination reduces contamination from the vacuum environment to a negligible level. The sample itself, however, is often a serious source of contamination; and to overcome this problem, a heating device is employed which heats the sample 'in situ'. On many samples the heating device is completely effective in reducing contamination to an insignificant level, and it was used to obtain the STEM image presented here.

Sample Preparation

Log phase S. aureus grown on nutrient agar was incubated with 3C phage at 30°C for 30 - 90 minutes. Samples were taken by placing a Formvar-carbon-coated grid (for STEM), or a SiO_2 sliver (9 mm x 1 mm x 0.4 mm) for low-loss microscopy, face-down on the nutrient agar. Similarly, log phase E. coli B grown on nutrient agar (37°C) were inoculated with T4-coliphage and harvested after 10-30 minutes. STEM grids were stained with 2% filtered aqueous uranyl acetate. The slivers with attached phage-bacteria specimens were immediately fixed in 1.5% gluteraldehyde in 0.1 M cacodylate buffer (pH 7.4) at room temperature for 1 - 18 hours. They were then washed in 0.1 M cacodylate buffer, rinsed in distilled water, and post-fixed for 1 hour in 1% aqueous OsO_4 at room temperature. To protect the samples, they were placed in small wire baskets,[3] dehydrated in acetone, dried by the critical point method, and coated with either carbon-gold-palladium, or carbon-platinum-palladium. The coating thickness varied from 25 Å - 50 Å. To improve the electron scattering properties of the phages, some samples were stained en bloc with 2% aqueous filtered uranyl acetate, 2% aqueous filtered phosphotungstic acid (pH 7.4), or 2% filtered uranyl acetate in acetone.

Isolated preparations of T4 phage were obtained by inoculating log phase E. coli B in a yeast extract broth with T4, and harvesting the phage after 5 hrs incubation at 37°C by millipore filtration. The filtered phage were then washed and centrifuged in tris buffer or 0.1 M phosphate buffer (pH 7.3).

Results

The resolution of the microscope was evaluated by examining a GaAs-GaAsP superlattice with a 250 Å period (see Fig. 1). The superlattice sample was coated with approximately 50 Å of gold-palladium. Point-to-point resolution of 20 Å is clearly indicated (Fig. 1). If the width of the dark space definition of resolution is used, the best resolution is 7 Å. When thin samples are examined in the scanning transmission mode, the point-to-point resolution is 7 Å.[2]
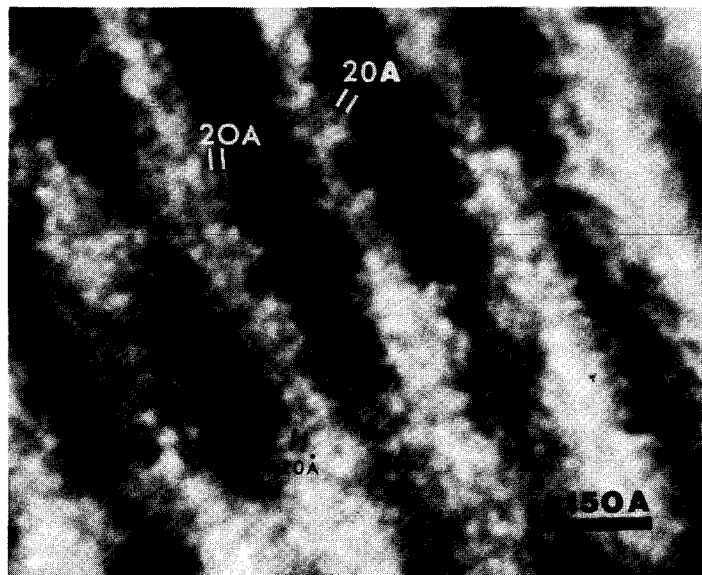
Figure 1. Low-loss image of GaAs-GaAsP
superlattice coated with approximately
50A gold-palladium showing 20A point
to point resolution.

It is possible to visualize the phage ultrastructure; head, neck, end plate, (Figs. 2 — 8) and attachment (Fig. 8) without resorting to replication, 3-dimensional reconstruction, or serial sectioning. Preliminary data suggest that some internal or compositional information can be visualized in addition to the surface structure. Micrographs of specimens treated with heavy metal stains show specific light and dark regions, which seem to correspond to stain localizations. See, for example, the outlining of the nuclear region in S. aureus (Fig. 9). Unstained phage preparations which are coated with an extremely thin layer of metal produce low-loss images which suggest a periodicity to the T4 tail sheath, similar in morphology to that observed by conventional transmission electron microscopy (Fig. 2). Coliphages prepared in the same way and oriented for examination of their end plate, show the inner core of the tail (Fig. 5, arrow), and a sixfold symmetry, possibly corresponding to the 6 spikes which have been reported to aid in phage adsorption.[4] STEM images clearly show periodicity of the phage tail sheath and the classical end-plate with its associated tail fibers (Fig. 3).

Figure 5 shows newly liberated T4-coliphages and the remains of the bacterial cell (E. coli) at 30 minutes after phage inoculation.

Figures 6 and 7 show stained (uranyl acetate), metal-coated 3C staphylococcal phages. The head (h), neck (n), tail (t), and lobular end-plate (ep) of these minute bacteriophages can be clearly seen; and for the first time, the lobular projections arising from the end-plate can be examined in 3-dimensions at a magnification high enough to show its shape (Fig. 7). Unstained, more thinly coated samples reveal some internal phage structure. Figure 8 visually demonstrates that the 3C tail is indeed a hollow tube, as was postulated by Bradley.[5] This tubular configuration is especially apparent at the point where the tail enters the bacterial cell wall (arrow).

References

1. Wells, O., Broers, A., Bremer, C., Appl. Phys. Lett. 23, 353, (1973).
2. Broers, A. N., Appl. Phys. Lett., 22, 610, (1973).
3. Broers, A. N., Panessa, B. J., and Gennaro, J. F., SEM/75, Proc. 8th Annual SEM Symp. IITRI, p. 233 (1975).
4. Simon, Lee D. and Anderson, T. F., Virology, 32, 279 (1967); and Virology 32, 297, (1967).
5. Bradley, D., J. Ultrastruct. Res., 8, 552, (1963).
6. Tikhonenko, Ultrastructure of Bacterial Viruses, Plenum Press, New York, (1970).
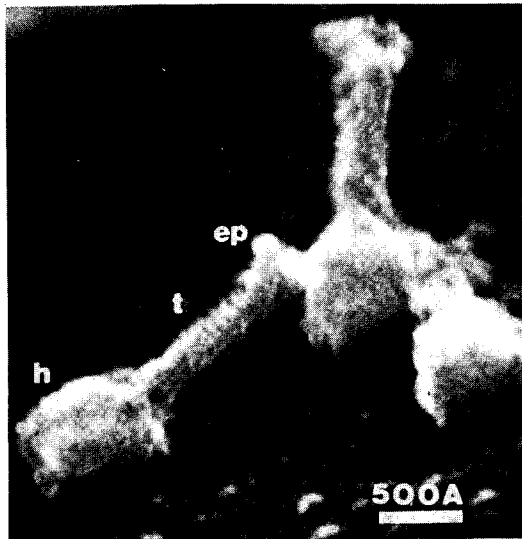
Figure 2. Unstained, thinly coated (less than 50A of carbon-gold-palladium) washed T4 bacteriophage.There seems to be a periodicity to the tail sheath similar to that observed in TEM and STEM micrographs (Fig. 3)

Figure 3. This STEM sample was prepared by air drying washed T4 coliphage onto a Formvar-carbon coated grid, and staining the preparation with 2% filtered uranyl acetate. The structural units of the untriggered phage can be clearly seen.
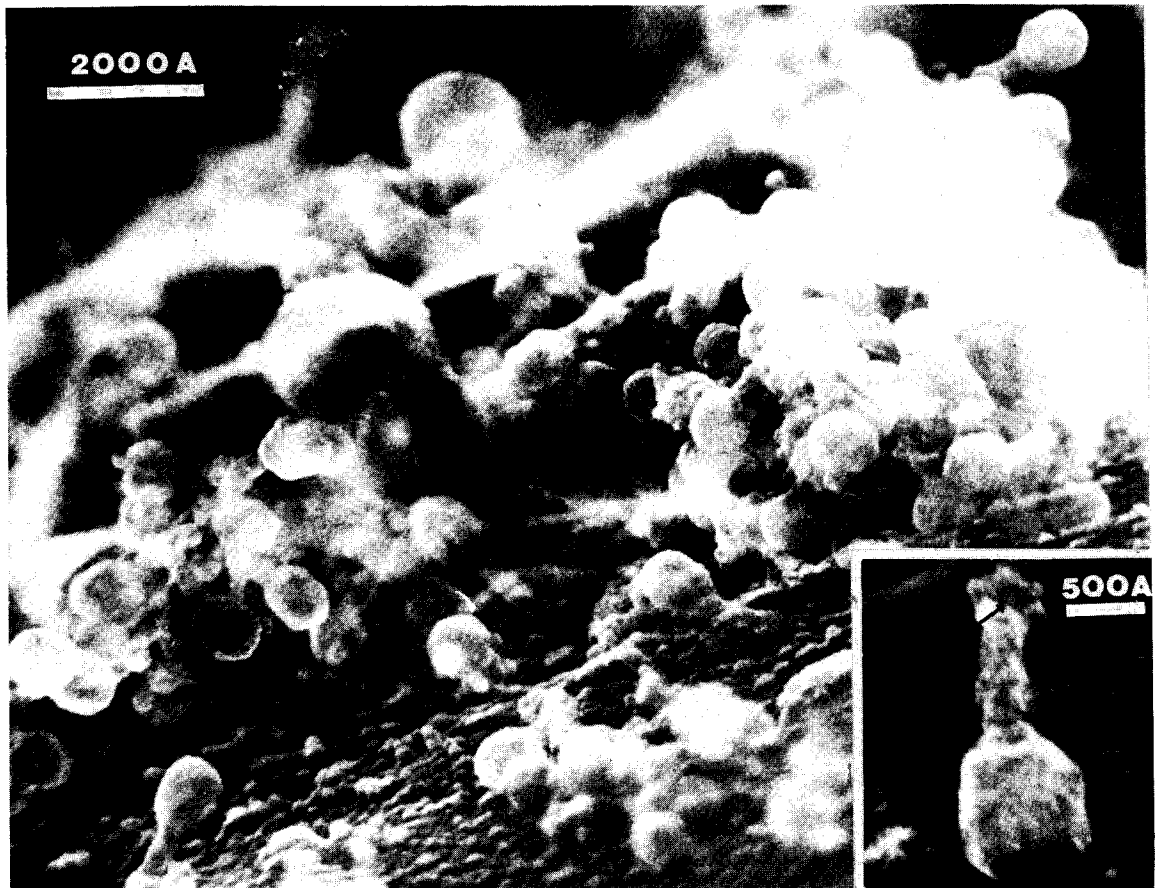
Figure 4 (large). A stained, metal coated preparation showing the liberation of coliphages from their bacterial host cell at 30 minutes after phage inoculation.Figure 5 (small). The end-plate of a T4 phage possesses 6 projections which correspond in number and size to the spikes which play a role in phage attachment. At the center of the end-plate, the core can be distinguished (arrow). Same preparation as fig.2.
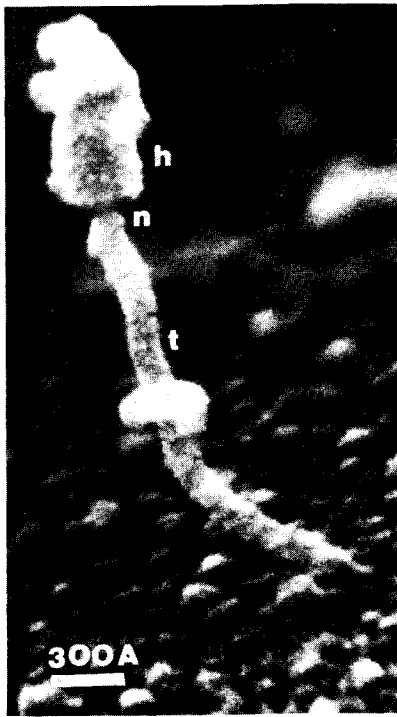
Fig. 6: Newly liberated 3C-bacteriophage. Minute particles cling to the head (h) and tail (t) of the phage. (n) is the neck region. Stained with uranyl acetate.

Fig. 7: End plate of a 3C phage showing the lobular projections similar to the Type III end plate postulated for Group IV phages[6].

Fig. 8: The tail of the 3C-phage appears hollow (arrow) as it enters the S. aureus cell wall. Unstained preparation.

Fig. 9: S. aureus cells in different stages of division. These cells were en bloc stained with PTA and show a type of contrast which may be representative of stain localizations. The darkened areas around the nuclear region of the cells would be areas devoid of stain, whereas the brighter outer regions of the cell wall suggest areas which scatter more electrons and therefore are of higher atomic number. We feel that the stain may enhance the natural electron scattering properties of these biological specimens and with further experimentation, may provide a means to study high resolution

Microanalysis by Electron Spectrometry of Inner-Shell Excitations

V.E. Cosslett and R.D. Leapman

The Cavendish Laboratory, University of Cambridge, England.

Microprobe analysis as generally practised is based on the detection of characteristic X-ray quanta emitted from elements in a specimen under the impact of an electron beam. An alternative possibility is to detect electrons that have lost the corresponding energy by inner-shell excitations. With a sufficiently thin specimen these high-loss electrons are transmitted in a narrow forward beam, which can be analysed with a magnetic spectrometer; those that have excited (e.g.) the Carbon K-line can be counted. The efficiency of collection is high compared with X-ray detection. The technique is particularly valuable for elements of low Z, which have a very low fluorescent yield and have K-lines of long wavelength making detection efficiency also very low. It can also be applied to the L and M spectra of heavier elements. In optimum conditions, electron spectrometry has a theoretical detection limit of the order of 10^{-20}g, but in practice it is about 10^{-18}g at present. The chief complication is the presence of a background of 'noise' obscuring the wanted signal. This background is due to plasmon and single electron excitations, the cross-section for which is much greater than for K-excitation. The plasmon loss from a thick foil can also smear the sharpness of the K-edge signal. For this reason the thickness of specimen has to be limited to less than the mean free path of the main plasmon excitation. Improvements in deconvolution of the loss-spectrum should allow the theoretical detection limit to be approached (Egerton and Whelan, 1974).

As part of a systematic study of the value of the method in the microanalysis of multi-component alloys, especially for carbides and nitrides, we have determined experimentally the mean free paths for K-, L- and M- excitations for a number of representative elements. The corresponding cross-sections are difficult to derive theoretically, the literature containing estimates that differ by 50% or more for a given element. The apparatus used, a standard electron microscope fitted with a magnetic prism spectrometer below the camera chamber, has been described earlier (Wittry 1969), together with some experiments made to determine the order of magnitude of the characteristic loss signal (Wittry, Ferrier and Cosslett, 1969). Improvements in the accuracy of recording and a preliminary comparison of experimental and theoretical results have recently been reported (Ferrier and Hills 1974). Some values of the mean free path for K-excitation in carbon and aluminium have been measured elsewhere with a Castaing-Henry spectrometer built into a microscope column (Colliex and Jouffry, 1972; Egerton, 1975; Perez et al 1974).

Typical loss spectra are shown below for carbon-K, chromium -L and silver -M obtained at 60 kV from evaporated films of thickness in the range 20-40 nm, as indicated. The effective 'probe' size was 250 nm and the analysis time 2 - 10 mins. The background is subtracted either by extrapolation on the trace or by re-plotting on a log scale, as it falls approximately as $\triangle E^{-4}$ (Egerton and Whelan 1974). Knowing the plasmon loss mean free path we can then calculate the mean free path for the X-ray loss from the ratio of the intensities of the respective loss and no-loss peaks, from Poisson statistics (Colliex and Jouffrey, 1972). A wide objective aperture ($\sim$ 40 mrad) or none at all has to be used for these measurements since the K- loss electrons have an appreciably wider spread than theory gives. For accuracy in microanalaysis, however, a much smaller aperture ($\sim$ 5 mrad) is needed to optimise the signal/ background ratio. A smaller probe size (100 nm) also was used when investigating the limits of detection.

A comparison of experimentally determined and theoretical mean-free paths is shown in Table I. The theoretical values are obtained for K-excitation from an empirically modified Bethe expression (Green and Cosslett, 1961; Hills 1973) and for L- excitation from a treatment due to Burhop (1952), which was earlier found to differ from experiment (Green and Cosslett 1968). No calculation of the probability of M excitation appears to exist. An estimate of the detection limit for these elements is given in the last column of Table I. The relatively large experimental errors quoted arise from uncertainties in specimen thickness and in the mean free path for plasmon loss, and from inaccuracy in background subtraction. Incorporation of digital recording and computer processing of the signal should considerably reduce the error. The use of an electron gun of higher brightness would extend the detection limit by at least an order of magnitude and reduce the recording time. From experiments made at 500kV we also find an appreciable improvement in the signal to noise ratio at high voltage as well as the ability to analyse thicker specimens.

TABLE 1

Element	Loss	Theoretical Mean-Free-Path (μm)	Experimental Mean-Free-Path (μm)	Detection Limit (g)
Carbon	K	3.5*	3.6 ($\pm$ 15%)	1.4×10^{-18}
Aluminium	K	55*	50 ($\pm$ 20%)	2×10^{-16}
Aluminium	$L_{II,III}$	1.7^x	3.5 ($\pm$ 50%)*	2×10^{-17}
Chromium	$L_{II,III}$	5.9^+	4 ($\pm$ 20%)	2×10^{-16}
Iron	$L_{II,III}$	7.1^+	6 ($\pm$ 30%)	5×10^{-16}
Copper	$L_{II,III}$	10.5^+	9 ($\pm$ 20%)	5×10^{-16}
Silver	$M_{IV,V}$	—	9 ($\pm$ 30%)	2×10^{-15}

* See Hills (1973),   x see Colliex and Jouffrey (1972),   + L_{III}, from Burhop (1952)

The agreement of the measured mean free paths with theory is excellent for the K-loss, as is to be expected since the calculated values are ultimately based on experimental determination of the efficiency of characteristic X-ray production. The discrepancy in the L-values is due to the approximations in Burhop's treatment. For comparison, the mean free path at 60 kV for the chief plasmon loss is 60 nm in carbon and 80 nm in aluminium.

It should be emphasised that the detection limits given in the Table are for samples of the pure element. In a mixture or in chemical combination the detectability is worse by a factor of 2 to 10, depending on the nature of the matrix (Hills et al 1975).

References

Burhop, E.H.S. 1952. The Auger Effect (Cambridge: University Press)

Colliex, C and Jouffrey, B. 1972. Phil. Mag. 25, 491

Egerton, R.F. 1975. Phil. Mag. 31, 199

Egerton, R.F. and Whelan, M.J. 1974. J. Elect. Spectrosc. 3, 232

Ferrier, R.P. and Hills, R.P.T. 1974. Advances in Analysis of Microstructural Features by Electron Beam Techniques (London: The Metals Society),p.41

Green, M. and Cosslett, V.E. 1961. Proc. Phys. Soc. (Lond.) 78, 1206

Green, M. and Cosslett, V.E. 1968. J. Phys. D. (Appl. Phys.) 1, 425

Hills, R.P.T. 1973. Ph.D. Dissertation, Cambridge

Hills, R.P.T., Ferrier, R.F., Leapman, R.D. and Cosslett, V.E. 1965. Proc. 7th
    Internat. Conf. X-ray Optics and Microanalysis, Moscow 1974 (in the press)

Perez J.P., Sevely, J. and Jouffrey, B. 1974. Proc. 8th Internat. Congress
    Elect. Microsc. Canberra, I, 380

Wittry, D.B. 1969. J. Phys. D (Appl. Phys.) 2, 1757

Wittry, D.B., Ferrier, R.P. and Cosslett, V.E. 1969. J. Phys. D. (Appl. Phys.)
    2, 1767

Carbon 20 nm
No objective aperture

Intensity arb. units

| | | | | |
20
15
10
5

400   300   200   100   0

Energy loss eV

Silver 33nm on carbon 10nm
No O.A.

Intensity arb units

15

10

5

500   400   300

Energy loss eV

Chromium 25nm on carbon 10nm
O.A. 100 µ

Intensity arb units

20

15

10

5

+ 100 eV

600   500   400   300   100   0

Energy loss eV
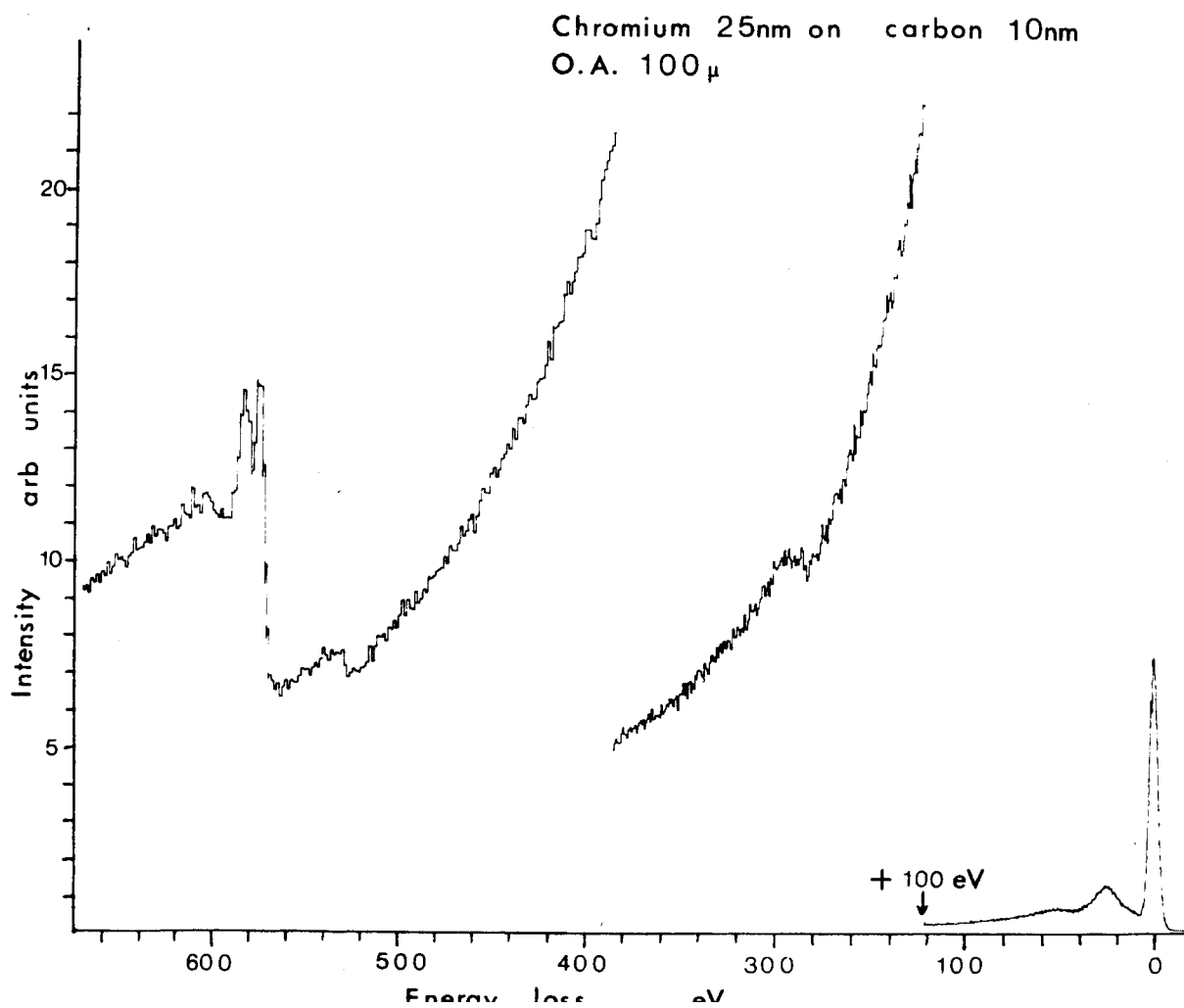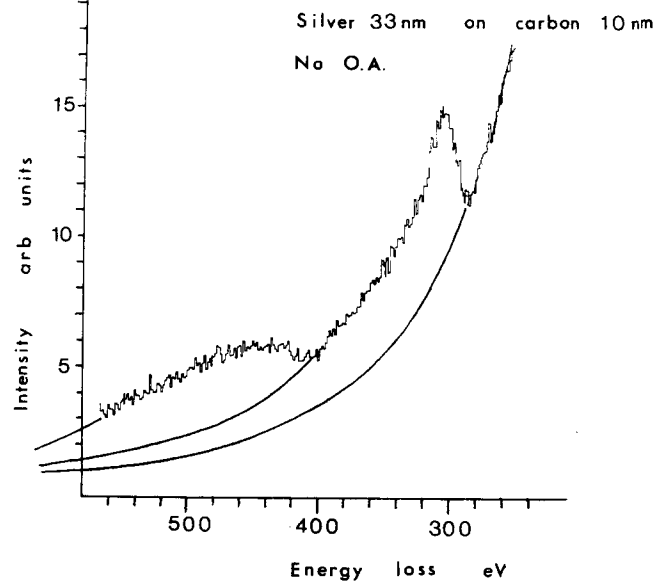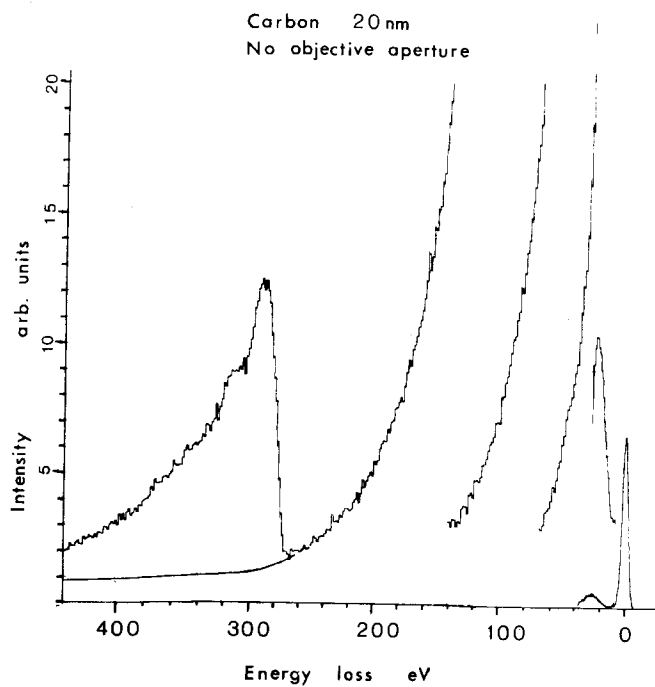
Observation of Dynamic Deformation by Stereoscopic SEM

E.J. Chatfield and V.H. Nielsen
Department of Applied Physics
Ontario Research Foundation
Sheridan Park, Mississauga
Ontario, Canada

INTRODUCTION

The requirement for stereo observation in the SEM has been discussed by a number of authors.[1,2,3,4] A direct consequence of the high depth of focus which the SEM offers is that surface topography is often difficult to interpret. In fact, it has been shown the validity of even a magnification marker can be questioned, although these continue to be used. Unfortunately the angles presented by micro features on a rough specimen are not known, and such "magnification" markers can be misleading if single images are interpreted in a subjective manner. When dynamic events are observed in the SEM it is particularly important that these be recorded in stereo; in this way all data which can assist in the interpretation of the event are then available. This paper describes improvements in a dynamic stereo observation system described earlier,[5,6] and examples of its applications to the study of dynamic events will be shown using videotape recordings.

SYSTEM DESIGN

The after lens deflection (ALD) unit described previously has been redesigned for compatibility with the Cambridge specimen current amplifier and all of the available X-ray spectrometers. Figure 1 shows the new after lens deflection unit. This attaches, as previously, to the underside of the final lens plate. In this new design the final aperture alignment assembly is replaced by a new assembly which permits two concentric rotations to be introduced into the specimen chamber. One of these is used, as before, for final aperture alignment and the outer one is used to rotate the after lens coil. In this way none of the existing ports on the specimen chamber have been compromised. Figure 2 shows the stereo control module. In addition to stereo angle, dynamic astigmator controls are provided for

both left and right images, together with a means for switching manually
to each of these.

Recording of Dynamic Experiments

The system allows full flexibility of search and magnification
changes during the recording of the events. However, the operator soon
discovers that focussing of the image is more conveniently achieved by
adjustment of the Z stage motion rather than by adjustment of the final
lens current. Changes of final lens current lead to changes of scan
rotation which require further adjustment of the ALD coil. It has been
found that after initial adjustments no further changes to vertical
convergence or astigmatism are required if focussing is effected using the
Z stage motion. The system has been used to observe a number of dynamic
deformation events. Figure 3 shows a stereo pair of thin silver wire
after it had been fractured in situ, and Figures 4A, 4B, 4C, and 4D show
a series of stereo pairs photographed directly from the TV monitor at
a magnification of 2000, whilst the deformation was in progress. Some
experiments using low kilovoltage beams have been performed, in which
uncoated biological hard tissues have been deformed. These experiments
indicate that microdissection can be performed within the instrument with
full depth perception provided for the operator. The videotape recordings
of uncoated materials show that specimen charging in many cases is less
of a problem at TV scan rates than it is under slow scan recording conditions,
a phenomenon also observed by Nixon [7].

Application to X-Ray Measurements

Measurement of X-ray emission from rough specimens by either
energy or wavelength dispersive methods is often compromised by the specimen
topography; accurate quantitative measurements are particularly difficult
since the angle of X-ray take-off is unknown. The problem, and some
methods for its solution, have been discussed by Bomback[8].

The real time aspect of this system will permit the X-ray take-off
angle to be either measured or alternatively to be adjusted to a pre-set

value by manipulation of the specimen stage controls before the X-ray measurements are made. In this way more accurate measurements will be possible from rough specimens.

REFERENCES

1.   Boyde, A.,   Scanning Electron Microscopy 1971,
         Proceedings of the 4th Annual SEM Symposium, I.I.T.
         Research Institute, Chicago, Illinois, 1971, 1-8.

2.   Lane, G.S.,   J. Sci. Instrum., 1969, 2,   565-569.

3.   Boyde, A., Scanning Electron Microscopy 1974,
         Proceedings of the 7th Annual SEM Symposium, I.I.T.
         Research Institute, Chicago, Illinois, 1974, 93-108.

4.   Wells, O.C.,   1957 Ph.D. Thesis, Cambridge.

5.   Chatfield, E.J., et al,   Scanning Electron Microscopy 1974,
         Proceedings of the 7th Annual SEM Symposium, I.I.T.
         Research Institute, Chicago, Illinois, 1974, 117-124.

6.   Chatfield, E.J. and Nielsen, V.H.,   Proceedings of MAS, 1974,
         28A - 28E.

7.   Nixon, W.C.,   Proceedings of MAS, 1974.

8.   Bomback, J.L., Scanning Electron Microscopy 1973,
         Proceedings of the 6th Annual SEM Symposium, I.T.T.
         Research Institute, Chicago, Illinois, 1973, 98-103.
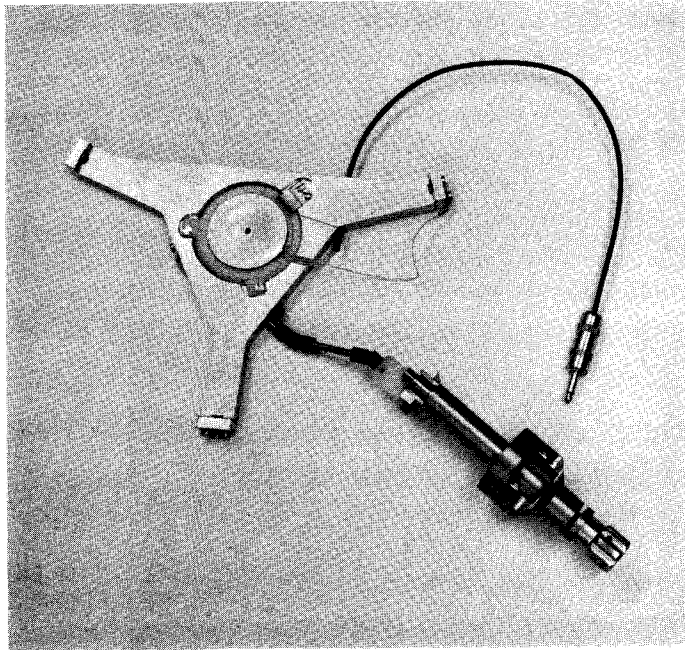
Figure 1. ALD assembly, showing concentric aperture alignment and coil rotation controls.
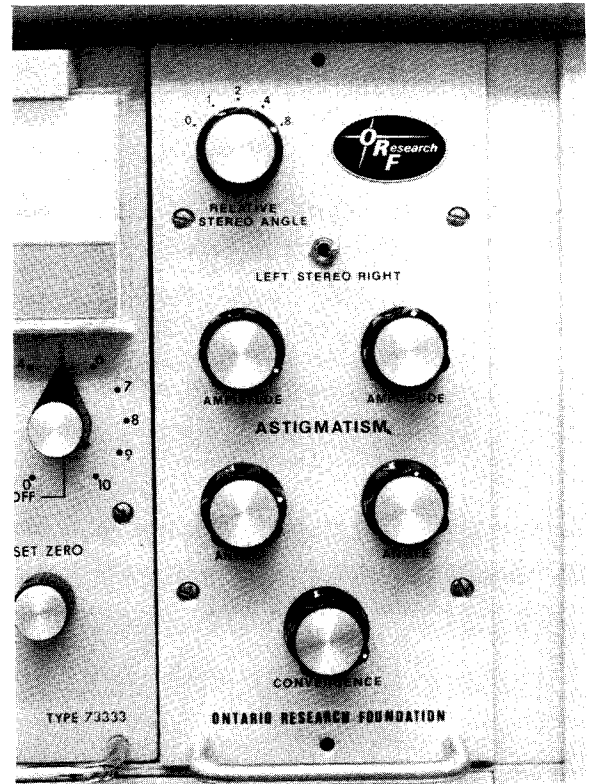
Figure 2. Stereo Control Module
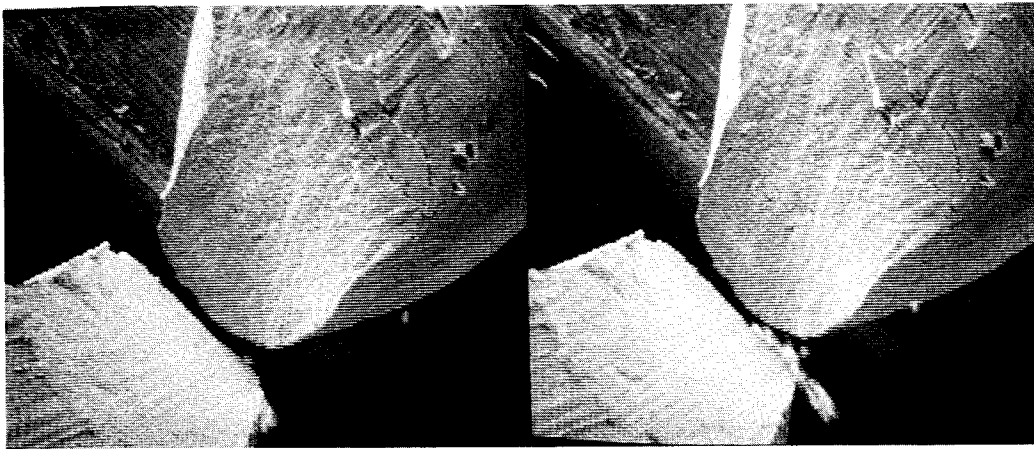
Figure 3. Thin silver wire after fracture in situ, X200
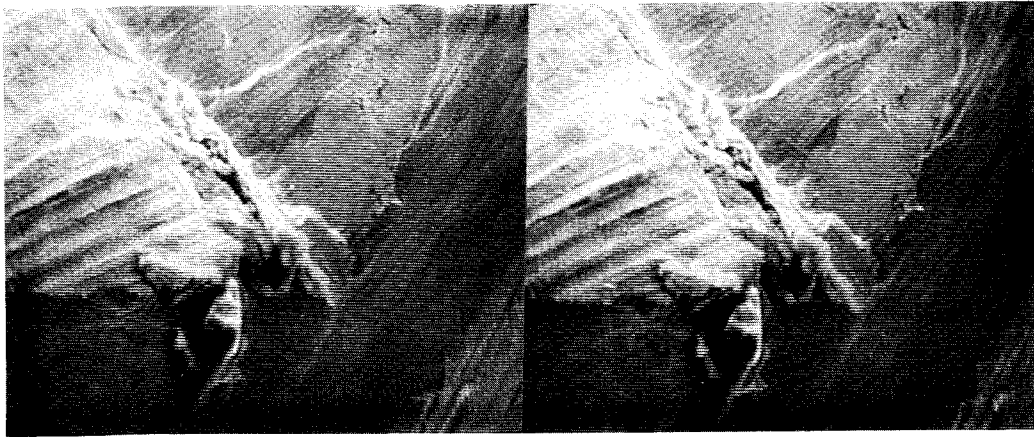
(A)
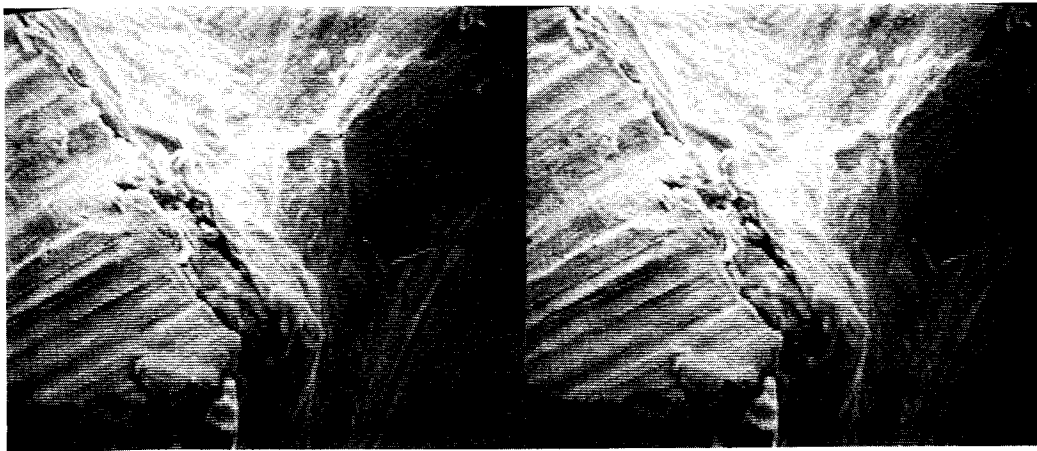
(B)
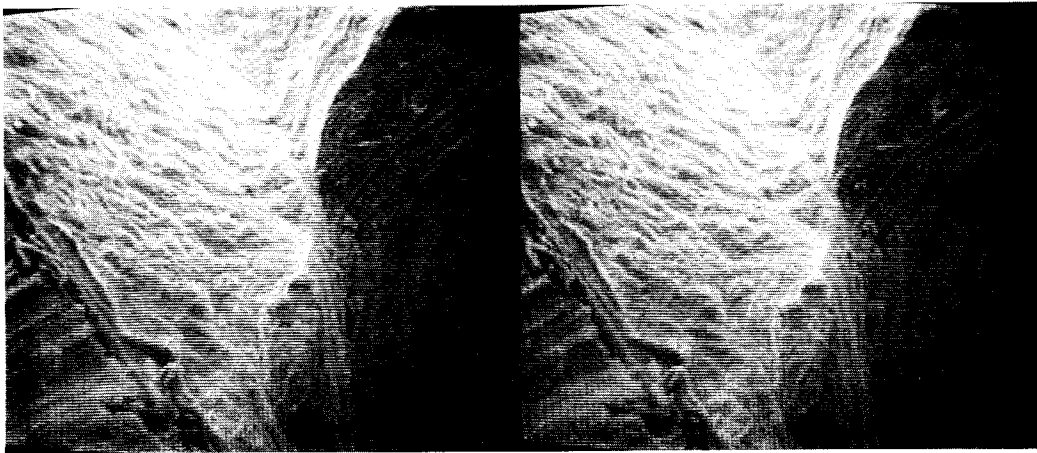
(C)
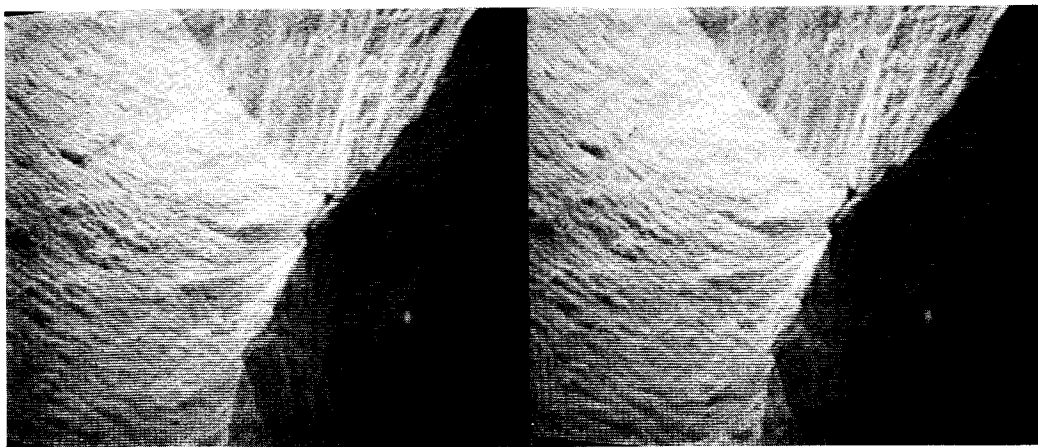
(D)

Figure 4.   Series of Stereo Pairs of progressive deformation of a
silver wire, taken directly from the TV monitor, X2000

HIGH CONTRAST OBSERVATION OF MAGNETIC DOMAIN WITH HIGH VOLTAGE SEM

by
R. Shimizu and T. Ikuta
Dept. of Appl. Physics, Osaka University, Osaka, Japan

M. Kinoshita and T. Murayama
Manufacturing Engneering Lab., Tokyo Shibaura Electric Co. Ltd.,
Kanagawa, Japan

H. Nishizawa and T. Yamamoto
Japan Electron Optics Lab. Co. Ltd., Tokyo, Japan

The observation of magnetic domain in materials of cubic anisotropy with SEM has provided a powerful tool to study internal irregularities of the crystal, such as residual strain gradients and inclusions which result in changes in magnetic domain configuration[1,2].

The mechanism of formation of the magnetic domain contrast in backscattered electron images has well been understood theoretically by applying both the analytical and Monte Carlo calculations[3-6]. This technique enables us to observe the magnetic domain in the bulk materials with much higher resolution than the conventional methods using Kerr effect and/or magnetic colloid. However, low contrast, usually estimated as only a few tenth percents even for such a high domain magnetization $B_{max} \sim 20000$ Gauss as iron with conventional commercial type SEM, has restricted wide application of this technique for practical use, and the observation of this type has been reported only for the materials of comparatively high domain magnetization, e.g., Fe, Fe-Si ($B_{max} \sim 20000$ Gauss) and Ni[7] ($B_{max} \sim 6300$ Gauss).

Considering the possible advantages, which outweigh the limitation, we have applied high voltage scanning electron microscopy for high contrast observation of magnetic domain of such a material of comparatively low domain magnetization ($B_{max} < 5000$ Gauss) in practical use for magnetic head as Mn-Zn ferrite ($B_{max} \sim 4800$ Gauss).

The samples were mounted on a sample stage specially designed for JSEM-200 (JEOL Co. Ltd.), which enables us to rotate the sample around the normal of the sample surface during the measurement. The Li-doped Si solid detector of 3x5 mm^2 size was also mounted on this sample stage and its position was easily changed to find optimal take off angle.

The experiment was done first to confirm the effectiveness of high voltage SEM by observing the magnetic contrast at 100 KV and 200 KV. In figure 1 shows the picture of the sample stage which is attached to JSEM-200 in the experiment. The photomultiplier tube of JSEM-200 can be independently used for secondary electron detection which enables us to confirm best focussing of electron microprobe for surface observation. The magnetic domain of Mn-Zn ferrites

observed at 100 and 200 KV are shown in figures 2a and 2b, respectively. From these figures, the contrasts of magnetic domains are found to increase with the accelerating voltage at the cost of the resolution.   The half of the sample was mechanically polished with 3 micron green carborandom in olive oil and the other was removed the surface damaged layer by heavy chemical etching.   It is worthy of note that even the maze pattern of comparatively low contrast can be observed in mechanically polished region which has no more mirror surface.   Since it seems difficult to observe this maze pattern by other conventional methods such as Kerr effect or magnetic colloid technique, high voltage SEM provides a useful tool for the inspection of magnetic devices without requiring any special technique for the observation as the other methods.

References

1.   D. E. Newbury, and H. Yakowits,   Proc. 19th Conf. on Magnetism and Magnetic Materials, American Institute of Physics, Boston (1973).

2.   D. J. Fathers, D. C. Joy, and J. P. Jakubovics,   Proc. 8th Int. Congress on Electron Microscopy, Canberra, 630-631 (1974).

3.   D. J. Fathers, D. C. Joy, and J. P. Jakubovics,   Proc. Symposium on Scanning Electron Microscopy/1973, IIT Reseach Institute, Chicago, 259-266 (1973).

4.   D. E. Newbury, H. Yakowitz, and R. L. Myklebust,   Appl. Phys. Lett. 23, 488-490 (1973).

5.   D. J. Fathers, J. P. Jakubovics, D. C. Joy, D. E. Newbury, and H. Yakowitz, Phys. Stat. Sol. (a) 20, 535-544 (1973).

6.   T. Ikuta, and R. Shimizu,   Phys. Stat. Sol. (a) 23,   605-613 (1974).

7.   D. E. Newbury, H. Yakowitz, and N. C. Yew,   Appl. Phys. Lett. 24, 98 (1974).
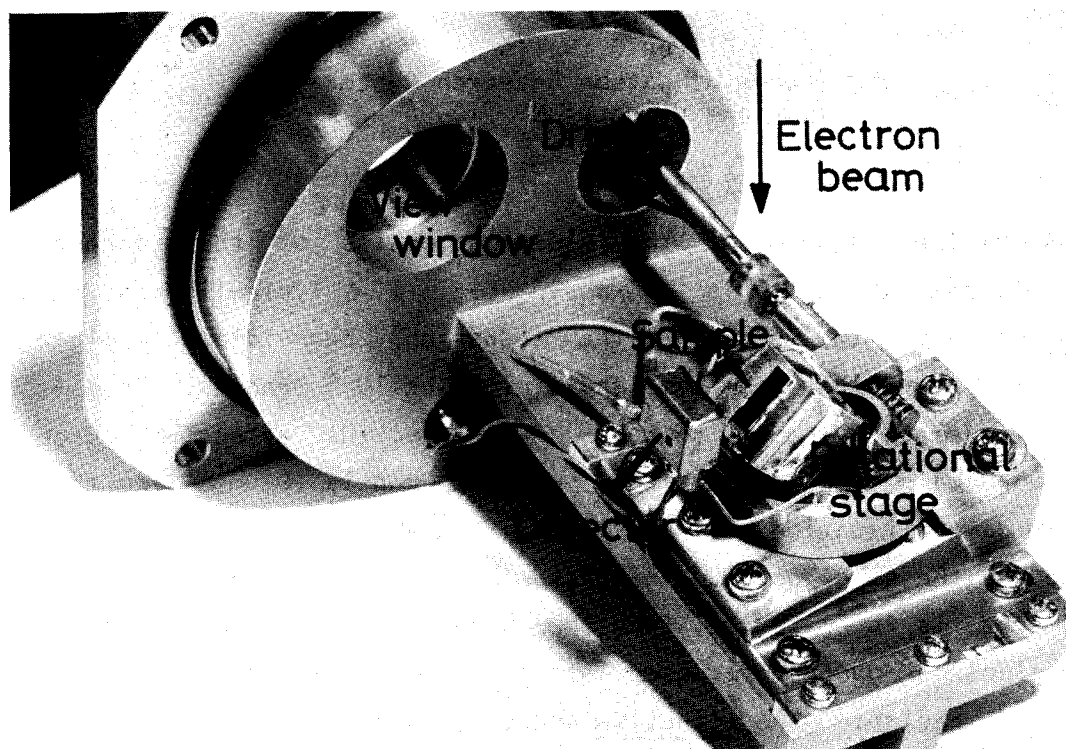
Figure 1.   Outer view of sample stage attached to JSEM-200.
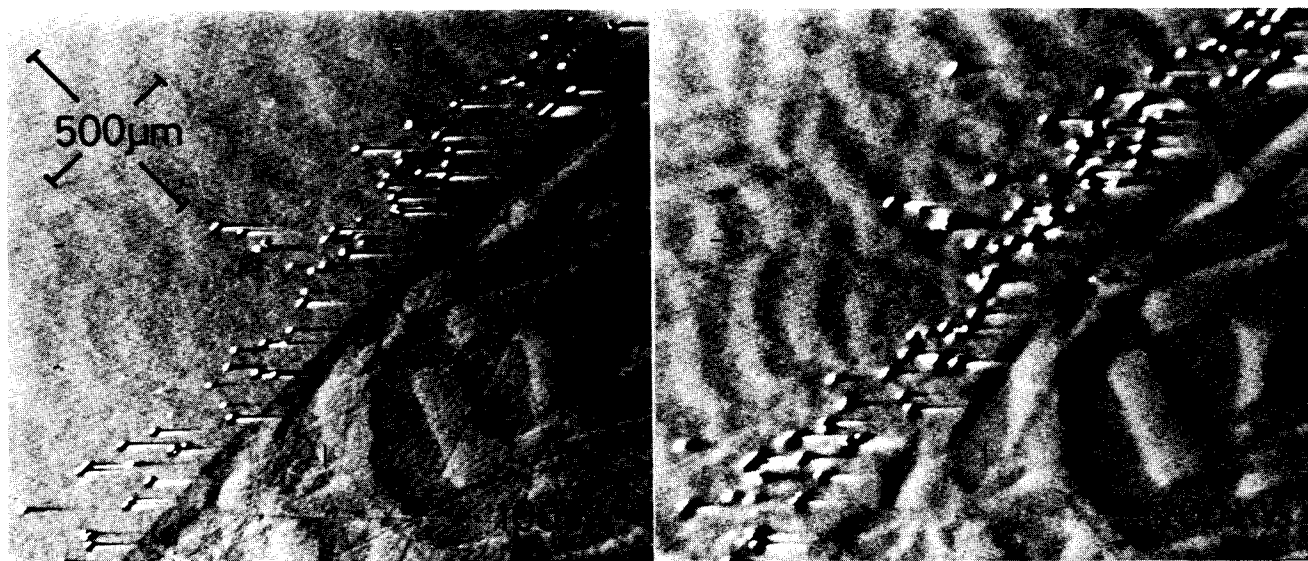
Figure 2.   Backscattered electron images of magnetic domains in
             Mn-Zn ferrite, (a) obtained at 100 KV, (b) at 200 KV.
             Upper half of the sample is mechanically polished and
             the other half chemically etched.

EXPERIMENTAL METHOD FOR MEASURING THE SOURCE SIZE IN THE SEM

Oliver C. Wells
IBM Thomas J. Watson Research Center
Yorktown Heights, NY 10598

A simplified diagram of the electron optics of the scanning electron microscope (SEM) is shown in Fig. 1. Typically, in the focussed spot on the specimen, the (Gaussian) beam diameter might measure 100 $\overset{o}{A}$, and the beam semi-angle might be 10^{-2} radian. This is obtained by demagnifying the source. Typically, the effective source diameter when using the rod-type LaB_6 electron gun is 10 μm[1], so that the column demagnification will be 10 μm/100 $\overset{o}{A}$ = 1,000. The semi-angle is scaled by the same factor. In other words, if the semi-angle in the focussed spot is 10^{-2} radian, then the cone of rays which is accepted from the electron gun and focussed into the spot will have a semi-angle of only 10^{-5} radian. The _effective_ source size must be measured using only these rays. The total source size will be larger than this because of the wide-angle rays which are stopped off lower down the column. (These wide-angle rays will, however, contribute to increasing the energy spread of the beam by means of the Boersch effect.)

The effective source size has been measured using the experimental arrangement shown in Fig. 2. Two sets of X-Y deflection coils are placed on the electron-optical axis below the electron gun, and a moveable mesh or aperture is placed below these. (In practice, there is also a third set of deflection coils, not shown in Fig. 2, which are used to adjust the effective angular alignment of the two sets of coils.) This represents an extension of an idea of Broers[1], in which only a single set of coils were used.

In theory, there are two operating modes which are possible. In Fig. 2(b), the current in the scan coils is adjusted so that $\theta_1/\theta_2 = 2.5$. Under these conditions, rays which leave the gun in different directions are selected in turn and deflected onto the axis of the SEM. The electron collector is in its usual position in the specimen chamber, so that only the rays which fall within the 10^{-5} radian semi-angle are collected to form the image. This gives an image of the type described

by Broers[1]   in which the bright lobes from the gun can be inspected and one of them can then be brought onto the axis of the SEM. This image is of the greatest value, because of the information that it can give on the condition of the rod.

The next step is shown in Fig. 2(c).   Here, the ratio between θ_1 and θ_2 has been adjusted so that a ray which leaves the gun along the axis is deflected so as to appear to come from different directions. In other words, the source appears to move, and a shadow image will be obtained from the mesh.   The sharpness of the shadow image should, ideally, be given by the source size. Here, the mesh is displaced by 15 cm along the axis from the source, and this will introduce an additional blurring of 15 cm times 10^{-5} radian = 1.5 µm, which in this case can be ignored. This mode of operation will depend partly on the ratio θ_1/θ_2, and partly on the strength of the first lens (because changing the strength of this lens will move the entrance pupil along the axis).

Some experimental results are shown in Fig. 3. This shows the effect of varying the ratio θ_1/θ_2. Fig. 3(a) was obtained by scanning only one set of coils, and the intensity diagram and the shadow image are superimposed. In Fig. 3(b) the ratio was adjusted to give a shadow image, and the sharpness of the waveform gave the expected effective source size which was close to 10 µm.

The most important feature of this method is that it makes it possible to measure the fraction of the beam diameter at the surface of the specimen which arises from the image of the source, as compared with the effective beam diameter, in which the beam is enlarged by aberrations and by interactions in the specimen.   (The question of diffraction is less simple.) This is achieved by moving the specimen into position while the beam is being scanned in the shadow mode, so that a high magnification image of the specimen is obtained through the windows of the mesh in the shadow image. The magnification of this image will depend on the demagnification in the column. The sharpness of this image can then be compared with the sharpness of

the shadow image of the mesh. The present status of this work is that the double image has been obtained and is being evaluated (Fig. 4).

I would like to thank L. W. Landermann and R. J. Gallo for technical assistance.

1. Broers, A. N., J. Vac. Sci. Technol., 10, 979-982, (1973).

LaB$_6$ROD

THE CROSSOVER
INCLUDES ALL RAYS

THE EFFECTIVE
SOURCE DIA = 10 μm
EFFECTIVE SEMI-ANGLE
= 10^{-5} RADIAN

THE INTERMEDIATE
LENSES ARE NOT SHOWN

FINAL LENS AND
BEAM-DEFINING
APERTURE

SPOT DIA.= 100 Å
SEMI-ANGLE
= 10^{-2} RADIAN

SPECIMEN
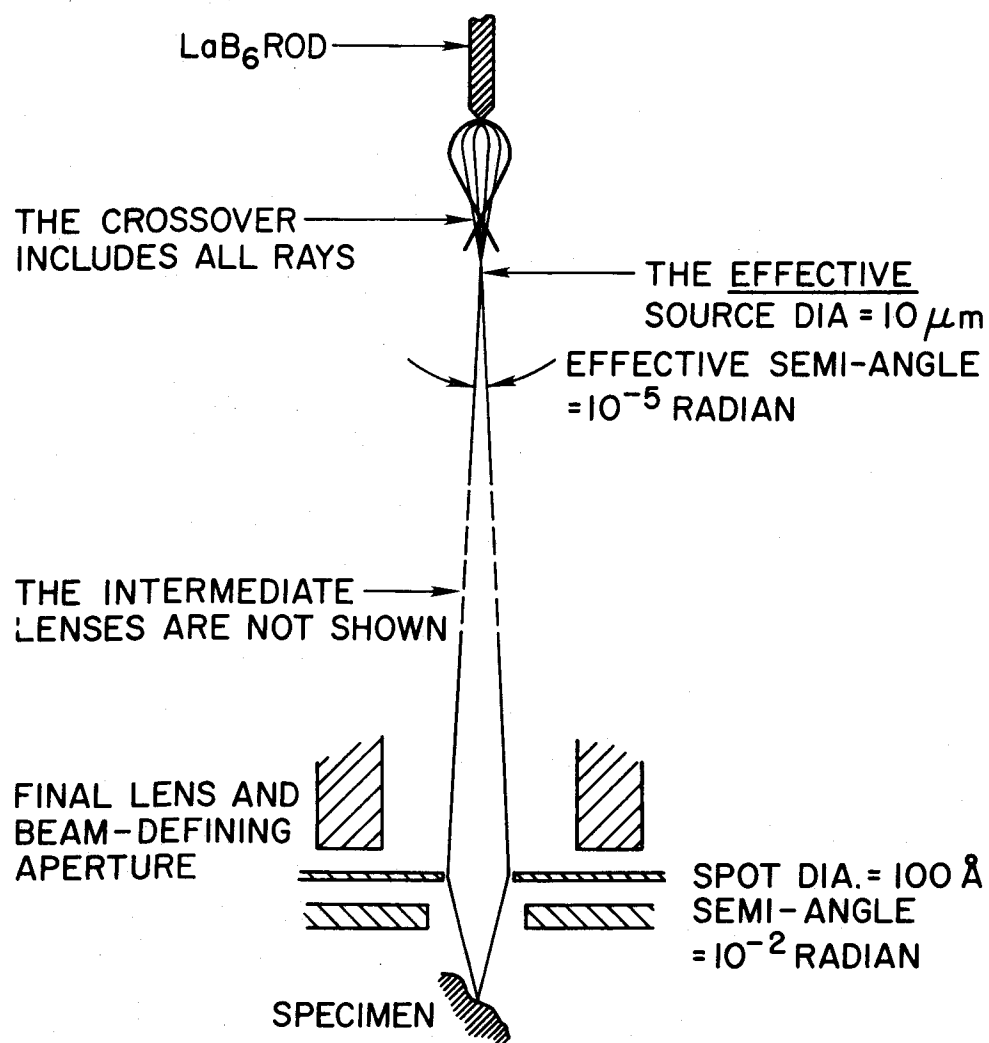
Fig. 1 Simplified ray diagram of SEM

ELECTRON
GUN

DEFLECTION
COILS

MESH OR
APERTURE

FIRST
LENS

β DIAGRAM:

•S

θ_1

$\dfrac{\theta_1}{\theta_2} = 2.5$

θ_2

SHADOW IMAGE
OF THE MESH:

•S   •S'

θ_1

$\dfrac{\theta_1}{\theta_2} = 0.73$

MESH

θ_2

entrance pupil
of the lens.
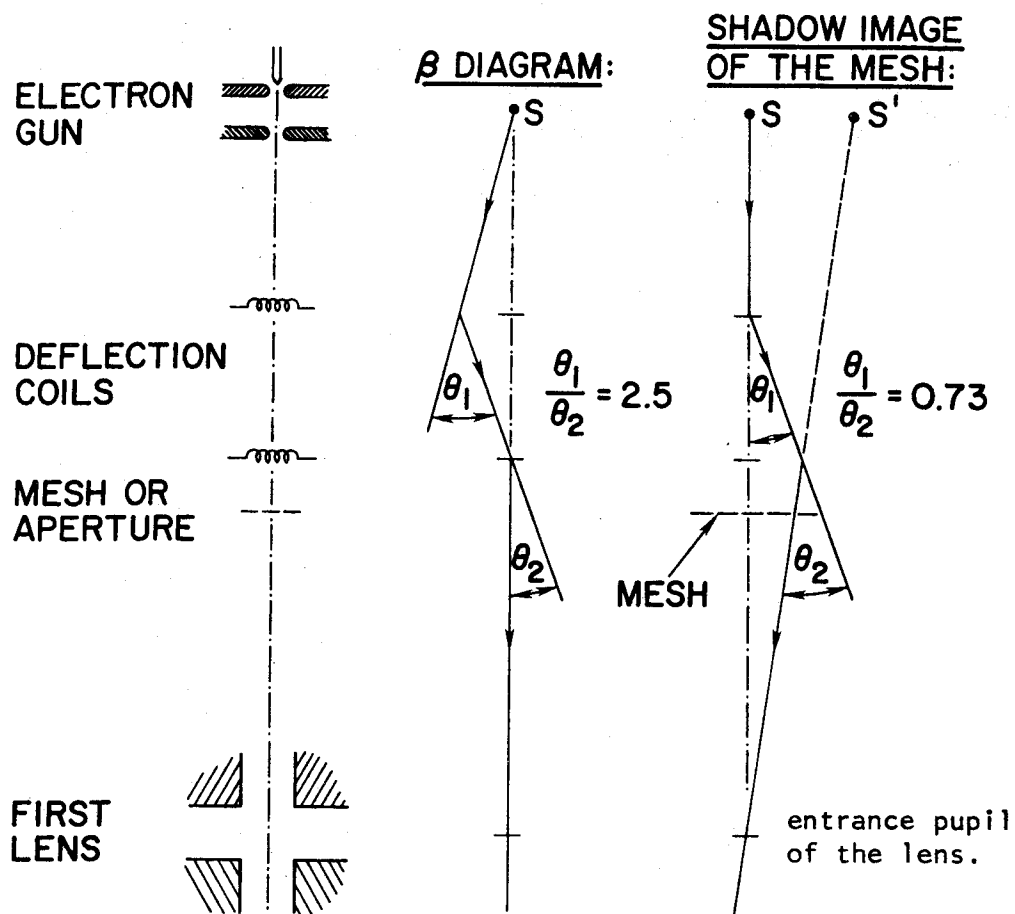
Fig. 2 (a) Experimental setup. (b) Ray diagram when obtaining an intensity diagram (c) Ray diagram for shadow image.
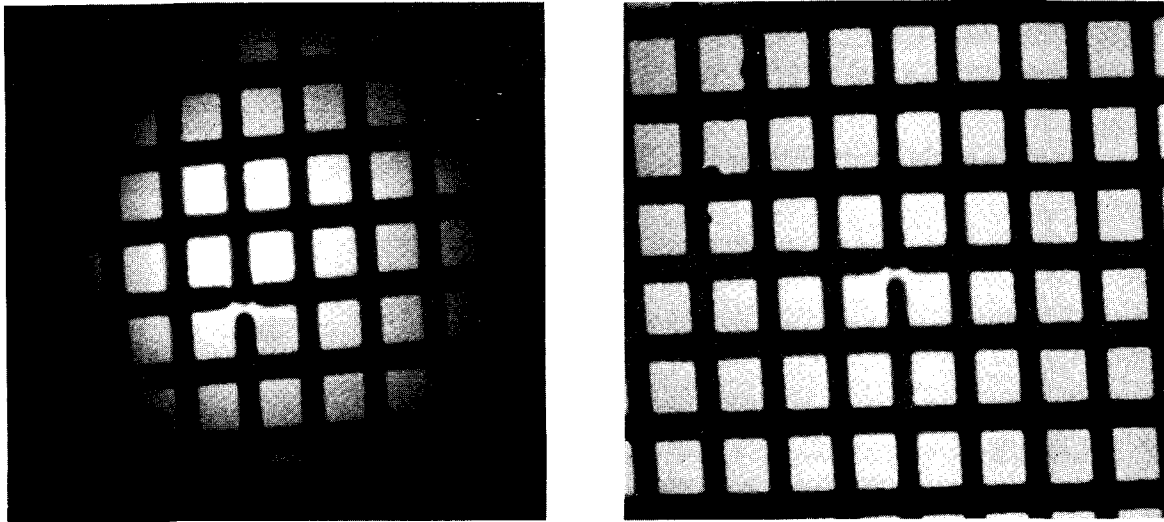
Fig. 3 (a) Superimposed intensity diagram and shadow image of 200-mesh copper grid. (b) Shadow image, obtained by adjusting the relative deflections.
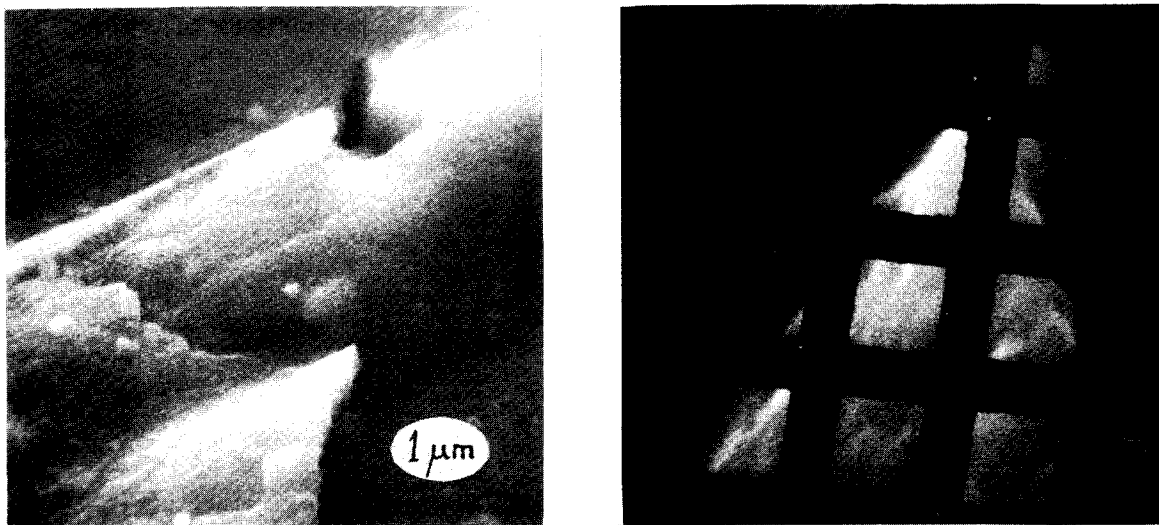
Fig. 4 Secondary electron image of aluminum specimen stub (θ = 45°, E = 20 kV). (b) Shadow image and topographic image superimposed.

AN ANALYTICAL SCANNING TRANSMISSION ELECTRON MICROSCOPE

H. von Harrach, C.E. Lyman, A.R. Walker, D.C. Joy* and G.R. Booker

Department of Metallurgy and Science of Materials, University of Oxford, Parks Road, Oxford OX1 3PH, England.

A scanning transmission electron microscope (STEM) with a field emission gun has been developed for quantitative microanalysis. The high brightness source combined with X-ray analysis, electron diffraction and electron energy loss analysis provides a technique of microanalysis from regions of thin specimens as small as a few hundred angstroms.

The electron optical lay-out of this microscope is shown in Figure 1. A triode field-emission gun is mounted in a UHV chamber with mu-metal walls for screening. The gun which can be operated at up to 100kV provides a virtual source; the position of this source is largely independent of the ratio of the acceleration voltage to extraction voltage. Two conventional magnetic lenses are used to obtain a probe that can be varied from 10Å to about 1μm diameter. The specimen can be inserted into the bore of the objective lens for high-resolution STEM imaging. An energy-dispersive X-ray detector is positioned on the transmission side of the specimen. The X-ray spectra are accumulated by a multichannel analyser (MCA) and stored on paper tape. At a probe size of 100Å a probe current of about 1nA should generate sufficient X-rays for analysis of particles less than 500Å in diameter. A projector lens column of three mini lenses[1] is used for variation of the collection angle (range 0.05 to 10^{-4} rad.) for transmitted electrons and for selected area diffraction. Selected area diffraction patterns may be obtained by the rocking beam technique[2] using the high magnification of the projector lenses to select areas of less than 500Å or by the Grigson technique[3] using a stationary probe to define the region analysed. A magnetic prism electron spectrometer has been designed to provide energy-loss spectra and energy-selected STEM images or diffraction patterns. The MCA is used to store the data and transfer it to paper tape. The K-shell ionization loss spectra provide information for microanalysis of light elements.

The detection and signal processing system is shown in Figure 2. Detectors are mounted to collect X-rays, transmitted electrons at small and wide angles, backscattered electrons and specimen current. The scan system can be operated either at TV rates or at slow scan rates controlled by a digital scan generator[4]. In the latter case the signals are digitized in synchronism with the digitally scanned raster. Further processing may be carried out by storing the image data on tape and using an off-line computer.

Preliminary work has produced STEM images of about 100Å resolution at TV scan rates. The field emission gun has been operated at voltages up to 50kV. At a pressure of 5×10^{-10} torr a total emission current of several micro-amperes can be obtained. Measured values for the brightness in the probe are in the range $10^7 - 10^8$ A $cm^{-2}st^{-1}$. Following thermal conditioning of the field emitter, the probe current reaches 1% stability after 15 minutes and can be run stably for about 1 hour.

1. S.M. Juma and T. Mulvey, in Proc.of Eighth Int.Congress on Electron Microscopy, Canberra, 1, 134 (1974).
2. M.N. Thompson, in SEM 1973 (Newcastle) Conference Series No.18, The Institute of Physics, p.176 (1973).
3. C.W.B. Grigson, J.Elect. and Control, 12, 209 (1962).
4. D.C. Joy and G.E. Verney, SEM 1973 (Newcastle) Conference Series No.18, The Institute of Physics, p.50 (1973).

* Present address: Bell Telephone Laboratories, Murray Hill, New Jersey, USA.

Electron
Spectrometer

Projector Lens

Projector Lens

Collector Lens

Deflection Coils

X-Ray Detector
SPECIMEN

Objective Lens

Scan +
Alignment
Coils

Condensor Lens

Isolation Valve

Field-Emission
Source

10^{-6} Torr

10^{-7} Torr

10^{-10} Torr
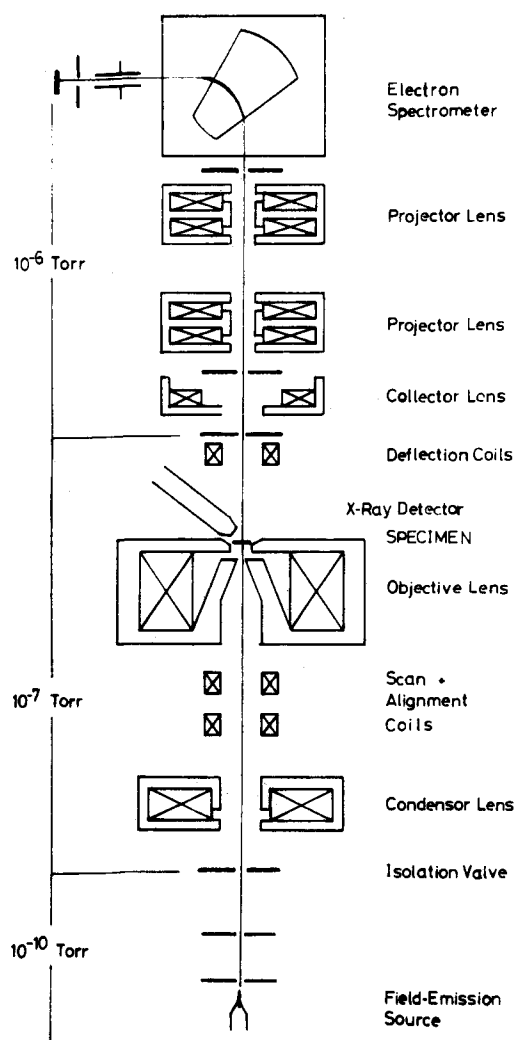
Fig.1. Schematic
diagram of electron
optical column.

Scaler

Preamp

X-rays

MCA

transmitted
beam

scattered

specimen current

backscattered

incident
beam

Scan
Generator

ADC

Clock

TV
Display

CRT

CAMAC

Mini
Computer

Paper
Tape
Punch
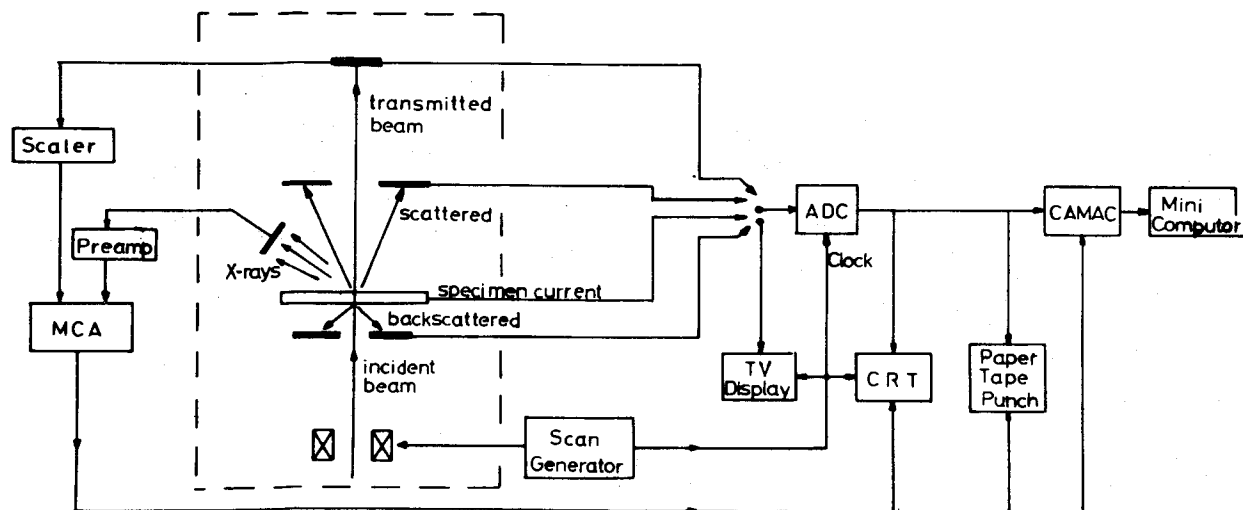
Fig.2. Block diagram of detection and signal processing systems.

AN IMPROVED SPECIMEN MOUNT FOR SCANNING ELECTRON MICROSCOPY

M. K. Lamvik and S. D. Lin

Enrico Fermi Institute, University of Chicago, Chicago, Illinois 60637

The development of a specimen holder for use without adhesives was originally motivated by the need to maintain an especially clean specimen environment in ion-pumped high vacuum scanning microscopes.[1] Since then, it has become clear that the system is very convenient and inexpensive in everyday use and would be of value in many types of scanning microscopes. We report here some recent improvements in the system.

The design is based on the use of a simple disc as the specimen mount, rather than a more complex shape such as a "stub." Since the disc may be the actual substrate upon which a specimen is obtained, no adhesive is needed to attach the substrate to a mounting stub. Commonly used discs include Millipore, Nucleopore, or Flotronic filters, glass cover slips, or discs of mica, glass, carbon, or various metals with or without a carbon coating. Noise in secondary electron micrographs may be reduced by choosing a substrate material that produces small numbers of secondary and back-scattered electrons. Aluminum has been found to be satisfactory. Although aluminum is not suitable in ultra high vacuum systems, in our microscope it is compatible with a vacuum of 5×10^{-8} torr in the specimen chamber. Metal discs are cheaper than stubs, because they can be made inexpensively by punching. The disc is a compact shape, and more specimens can be stored in a given volume with discs than with stubs.

The simplification in the shape of the specimen mount is achieved at the expense of adding complexity to the mounting position of the microscope; many specimen mounts are needed, but each microscope requires only one stage. We have chosen to mount the discs on supporting cylinders using caps with large central apertures (Fig. 1). Rims extend from the sides of the cap to facilitate handling with tweezers. Slots are cut between the two rims to form springs which hold the cap in place. The ring-shaped cap ensures good contact with the upper surface of the discs (providing electrical continuity with a conductive coating when insulating discs are used) and it applies the contact pressure over a large area (to avoid breaking delicate discs). Those who would use metal mounting discs exclusively need not exercise such care; in this case simple edge-clips have the advantage of exposing nearly all of the disc surface.

In general, no modification of a mounting stage is necessary, since the disc-supporting cylinder may simply be made in the shape of a stub (Fig. 2); this yields a disc-holding stub adapter that fits directly into the microscope. When it is desirable to study a large number of specimens efficiently, it is possible to mount several small discs under a single large cap (Fig. 3). Time spent in specimen exchange is thus minimized. There are often advantages to the use of transmission electron microscope grids in scanning electron microscopy,[2] and the disc holder concept may be extended to the multiple mounting of grids (Fig. 4).

Frequently it is useful to measure beam current for instrumental reasons or for the determination of secondary or backscattered electron yields. A small hole drilled in the metal disc specimen mount, with a corresponding recess in the supporting cylinder, constitutes an effective Faraday cage for this purpose.

We have found this simple mounting concept to be very versatile in a variety
of applications, and very inexpensive in routine use.

References

1. M. K. Lamvik and S. D. Lin, "A new specimen mounting system for scanning
    electron microscopy," J. Microscopy 101, 329 (1974).

2. M. K. Lamvik, "Scanning secondary electron microscopy of myofibrils using
    transmission techniques," in these Proceedings.
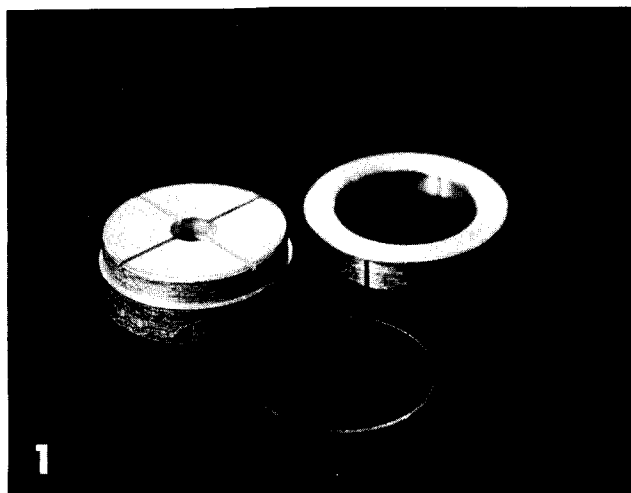
Fig. 1. Disc holder for the Hitachi HFS-2. The disc is held on the support-
ing cylinder using the ring-shaped cap at the upper right. The hole through
the cylinder and the channels across its face aid in pumping gas from the
rear of the disc. An 18 mm round glass coverslip is shown.
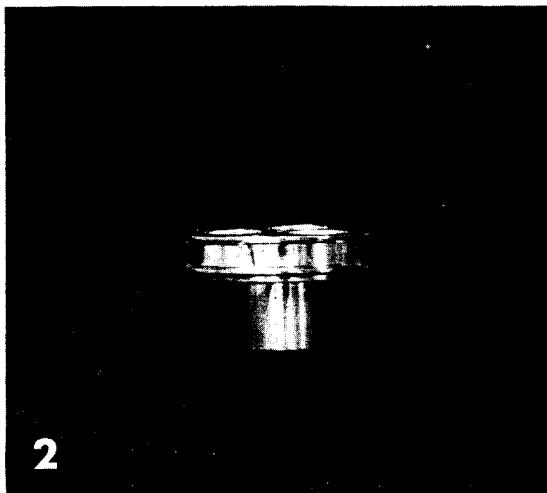
Fig. 2. Disc holder for Coates & Welter microscopes. Slots cut in the rim
of the cap form springs to hold the caps in place. All caps are made of
phosphor bronze.
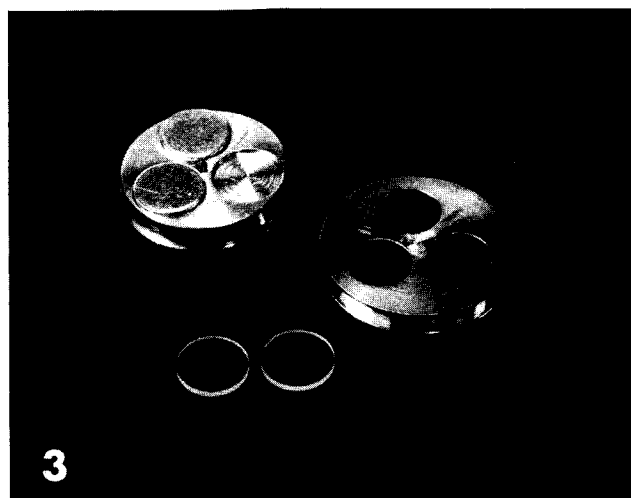
Fig. 3. Multiple disc holder. Two 8 mm aluminum discs are shown in place
on the holder; two glass discs are below.
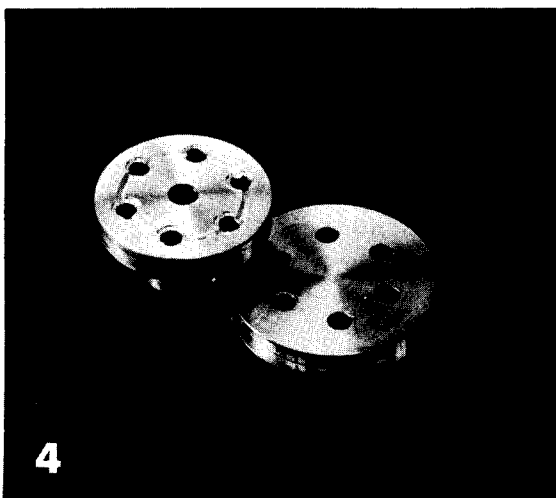
Fig. 4. Multiple grid holder. Six standard 3 mm electron microscope grids
are held over holes cut completely through the support.

A SIMPLE TRANSMISSION STAGE FOR A SCANNING ELECTRON MICROSCOPE[†]

P. S. D. Lin[*] and M. K. Lamvik[**]

*Enrico Fermi Institute and **Department of Biophysics
The University of Chicago, Chicago, Illinois 60637

Unlike a CEM or high resolution STEM, where the specimen is immersed between the pole pieces of the objective lens, a scanning electron microscope has its specimen stage situated off the lens field. After scattering with the specimen, electrons follow straight paths. It is rather simple to deduce the information from the signal. A transmission stage in a SEM is therefore a useful device for studying various scattering processes and the contrast thus generated.

The transmission stage can also be used in connection with the investigation of secondary and backscattered electron emission phenomena. Previously, a back-scattered electron detector was installed in one of the scanning microscopes in the laboratory.[1] Experiences indicate that back-scattered electrons can produce micrographs of high resolution and contrast for a certain type of surface structure.[2] They can also be used to reveal the interior organism of a biological specimen provided it is properly stained.[3,4] Nevertheless, quantitative information such as the minimum detectable mass, the limit of resolution as a function of specimen preparation methods, etc. were difficult to assess by using the back-scattered electron detector alone. This situation will certainly be improved with the aid of a transmission stage. For example, the stage can provide information about the size and mass of small particles that can be detected by collecting back-scattered electrons.

The transmission stage consists of an annular Si detector, a tubular detector-supporting arm, a high vacuum bellows and a mechanism for detector motion. There are no extra apertures at the present, but they can be added if necessary. For dark or bright field observations, the central hole of the detector is positioned directly below or away from the area of interest on the specimen (Figs. 1 and 2). Figs. 3 and 4 show stained tropomyosin tactoids[5] as examined in these two modes at a primary electron energy of 25 keV.

To put further studies on a quantitative basis, we have initiated measurements on the transmitted electron intensity as a function of mass thickness. The objects used are polystyrene spheres dispersed over a piece of very thin carbon film supported in turn by a holey plastic film. In each measurement, the sphere is first positioned close to the central area of the viewing screen, then the beam is scanned across the middle of the sphere and the signal is recorded photographically (Figs. 5, 6). One set of data deduced from such a measurement is shown in Fig. 7. Comparison between experimental results and theoretical calculations[6] is currently in progress.

References:
1. P.S.D. Lin and R.P. Becker, IITRI/SEM/1975, pp. 61-70.
2. P.S.D. Lin, these Proceedings.
3. J.L. Abraham and P.B. DeNee, IITRI/SEM/1974, pp. 251-258.
4. P.S.D. Lin and A.V. Crewe, these Proceedings.
5. Cohen et al., Cold Spr. Harb. Symp. Quant. Biol. 36, 205 (1971).
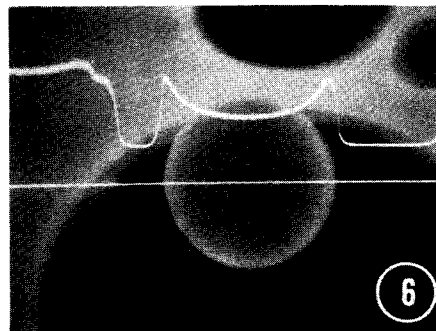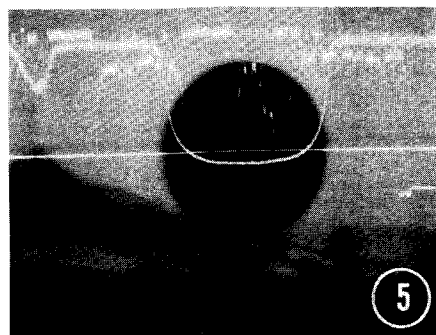6. M. K. Lamvik and A. V. Crewe, these Proceedings.
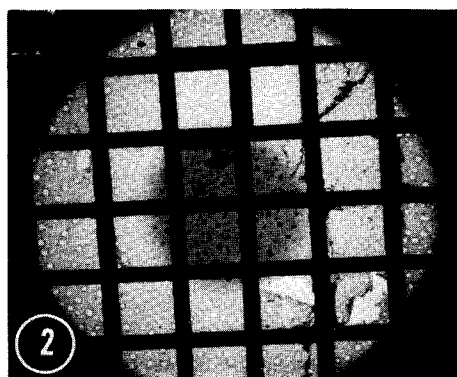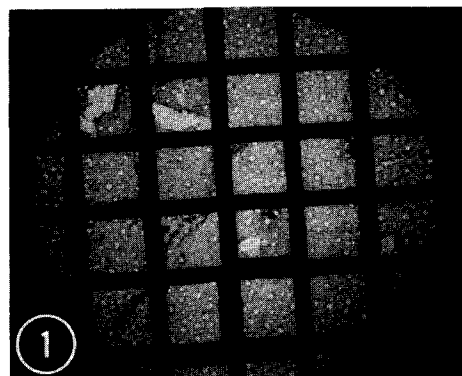
Figs. 1, 2. Total field of view as observed in bright (left) and dark (right, central region) field modes.
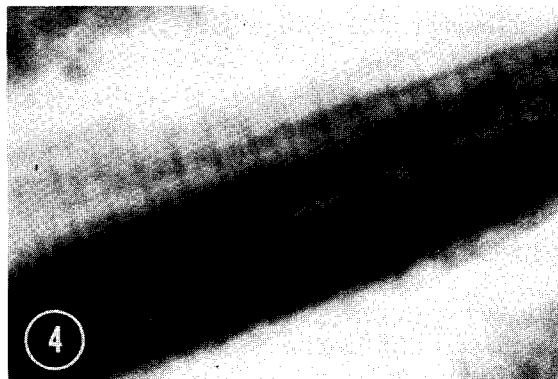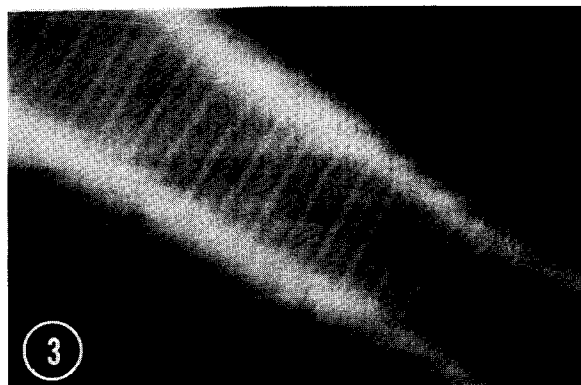
Figs. 3, 4. Bright (left) versus dark (right) field images of stained tropomyosin tactoids. Major periodicity, 395 Å. Signal inverted in Fig. 3.

Figs. 5, 6. Signals sampled over polystyrene spheres. Bright (left) versus dark (right) field. The extra signal in Fig. 5 is for normalizing intensity.
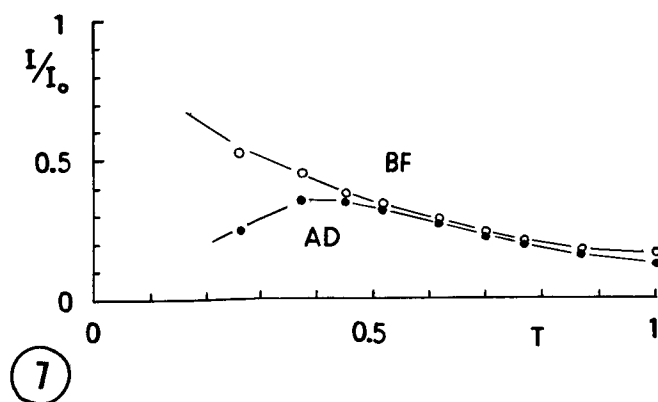

Fig. 7. Transmitted electron intensity I (normalized with I_o, the primary electron intensity) as a function of the normalized mass thickness T of the polystyrene sphere. BF, bright field. AD, dark field/annular detector.

QUANTITATIVE X-RAY ENERGY DISPERSIVE ANALYSIS

WITH THE TRANSMISSION ELECTRON MICROSCOPE

R.H. Geiss and T.C. Huang

IBM Research Laboratory
San Jose, California 95193

ABSTRACT

The addition of x-ray energy dispersive spectroscopy (EDS) to a transmission electron microscope (TEM) makes it possible to greatly extend the capabilities for characterization of materials on a micro-scale. Where the well-known uses of the TEM are combined with quantitative x-ray elemental analysis from the same small areas used for high resolution photography and electron diffraction, etc., a new dimension of significant importance is added to micro-characterization. Regions as small as 2000Å in diameter can be analyzed with conventional TEM optics, and with the strong pre-field condenser objective lens used in the Philips 301 STEM it is possible to analyze regions as small as 250Å in diameter and to do elemental mapping of areas up to approximately 0.2 mm square. This can be done without interferring with the normal TEM operational capabilities.

The purpose of this paper is to discuss in detail some of the factors which effect the TEM-EDS interface. Considered are detector placement and collimation, sample tilt, apertures and accelerating voltage. Equally important is a successful data processing scheme including corrections for detector efficiency and sample absorption, background subtraction and a profile-fitting method to reduce experimental data for quantitative analyses. This is an especially powerful tool for handling overlapped peaks. Using a straight forward analysis scheme the data may then be reduced to elemental composition with an accuracy and precision on the order of 1%.

FRAME B: An On-Line Correction Procedure
for Quantitative Electron Probe Microanalysis
with a Si(Li) Detector

C. E. Fiori, R. L. Myklebust, K. F. J. Heinrich
and H. Yakowitz
Institute for Materials Research
National Bureau of Standards
Washington, DC 20234

The correction procedure FRAME B has been developed for electron probe microanalysis with a lithium-drifted silicon detector. This program, which computes on-line mass fractions of the elements contained in the specimen, is a modification of the correction procedure FRAME [1]. The input data required are: x-ray intensities from the peaks of interest and the continuum intensities at two energies, the atomic numbers of all the elements present, the analytical lines used and the operating voltage. Other required parameters, such as atomic weights, the x-ray emergence angle and x-ray mass attenuation coefficients, are stored or calculated by the program. FRAME B is in FORTRAN IV; it requires less than 5,000 words of computer core, and will handle up to 13 elements.

The program includes a method for background correction which is an extension and amplification of schemes proposed by Ware and Reed [2], and by Lifshin [3]; this is discussed elsewhere in detail [4]. The expression used in this method predicts the intensity of the continuous radiation recorded in energy-dispersive x-ray spectrometry (EDS) [5] as a function of x-ray photon energy. The algorithm used is:

$$N(E) = [\frac{a(E_o-E)}{E} + \frac{b(E_o-E)^2}{E}] \cdot f_E \cdot [exp-(\mu(Be,E)t_{Be} + \mu(Si,E)t_{Si}^{D})] \cdot [1-exp-(\mu(Si,E)t_{Si})]. \qquad (1)$$

The notation is as follows: The observed count rate within a narrow energy range, ΔE, of x-rays centered around the energy $E(keV)$ is $N(E)\Delta E$. The energy of the primary impinging electrons is called $E_o(keV)$. The probability of absorption within the target of the emerging x-ray photon of energy E is called f_E. In the last two terms of equation (1), $\mu(Be,E)$, and $\mu(Si,E)$ are the mass attenuation coefficients (cm^2/g) for radiation of energy E of the beryllium window and the silicon in the detector. The symbols t_{Be} and t_{Si}^D denote estimates of the thicknesses of the beryllium window and the dead layer adjusted to optimize the fit below two keV, and t_{Si} is the detector thickness.

The continuous spectrum for a specific set of conditions is obtained as follows. From the value of $N(E)$ measured at two energy levels where there are no characteristic lines or detector artifacts (incomplete charge collection, pulse pile-up, double energy peaks and escape peaks), the parameters a and b in equation (1) are calculated. They in turn define, through equation (1), the value of $N(E)$ at any energy E. The procedure is illustrated by a spectrum from a complex mineral, Kakanui Hornblende (see figure 1). Table I shows the elements present and their respective concentrations. Figure 1 shows the recorded spectrum and the fit of the continuum. The triangles are the two points chosen for calculating a and b.

As pointed out by Ware and Reed [2], the absorption term f_E is dependent upon the composition of the target. Therefore, when the composition of the target is unknown, it is necessary to include equation (1) in an iteration loop as shown in figure 2. This flow diagram is a simplified description of the program. Application of the technique to quantitative electron probe microanalysis
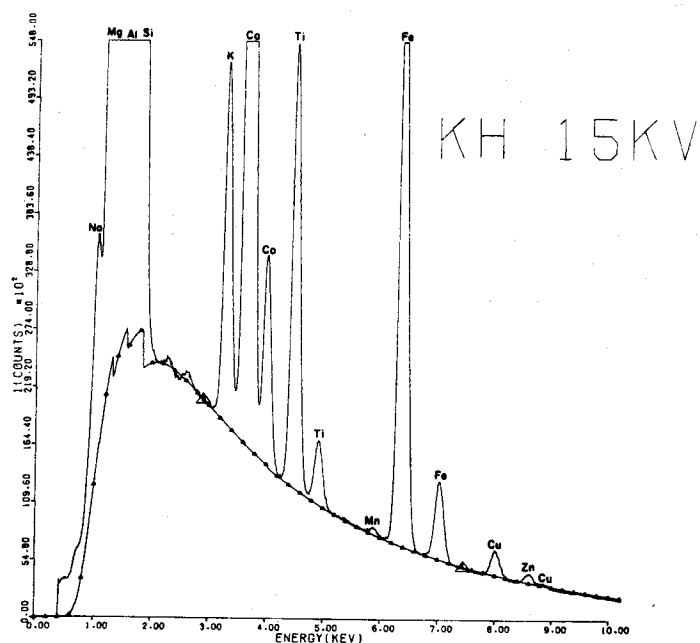
Figure 1. Background correction in Kakanui
Hornblende (see Table I). Fitted
continuum curve calculated with
equation (1). Note the presence
of Mn at 700 ppm.

was made by analyzing a series of well-characterized
iron-nickel alloys [6]. FRAME B was employed for the
evaluation of the measurements, and the results are
given in Table II.

Tests of FRAME B indicate that electron probe quanti-
tation with the energy-dispersive x-ray spectrometer can be
carried out simply and accurately whenever the resolution
of the spectrometer is adequate.
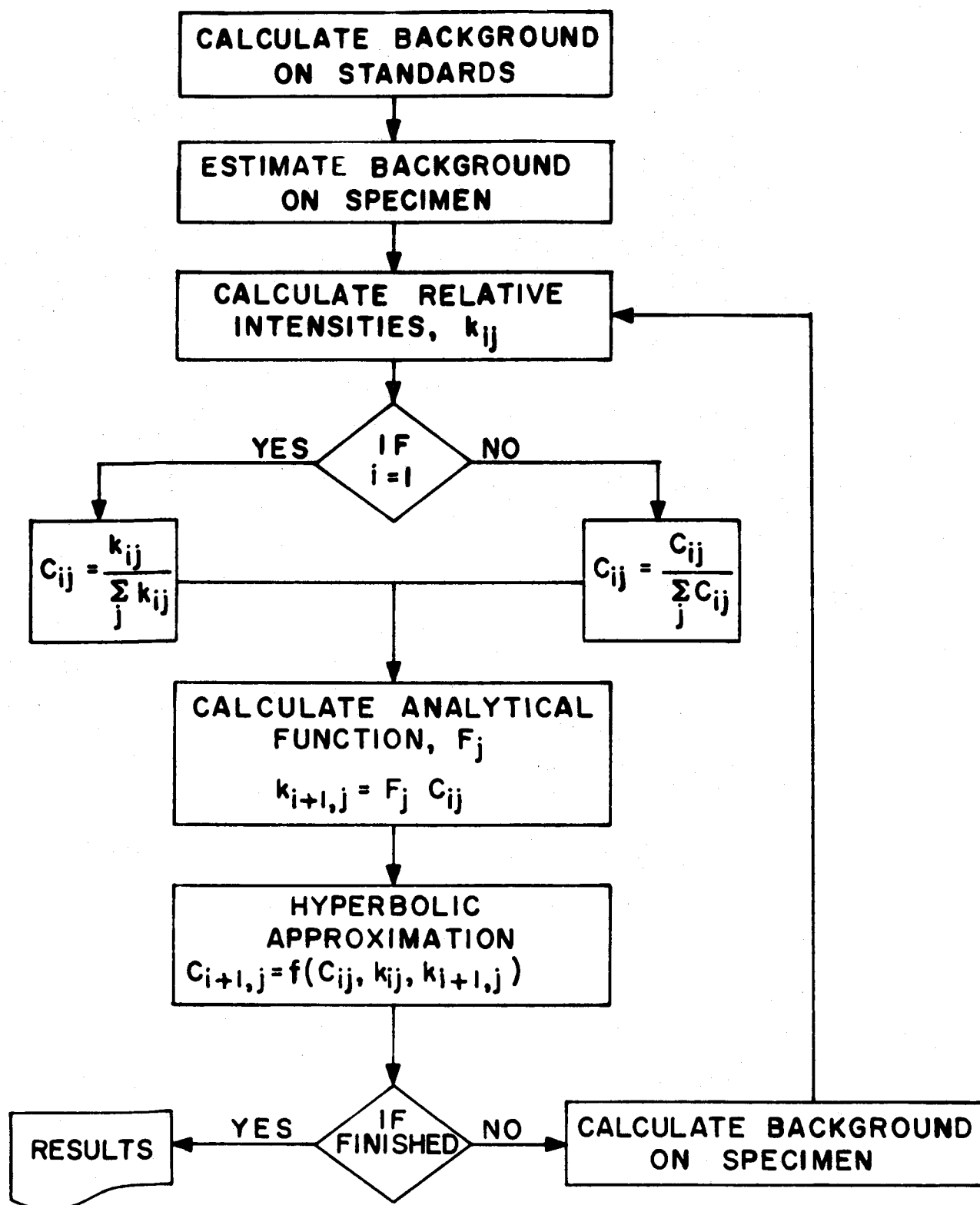
Figure 2. Flow diagram showing the iteration loop
for background correction of energy-
dispersive x-ray spectra.

Table I. Kakanui Hornblende

Element	Concentration (wt. %)
Na	1.93
Mg	7.721
Al	7.885
Si	18.87
K	1.7
Ca	7.36
Ti	2.626
Mn	0.0697
Fe	8.49
O	Balance

Chemical analysis of Kakanui Hornblende as reported by Jarosewich [7].

Table II. Analysis of Ni-Fe Alloys

	Chemical Analysis	FRAME B Calculated
Alloy #1	Fe .948	.943
	Ni .052	.052
Alloy #2	Fe .897	.897
	Ni .103	.103
Alloy #3	Fe .848	.854
	Ni .152	.149
Alloy #4	Fe .806	.811
	Ni .194	.191
Alloy #5	Fe .748	.757
	Ni .252	.249
Alloy #6	Fe .647	.657
	Ni .353	.347

References

[1] Yakowitz, H., Myklebust, R. L. and Heinrich, K. F. J.,
     U.S. National Bureau of Standards Technical Note 769,
     U.S. Government Printing Office, Washington, DC 20402
     (1973).

[2] Ware, N. G. and Reed, S. J. B., Phys. E: Scientific
     Instruments 1973, vol. 6 (1973).

[3] Lifshin, E., Proc. 9th Annual Conference of Microbeam
     Analysis Society, Ottawa, Canada, paper 53 (1974).

[4] Fiori, C. E., Myklebust, R. L., Heinrich, K. F. J.
     and Yakowitz, H., Prediction of Continuum Intensity
     in Energy-Dispersive X-ray Microanalysis, in press.

[5] Fitzgerald, R., Keil, K. and Heinrich, K. F. J.,
     Science 159, 528-529 (1968).

[6] Goldstein, J. I., Hanneman, R. E. and Ogilvie, R. E.,
     Trans. Met. Soc. of AIME 233, 812 (1965).

[7] Jarosewich, E., Chemical Analysis of Five Minerals for
     Microprobe Standards, Smithsonian Contributions to
     the Earth Sciences, no. 9, Smithsonian Institution
     Press, Washington, D. C. (1972).

AN APPROACH TO FULLY QUANTITATIVE ENERGY DISPERSIVE ELECTRON MICROPROBE ANALYSIS

D.G.W. Smith

Dept. of Geology

University of Alberta

Edmonton, Alta., Canada T6G 2E3

A scheme for fully quantitative energy dispersive electron microprobe analysis has been developed and tested on a wide range of materials of varying compositional complexity. 21 elements, including Na to Zn (except Ar) plus Zr and Ba, are determined automatically and simultaneously on any sample. Extension of the method to other elements of higher atomic number has not been tested but appears feasible.

The equipment used is an A.R.L. EMX microprobe fitted with an Ortec Si(Li) detector. Associated Ortec electronic components are: a 450 research amplifier, 454 timing filter amplifier, 436 100 MHz discriminator, 404A pulse pile-up rejector and a 6220 MCA. The 6220 incorporates facilities for automatic correction of deadtime and pulse pile-up related counting losses. At a counting rate of 1000 pps at 5.9 keV, the system has a FWHM (above background) of 154 eV. The MCA is interfaced via a Texas Instruments 733 cassette tape terminal to an IBM 360/67 computer.

Spectra from a calibration standard, working standards and all samples are acquired at a 15 kV operating voltage, and then processed through a FORTRAN IV computer program that performs the following functions: 1) identifies major peaks present and determines apparent energies; 2) adjusts observed intensities in all channels for zero and amplifier gain shifts, using positions of peaks in either the calibration standard or a sample itself; 3) strips escape peaks; 4) calculates background intensities; 5) integrates characteristic intensities using 1.2 x FWHM range; 6) corrects for overlap; 7) corrects for matrix effects to background and characteristic radiation; 8) iterates procedure until convergence is achieved; 9) calculates and prints corrected concentrations of elements present, together with ZAF corrections, etc.

Significant improvements in accuracy and detection limits have resulted from a new expression for atomic number dependence of continuum intensity[1];

$$I_\nu = f(E_\nu, E_0) \cdot (\bar{Z})^n, \text{ in which } n = 1.159 + (0.1239 - 0.02857.\ln E_0) \cdot (E_\nu - 2.044),$$

and where: I_ν is the continuum intensity at an energy E_ν and $f(E_\nu, E_0)$ is a function of E_ν and operating voltage (E_0). For spectra acquired at fixed E_0 and probe current, $f(E_\nu, E_0)$ is constant and observed continuum intensities are dependent only on average atomic number $(\bar{Z})$ and its exponent n. This can be calculated for all continuum energies.

The observed continuum intensity for diamond, a high purity substance with a spectrum free of characteristic peaks, is divided by $(\bar{Z})^n$ and corrected for matrix effects. The spectrum thus obtained is termed the *normalised background*. For each channel, representing a small energy range about E_ν, all energy dependent terms are constant, for spectra obtained at the same operating voltage. To calculate the background for any sample it is merely necessary to multiply the normalised background spectrum by $(\bar{Z})^n$ for that sample and adjust for matrix effects on the basis of available information on composition. For a standard, this adjustment is made only once, but for an unknown, it forms part of the iterative correction procedure. An advantage of this approach is that detector absorption effects are faithfully reproduced in the normalised background and thereby automatically incorporated when background corrections are made for samples. Hence, the Be window, Au contact-surface layer and detector dead-layer thicknesses need not be known.

Because spectra may be acquired with different probe currents and counting periods, calculated continuum intensities must be scaled to the observed spectrum. To achieve this, the lowest running average ratio of observed to normalised background for ten adjacent channels (R_L) is found. This is used to define an upper limit (R_U): $R_U = R_L \cdot (1 + 3.5/\sqrt{I})$ where I is the total counts observed in any given channel of the sample spectrum. A final average ratio (R_A) is calculated using only channels where the local ratio $R < R_U$. R_A then defines the scaling factor which is applied to calculated background. Those parts of the spectrum with an energy less than 2 keV are not used for this purpose because of the steep slope of the continuum in the region of rapidly falling detector efficiency. Also, regions higher than 9 keV are ignored because the generally low intensities result in poor counting statistics. This procedure gives very satisfactory low residual intensities in regions free of characteristic peaks, pile-up and tailing effects. When background corrections are applied in this way to materials of well known composition, statistical variations (for about 1,200,000 counts/full spectrum) generally exceed significantly any systematic deviations from baseline in regions free of characteristic peaks. Typical spectra, before and after background removal, are shown in Fig. 1.
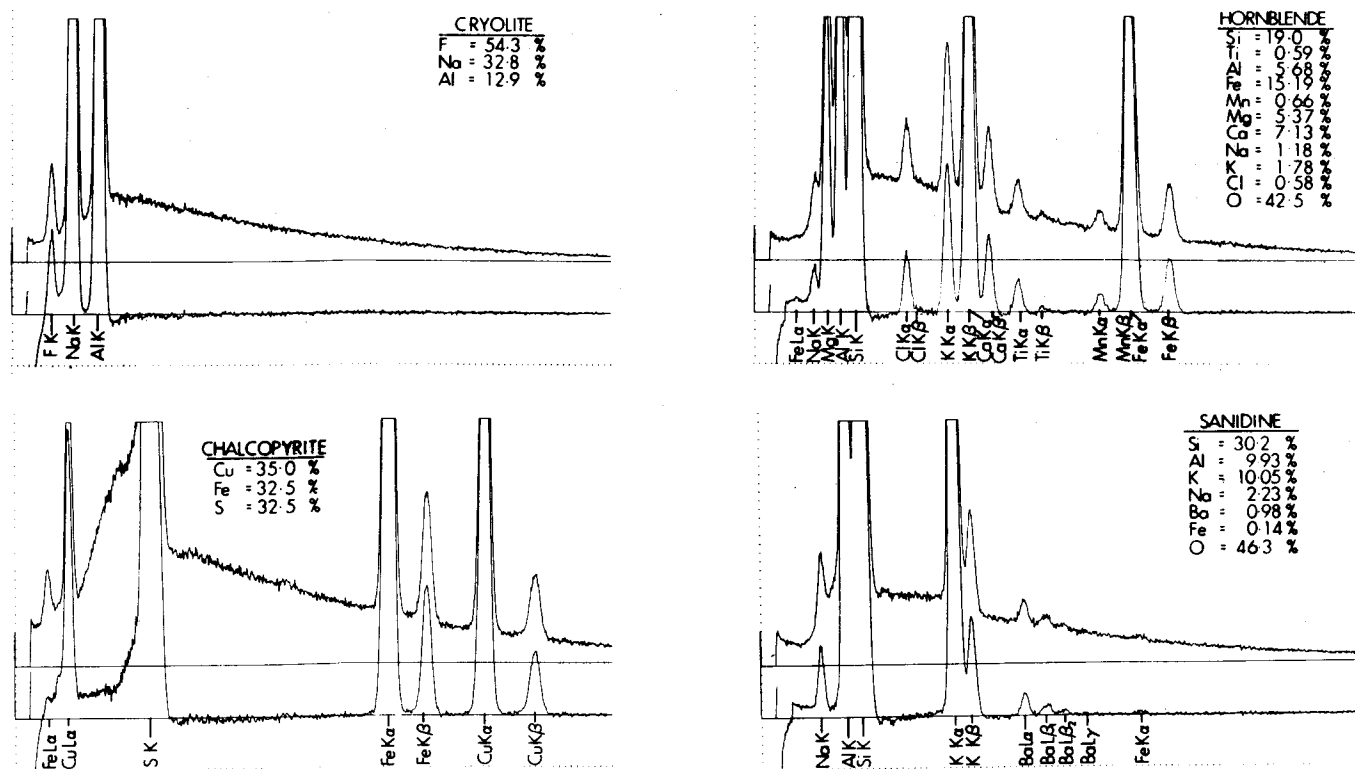
Figure 1: Typical spectra before and after subtraction of background and escape peaks. Uncorrected spectra are displaced vertically by an arbitrary and constant amount for clarity, the zero baseline being shown in both cases. Note well defined tailing and shelving effects apparent on the low energy side of the S K peak of chalcopyrite. In cryolite, the Al K peak, which is less energetic than the Si absorption edge of the detector, shows no comparable feature.

With the resolution currently available in EDA, accurate overlap corrections are essential for fully quantitative analysis. Table 1 shows overlap corrections for the particular system described here. For each element (Y) the overlap found experimentally in the energy regions used for analysis of each of the other elements (X), is expressed as a percentage of the intensity in the analysis peak of the element Y. The values indicated are used, in effect, to solve a series of 21 simultaneous equations to calculate overlap parameters for a particular sample. Before overlap corrections are made, they must be adjusted for any differential matrix effects. These range from very small effects

between Kα and Kβ peaks in simple substances through somewhat more complex situations where absorption edges of other elements present in a sample intervene between the Kα and Kβ peaks, to large differential corrections which must be applied between K and L radiation of the same element.

	Na	Mg	Al	Si	P	S	Cl	K	Ca	Sc	Ti	V	Cr	Mn	Fe	Co	Ni	Cu	Zn	Zr	Ba	
Na	100																					Na
Mg	2.18	100																				Mg
Al	0.46	1.34	100	0.01																		Al
Si	0.20	0.26	0.87	100	0.11															85.7		Si
P	1.55	1.70	2.04	5.50	100	0.30														3.66		P
S	0.91	0.92	1.03	1.25	2.75	100	0.64													1.13		S
Cl	0.60	0.51	0.50	0.55	0.68	1.35	100															Cl
K	0.36	0.29	0.24	0.23	0.26	0.35	0.54	100	3.75													K
Ca	0.28	0.20	0.15	0.14	0.16	0.20	0.32	0.64	100	5.26												Ca
Sc	0.25	0.16	0.10	0.05	0.06	0.12	0.18	0.32	0.48	100	11.35									87.91		Sc
Ti	0.23	0.15				0.08	0.09	0.10	0.20	0.39	100	13.30								0.32		Ti
V	0.22	0.14					0.06	0.07	0.09	0.15	0.31	100	13.03							0.12		V
Cr	0.21	0.14							0.06	0.07	0.12	0.24	100	11.76								Cr
Mn	0.27	0.15								0.05	0.06	0.11	0.18	100	9.00							Mn
Fe	0.85	0.18									0.03	0.04	0.09	0.15	100	5.87						Fe
Co	1.00	0.41										0.02	0.03	0.07	0.13	100	3.27					Co
Ni	1.20	0.50												0.01	0.06	0.11	100	1.49				Ni
Cu	25.5	0.64														0.05	0.10	100	0.91			Cu
Zn	218.	1.28															0.03	0.08	100			Zn
Zr	1.20	1.18	2.00	4.87	85.9	4.39														100		Zr
Ba	1.84	0.38				0.07	0.75	1.37	89.7	29.5	3.57	2.16									100	Ba

----- overlapped element -----

(left margin vertical label: *overlapping element*; right margin vertical label: *overlapping element*)

Table 1: Overlap coefficients expressed as percentages of measured intensities (1.2 FWHM) in analysis peaks of overlapping elements. N.B.: where L line overlap coefficients are expressed as percentages of associated K lines, full differential ZAF corrections are applicable. Coefficients in this table are applicable only at the operating voltage used (15 kV) and, strictly, only at the average counting rate of 3000/sec (full spectrum) at which they were obtained. Changes in counting rate producing significant peak broadening will change the coefficients. Also, they are applicable only to a particular detector resolution.

Table 1 illustrates several important features: tailing and shelving effects are seen on the low energy side of Kα peaks, and these become progressively more severe as the energy of the parent peak approaches the Si absorption edge of the detector. Tailing virtually disappears for peaks on the low energy side of the Si edge. With accurate calculation of continuum intensities, it is possible to determine the magnitude of such effects and, where necessary, to apply precise corrections for them in the overlap subroutine. Particularly in the transition metals, overlap of Kβ onto Kα peaks of adjacent higher atomic number elements is substantial, reaching a maximum for Ti Kβ overlapping V Kα. Large overlap corrections are indicated at low energies where L lines of elements such as Cu and Zn are present. The problem is most severe for Zn L which is virtually superimposed on the Na K peak; the indicated overlap parameter is over 200% (relative to Zn Kα) when corrected for differential matrix effects. When L line intensities are calculated by reference to K line intensities for the purposes of overlap corrections, full differential ZAF corrections are applicable.

Small negative overlap values (not indicated in Table 1) were found for several hundred eV on the high energy side of absorption edges. This indicates that observed intensities fall below the calculated background in these regions. The effect increases as absorption edges occur at lower energies (and also as operating voltage is increased). Thus it appears that it is related to inadequacies in the characteristic absorption correction, at least when this is applied to continuum radiation. Preliminary investigations indicate better fits using a modified sigma term in this correction: as ($\overline{Z}$) decreases, so a smaller constant is required, in line with suggestions made by Reed[2].

It is inconvenient to run standards for all 21 elements automatically determined in this procedure - particularly when many elements will not be present in detectable amounts in most samples. For this reason a default standard option is included. Because of the long term stability of the instrument, the ratio of intensities for two samples obtained at the same probe current and a particular operating voltage, does not change substantially for long periods of time. Therefore, pure metals or simple compounds of each of the elements are run together with the calibration standard when the program is

initially established, and rerun periodically thereafter. The intensity in the analysis peak of each element is compared to that in the full spectrum of the calibration standard acquired with the same beam current, operating voltage and counting time. With this information stored, for any analytical run the intensities that would have been observed for the simple compounds or metals had they been run as standards, can be calculated. In practice it is totally unnecessary to run a standard when less than $\sim$ 1% of an element is anticipated. Also, when an element is encountered unexpectedly in a sample during analysis, a reasonably accurate concentration is obtained by automatic reference to a default standard. The calibration standard should be a homogeneous compound with intense peaks at both ends of the energy spectrum recorded. Although Ni_2Si has been used in this capacity[3], many samples of this compound vary somewhat in composition. Willemite (Zn_2SiO_4) is a useful alternative, particularly varieties containing minor Mn which makes the mineral strongly cathodoluminescent and, therefore, useful also for beam locating and focussing purposes. Willemite has Zn L and Si K peaks at the low energy, and Zn $K\alpha$ and $K\beta$ peaks at the high energy, end of the spectrum; these are very suitable for calculating zero and amplifier gain shift factors.

One measure of the success of this approach to background and overlap corrections is the extent to which elements not present in materials of known composition are also absent in the list of concentrations determined. Table 2 shows concentrations obtained for all 21 elements (plus calculated oxygen) for a series of such materials, together with the accepted concentrations. All elements found in concentrations of < 0.03% have been set to zero within the correction program, this being the estimated lower limit of sensitivity for the experimental conditions (probe current, counting time, etc.). All concentrations not underlined were determined against default standards. Deviations from ideal 100% totals are no greater than would be anticipated in conventional WDA. Where applicable, calculations of proportions of cations indicate that structural formulae are also satisfactory.

	FORSTERITE		SANIDINE		ANHYDRITE		SPHALERITE		TROILITE		OBSIDIAN		GLASS WRAB-4		GLASS BCR-1		ILMENITE			
O	45.58	45.48	45.92	46.28	46.06	47.01	-	-	-	-	49.13	48.63	44.52	45.01	44.69	44.73	31.40	31.72	30.57	O
Na	-	-	2.10	2.23	-	-	-	-	-	-	3.04	3.01	1.89	1.70	2.58	2.50	-	-	-	Na
Mg	34.29	34.56	-	-	-	-	-	-	-	-	-	0.04	6.15	5.68	1.97	2.10	0.43	0.58	0.41	Mg
Al	-	-	10.22	9.93	-	-	-	-	-	-	6.88	6.94	9.52	9.56	7.12	7.39	-	-	-	Al
Si	19.97	19.96	30.22	30.23	-	-	-	-	-	-	34.58	34.56	22.48	22.57	25.71	25.72	-	-	-	Si
P	-	-	-	-	-	-	-	-	-	-	-	-	-	-	0.14	0.20	-	-	-	P
S	-	-	-	-	23.62	23.55	33.32	33.10	36.48	36.50	-	-	-	-	-	0.03	-	-	-	S
Cl	-	-	-	-	-	-	-	-	-	-	0.30	0.36	-	-	-	-	-	-	-	Cl
K	-	-	10.15	10.05	-	-	0.06	-	-	-	4.20	4.18	0.05	0.13	1.39	1.42	-	-	-	K
Ca	-	-	0.23	0.01	30.27	29.44	-	-	-	-	0.61	0.54	8.03	8.23	4.95	5.04	-	-	-	Ca
Sc	-	-	-	-	-	-	-	-	-	-	-	-	-	-	-	-	-	-	-	Sc
Ti	-	-	-	-	-	-	-	-	-	-	-	0.04	0.44	0.41	1.42	1.36	28.78	28.59	29.78	Ti
V	-	-	-	-	-	-	-	-	-	-	-	-	-	-	-	0.04	0.37	0.17	0.37	V
Cr	-	-	-	-	-	-	-	-	0.06	0.08	-	-	-	-	-	-	-	-	-	Cr
Mn	-	-	-	-	-	-	-	-	-	-	-	0.05	0.12	-	0.13	0.14	0.32	0.23	0.30	Mn
Fe	-	-	0.11	0.14	-	-	2.68	2.90	63.05	63.16	1.18	1.34	6.77	6.69	9.61	9.60	38.67	38.69	38.58	Fe
Co	-	-	-	-	-	-	-	-	0.24	0.05	-	-	0.04	-	0.05	-	-	-	-	Co
Ni	0.05	-	-	-	-	-	-	-	-	0.10	-	-	-	-	-	-	-	-	-	Ni
Cu	-	-	-	-	-	-	-	-	-	-	-	-	-	-	-	-	-	-	-	Cu
Zn	0.05	-	-	-	0.05	-	64.78	64.10	0.45	-	0.07	-	-	-	0.08	0.01	0.03	0.01	-	Zn
Zr	-	-	-	-	-	-	-	-	-	-	-	-	-	-	-	-	-	-	-	Zr
Ba	0.06	-	1.01	0.98	-	-	-	-	-	-	-	-	-	-	0.18	0.08	-	-	-	Ba

Table 2: Typical analyses obtained using techniques outlined above. The first column of each pair shows results of energy dispersive analysis; values not underlined were obtained by the default standard option; all oxygen values are calculated by difference from 100%. The second columns show the best available information on composition. The third column of the ilmenite analysis shows values obtained using the default option for all elements, including majors.

REFERENCES:
1. SMITH, D.G.W., GOLD, C.M. & TOMLINSON, D.A. (1975): The atomic number dependence of the X-ray continuum intensity and the practical calculation of background in energy dispersive electron microprobe analysis. X-ray Spectrom. (submitted January 1975).
2. REED, S.J.B. (1975): The shape of the continuous X-ray spectrum, and background corrections for energy-dispersive electron microprobe analysis. X-ray Spectrom., 4 (in press).
3. REED, S.J.B. & WARE, N.G. (1973): Quantitative electron microprobe analysis using a lithium drifted silicon detector. X-ray Spectrom., 2, 69-74.

A COMPUTER PROGRAM FOR SPECTRUM ANALYSIS

R. M. Keyser, D. M. Bartell, and R. S. Moneymaker
ORTEC, Incorporated
Oak Ridge, Tennessee 37830

SEEK is a computer program for X-ray energy-dispersive spectrum analysis (calculation of the area above background of all peaks of interest). It performs background calculation, peak generation, goodness-of-fit estimates, and intensity calculations for complex X-ray spectra. The program requires for its hardware configuration a computer with 16K words of memory, a single drive floppy disk, an input-output terminal, and a multichannel analyzer system.

The inputs required from the operator are the elements of interest and the sequence of steps to be performed. If a user is running a series of like samples or desires several analyses on a single sample, he can define the analysis process using the "LEARN" mode, and the computer will automatically execute the sequence of steps on all of the samples without operator input or intervention.

The program displays on the CRT of the multichannel analyzer the results as each step is performed, thus enabling the user to visually inspect the accuracy of the analysis. This visual inspection, along with the goodness-of-fit (reduced chi-squared) values output by the program, insures the user that he has obtained a good analysis or gives him an indication of where an error in the analysis may have occurred.

When a user first receives his system, he must run a calibration for his detector. The calibration routine calculates a complex peak shape consisting of a gaussian plus a low energy tail[1]. Since the peak shape varies as a function of energy, the peak shape vs. energy relationship must be defined and stored for later use.

SEEK can be compared with existing X-ray spectral analysis programs that run on a minicomputer. Harrison and Eldred[2] have a highly automatic program for X-ray analysis. They have made assumptions that are appropriate for proton excitation of aerosol samples and include in their X-ray library only those lines that are needed for their studies. SEEK achieves automation through its LEARN mode and is thus not limited to aerosols. The X-ray lines (up to 18 per element) for all the elements from carbon through uranium are included in the SEEK X-ray library[3]. The spectra deconvolution technique described by Schamber[4] requires the storage of pure element spectra for the elements being analyzed. The use of a calibrated peak shape eliminates this storage requirement. SEEK allows the user to obtain concentrations using multi-element standards with the computer code MAGIC[5] or with a working curve. The user may obtain K ratios from pure element standards if desired.

Once the calibration has been performed, it need not be repeated unless the characteristics of the detector counting system change or a different detector is used. A simple routine can be run on a regular basis to check the calibration of the multichannel analyzer.

The actual spectrum analysis begins with the calculation of the background. The background is determined automatically without operator intervention or peak region definitions.

Once the background has been calculated, the original spectrum is compressed into the first half of the multichannel analyzer display and the background is drawn in the second half. Although the displayed spectrum has been compressed into 512 channels, the original data (1024 channels) is stored on the disk and used in all subsequent calculations. The spectrum is compressed on the display only for the purpose of allowing the user to visually examine the results of the analysis as each step is executed.

When running in the automatic mode, the multichannel analyzer display is not used, thereby enabling data to be acquired while the previous analysis is being performed.

Once the background has been calculated, the user can determine the peak areas and intensities by generating on the background synthetic peaks using the peak-shape information obtained from the original calibration. The user then compares the synthetic spectrum to the original data. The process continues until the synthetic spectrum "matches" the original data. He may then ask for a report of the intensities. The accuracy of the analysis can be determined by both visual inspection and the goodness-of-fit information contained in the report.

The following is a partial list of the commands available in the SEEK program:

Analysis Commands

1. BACKGROUND - Calculate the background over the specified energy range.

2. ADD (element name, line) - The input specifies which X-ray line family for the element specified is to be added to the background and compared to the original data.

3. ADDEN (energy, scale factor) - Add a single peak at the specified energy and scale the peak height (if desired) by a factor between 0 and 1.

4. SCALE (element name, line or line family, scale factor) - This program is used to change the relative amplitudes of peaks which have been added with the ADD routine. The peak amplitude is multiplied by the scale factor, and the previous peak is replaced by a peak of the "scaled" amplitude.

5. CANCEL (element name, line, or line family) - Remove from the synthetic spectrum the specified element line or line family.

6. REPORT - Output the results of the analysis. The following information is output for each peak: element name, line energy, intensity, and final residue of the peak region.

Utility Commands

1. LINE (energy) - Output all X-ray lines (for all elements) that are within two channels of the specified energy.

2. LINES (low energy, high energy) - Output all X-ray lines (for all elements) that are between the two specified energy limits.

3. PEAKS (element name) - List all X-ray lines for the specified element.

4. SMOOTH - Smooth data in the multichannel analyzer using a third order, linear least-squares-fit to the data.

5. SHIFT (n) - Shift the spectrum in the multichannel analyzer to the left or right "n" channels.

6. GAIN (element, line, channels) - Restructure data in the multichannel analyzer which was taken at the wrong gain.

7. KEEP (filename) - Store the spectrum in the multichannel analyzer on the floppy disk under the specified filename.

8. RESTORE (filename) - Load the spectrum of the specified filename from the floppy disk into the multichannel analyzer.

Protocol

1. DESCRIBE (filename) - List a description of the protocol (LEARN mode) file stored on the disk. The following information is output: number of steps, energy analysis limits, gain, offset, and the sequence of commands to be executed.

2. FORGET - Remove the last step from the protocol (LEARN mode) file.

3. AUTOMATIC (filename, number of iterations) - Execute the sequence of commands in the specified protocol file the specified number of times. Data is being taken while the analysis of the previous spectrum is being performed.

The example analysis (Figures 1 through 3) is for a stainless steel sample. The copper X-rays are from the specimen mount.

Concentrations determined using SEEK and MAGIC agree well with wet chemical analyses. Examples of this agreement will be given at the presentation.

REFERENCES

1. Gunnink R., and Niday, J. B.   UCRL-51061 1 (1972)

2. Harrison, J. F. and Eldred, R. A.   Advances in X-ray Analysis 17, 560 (Plenum Press, New York, 1974)

3. Johnson, G. G., Jr. and White, E. W.   X-ray Emission Wavelength and KeV Tables for Nondefractive Analysis, ASTM Data Series DS 46 (American Society for Testing and Materials, Philadelphia, 1970)

4. Schamber, F. H.   Proceedings Eighth National Conference on Electron Probe Analysis, 85A (1973)

5. Colby, J. W.   Advances in X-ray Analysis 11, 287 (Plenum Press, New York, 1968)

```
*BACKGROUND
*ADD("SI","K")
SI    KA1      1.740  KEV
SI    KB1      1.836  KEV
*ADD("MO","L")
MO    LA1      2.293  KEV
MO    LA2      2.289  KEV
MO    LB1      2.394  KEV
MO    LB2      2.518  KEV
MO    LB3      2.473  KEV
MO    LB4      2.455  KEV
MO    LG1      2.623  KEV
MO    LL       2.015  KEV
*ADD("CR","K")
CR    KA1      5.414  KEV
CR    KA2      5.405  KEV
CR    KB1      5.946  KEV
*ADD("MN","K")
MN    KA1      5.898  KEV
MN    KA2      5.887  KEV
MN    KB1      6.489  KEV
*ADD("FE","K")
FE    KA1      6.403  KEV
FE    KA2      6.390  KEV
FE    KB1      7.057  KEV
*ADD("NI","K")
NI    KA1      7.477  KEV
NI    KA2      7.460  KEV
NI    KB1      8.263  KEV
*ADD("CU","K")
CU    KA1      8.046  KEV
CU    KA2      8.026  KEV
CU    KB1      8.904  KEV
*
```


FIGURE 2. LOWER SPECTRUM-STAINLESS STEEL
ORIGINAL SPECTRUM. UPPER SPECTRUM -
SEEK GENERATED SPECTRUM

FIGURE 1. EXAMPLE OF SEEK INPUT/OUTPUT
DURING ANALYSIS

*REPORT

*** REPORT ***

STAINLESS STEEL SAMPLE
MAR 5 1975

DATA COLLECTION TIME (SEC):   400.000

ELEMENT	LINE	ENERGY (KEV)	INTENSITY (CPS)	RESIDUAL ERROR (CHI-SQ)
SI	KA1	1.740	6.078	7.671
	KB1	1.836	0.081	6.003
CR	KA1	5.414	196.969	4.008
	KA2	5.405	98.437	3.976
	KB1	5.946	36.447	6.707
MN	KA1	5.898	16.078	6.403
	KA2	5.887	8.034	6.151
	KB1	6.489	3.312	4.537
FE	KA1	6.403	516.600	4.455
	KA2	6.390	258.135	4.454
	KB1	7.057	106.589	4.988
NI	KA1	7.477	46.541	4.607
	KA2	7.460	23.253	4.646
	KB1	8.263	9.630	1.876
CU	KA1	8.046	27.078	3.100
	KA2	8.026	13.528	3.325
	KB1	8.904	5.611	0.918
MO	LA1	2.293	3.853	4.764
	LA2	2.289	0.385	4.764
	LB1	2.394	1.724	4.644
	LB2	2.518	0.038	4.929
	LB3	2.473	0.115	4.838
	LB4	2.455	0.115	4.786
	LG1	2.623	0.038	4.732
	LL	2.015	0.119	6.661

*

FIGURE 3. A SEEK REPORT

QUANTITATIVE ANALYSIS WITH AN ENERGY DISPERSIVE DETECTOR
M.F. Ciccarelli, R.B. Bolon and E. Lifshin
General Electric Corporate Research and Development

A FORTRAN program has been written for quantitative analysis with an energy dispersive spectrometer system. Spectral data from a multi-channel analyzer is first transferred into an Interdata computer system described previously[1]. Background subtraction on samples and standards is done using the parabolic fitting technique first described by Lifshin[2] with added modification that the absorption edges in "observed" space are corrected for detector broadening. The remaining spectra consisting of a series of isolated or overlapping characteristic peaks is then least squares fit to a series of gaussians. Appropriate selection of the gaussian parameters is based on careful measurement of the detector resolution as a function of energy and an energy calibration using peak centroid positions measured on standards.

Basic to the philosophy of the program is the approach that sample spectra can be fully characterized by a superposition of standard spectra, providing that the superposition begins in "generated" space. This avoids difficulties caused by the variation in matrix absorption. Furthermore, unlike with crystal diffraction spectrometer measurements, improved counting statistics can readily be achieved by the use of data simultaneously collected from several lines within a spectral series.

1. W.T. Hatfield, M.F. Ciccarelli, R.B. Bolon and E. Lifshin, "A Real Time Approach to Laboratory Automation" Proceedings of the Ninth Annual Conference of the Microbeam Analysis Society, Ottawa, Canada July 1974.

2. E. Lifshin, M.F. Ciccarelli, R.B. Bolon, "Determination of the Energy Distribution of the Continuum and the Ratio of Indirect to Direct X-ray Fluorescence", Proceedings of the Eighth National Conference on Electron Probe Analysis, New Orleans, Louisiana, August 1973.

LEAST SQUARES PEAK FITTING WITHIN THE ZAF ITERATION LOOP

Carl J. Maggiore and Michael J. Foster

Princeton Gamma-Tech, Inc.

Box 641

Princeton, N.J. 08540

In addition to the usual limitations of the electron microprobe technique for quantitative analysis, a Si(Li) spectrometer further restricts the applicability of the method because of difficulties in analysing the spectra obtained. The poor resolution of the spectrometer relative to the separation of the lines means that some peaks of interest will be incompletely resolved. The poor peak to background ratio inherent with electron excited samples and the presence of absorption edges in the spectra mean that simple linear backgrounds under the peaks are not adequate. The spectra are further complicated by the presence of escape peaks 1.74 keV below each peak and count-rate dependent pile up peaks. Also the peak shapes are only approximately Gaussian due to incomplete charge collection in the Si(Li) crystal. Since the ZAF correction procedure depends on the ratio of peak intensities in the unknown relative to standards, quantitative results can be no better than the determinations of backgrounds and peak overlaps.

A computer program has been written that incorporates multiple least squares fitting of the background subtracted spectra to standards. Following the work of Lifshin et al.[1] and Fiori et al.[2] the bremsstrahlung background with absorption edges is modeled with a parabolic background shape and the absorption correction $f(\chi)$. Since the absorption effects are dependent on the sample composition and are calculated using the function $f(\chi)$ in the ZAF correction procedure, the program was written to subtract the background within the ZAF iteration loop. Similarly the least square fitting of the background subtracted spectrum to the background subtracted standard is performed within the iteration loop. Figure 1 is a flow

diagram of the program. The ZAF corrections are the same as those used in the National Bureau of Standards program FRAME.[3]

Spectra from pure element standards are used because the actual peak shapes obtained depend on the particular spectrometer. Incomplete charge collection in the Si(Li) crystal results in a tail on the low energy side of a peak; the exact details of this non-Gaussian behavior of the spectrometer vary from crystal to crystal and are not easily modeled. An additional advantage of this method is that the escape peaks are correctly accounted for in those cases where an escape peak interferes with another element of interest. Pile up peaks are not corrected for.

The program operates on a CAI LSI-2 minicomputer with flexible disk and 8K of core. Because of the particular system software used there is no requirement for permanent core storage of programs, however, for reasons of speed approximately 2K of core is needed for data storage.

[1]E. Lifshin, M.F. Cicarelli and R.B. Bolon, Practical Scanning Electron Microscopy (J.I. Goldstein and H. Yakowitz, eds.) Plenum, New York (1975).

[2]C.E. Fiori, R.L. Myklebust, K.F.J. Heinrich and H. Yakowitz, private communication.

[3]H. Yakowitz, R.L. Myklebust and K.F.J. Heinrich, NBS Tech Note 796 (1973).

STANDARD SPECTRA,
COMPOSITION OF STANDARDS,
E_O, Ψ , θ

↓

CALCULATE ALL
NECESSARY FACTORS
FOR THE CORRECTIONS

↓

CALCULATE BACKGROUNDS
IN STANDARD SPECTRA

↓

ESTIMATE CONCENTRATIONS
IN UNKNOWN ← UNKNOWN SPECTRUM

↓

CALCULATE BACKGROUND
IN UNKNOWN SPECTRUM
USING ESTIMATED
CONCENTRATIONS

↓

COMPUTE K-RATIOS USING MULTIPLE LINEAR
REGRESSION TO FIT STANDARDS TO UNKNOWN
(ALL SPECTRA ARE BACKGROUND SUBTRACTED)

↓

ZAF   CORRECTION
USES OLD ESTIMATES OF CONCENTRATION
AND NEW K-RATIOS TO COMPUTE NEW
ESTIMATES OF CONCENTRATION

↓

NO   TEST FOR CONVERGENCE

↓ YES

OUTPUT RESULTS

Figure 1.   Flow diagram of the computer program to
calculate the K-ratio within the ZAF
iteration loop.

THE HIGH COUNTING RATE LIMITS ON ANALYTICAL
PRECISION DUE TO DEADTIME LOSSES

D. A. Gedcke

ORTEC, Inc.
Oak Ridge, Tenn.

The development of the time variant baseline stabilizer[1,2]), and the pile-up compensated livetimer[1,4,5]) has been instrumental in allowing operation of the Si(Li) energy spectrometer at exceptionally high counting rates where deadtime losses are in excess of 70 percent[1,3,4,5]). These developments have greatly reduced the systematic errors at high counting rates. Consequently, it becomes important to examine the counting rate limits set by counting statistics at high deadtimes.

Two extreme types of deadtime are considered: extending, and non-extending. Although most systems are combinations of both types[6]), extending deadtime is the dominant effect in energy spectrometers with shaping time constants longer than 4μsec. The relationship between the true input rate r_i, the observed output rate r_o, and the deadtime per isolated pulse T is

Non-extending:

$$r_o = r_i \; (1 - r_o T) \tag{1}$$

Extending:

$$r_o = r_i \; \exp \; (-r_i T) \tag{2}$$

These relations are plotted in Figure 1. Note that all the expressions presented in this paper apply to the usual situation where the counting interval is long compared to either the deadtime T, or the mean spacing between pulses[6,7,8]).

Systems With Realtime Clocks

For systems operating with a realtime clock the relative standard deviation in the observed counts for a preset real time t is[6,8])

Non-extending:

$$\left(\frac{\sigma_o}{r_o t}\right)_R = \left(\frac{T}{t}\right)^{1/2} \left[r_i T \left(1 + r_i T\right)\right]^{-1/2} \tag{3}$$

Extending:

$$\left(\frac{\sigma_o}{r_o t}\right)_R = \left(\frac{T}{t}\right)^{1/2} \left[\frac{1 - 2r_i T \exp\left(-r_i T\right)}{r_i T \exp\left(-2r_i T\right)}\right]^{1/2} \tag{4}$$

Figure 2 shows that the precision in the observed counts reaches a minimum at $r_i T = 0.77$ for extendable deadtimes. For higher input rates the precision deteriorates rapidly. Without a livetime clock, the input rate must be calculated from the observed rate and the known deadtime T through equation (1) or (2). Consequently, the relative standard deviation in the calculated true rate is given by

Non-extending:

$$\left(\frac{\sigma_i}{r_i}\right)_R = \left(\frac{T}{t}\right)^{1/2} \left[\frac{1 + r_i T}{r_i T}\right]^{1/2} \tag{5}$$

Extending:

$$\left(\frac{\sigma_i}{r_i}\right)_R = \left(\frac{T}{t}\right)^{1/2} \left[\frac{\exp\left(-r_i T\right) - 2r_i T}{r_i T \left(1 - r_i T\right)^2}\right]^{1/2} \tag{6}$$

As Figure 3 shows, the error is infinite at $r_i T = 1$ for the extendable deadtime due to zero slope in equation (2). For either type of deadtime the improvement in precision is less than a factor of 2.5 for input rates in excess of $r_i T = 0.2$. In practice the deadtime T is never known very accurately, and the type of deadtime loss equation is uncertain. Consequently, for accurate results, systems without livetime clocks must be operated below $r_i T = 0.2$ and preferably below $r_i T = 0.1$, where deadtime corrections are small, and knowledge of the type of deadtime is not critical.

Systems With Livetime Clocks

A livetime clock counts elapsed time only when the system is not dead. The relationship between elapsed real time t and the corresponding live time t_ℓ is[9])

Non-extending:

$$t_\ell = t\,(1 - r_o T) \tag{7}$$

Extending:

$$t_\ell = t \exp\,(-r_i T) \tag{8}$$

By dividing the observed counts by the live time the true input rate is obtained

$$\frac{r_o t}{t_\ell} = r_i \tag{9}$$

It can be shown[9]) that the variance in the observed counts in a preset livetime is equal to the observed number of counts.

What is important to the microanalyst is obtaining the best precision in the least amount of <u>real</u> time. Hence, the precision in measuring the true input rate in a fixed real time must be calculated for the livetimer as a function of counting rate. The result is[9])

Non-extending:

$$\left(\frac{\sigma_i}{r_i}\right)_L = \left(\frac{T}{t}\right)^{1/2}\left[\frac{1 + r_i T}{r_i T}\right]^{1/2} \tag{10}$$

Extending:

$$\left(\frac{\sigma_i}{r_i}\right)_L = \left(\frac{T}{t}\right)^{1/2}\left[\frac{\exp\,(r_i T)}{r_i T}\right]^{1/2} \tag{11}$$

For extending deadtimes, Figure 4 shows that the best precision is obtained for $r_i T = 1$. However, over the range $0.2 \le r_i T \le 1$ the precision changes by a factor of less than 1.5. Consequently, this has been denoted as the optimum operating range. In particular, there is no value in operating above $r_i T = 1$ since statistical precision deteriorates and pulse pile-up distortion becomes severe. Even with non-extending deadtime there is little gain in precision above $r_i T = 1$. The optimum range corresponds to deadtime losses between 17 and 63 percent.

In an energy spectrometer with pulse pile-up losses the deadtime is normally extendable, with $T = T_w + T_p$, where T_w is the width of the pulse above noise and T_p is the time from the start of the pulse to peak amplitude[5]). Figure 6(a) shows the residual error in a livetimer designed to include compensation for pile-up losses. The residual error is less than one percent well past the 63 percent deadtime point. Energy resolution and baseline stability for this system also hold well past the 63 percent deadtime loss value[1]).

It can be concluded that the statistical error due to deadtime losses sets the upper limit on counting rates with state-of-the-art energy spectrometers. The optimum operating range lies between 17 and 63 percent deadtime. This corresponds to an amplifier duty cycle between 12 and 58 percent, in Figure 6(b), where the amplifier duty cycle is given by $\exp(-r_i T_w)$. In practice there is little to be gained by exceeding the the 40 percent duty cycle (50 percent deadtime).

REFERENCES:

1. N. Karlovac and D. A. Gedcke, Proceedings of the Eighth National Conference on Electron Probe Analysis, New Orleans, (August 1973), 17.

2. N. Karlovac and T. V. Blalock, An Investigation of the Count Rate Performance of Baseline Restorers, 1974 Nuclear Science Symposium, Washington, D. C., (December 1974), proceedings to be published in IEEE Trans. Nucl. Sci.

3. K. Kandiah, ibid ref. 1, 12, and references quoted therein.

4. Peter J. Statham, Proceedings of the Ninth Annual Conference of the Microbeam Analysis Society, Ottawa, (July 1974), 55.

5. D. A. Gedcke, Quantitative Scanning Electron Microscopy, (Ed., D. Holt, M. Muir and P. Grant), Academic Press Inc., London, (1975), chap. 12.

6. J. W. Müller, Nucl. Instr. and Meth., 112, (1973), 47.

7. J. W. Müller, Nucl. Instr. and Meth., 117, (1974), 401.

8. A. F. Para and M. M. Bettoni, Nucl. Instr. and Meth., 70, (1969), 52.

9. D. A. Gedcke, to be published.
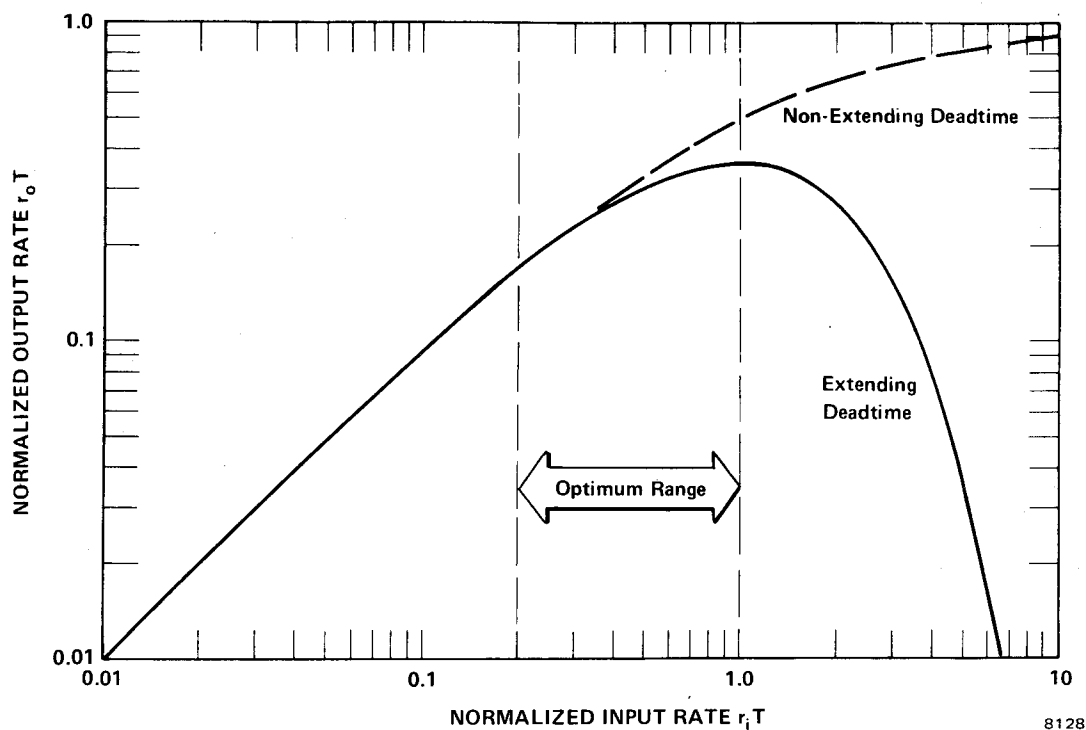
Figure 1. Output rate versus input rate for extending and non-extending
deadtime systems.
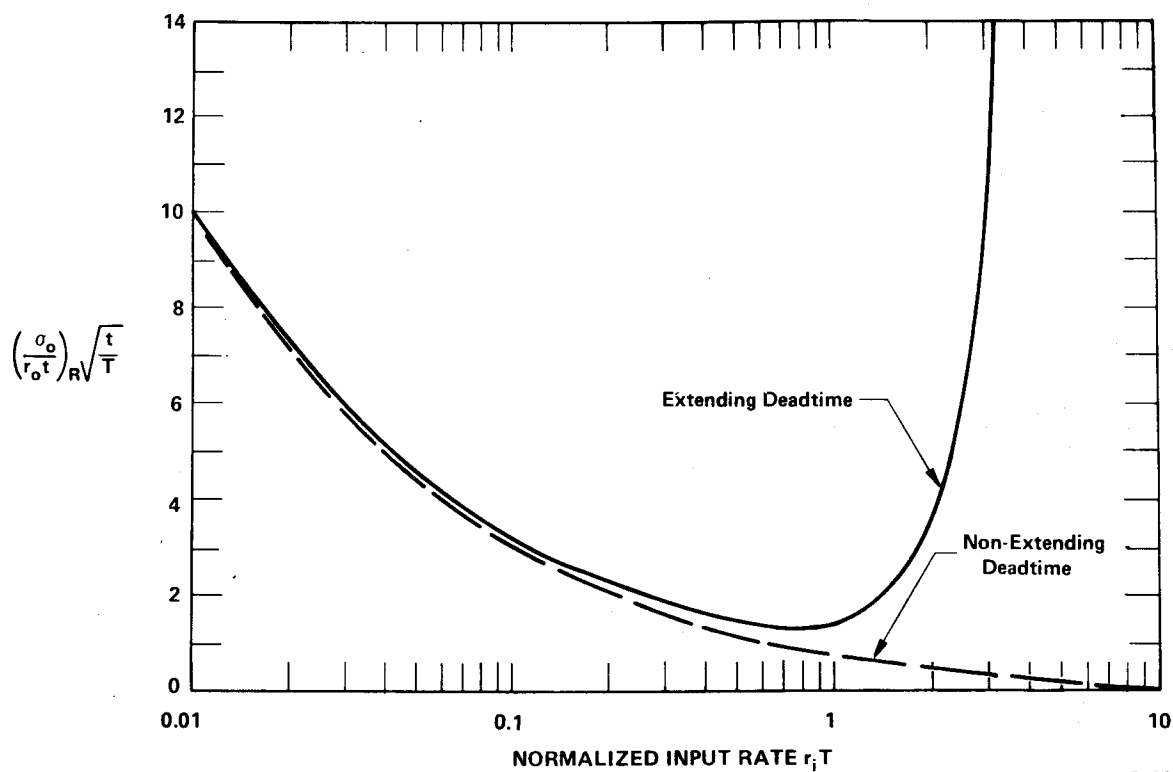
Figure 2. Relative standard deviation in the observed counts for a preset
real time t and a deadtime T.
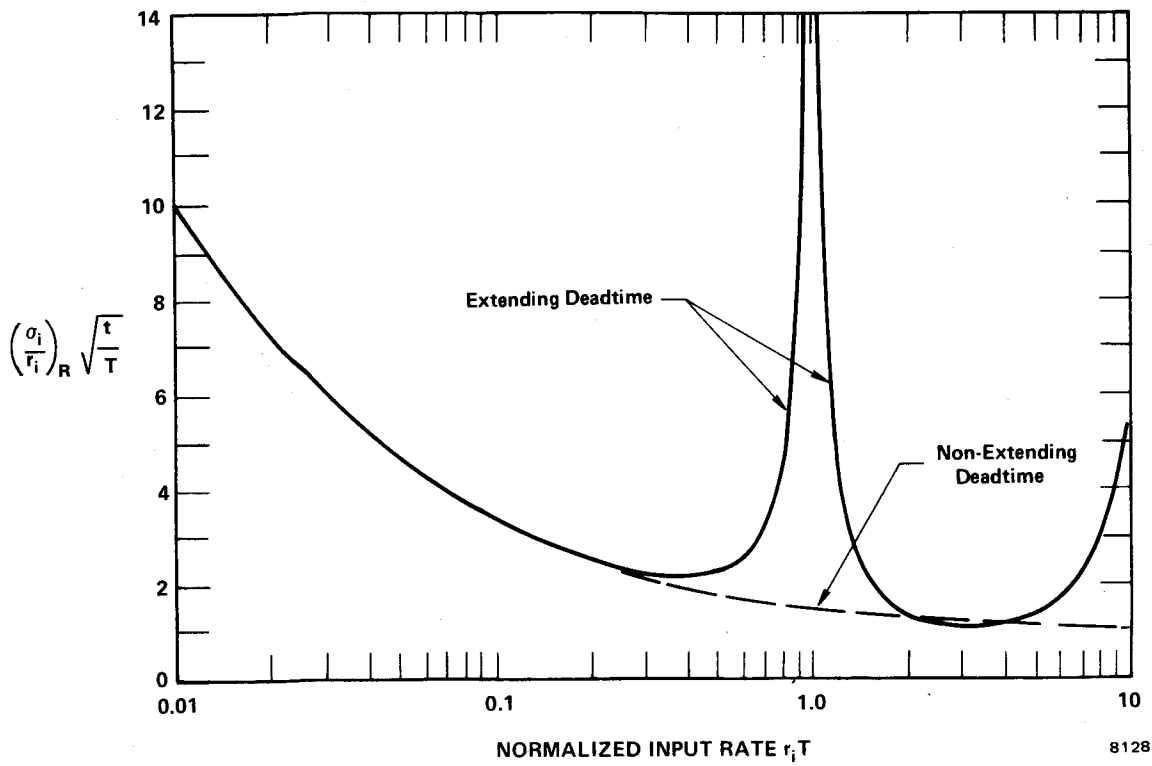
Figure 3. Relative standard deviation in the calculated input rate with a realtime clock.
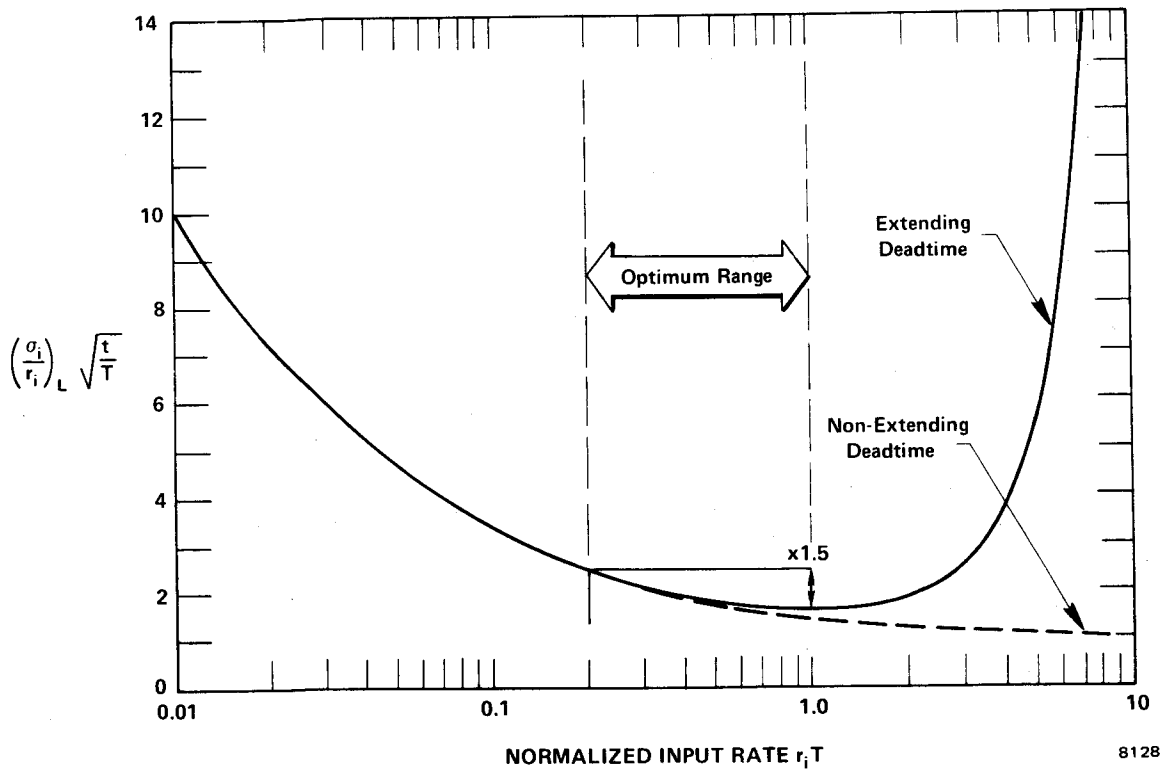
Figure 4. Relative standard deviation in the measured input rate with a livetime clock and fixed real time.
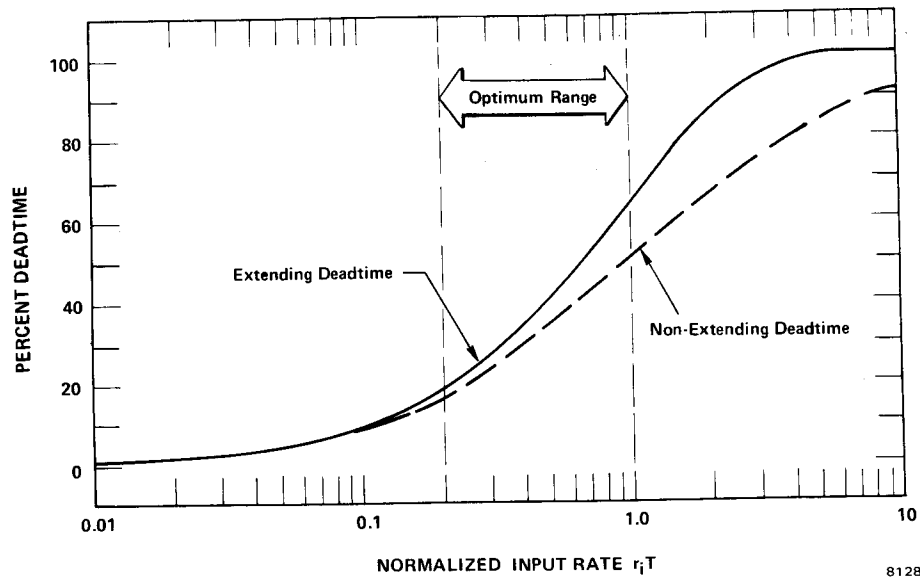
Figure 5. Percent deadtime for extending and non-extending deadtime systems. The percent livetime is the difference between the percent deadtime and 100%.
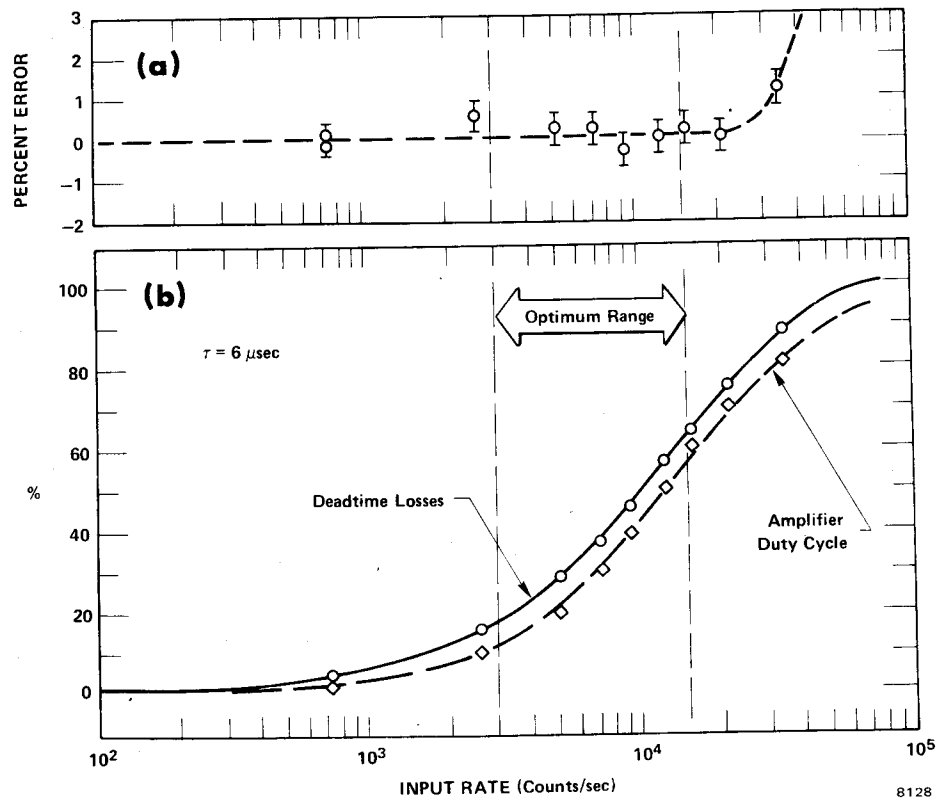
Figure 6. (a) The residual deadtime correction error with a pile-up compensated livetimer. The error is measured by monitoring the counts in the silver $K\alpha$ line from a ^{109}Cd source as the total counting rate is varied by an ^{55}Fe source.
(b) The raw deadtime losses before correction. The corresponding amplifier duty cycle has been added for reference.

ON THE USE OF A VARIABLE GEOMETRY PROPORTIONAL COUNTER FOR X-RAYS
MICROANALYSIS OF LIGHT ELEMENTS WITH AN ELECTRON MICROSCOPE

A.Armigliato, G.G.Bentini, P.Bergamini[+] and I.Vecchi

CNR-LAMEL, Via Castagnoli, 1 - 40126 Bologna (Italy)

[+]CISE, Via Redecesio, 12 - Segrate, Milano (Italy)

In a previous paper (1) we reported the results of an experimental work
in the field of X-ray microanalysis, carried out with a transmission electron
microscope (TEM) equipped with a crystal spectrometer. The analytical
data obtained from specimens of a few binary alloys demonstrated the good
capability of the technique, particularly in the case of thin films.
Nevertheless, the low production of characteristic X-rays by thin specimens
and the intrinsic low efficiency of the wavelength dispersive technique re
quire generally high beam currents, in order that a reasonable counting
rate can be achieved. However, too intense beams are not always allowed,
since they often damage the specimen.

An alternative is represented by the Si(Li) detectors which can be used
in an energy dispersive mode and exhibit very high efficiency and good res
olution. Anyway it is usually impossible to detect the soft X-rays coming
from elements below Z=11 (Sodium) because of the window mounted in front of
such detectors.

Therefore, in order to improve the efficiency of our X-rays measurements
whilst retaining the capability of analysing light elements such as Boron,
Carbon and Oxygen we have tried to employ in our TEM an end-window variable
geometry flow proportional counter, in an energy dispersive mode.
In this detector, which was first realised at Harwell by Cairns et al.(2)
and is available from J&P Engineering, Reading, England, the window assemb
ly is placed at the end of a nosepiece which can be put in close contact
with the microscope column. The active volume of the counter can be vari
ed by changing the anode-to-window distance, which is accomplished by simply
rotating from outside a calibrated dial. This feature permits the anode
to be moved to a position corresponding to the mean penetration depth of a
given radiation: in this way it is possible to optimize the detection effi
ciency for X-rays of a selected energy.

In Fig.1 is shown the counter as attached to our Siemens Elmiskop 101
electron microscope; the two permanent magnets and their polar pieces,
which prevent the backscattered electrons to enter the window, are also
clearly visible.

The experimental set-up we used in our preliminary measurements is dis
played in the block diagram of Fig.2. The electrical signal from the
counter is first amplified by the built-in head amplifier, then the pulse
is fed into the main amplifier, which is connected to a multichannel anal
yser and to a ratemeter.

As to the window, which is perhaps the most crytical part of the counter,
we have first chosen a Mylar film 2 μm thick, aluminised on its inside
surface, so as to ensure continuity of the electrical field.
In addition, a high transmission support grid is put in contact with the
outer surface of the window, in order to prevent its stretching, which may
cause breaking of the internal conductive layer.

A first set of experimental spectra is shown in Figs.3-6.
In Fig.3 is shown the BK ($\sim$185 eV) peak together with the CuL ($\sim$930 eV) one as a reference; in Fig.4 the CK ($\sim$282 eV) peak is displayed, still with the CuL one.   From the resulting calibration straight line it comes out that the resolution is about 90% both for the BK and the CK peaks.   These figures are in good agreement with the ones that can be deduced from the theoretical resolution R for a proportional counter (3):

$$R = \frac{38}{\sqrt{E(keV)}} \%$$

This means that the electrical field distribution within the active volume of this end-window counter approximates to the idealised situation which is presumed to exist in a good side-window detector.

In Fig.5 are shown the Cu-L and the SiK ($\sim$1.7 keV) peaks, whereas in Fig.6 are displayed the OK($\sim$523 eV) and the SiK peaks as generated by a SiO_2 specimen.   In the low energy side of the OK peak is visible a poorly resolved peak, which occurs at the position of the CK line: this is due to a Carbon layer grown onto the specimen.

As to the X-rays counting rate, it has been improved by just about a factor of three (BK line) with respect to the one of our crystal spectro meter. This figure can be possibly still improved by using a thinner window (e.g. <1 μm polypropylene) or moving the detector closer to the microscope column, but is anyway limited by the narrow gap between the pole pieces of the objective lens.

(1) A.Armigliato, P.Bergamini and L.Morettini, Proc.9th Annual Meeting MAS (Ottawa 1974) Paper No.15
(2) J.A.Cairns, C.L.Desborough and D.F.Holloway, Nucl. Instr. and Meth. 88, 239 (1970)
(3) R.Jenkins, Proc. 9th Annual Meeting MAS (Ottawa 1974) p.1.
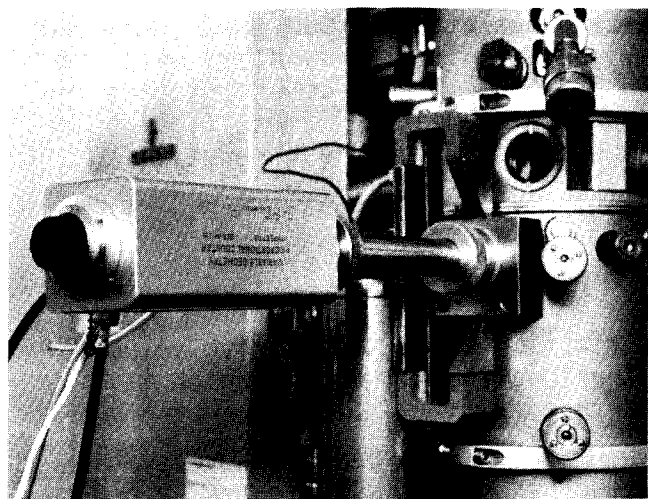
Fig.1
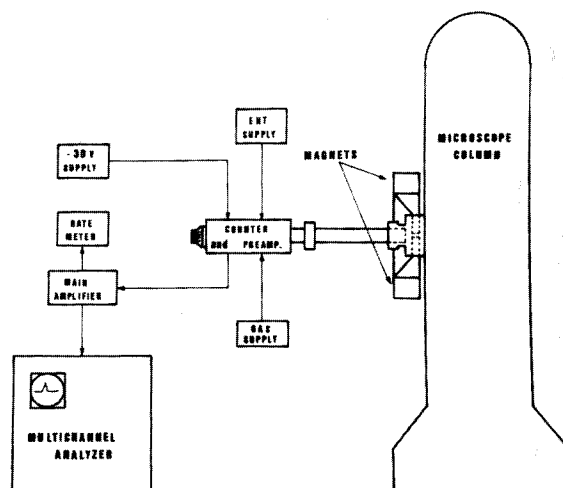
Fig.2
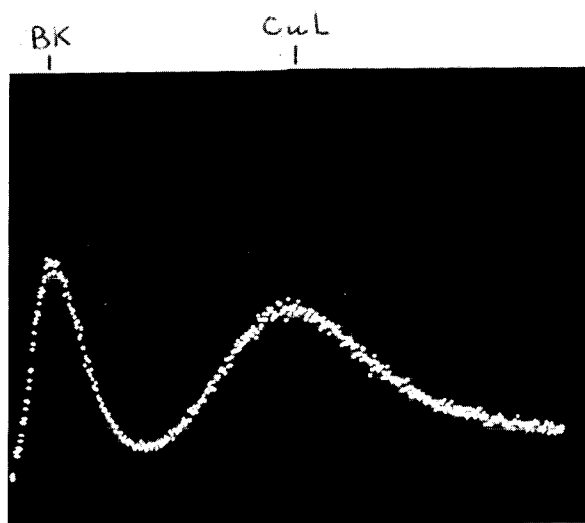
Fig.3
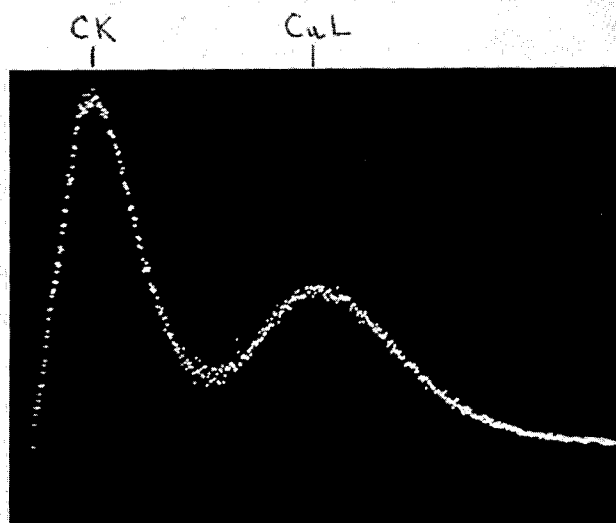
Fig.4
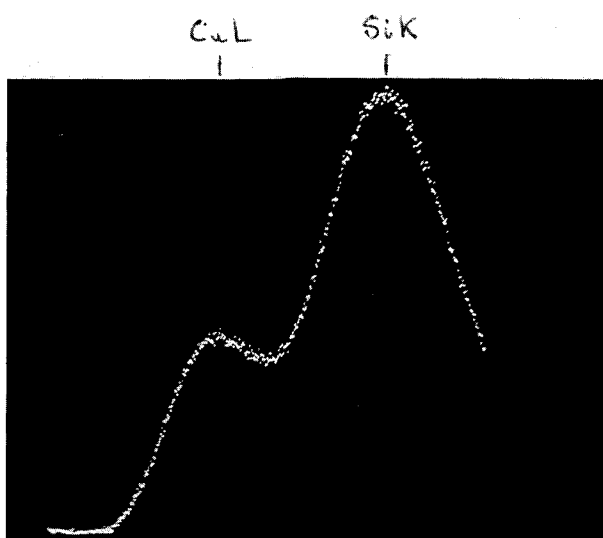
Fig.5
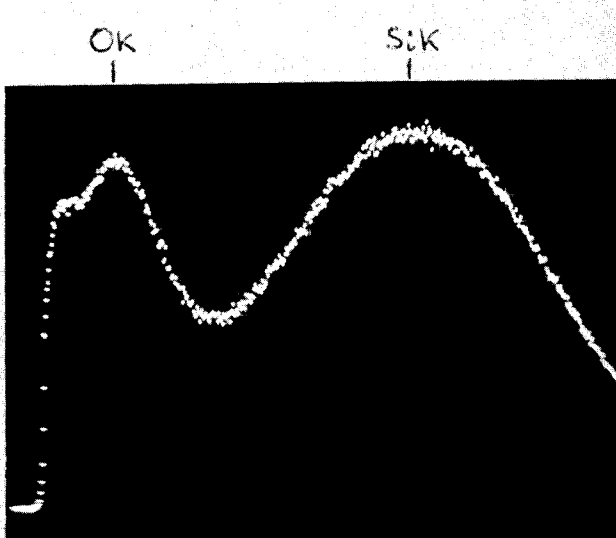
Fig.6

ELECTRON BEAM MICROANALYSIS OF ENVIRONMENTAL
SAMPLES USING A HIGH RESOLUTION SCANNING ELECTRON
MICROSCOPE WITH AN ENERGY DISPERSIVE X-RAY
ANALYZER (SEM-EDXRA)

Michael M. Reddy, New York State Department of Health,

Division of Laboratories and Research, Environmental Health Center,

New Scotland Avenue, Albany, New York

Research activities in the Environmental Health Center, New York State
Department of Health include characterization of particulate pollutants in
air and water. Identification of these particulates is facilitated by high
resolution morphological information and semi-quantitative elemental analysis
which can be obtained with a scanning electron microscope coupled to an energy
dispersive x-ray analyzer. With this system particulate pollutants can be
identified and their association with other elements indicates their probable
source and mechanism of distribution.

An ETEC Autoscan scanning electron microscope with a Princeton Gamma
Tech solid state x-ray detector (resolution 152 ev at 5.9 kV) and a Northern
Scientific NS 880 computer based x-ray analysis system were recently placed
in operation. The configuration of the SEM sample chamber is presented
in Fig. 1. As a preliminary test of the applicability of this system for
the characterization of particulates an examination of air particulates
collected from a site exhibiting significant dustfall was performed. In
addition, estimations of the minimum concentration of several elements in
a carbon matrix were calculated using carbon standards containing a known
amount of individual elements.

a) Air particulates. Air particulates were mounted on an aluminum
stub and coated with a 200Å layer of carbon using a Denton Vacuum Evaporator.
During the study the SEM instrument parameters used were: 20 kV accelerating
potential, 0.3 n amps specimen current, 45° specimen tilt and 25 mm working
distance. Representative particles, examined at low magnification (Fig. 2A)
were irregularly shaped with an average diameter of several hundred microns.
Particles of this size would settle out shortly after emission in close
proximity to their source. Details of one of these particles were revealed
at higher magnification (Fig. 2B). This morphology is characteristic of fly
ash and oil soot particulates commonly found as dustfall in industrial areas.
Figure 2B also shows small particulates, less than 10μm in diameter, attached
to the particle. These smaller particulates were seen clearly at higher
magnification (Fig. 2C), where particulates 0.2μm in diameter and larger
appeared both on the surface and within cavities leading from the surface
of the large particle.

Elemental analysis of particles shown in Fig. 2A was done with EDXRA.
Particles 100μm in diameter and larger showed only weak x-ray emission lines
for silicon and iron. The characteristic x-ray lines observed for these
particles depends on their composition and on the detection limits for the
SEM-EDXRA system (see section b). Sulfur Ka x-ray emission was monitored from
the area shown in Fig. 2C; results of this scan are shown in Fig. 2D. A
high level of sulfur x-ray intensity in Fig. 2D correlates well with the
irregular 2μm diameter particulate in Fig. 2C. An analysis of this particle
was performed using a 100 sec counting time and reveals a weak peak for silicon
and intense, approximately equal peaks for sulfur and calcium x-rays, thus
demonstrating the particle to be composed primarily of calcium sulfate (Fig. 3).

b) Element detection limits in a carbon matrix. An estimate of the

minimum detectable element compositions in carbonaceous particulates
(i.e., coal dust, coke and oil soot) was made using carbon reference
samples. These samples consisted of a blank and six standards each con-
taining 1% of an element (calcium, copper, iron, magnesium, phosphorus
or zinc). Measurements were made for 100 sec (live time) using the instru-
ment settings described. A Princeton Gamma Tech pulse pile-up rejector and
live time corrector were used for all measurements. System deadtime was
always less than 20%.

The area analyzed on each stub was 81 x $10^4 \mu m^2$. Counts for each element
were integrated over a region centered on the Ka emission line for the
element and having a width of 1.2 times the detector resolution at that
energy. Total counts for the region centered on the zinc Ka peak were
determined for a blank carbon sample and a 1% zinc containing carbon speci-
men six times at the same spot and at six different locations on the sample
(see Table I). Measured count rate uncertainty due to instrument instability
and sample inhomogeniety appeared to be less than three percent.

Background counts for each integrated peak were determined using back-
ground regions on either side of the peak region for the sample containing
1% zinc and the blank sample and by measuring the integrated peak intensity
of the blank stub. These background counts were in good agreement.

Measured count rates have been used with the equation presented by
Ziebold (1) for determination of the minimum detectable content of an
element in a carbon matrix

$$C = \left(\frac{NC - NB}{NS - NB} \right) CS$$

where C is the minimum detectable content of the element, NC the minimum
significant number of counts within the region centered on the peak of
interest, NB the mean count taken for the background, NS the mean count
from the standard and CS the content of the element in the standard. The
minimum significant number of counts in a region is three standard deviations
of the background above the mean background count (see Table II). Results
indicate that for typical carbonaceous air and water particulate pollutants the
SEM-EDXRA system will be able to perform quantitative analysis for calcium
and iron. Magnesium and zinc may be identifiable whereas copper and phos-
phorus are below detection limits.

Reference
    1. T. O. Ziebold, Anal. Chem. 39 858-861 (1967).
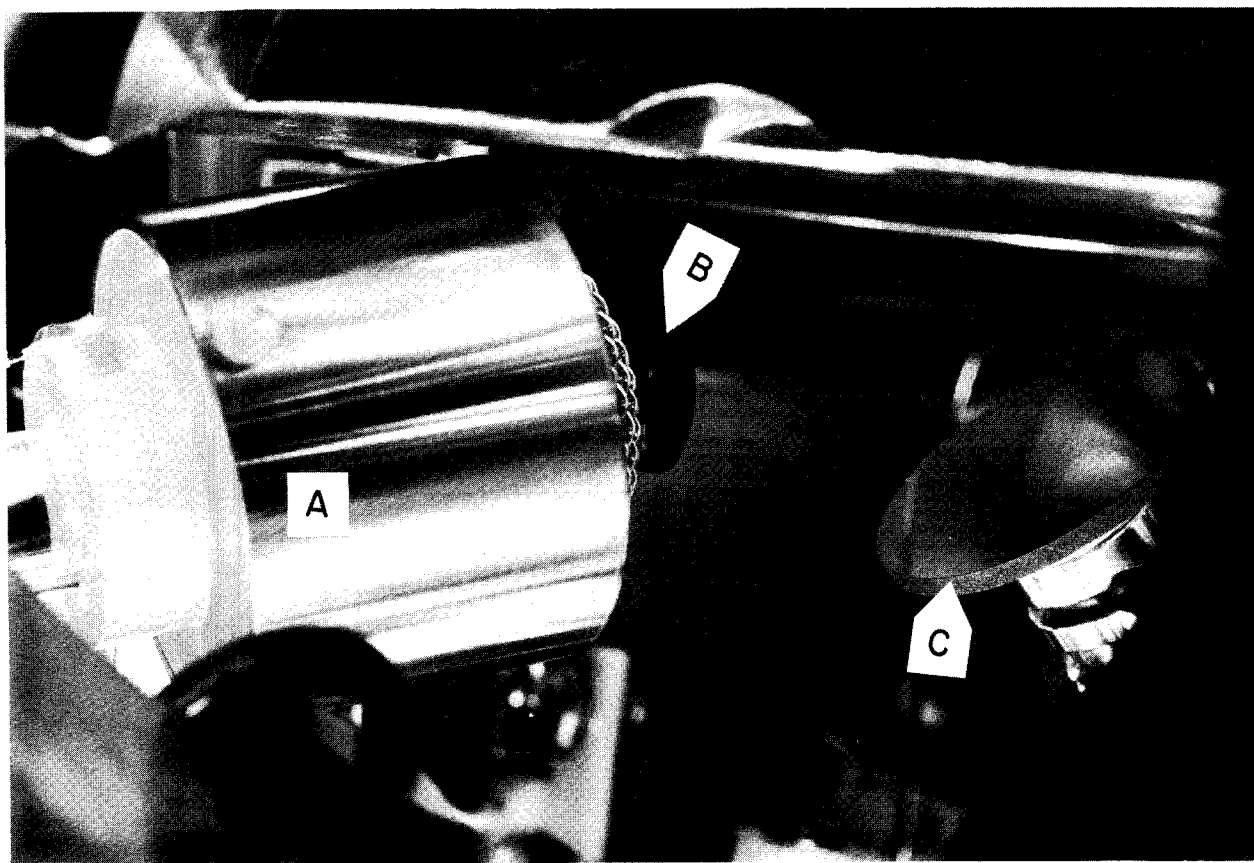
Fig. 1. ETEC specimen chamber during electron beam microanalysis:
A) secondary electron collector, B) collimator for the
solid state x-ray detector and C) polished carbon specimen.
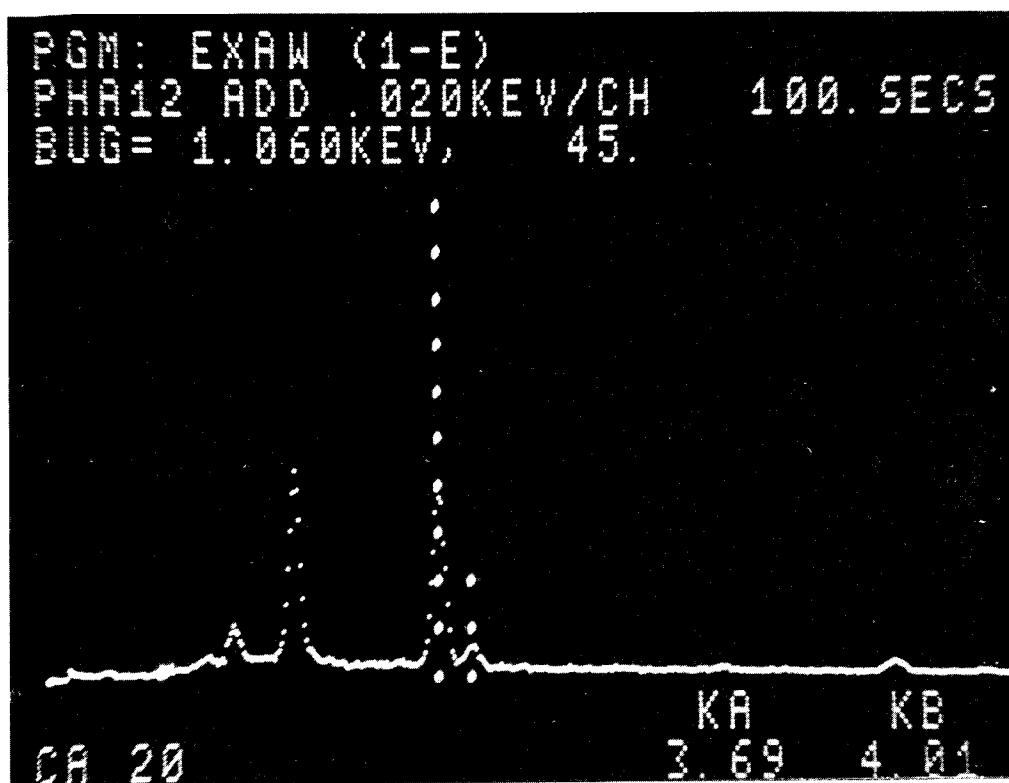
Fig. 3. X-ray energy spectrum of the particle in Fig. 2C exhibiting
high sulfur Ka x-ray emission, demonstrating the peaks for
calcium and sulfur of approximately equal intensity.

Table I. Mean gross counts per hundred seconds and
experimental standard deviation in a zinc
Ka peak region for a blank and a 1% zinc
containing carbon sample.

Sample Position	Sample	Mean gross counts 100 sec	σ counts/100 sec
stationary	1% Zn	8328	158
	blank	419	16
rotated after each count	1% Zn	8334	259
	blank	417	22

Table II. Estimated minimum detectable content (C) of calcium,
magnesium, phosphorus and zinc in a carbon matrix.

Element	NB counts 100 sec	3σB counts 100 sec	NS counts 100 sec	C (%)	Analytical values for coals * MEAN* (%)	MIN* (%)	MAX* (%)
Ca	1191	135	2746	0.1	0.77	0.05	2.67
Mg	1119	186	2911	0.1	0.05	0.01	0.25
P	1795	93	2915	0.1	0.007	0.0005	0.04
Zn	417	66	8334	0.01	0.03	0.0006	0.5

* R. R. Ruch, H. J. Gluskoter and N. F. Shimp, Occurrence and distribution
of potentially volatile trace elements in coal, Illinois State Geological
Survey, Environmental Geology Notes, No. 72, August 1974, Table 5 Mean
Analytical values for 101 coals, p. 18.
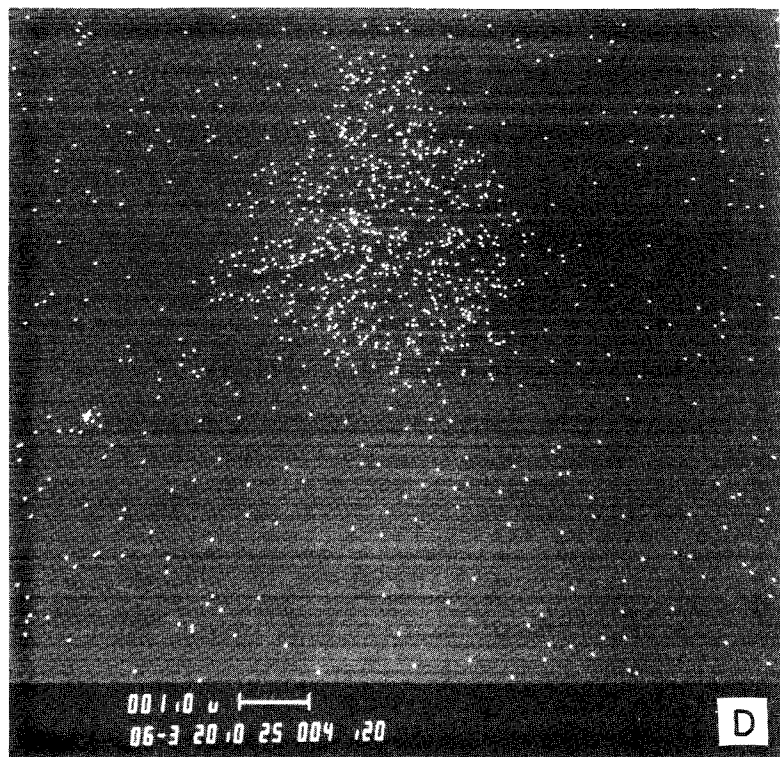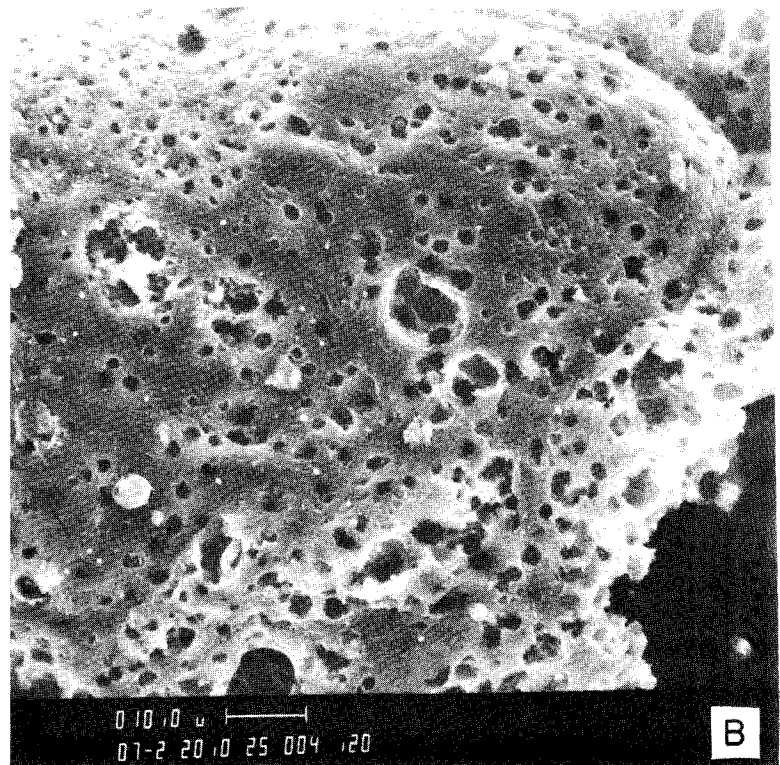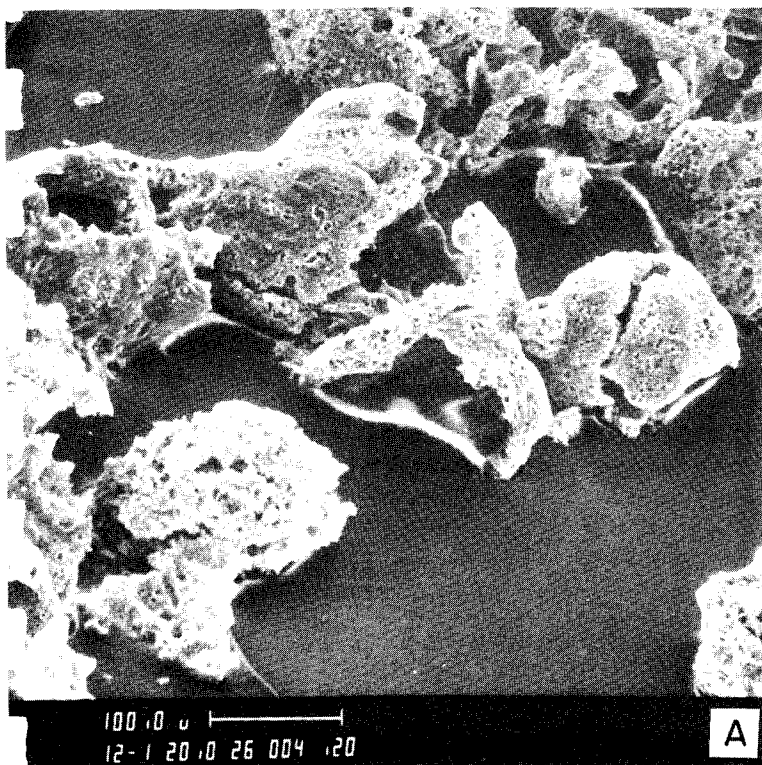
Fig. 2. Secondary electron image of air particulates: A) several
particles at low magnification, B) surface detail of one
particle showing numerous adsorbed particulates, C) several
micron and submicron particles on the surface of a larger
particle, D) sulfur Kα x-ray distribution map for the area
shown in 2C. High intensity sulfur x-ray emission originates
in a region occupied by a 2μm diameter particulate in the
center of Fig. 2C.

SAMPLE MASS DETERMINATION FROM COMPTON SCATTERING USING AN X-RAY PROBE ENERGY DISPERSIVE ANALYZER

H. L. Cox, Jr. and P. S. Ong
The University of Texas System Cancer Center
M. D. Anderson Hospital and Tumor Institute
Houston, Texas 77025

This paper reports an investigation using the Compton profile to measure the total sample mass of biological specimens, analyzed by an x-ray probe energy dispersive microanalyzer. The energy dispersive x-ray fluorescent spectrum, obtained by photon excitation, contains fluorescent x-rays emitted from the trace elements and incident radiation scattered by the low atomic number elements present in the sample. Since the composition of major elements in biological specimen matrices is reasonably constant, Compton scattered radiation is proportional to the sample mass requiring only a simple calibration method to determine the total mass of the specimen. Also, a Compton profile analysis is easily incorporated into a computerized data work-up scheme for routine specimen analyses. The results of trace element determination can therefore be expressed in weight fractions and the only information required is that supplied directly by the x-ray spectrum.

The major elements in any biological specimen consists of C, H, O and N. The fluorescent x-radiation emitted from these atoms is usually absorbed in the window of the Si(Li) detector, but the incident x-rays scattered by them is not. This scattering is extremely intense and consists of both elastic and inelastic components. Zeitz [1] has given a relationship for the total scattering per gram from an amorphous sample as,

$$I_{sc} = N \sum_{i=1}^{n} I_i^a (E_1, 2\theta) \frac{C_i}{A_i} \quad , \tag{1}$$

In Eq. 1, $I_i^a (E_1, 2\theta)$ is the total scattered intensity per atom, C_i is the weight fraction of element i, A_i is the atomic weight of element i, and N is Avogadro's number. The summation is carried over all the n elements present and E_1 and 2θ refer to the incident photon energy and scattering angle, respectively. The total scattered intensity is the sum of the elastic ($F_x(s)$) and inelastic ($S(s)$) portions as given by,

$$I_i^a (E_1, 2\theta) = \left(\frac{d\sigma}{d\Omega}\right)_T [F_x^2(s) + B^3 S(s)] \quad . \tag{2}$$

In Eq. 2, B is the Breit-Dirac [2] correction factor; s is the scattering variable, related to the incident photon energy and scattering angle by $s = (\sin \theta / \lambda)$; and $(d\sigma/d\Omega)_T$ is the Thomson cross section for the intensity scattered by a free electron [2], and given by,

$$\left(\frac{d\sigma}{d\Omega}\right)_T = \left(\frac{e^2}{m_0 c^2}\right)^2 \frac{1}{2} (1 + \cos^2 2\theta) \quad . \tag{3}$$

The symbols e, m_0 and c have their usual meaning as the electronic charge, electron rest mass and speed of light.

Since the total scattered intensity is the sum of the elastic and inelastic scattered portions, the inelastic (or Compton) component is also proportional to the total mass of the scattering material. An integration over the Compton profile has been used in this research program to measure the total mass of biological specimens. The energy difference between the center of the Compton peak and the center of the coherent scattered peak in the Compton effect (3) is given by,

$$\frac{1}{E_2^0} - \frac{1}{E_1} = \frac{2 \sin^2\theta}{m_0 c^2} \quad , \tag{4}$$

where E_2^0 is the energy at the Compton peak center. In x-ray fluorescent analysis, total scattering angles of 90 degrees are used and the energy separation between the Compton and the coherent peaks is 470.5 eV and 575.6 eV for Zr and Mo Kα radiation, respectively. Modern solid state detectors can easily resolve these energy differences and the Compton contribution can be studied separately for total mass determinations.

Two instruments using monochromatic Zr and Mo excitation radiation have been developed in this laboratory for trace metal analysis in biological specimens (4,5,6). The spectrum of an elemental analysis of lung tissue is shown in Fig. 1 obtained by the FRIEDA system (4) using Zr excitation radiation. In Fig. 2, a calibration curve is shown with the integrated Compton intensities plotted against total mass using filter paper standards. Lung tissue masses were predicted to within 10 per cent of their actual masses using the filter paper calibration scheme. An emperical equation was derived from this procedure for lung tissue and given by,

$$M = 1.473 \times 10^{-4} I_{cp} + 0.191 \quad , \tag{5}$$

where I_{cp} is the integrated Compton intensity and the units are in milligrams.

Many Compton mass determinations have been performed for heart, liver and kidney tissue as well as hair. The masses predicted from the Compton measurements have been within 10 to 25 per cent of the actual masses for these tissues, using pure carbon scattering standards. An investigation is underway to determine the most suitable standard for a specific tissue. In addition to an experimental approach to this problem, a theoretical study has been carried out to calculate total Compton scattered intensities using a theory proposed by Block and Mendelsohn (7). Accurate theoretical values for the total scattering per unit mass can be calculated using improved scattering factors in Eqs. 1 and 2, and by choosing realistic weight fractions for the major elements found in specific types of tissue. Theoretical calculation of the total Compton cross section and the total scattering per gram can be incorporated into the computerized data work-up scheme. The advantages of these two methods of approach, experimental vs theoretical, will be discussed and evaluated in this paper.
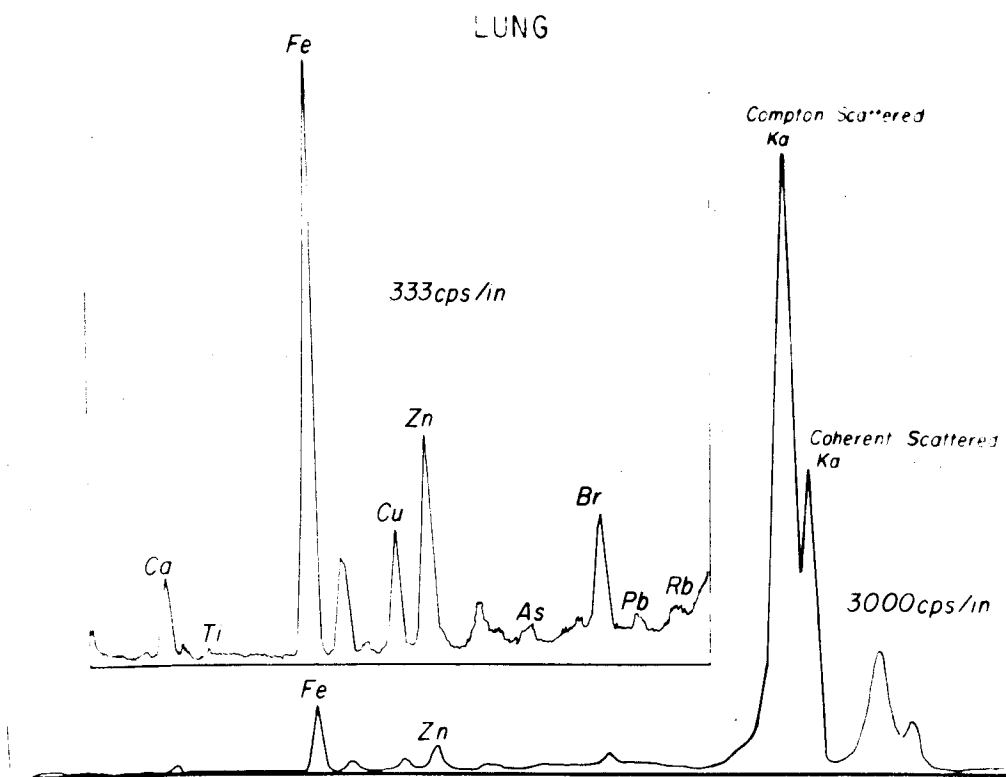
Fig. 1. X-ray fluorescent spectrum emitted by trace elements in lung tissue using ZrKα excitation radiation.
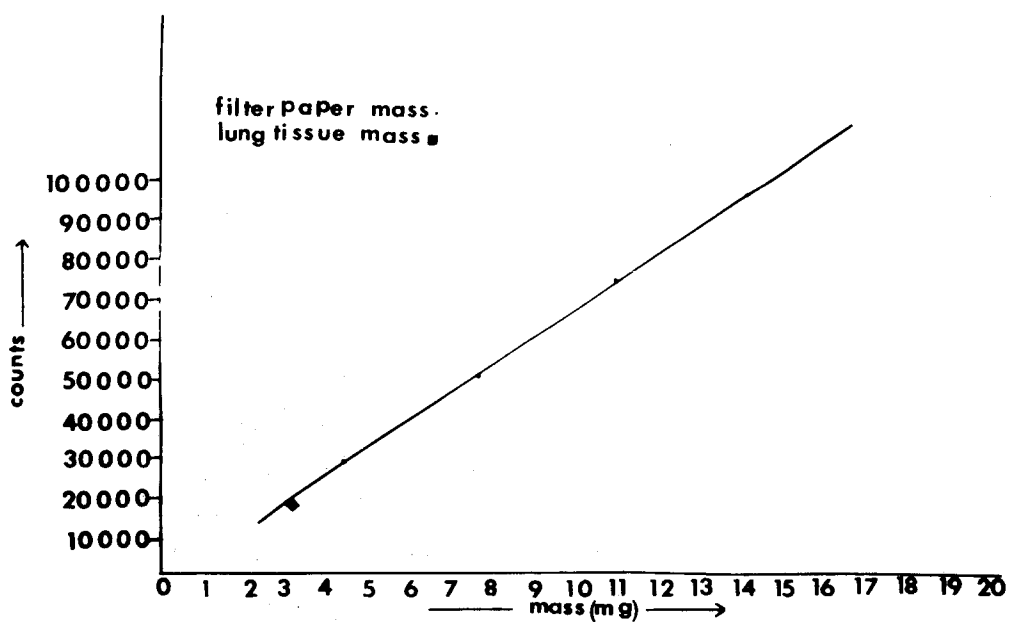
Fig. 2. Calibration curve showing relationship between integrated Compton profile intensities and total sample mass for filter paper and lung tissue.

REFERENCES

1. Zeitz, L.: X-ray emission analysis in biological specimens. In Prog Anal Chem Vol 3, pp35-73, X-ray and Electron Probe Analysis in Biomedical Research, K. M. Earle and A. J. Tousimis, Eds., Plenum Press, New York, 1969.

2. James, R.W.: The Optical Principles of the Diffraction of X-rays: The Crystaline State, Vol. II. Sir Lawrence Bragg, Ed., G. Bell and Sons Ltd., London, 1950.

3. Compton, A.H.: A quantum theory of the scattering of x-rays by light elements. Phys Rev 23:483-502, 1923.

4. Ong, P.S., P. K. Lund, C. E. Litton, and B. A. Mitchell: An energy dispersive system for the analysis of trace elements in human blood serum. In Advances in X-ray Analysis, Vol 16, pp124, Plenum Press, New York, 1973.

5. Ong, P.S. and H. L. Cox, Jr.: A monochromatic x-ray probe for the analysis of trace elements. Proc Microbeam Analysis Soc, 9th Ann Conf, Ottawa, Canada, July 22-26, 1974.

6. Ong, P.S. and H. L. Cox, Jr.: A line focusing x-ray monochromator for the analysis of trace elements in biological tissues. Submitted for publication, Med. Phys.

7. Block, B.J. and L. B. Mendelsohn: Atomic L shell Compton profiles and incoherent scattering factors: Theory. Phys Rev A, 9:1:129-155, 1974.

QUANTITATIVE MICROPROBE X-RAY ANALYSIS AND X-RAY IMAGING
TECHNIQUES OF BORON-BERYLLIUM COMPOUNDS

D. D. McCoy, W. F. Morris, and R. G. Gutmacher

University of California
Lawrence Livermore Laboratory
Livermore, California 94550

This paper describes our methods for the identification and quantitative analysis of microscopic phases in boron-beryllium specimens. Reasonably accurate determinations of the concentrations of low-atomic-number elements are shown to be possible. The identification of new and unexpected phases is made easier by the selective display of x-ray scanning images of individual phases with the aid of a device we call a "Count-rate Discriminator."[1,2]

The samples we analyzed had been prepared either by hot-pressing or arc-melting. Arc-melting generally resulted in multiphase specimens. Due to the uncertainty of the present ZAF correction techniques, especially with regard to low-atomic-number elements, it was thought advisable to prepare compound standards. Standards having the nominal compositions Be_4B, Be_2B, BeB_2 and BeB_6 were prepared by a hot-pressing technique. Fine powders of beryllium and boron were wet-blended, vacuum-dried, and cold-pressed into a cake. The cake was then pressed at $1800°C$ for one hour in 350 torr of argon, to minimize the loss of beryllium. Sufficient standard material was prepared to permit both chemical and microprobe analyses.

Standards and samples were prepared for microprobe analysis using standard metallographic techniques. The final polish was done with 1 μm diamond powder on silk cloth.

For this work, one spectrometer of our ARL Electron Microprobe (Model 21000) was fitted with a lead lignocerate pseudocrystal and a thin-window gas-flow proportional counter. The window material was a supported poly- propylene film of 100 nm thickness. The counting gas was P-10 at a flow- rate of 0.03 SCFH. The detector was operated at an applied potential of 1.675 KV.

A beam voltage of 10 KV was used for the generation of Be Kα and B Kα x-rays. The target currents were normally about 150 nA for boron and 400 nA for beryllium. Typical count-rates and peak-to-background ratios, obtained on pure element standards, were for Be Kα: 1600 counts/sec, 148:1; for B Kα: 7000 counts/sec, 55:1.

The absorption correction factor is the most significant of the three correction factors for this analysis. The magnitude of the absorption effect is illustrated in Figures 1 and 2, in which calculated k-ratios are plotted against the weight percent of beryllium and boron. The k-ratios were calculated by back-calculation in the ZAF expression starting with the concentration values for B and Be in various compounds. Note that B Kα is strongly attenuated by beryllium. As the compounds become richer in beryllium, increasing attenuation of B Kα x-rays may be expected. The atomic number effect is almost negligible because beryllium and boron are neighboring elements. The fluorescence effect is negligible due to the very low fluorescence yield of B Kα.

The four compound standards were analyzed for beryllium and boron, and the k-values were corrected using the MAGIC program.[3] There was con- siderable disagreement between these results and the chemical analyses. We decided that the mass attenuation coefficients used in the MAGIC program, which were taken from Heinrich's data,[4] were probably incorrect. We modi- fied MAGIC to use Henke's mass attenuation coefficients.[5] Figure 3 shows

the relationship of theoretical k-ratios calculated using Heinrich's and Henke's values for the mass attenuation coefficients. Experimental k-ratios obtained from the analysis of the four compound standards are also plotted. Most of the experimental points fall on the curves generated from Henke's attenuation coefficients and do so over a wide range of compositions.

The correction factors for the three effects (absorption, atomic number, and fluorescence) are given for two of the compound standards in Table I. The absorption correction factors using both Heinrich's and Henke's values for the mass attenuation coefficients are tabulated, to show the magnitude of the difference.

Table I. Correction Factors

Compound	Element	Absorption Factor Heinrich	Henke	Atomic Number Factor	Fluorescence Factor
BeB$_6$	Be	1.566	1.924	1.021	1.000
	B	1.915	2.078	0.997	1.000
Be$_4$B	Be	1.184	1.225	1.005	1.000
	B	12.21	14.47	0.981	1.000

As we predicted, the absorption correction factor for boron becomes quite large at high beryllium concentrations. The difference between the absorption factors calculated using Henke's and Heinrich's data is significant throughout. Subsequent analyses were made using Henke's values for the mass attenuation coefficients.

Most of our analyses were done on several samples of nominal composition BeB$_6$. The results from four such samples are given in Table II, in which the compositions derived by microprobe and chemical analyses are compared with the theoretical composition.

Table II.   Analysis of BeB_6 Specimens

Sample No.	Theoretical Composition BeB_6, Wt. %		Microprobe Analysis Wt. %	Chemical Analysis Wt. %
144	B	87.80	88.30	87.30
	Be	12.20	11.70	12.20
146	B		87.39	87.74
	Be		12.61	11.03
147	B		88.15	87.38
	Be		11.85	11.45
148	B		87.90	75.44
	Be		12.10	13.41

The agreement between microprobe and chemical analyses is satisfactory, except for specimen 148.   Chemical results showed a high value for oxygen and some carbon.   With the microprobe we confirmed the presence of inclusions of beryllium oxide, which fluoresced blue under the electron beam, and some carbon inclusions.   In our quantitative analysis, we had deliberately avoided these inclusions.   We conclude that quantitative determinations of these low-atomic-number elements with the microprobe are feasible, if the mass attenuation coefficients are known with reasonable accuracy.

Good x-ray scanning images, which are essentially photographs taken in the "light" of characteristic x-rays, reveal important complementary information to the quantitative element determinations.   In a multiphase system it is valuable to know how the phases are distributed with respect to each other.   In conventional x-ray scanning techniques, phases can be distinguished from each other if they contain different elements.   However,

if the phases contain the same elements but in different ratios, it becomes much more difficult to distinguish the phases from each other. One may still do so by discriminating on the basis of x-ray count-rates, which will be different for the particular element in each phase. A "count-rate discriminator," which enables one to display each phase of a multiphase system separately, without interference by other phases or background, was built in our laboratory. Its construction and method of operation have been described.[2]

One of the beryllium-boron specimens was found to contain three major phases: Be_2B, Be_2B_3 and Be_2B_5. The distribution of the three phases was obtained using B $K\alpha$ x-rays and the count-rate discriminator. These x-ray scanning images are shown in Figs. 4-6. The Be_2B phase is contaminated by inclusions containing iron and calcium.

In another specimen a previously unreported phase approaching Be_2B_3 in composition was discovered by close examination of B $K\alpha$ and Be$K\alpha$ x-ray scanning images obtained with the count-rate discriminator. This phase was not observed by metallographic examination. The use of count-rate discrimination in producing x-ray scanning images yields valuable information concerning phase distributions that is otherwise difficult to obtain.

References

* Work was performed under the auspices of the U.S. Energy Research & Development Administration.

1. D. D. McCoy, B. H. Shue, and R. G. Gutmacher, U.S. Patent 3,737,789 (5 June 1973).

2. D. D. McCoy and R. G. Gutmacher, Rev. Sci. Instr. 46, No. 4 (1975), in press.

3. J. W. Colby, "Quantitative Microprobe Analysis of Thin Insulating Films," in Advances in X-ray Analysis 11, Eds. J. B. Newkirk, G. R. Mallett, H. G. Pfeiffer (Plenum Press, New York 1968) p. 287.

4. K. F. J. Heinrich, "X-ray Absorption Uncertainty" in The Electron Microprobe, Eds. T. D. McKinley, K. F. J. Heinrich, D. B. Wittry (Wiley, New York 1966) p. 296.

5. B. L. Henke, R. L. Elgin, R. E. Lent, and R. B. Ledingham, Norelco Reporter 14, 112 (1967).
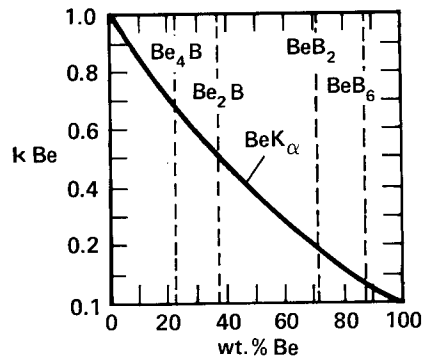
Figure 1. The k-ratios of beryllium for beryllium borides.
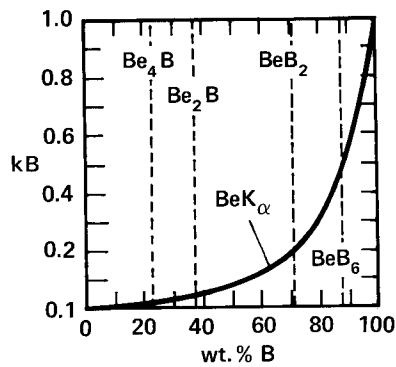
Figure 2. The k-ratios of boron for beryllium borides.
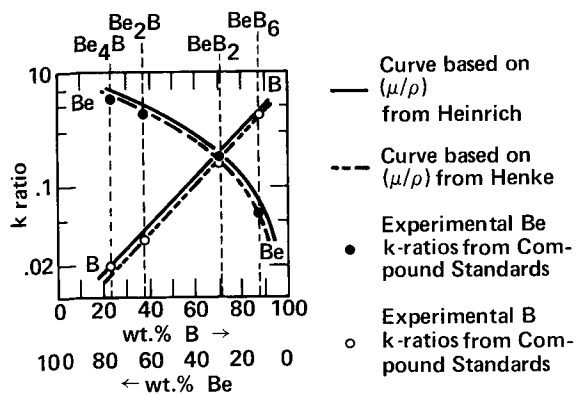
Figure 3. Comparison of k-ratios as a function of mass absorption coefficients.

Figure 4. B K_α x-ray scanning image, showing the Be_2B phase. The black-imaged inclusions in this phase contain iron and calcium impurities. Count-rate B K_α 430 counts/sec.
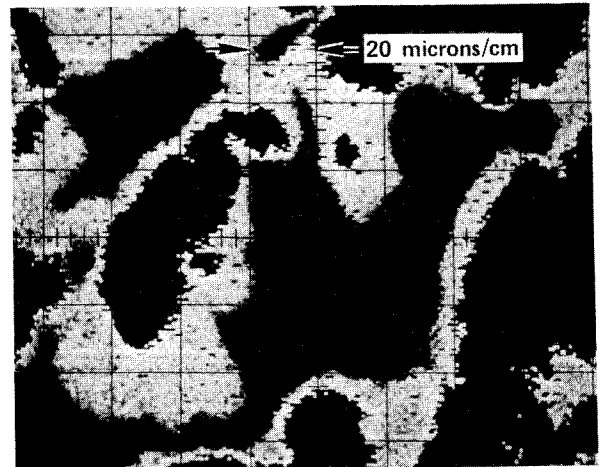
Figure 5. B K_α x-ray scanning image of the Be_2B_3 phase. Count-rate of B K_α: 1760 counts/sec.
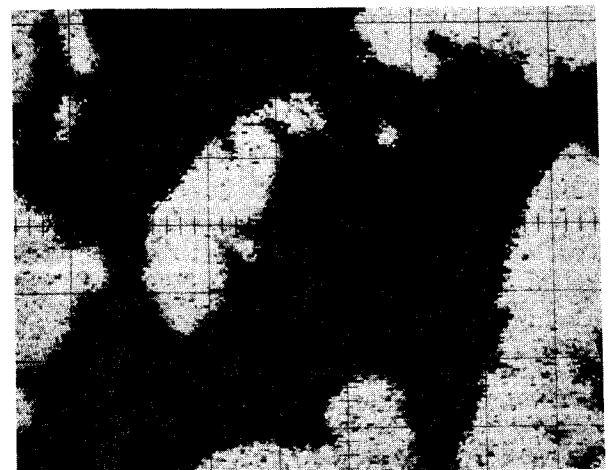
Figure 6. B K_α x-ray scanning image of the Be_2B_5 phase. Count-rate of B K_α: 3720 counts/sec.

7

MICROPROBE TECHNIQUE FOR DETERMINING THE THICKNESS OF Ag$_2$S FILMS AS A FUNCTION OF SULFUR VAPOR PRESSURE AT SATURATION AND BELOW

G. DiGiacomo
IBM System Product Division, Poughkeepsie, N.Y.

ABSTRACT

This is a microprobe technique for determining the Ag$_2$S thickness as a function of temperature and sulfur vapor pressure. The technique is applied to Ag paste films of known area, screened on ceramic substrates and exposed to sulfur vapors. The Ag$_2$S film thickness is determined by electron microprobe on the basis of Skα intensity. The intensities are calibrated with Ag$_2$S films of known thickness, obtained by independent method. The sulfur intensity is proportional to the film thickness and gas vapor pressure. This microprobe technique is important in the evaluation of sulfur reaction kinetics.

Microprobe analysis offers a unique approach for the quantification of the reaction kinetics. The approach is unique as it is capable of quantitative analysis in thin films with the accuracy, resolution, and flexibility exacted in such applications. This experiment deals strictly with the sulfur-silver system. The reaction rates were determined at 55°, 85°, and 125°C with saturated and unsaturated sulfur vapor pressure. Control Ag2S films of known thicknesses, varying from 0.5 to 3.0 μm were used to generate a calibration curve of Skα intensity versus Ag$_2$S thickness. The control films were initially measured by the sectioning method with an accuracy of $\sim$10%. These sections were cut at 60° from the normal to the film surface such that the film thickness is expanded by a factor of three, thus allowing reliable measurement of the thinner films. The other portions of the sectioned specimens were analyzed by electron probe at 20kv with the beam at normal incidence to the surface. The Skα intensities from the various films were plotted against the films thicknesses (Fig. 1). The calibration curve shows that the Skα intensity has a sublinear relationship with film thickness beyond 2 μm. For films < 2 μm, the relationship can be considered linear within an error of $\leq$ 10%. The anlaysis of unknown films was carried out using the slope, k, of the calibration curve generated by the control samples. To determine the reaction rate, μg/kh, the following expression was derived:

$$\dot{Q} = A \ \frac{\int_s I}{kt} \tag{1}$$

where $\quad$ A $\quad$ = $\quad$ film surface area, cm^2

$\qquad \int_s \quad$ = $\quad$ film density, g/cm^3

$\qquad$ I $\quad$ = $\quad$ X-ray intensity, cps

$\qquad$ k $\quad$ = $\quad$ calibration slope, cps/cm

The results obtained with silver films, directly exposed
to sulfur, are shown in Fig. 2 and Fig. 3, and summarized in
Table 1.

TABLE 1 - Ag_2S Reaction Rate vs. Temperature

	Temperature, $^{\circ}C$		
	125°	85°	55°
Po, ppb	7000	500	50
μm/hr	0.35	0.030	0.0027
$\dot{Q}$, μg/khr	1570	135	12

Where Po is the sulfur saturated vapor pressure in parts per
billion.

On the basis of the above results, the reaction rate, g/khr,
can be written as:

$$\dot{Q} = \left(\frac{A}{\int} \right) P_O \qquad (2)$$

where $\quad A = 2.7 \times 10^{-2}$ cm^2

$\int = 0.12 \left(\dfrac{\mu g}{khr \cdot ppb \cdot cm^2} \right) - 1$

$A = 0.22$ μg/khr - ppb

Eg. 2 is not applicable when the vapor pressure is below saturation,
since the raaction rate decreases faster than the vapor pressure
(TABLE 2), such that considerable error can be made. Below
saturation, the Kinetics follow B.E.T. adsorption isotherm of
type III, which adequately describes the behavior:

$$r = k \frac{P/Po}{(1-P/Po) \left[1 + (K-1) \, P/Po \right]}, \; \mu\text{m/hr}$$

where K is a function of temperature

TABLE 2 - Ag2S Reaction Rate vs. Sulfur Vapor Pressure

Temp.	S8 Vapor Pressure	Relative Pressure P/Po	Reaction Rate μg/khr
85^0	500ppb	1.00	150
"	375	0.75	50
"	250	0.50	30
"	150	0.30	15
"	50	0.10	8
125^0	7000	1.00	1650
"	5250	0.75	880
"	3500	0.50	650
"	2100	0.30	300
"	700	0.10	100
"	350	0.05	45

Acknowledgment
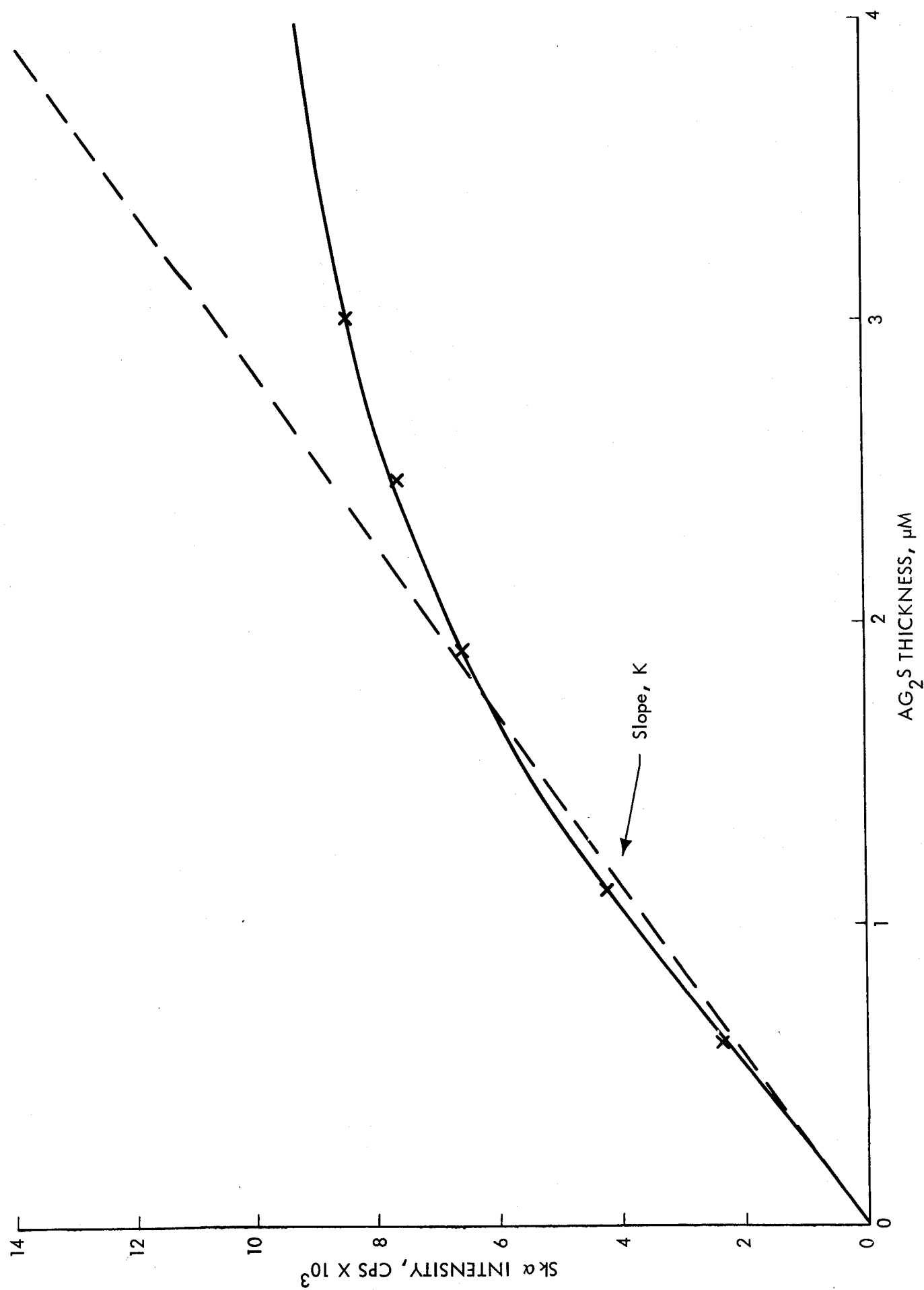
FIGURE 1. CALIBRATION CURVE FOR AG$_2$S THICKNESS 30 KV – 10^{-7} A
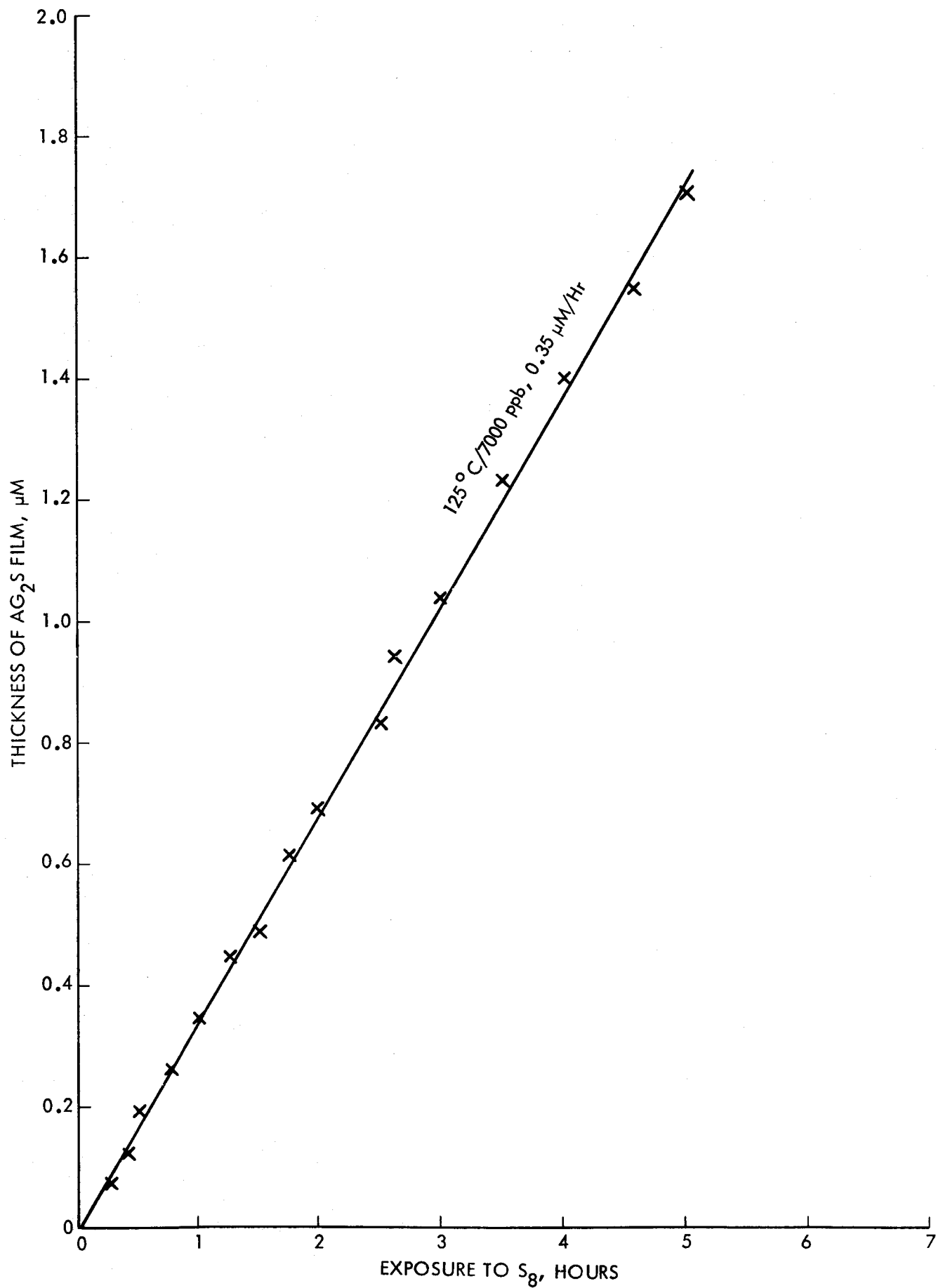
FIGURE 2. AG$_2$S FILM THICKNESS VS EXPOSURE TIME AT 125°C
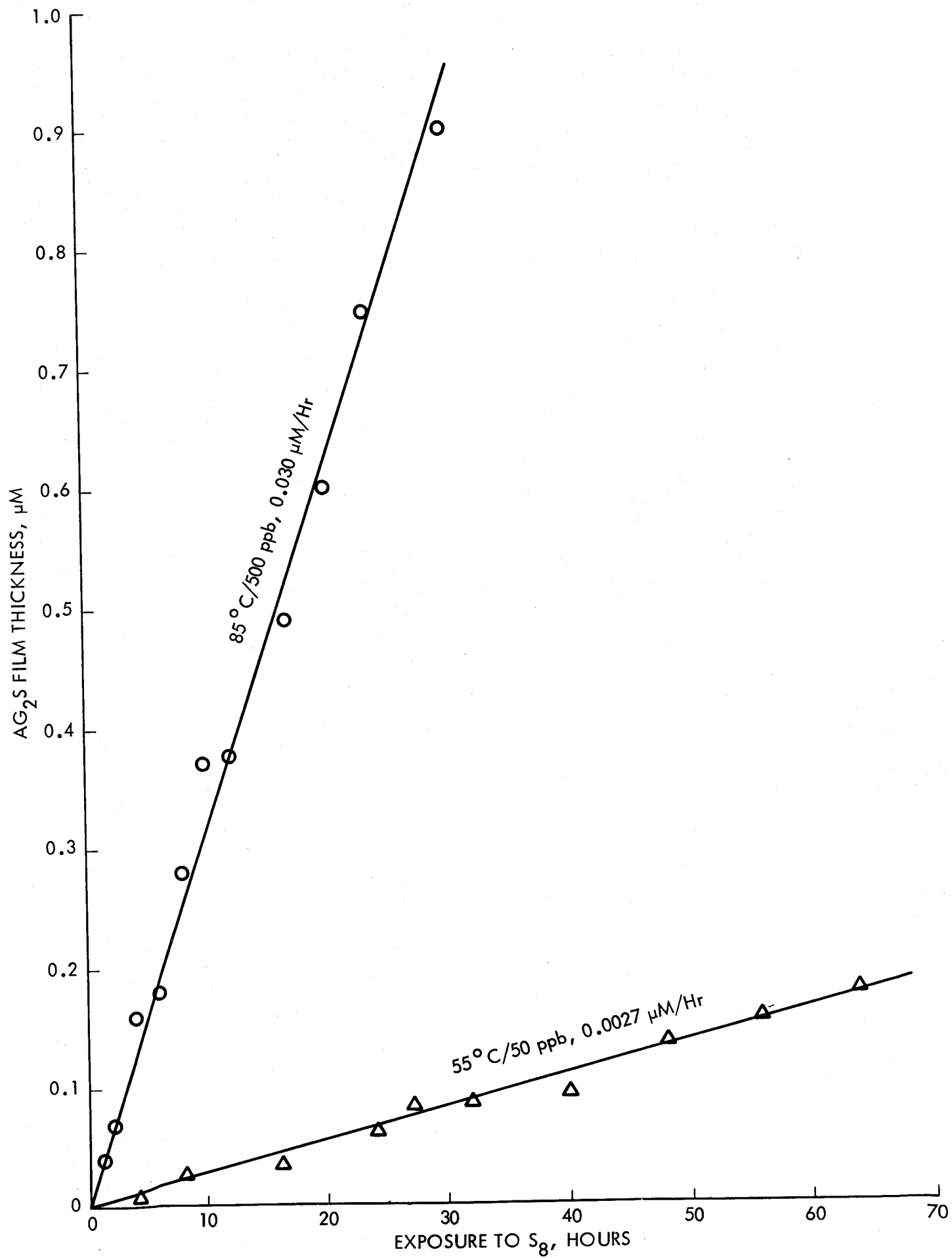
FIGURE 2. AG₂S FILM THICKNESS VS EXPOSURE TIME AT 85° AND 55°C

The plot shows AG$_2$S FILM THICKNESS, μM (y-axis, 0 to 1.0) versus EXPOSURE TO S$_8$, HOURS (x-axis, 0 to 70).

Upper line (circles): 85°C/500 ppb, 0.030 μM/Hr

Lower line (triangles): 55°C/50 ppb, 0.0027 μM/Hr

AMBIGUITIES IN THE IDENTIFICATION OF ASBESTOS FIBERS IN LIQUIDS

D. R. Beaman and D. M. File[*]

The Dow Chemical Company
Midland, Michigan 48640

Asbestos fibers in liquid samples can be identified on the basis of their morphology or elemental composition or crystal structure. There are, however, difficulties with each mode of identification that often lead to large errors in the measured fiber concentrations.

Asbestos morphology is distinctive but not sufficiently so to always allow morphological distinction between asbestos fibers and: diatoms, diatom fragments, oxides (Fe, Ti, and Si, are common), clays, non-asbestiform silicates (mica and talc fragments, etc.), metal fragments, fiber glass, synthetic fibers, cellulose, salts, bacteria, plant fragments and other organic debris. These interferences are most troublesome when studying amphiboles but persist to some extent in identifying chrysotile, not withstanding its distinctive tubular or hollow core appearance in the transmission electron microscope and its characteristic fibril diameter of 300-400$\overset{o}{A}$. The hollow core criterion is unreliable because chrysotile fibrils are susceptible to thermal and chemical damage. The hollow core disappears as Mg is leached out (1). Some chrysotile fibrils are solid (2) and others contain amorphous material in the core (3). In a series of seven water samples of low chrysotile concentration between 40 and 100% (mean of 70%) of the fibers identified as chrysotile had the distinctive tubular appearance. When a fiber is defined as any particle with a length to diameter ratio greater than three the fraction of fibers that are asbestiform varies widely between different sample types and even within a specific sample category, e.g. in 50% caustic solutions, 3 to 99% of the fibers were chrysotile while 19-82% of the fibers in Duluth tap water were amphibole.

[*]Present address - Cameca Instruments, Inc, Elmsford, N.Y.

Selected area electron diffraction (SAED) patterns can be used to compliment morphological observations but as shown in Figures 1 and 2 the fraction of asbestiform fibers that will provide distinct electron diffraction patterns is often less than one and varies dramatically with the fiber diameter. The larger fibers are opaque to the electron beam while there is insufficient diffracted intensity from the smaller fibers to allow visual pattern recognition in the transmission electron microscope (TEM). It is possible to use the data in Figure 1 to correct measured concentrations for SAED inadequacies. The correction may be made on the basis of the size distribution observed in the sample, e.g., for every identified amphibole with a diameter of 0.1 μ there are three amphiboles that would fail to give an identifiable diffraction pattern. This correction can only be applied to fibers with cummingtonite-grunerite chemistry. Such a correction is less appropriate in the case of chrysotile because of its structual instability. Most chrysotile fibers in beer gave ambiguous patterns (4) and the pattern tended to fade as Mg was leached from the structure (1). Grinding degraded the SAED pattern (5) and increased the susceptibility to damage by the electron beam.

The elemental composition of a fiber can be obtained by using an energy dispersive spectrometer (EDS) accessory on the TEM. The EDS, however, is not a panacea and does introduce complexities that can lead to misinterpretation. The most serious problem is the adjacent material and coatings often associated with the fiber. There are geometrical constraints that can cause absorption anomolies and that limit the region of the TEM grid from which accurate elemental composition can be obtained. The composition of the minerals of interest is far from stoichiometric and different minerals may have compositions that are not distinguishable with an EDS. The observed elemental intensities (ratioed to Si) vary with fiber diameter (Figure 3) and the variation must be taken into consideration when classifying fibers. Much of the observed variation with size can be explained on the basis of reduced absorption with decreasing fiber size.

With fiber identification based on fiber morphology and the
EDS spectrum and the SAED pattern it is possible to eliminate many of
the ambiguities that arise and lead to incorrect fiber concentrations
when counting is based only on one or two of these criterion. In a
TEM equipped with an EDS it was possible to measure mineral fiber
concentrations with a precision of ±30%.

REFERENCES

1. Cunningham, H. M. and Pontefract, R. D., J. Assoc. Offic. Anal.
    Chem., Vol. 56, 1973, p 976.
2. Yada, K., Acta Cryst., Vol. 23, 1967, p 704.
3. Maser, M., Rice, R. V. and Klug, H. P., American Mineralogist,
    Vol. 45, 1960, p 680.
4. Biles, B. and Emerson, T. R., Nature, Vol. 219, 1968, p 93.
5. Speil, S. and Leineweber, J. P., Environ. Res., Vol. 2, 1969, p 166.
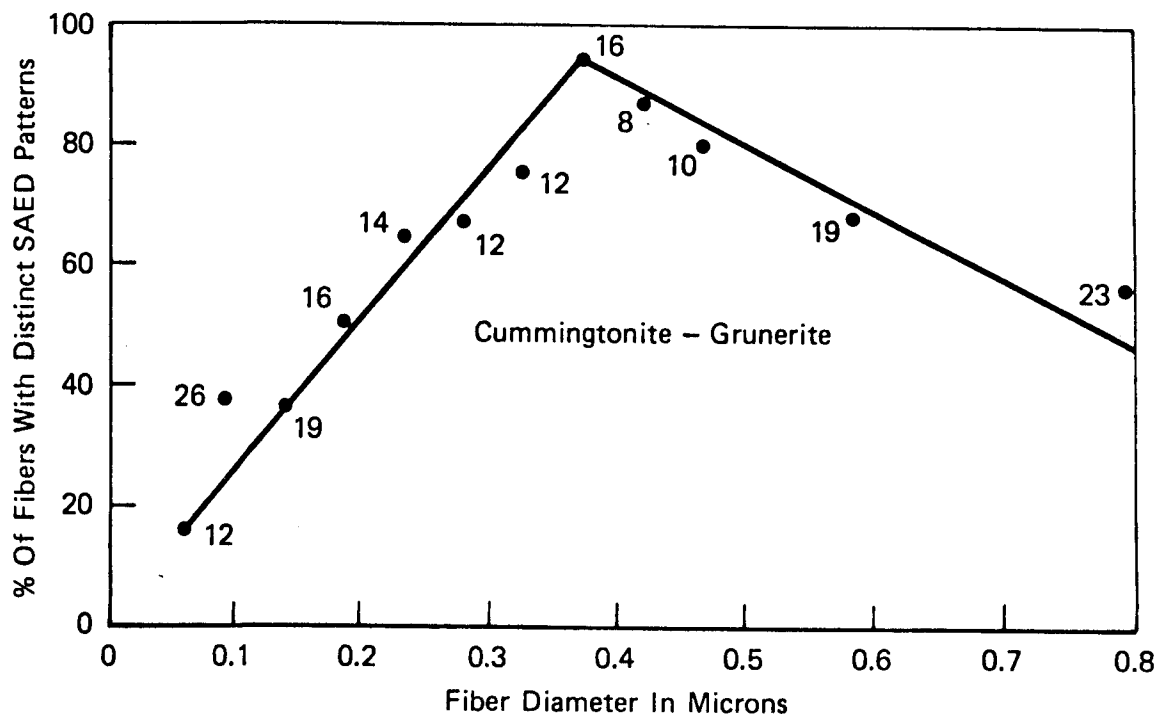
Fig. 1. The percentage of amphibole fibers of a given size that give distinct SAED patterns
is shown to depend upon the fiber diameter. The cummingtonite-grunerite standard was
examined in a Philips EM300 transmission electron microscope at 80Kv. The numbers
beside each point indicate the number of fibers of that size examined.
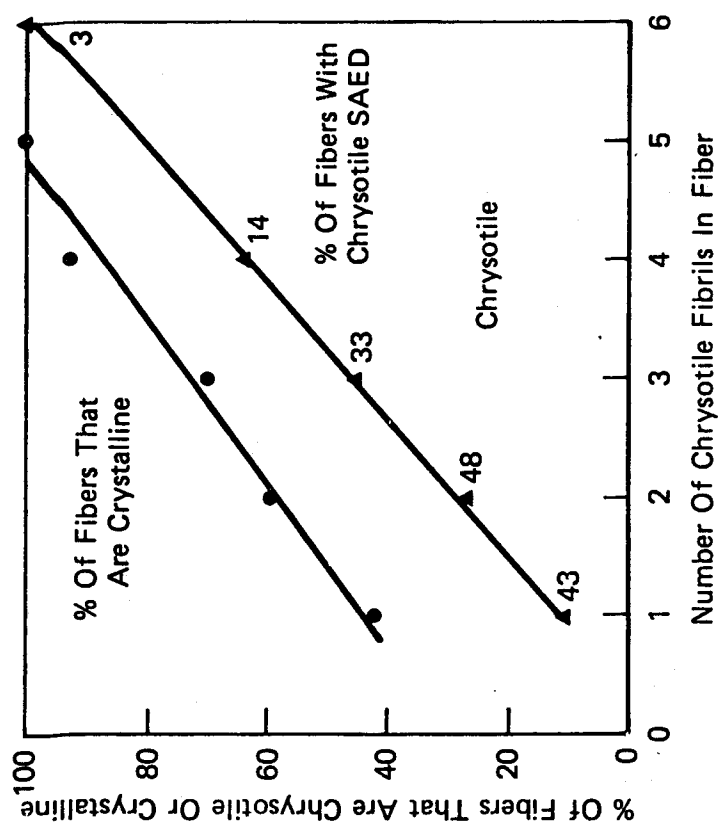
Fig. 2. The percentage of chrysotile fibers of a given size that give distinct SAED patterns is shown to depend upon the number of fibrils in the fiber. The sample was a Wards standard from the Thetford Mine, Quebec. The numbers beside each point indicate the number of fibers of that size examined. The percentage of fibers exhibiting crystallinity, regardless of the quality of the SAED pattern, is also plotted.
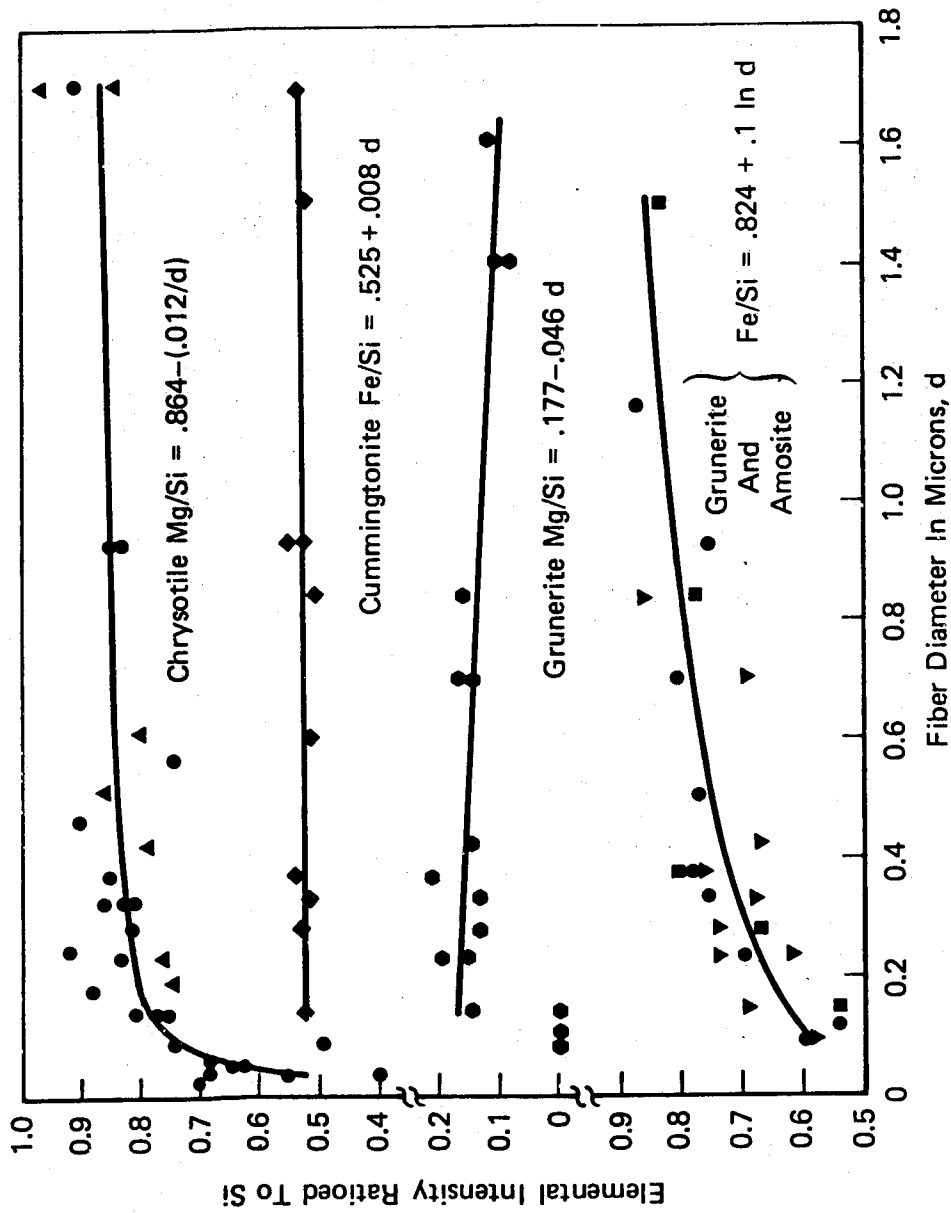
Fig. 3. The intensity of Fe or MgKα ratioed to SiKα is plotted as a function of fiber diameter, d, for several mineral standards. The fit to the experimental data is given by the expression indicated for each curve. All the data are for a Philips EM300 operated at 80Kv and equipped with a side entry EDS with the sample tilted at 39°.

Electron Microprobe Whole Rock Analysis of 20mg Samples

By

R. Brown and O. Mullins, Jr.

Lockheed Electronics Company, Houston, Texas

Whole rock analyses with the electron microprobe have been made since 1964 (2, 5 - 8, 10). Techniques utilized for sample preparation involve: 1) pellets pressed from rock powders; 2) fusion of the rock powder with a flux and quenching to form a glass; 3) fusion and quenching without flux. The need for high quality major element analyses of small samples (10-20mg) has resulted from the shortage of some samples, e.g., lunar rake samples of 100mg allocation. Electron microprobe whole rock analysis has been investigated with such application in mind.

We have chosen to develop the method of direct fusion of rock powder for several reasons: 1) weighing of the sample is not required; 2) standards do not have to be synthesized-mineral standards can be utilized; 3) existing data reduction programs can be applied; 4) maximum sensitivity of the x-ray measurements can be achieved since there is no dilution of the rock powder with a fusion flux. The rock powder is melted on a metallic strip heater using low voltage and high current (3Va.c., 300A). The heater is contained in a vessel pressurized with argon. Sample weights are $\sim$ 20mg; melt temperatures of 1600-2000C$^\circ$ are used with run times of 20 seconds. Argon is flushed over the melted sample as the temperature is rapidly dropped, quenching the sample to a glass bead. Chemical changes are minimized by using short melting times and by selecting metal strips which interact minimally with the sample. Both Mo and Ir strips have been used.

Average relative errors obtained from a suite of basalts (12 samples), Leg 34, Deep Sea Drilling Project are shown in Table I, together with the compositional range of the oxides. Errors for all oxides, but Na_2O, were obtained by comparing microprobe data with data obtained by x-ray fluorescence analysis on the same samples (9). Na_2O values are compared with neutron activation analytical data (9). Errors reported are within acceptable limits for electron microprobe analyses. For rock types ranging in composition from basalt to granite, errors are typically <5% relative for the oxides (Table II).

Agreement between microprobe analyses and x-ray fluorescence values for the Leg 34 basalts is good and illustrates that the technique can provide good quality major element analyses; however, larger errors indicated in Table II show that not all rocks are equally accommodated by the technique. Rocks with high Mg concentrations, i.e., peridotites, are difficult to quench to a glass; instead olivine crystals form with interstitial glass. Granites and rocks with high SiO_2 concentrations are extremely viscous and tend to form heterogeneous glasses. It has been demonstrated that when the technique is applied to rocks of limited compositional range high quality major element analyses can be produced.

TABLE I

Compositional range and average relative error (%) of Leg 34 Deep Sea Drilling
Project basalts.

OXIDE	RANGE (wt. %)	AVE. RELATIVE ERROR (%)
SiO_2	49.02 - 50.47	0.9
TiO_2	1.18 - 2.35	1.8
Al_2O_3	12.90 - 15.54	0.9
FeO	8.87 - 13.41	2.2
MnO	0.14 - 0.22	11.0
MgO	5.55 - 7.44	1.2
CaO	9.59 - 12.84	0.8
Na_2O	2.55 - 3.13	3.9
K_2O	0.11 - 0.66	20.6
P_2O_5	0.09 - 0.22	4.9

TABLE II

Microprobe analyses of standard rocks compared with recommended values.

	USGS AGV-1		USGS BCR-1		USGS G-2		USGS GSP-1	
	a	b	a	b	a	b	a	b
SiO_2	60.64	59.62	53.00	55.39	67.93	69.63	67.89	67.95
TiO_2	0.88	1.05	2.32	2.24	0.47	0.50	0.63	0.67
Al_2O_3	17.47	17.43	13.34	13.83	15.87	15.52	14.88	15.38
FeO	6.49	6.17	12.36	12.31	2.30	2.40	3.74	3.93
MnO	0.08	0.10	0.19	0.18	0.03	0.03	0.04	0.04
MgO	1.68	1.55	3.58	3.52	0.78	0.77	0.98	0.97
CaO	5.18	4.95	7.19	7.03	2.13	1.95	1.88	2.04
Na_2O	4.26	4.30	3.17	3.32	4.86	4.10	2.69	2.82
K_2O	2.98	2.92	1.65	1.73	4.77	4.54	5.54	5.58
P_2O_5	0.52	0.50	0.38	0.37	--	0.14	0.35	0.28

a) Microprobe analyses were obtained using an A.R.L. EMX-SM electron
microprobe with spectrometers equipped with ADP, LiF and RbAP
analyzing crystals. Mineral standard oligoclase (Si, Al, Na),
clinopyroxene (Ca, Fe, Mg), kaersutite (Ti), orthoclase (K),
rhodonite (Mn), and apatite (P) were used for analysis. An
acceleration potential of 15kv and sample current of 0.02
microamperes on clinopyroxene with 20 micron spot size were
used with counting times of 20 seconds per sample point and 10
points per sample were typically analyzed. No alkali losses
were detected due to beam loading. X-ray intensities were
corrected for instrument parameters, i.e. drift, dead-time,
background, and matrix effects using a Bence, Albee type of
correction program on a PDP 11/2C computer (1, 3).

b) Flanagan's mean values (1973) corrected for H_2O and CO_2 losses (4).

REFERENCES

1. Albee, A. L. and Ray, L. (1970) Correction factors for electron probe microanalysis of silicates, oxides, carbonates, phosphates, and sulfates. *Analytical Chemistry, 42, 1409-1414.*

2. Arrhenius, G., Fitzgerald, R., Frediriksson, K., Holm, B., Sinkankas, J., Bonatti, E., Bostrom, K., Lynn, D., Mathias, B., Ceballe, T. and Korkisch, J., 1964. Valence band structure and other La Jolla problems in microprobe analysis. *Electrochem. Soc. Meeting, Washington, Abstr., 214, 100-103.*

3. Bence, A. E. and Albee, A. L. (1968) Empirical correction factors for the electron microanalysis of silicates and oxides. *Journal of Geology 76, 382-403.*

4. Flanagan, F. J. (1973) 1972 values for international geochemical reference samples. *Geochim. Cosmochim. Acta 37, 1189-1200.*

5. Gulson, B. L. and Lovering, J. F. (1968) Rock analysis using the electron probe. *Geochim. Cosmochim. Acta 32, 119-122.*

6. Mori, T., Jakes, P., and Nagaoka, M. (1971) Major element and analysis of silicate rocks using electron probe microanalyzer. *Science Reports of Kanazawa University 16, 113-120.*

7. Nicholls, I. A. (1974) A direct fusion method of preparing silicate rock glasses for energy-dispersive electron microprobe analysis. *Chemical Geology, 14, 151-157.*

8. Reed, S. J. B. (1970) The analysis of rocks in the electron probe. *Geochim. Cosmochim. Acta 34, 416-421.*

9. Rhodes, J. M., Blanchard, D. P., Rodgers, K. V., Jacobs, J. W., and Brannon, J. C. (1975) Petrology and chemistry of basalts from the Nazca Plate: Part 2 - Major and trace element chemistry. *Initial Reports of the Deep Sea Drilling Project 34, (In preparation).*

10. Rucklidge, J. C., Gibb, G. F., Fawcett, J. J., and Gasparrini, E. L. (1970) Rapid-rock analysis by electron probe. *Geochim. Cosmochim. Acta 34, 416-421.*

MICROSCOPIC INVESTIGATIONS OF COAL FLY ASH PARTICLES

Judy E. Baker, Charles A. Evans*

Andrew Loh, David F.S. Natusch+

Introduction

Coal combustion is known to be one of the largest anthropogenic contributors of particulate air pollution (1). With the expected increase in the combustion of coal in the next decade, it becomes desirable to study the nature of these particles, commonly known as fly ash particles, by optical and electron microscopic techniques with which individual particles can be studied.

A fly ash sample is very difficult to study under a microscope since the particles are extemely heterogeneous and a few mg of sample can contain thousands of different particles. It is thus desired to separate the fly ash particles as much as possible before microscopic studies are carried out.

In this study, a single fly ash sample has been separated into fractions based on differences in their physical properties of size, ferromagnetism and density. Each fraction has been observed with microscopic techniques where the morphological characteristics and elemental analysis of individual particles has been studied. Fly ash particles are known to be hollow and encapsulated (2) and this study reports on the extent of these particles in the different size ranges and in the magnetic and non-magnetic fractions.

Experimental

a) Particle Fractionation - the fly ash sample was first sized by sieving the particulate sample through a series of sieves. Each sized fraction was then separated into ferromagnetic and non-ferromagnetic portions by the use of a small permanent magnet. Each of these samples was then separated into 4 density fractions using a series of solutions of varying densities. The fractions were weighed so that density distributions could be determined. The 3 separations have been performed on 1 fly ash sample dividing it up into 32 sub-samples according to a 4 x 2 x 4 matrix based on size, ferromagnetism and density respectively.

b) Observation of these encapsulated particles can be made by breaking the particles open by the simple procedure of gently rolling a cylindrical metal bar across particles deposited on a standard electron microscope sample stub. This cracks the thin outer shells and exposes the contents of the particles. The extent of hollow and encapsulated particles was determined by comparing density distributions of crushed and uncrushed particles. Crushing of particles was carried out in a boron carbide mortar and pestle.

* Materials Research Laboratory, University of Illinois
+ School of Chemical Sciences, University of Illinois, Urbana 61801

c) Microscopic examination was carried out with a JEOL JSM-U3 scanning electron microscope (SEM) equipped with an Ortec energy dispersive Si(Li) detector and an Ortec Model 6200 Multi-channel analyzer, a JEOL Jx50A electron microprobe (EMA) with 2 wavelength dispersive X-ray spectrometers and a Leitz polarizing microscope.

The particles were deposited on Cambridge-type stubs using double-sided adhesive tape. The samples were made conducting by coating with carbon using a Denton DV-503 vacuum evaporator.

Results and Discussion

a) Particle Fractionation

The thirty-two separated fractions have been analyzed for elemental constituents to map out the distribution of major, minor and trace elements in the fractions. Each sub-sample has been studied with the optical microscope and with the scanning electron microscope.

Elemental ratios of Al, Si and Fe have been obtained by ratios of X-ray peak intensities. Results indicate that these ratios are fairly constant with particle size, for a given density range, indicating the matrix composition is probably not a function of particle size. This is also shown by optical microscopy where particles with different optical properties can be seen but the relative amounts of the different types of particles are fairly constant through the different size ranges.

Fly ash particles in the non-magnetic fraction have predominantly alumino-silicate matrices while the magnetic fraction have iron-based matrices. This has been seen by other workers (3). Optical microscopy and elemental analysis have shown that the density and ferromagnetic separations are effective in separating out matrices in the fly ash particles.

b) Particle Morphology

A variety of fly ash samples from several coal-fired power plants have been studied to determine the detailed morphology of fly ash. Microscopic observation has shown that fly ash particles <74 μm are almost completely spherical while the large particles (>74 μm) contain unburned coal particles and many large webb-like structures which have many spherical inclusions.

Many of the spherical particles have smooth surfaces and comprise the bulk of fly ash. A number of spheres have rough surfaces, apparently covered with a layer of irregularly shaped particles. These spheres make up about 10-20% of the magnetic particles and their X-ray spectra show only peaks for iron. These particles appear morphologically similar to particles in the lunar soil (4).

c) Encapsulating Particles

The spherical particles show 3 distinct forms, solid spheres, hollow spheres and hollow spheres with smaller spherical particles within them (Fig. 1). Two types of encapsulating particles can be distinguished.

1) Those with very thin shells containing a large number of small particles (>20 particles).

2) Those with thick shells containing a fewer number of small particles (2-10 particles).

If the particles were coated with a film of conducting material prior to breaking and were not recoated after breaking, then the uncoated inner surface of the hollow particles and the uncoated encapsulated particles can be easily identified by their high contrast on the cathode ray display. This is because fly ash particles are not good conductors and consequently charge up and scatter more electrons towards the electron detector causing the display to show regions as bright spots. Particles can also be imbedded in epoxy so that a cross-section of these particles can be seen. Semi-quantitative estimates have been made by simply counting the number of hollow and encapsulating particles in a field of view.

One fly ash sample was sized and magnetically separated as above. Each of the non-magnetic fractions was separated into 2 portions. A density separation was carried out on one portion while the other was thoroughly crushed with a boron carbide mortar and pestle before carrying out a density separation. The hollow and encapsulated particles are expected to concentrate in the less denser fractions before crushing, however, after crushing their densities are expected to increase and fall into the density ranges of the matrix compounds.

It can be seen from Figures 2 A-D that most of the hollow and encapsulated particles concentrate in the particle size ranges 20-44 µm and 44-74 µm.

It is also seen from these figures that after crushing the majority of these particles fall into the density range 2.5 - 2.9 showing that the matrix composition is similar for the different particle sizes.

X-ray analysis on the SEM and EMA has shown that the encapsulating and encapsulated particles have elemental compositions which are very similar showing that these particles were probably formed from the same molten fly ash matrix material.

Conclusion

The mechanisms which produce hollow spheres and encapsulated particles are not known but it is suggested that these particles are formed when films of molten fly ash matrix material are entrained into the flowing combustion gases and form bubble-like spheres. If the film happens to surround a number of small molten droplets, encapsulation occurs.

It has been shown that encapsulating particles occur to a significant extent and tend to predominate in particles with diameters 20 - 74 μm. Commercial precipitators collect the larger particles more efficiently and the presence of these particles can be an environmental plus since it forms a natural mechanism for the removal of small micron and sub-micron particles which have greater environmental effects.

A study of the morphology and elemental composition of fly ash particles is important since the ultimate goal is in the mechanism of the formation of these particles so that we may better control the emission of these particles into our precious environment.

References

1. Robinson E., and Robbins R. C., Am. Petrol. Inst. Publ. No. 4076 (1971).

2. McAdams, H. T., private communication, Calspan Corporation, Buffalo, New York.

3. Harvey R. D., "Petrographic and Mineralogical Characteristics of Carbonate Rocks Related to Sulfur Dioxide Sorption in Flue Gases," Final Report to U.S. Environmental Protection Agency, July, 1971.

4. McKay, D. and Ladle, G., "Scanning Electron Microscope Study of Particles in the Lunar Soil", p. 179, Proc. Scanning Electron Microscopy Conf., Chicago, Illinois, April, 1971.

Figure 1: Hollow Fly Ash Particle with small spherical
particles inside. Print Magnification - 5000X.

10 µm

Figure 2: Density distributions for the crushed and uncrushed
           fly ash particles.
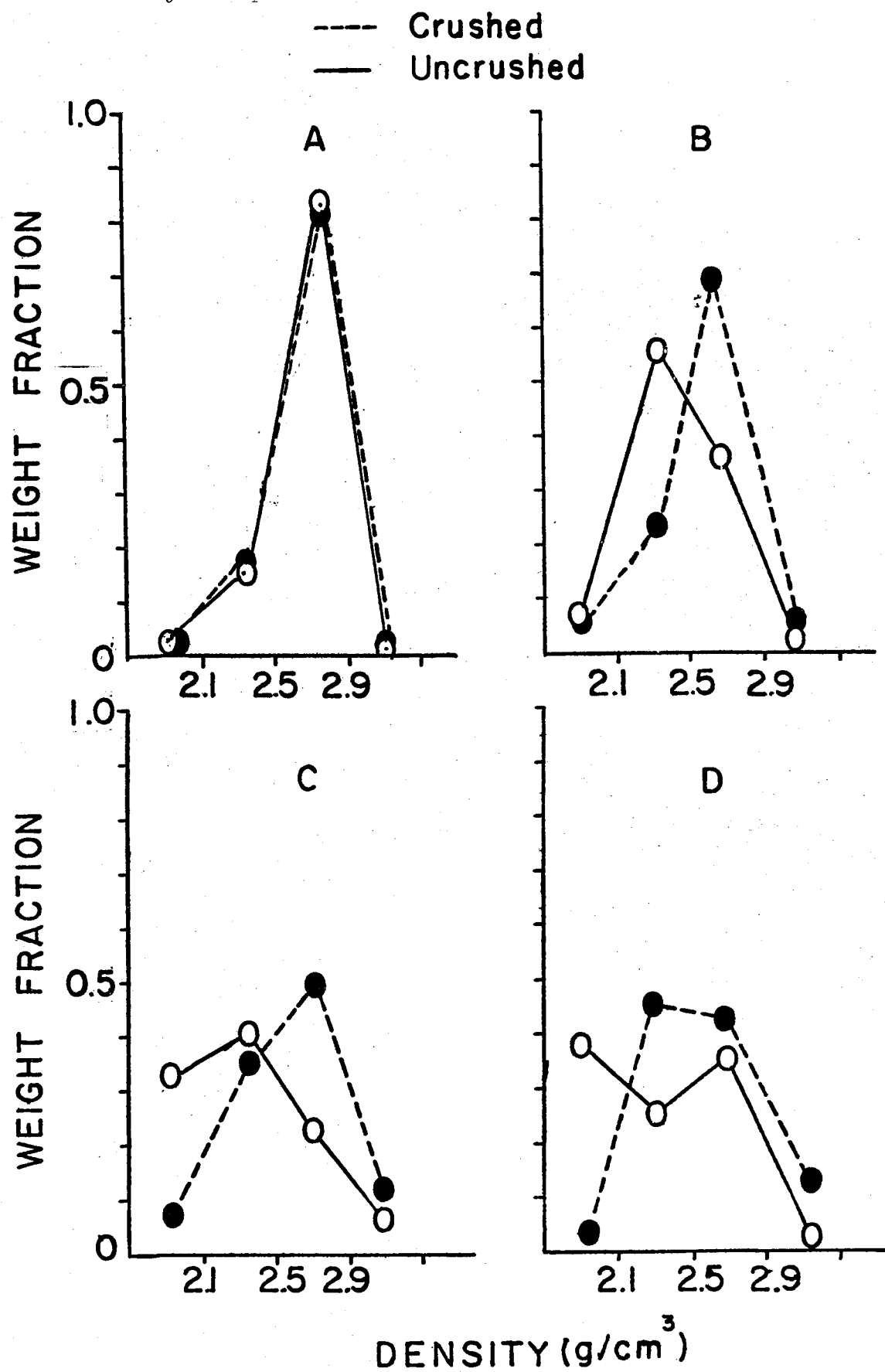
---- **Crushed**

—— **Uncrushed**

DENSITY (g/cm³)

PARTICLE DIAMETER: A - <20 μm, B-20-44 μm
                    C - 44-74 um. D - >74 um

APPLICATIONS OF QUANTITATIVE ELECTRON BEAM ANALYSIS OF MICROPARTICLES IN AIR POLLUTION RESEARCH

John T. Armstrong, Department of Chemistry
Peter R. Buseck, Departments of Chemistry and Geology
Arizona State University, Tempe, Arizona 85281

The composition of individual airborne microparticles is of great importance for determining emission sources, mechanisms of formation, and health effects. Despite this importance, virtually all particulate analyses are performed on bulk samples. Critical information is thus lost concerning: (a) the sources of the aerosol, (b) the relative contributions to the aerosol from the different sources, (c) the mechanisms of particle formation, (d) the mechanisms of particle fractionation other modifications, and (e) the possible effects on vegetation and human health of the various particle components.

Friedlander (1) has noted that elemental concentrations in bulk particulate samples are "not sufficient to define the state of a polluted atmosphere or its effects on public health, weather modification, and so on. The molecular state as well as the phase in which the substance is present may be of determining importance..."

Electron beam instruments are ideally suited for such complete chemical analyses of individual particulates (e.g., ref. 2). Some attempts in the past have been made to develop procedures for quantitative analyses of microparticles (e.g., 3,4). Such procedures, however, have required particulate standards or unusual operating conditions which have limited their applicability.

By utilizing the correction procedures which we have developed (5,6) it is possible to perform routine, accurate quantitative analyses on microparticles using conventional flat standards. This ability opens up important new applications for the electron microprobe in environmental research.

In this paper, we will consider the different approaches currently used to characterize airborne particulates and their sources. We will briefly discuss the assumptions required and the difficulties involved in these approaches. We will then show the important complementary information which can be obtained by quantitative electron microprobe and SEM analyses of individual particles.

Commonly, attempts to characterize the sources of airborne particulate material have relied on using a series of "tracer" elements (assumed to have come exclusively from one or more sources whose emissions are assumed to have known composition) in mass balance calculations to determine the relative contributions from the various sources (1,7). The size distribution of the particles (8) and diurnal variation data (9) can provide supplemental information to resolve the various sources.

There are problems associated with the mass balance approach: (a) there may be unknown sources for the aerosol, or sources for which the composition or size distribution is not known; (b) the average concentrations and size distributions for given sources may not represent the range of concentrations actually contributing to the aerosol; and (c) the mechanisms of source fractionation and modification may not be adequately known.

The problem of unknown sources and their compositions and size distributions is one which is solved by more extensive source sampling and investigation. The problems of source compositional variations and fractionation are inherent in the elemental analysis of bulk samples, sized or not.

The quantitative chemical analysis of individual particles in ambient and source samples can provide much valuable supplemental information to alleviate the above problems. By analyzing individual particles, it can be determined if there are elements unique to one source which can be used as tracers. The exact compositions of the different components from the various sources can be determined-- as they exist in the airborne particles. Thus, the problems of fractionation and modification from the initial source can be taken into account.

By performing quantitative analyses on individual particles, we have been able to characterize sources and their contributions in a manner which would be impossible by bulk analyses. We have been able to distinguish between the emissions of two neighboring scrap iron foundries engaged in the same type of operation. We have determined a variety of different zinc sources in a metropolitan area. We have been able to examine the contributions of flyash in dusty areas. We shall discuss these and similar results.

Quantitative electron beam analysis of individual microparticles does not supplant but rather supplements analytical techniques commonly used in environmental chemistry. By employing several techniques in conjunction, the various procedures

for characterization of particulate samples, such as mass balance and size distribution can be developed more fully and more effectively. As a result, much valuable information can be gained regarding the health effects and eventual control of air pollution. In addition, valuable information can be gained regarding environmental pathways and geochemical cycles of numerous elements.

REFERENCES

1. S.K. Friedlander, Env. Sci. & Tech., 7, 235, 1973.

2. W.C. McCroneand J.G. Delly, "The Particle Atlas," Vol. 1-4, Ann Arbor Sci. Publ., Ann Arbor, Michigan, 1973.

3. M. Bayard, in "Microprobe Analysis," C.A. Andersen, Ed., Wiley-Interscience, 1973, pp 323-348.

4. E.W. White, P.J. Denny, and S.M. Irving, in "The Electron Microprobe," T.D. McKinley, K.F.J. Heinrich, and D.B. Wittry, Ed., John Wiley and Sons, New York, N.Y., 1966, pp 791-804.

5. J.T. Armstrong and P.R. Buseck, Abstract, 167th Nat'l. Mtg., Amer. Chem. Soc., Div. of Anal. Chem., Los Angeles, Cal., Apr. 1-5, 1974, pap. 105.

6. J.T. Armstrong and P.R. Buseck, submitted to Anal. Chem., 1975.

7. M.S. Miller, S.K. Friedlander, and G.M. Hidy, in "Aerosols and Atmospheric Chemistry," G.M. Hidy, Ed., Academic Press, New York, N.Y., pp 301-312.

8. E.S. Gladney, W.H. Zoller, A.G. Jones, and G.E. Gordon, Env. Sci. & Tech., 8, 551,1974.

9. J.J. Wesolowski, W. John, and R. Kaifer, in "Trace Elements in the Environment," E.L. Kothny, Ed., Adv. Chem. Ser., 123, 1973, pp 1-16.

IMPROVEMENTS IN RAPID MULTI-ELEMENT ANALYSIS

USING A MATRIX OF CONCENTRATION DEPENDENT

CORRECTION COEFFICIENTS

Jack W. Leitner

Applied Research Laboratories

Sunland, California 91040

Following the work of Ziebold and Ogilvie[1] which showed that the correction of data could be accomplished by a correction coefficient based on representing the interaction of pairs of elements, Bence and Albee[2] showed that multi-element systems, particularly mineral specimens could be treated by a similar procedure. The appropriate equation for a multi-component system is:

$$\frac{C_j}{K_j} = \Sigma \, a_j^i \, C_i \tag{1}$$

where a_j^i gives the influence of element i on the C/K for element j in a binary system.

Bence and Albee also showed that geological specimens could be treated by considering the metallic elements to be present as oxides and their method has been widely used for such specimens because of the ease with which corrections can be calculated using an on-line computer of modest memory. Furthermore, the method seems well suited to geological specimens since the values of the coefficients tend to be greater than but near unity due to oxygen dilution and because cases of strong fluorescence enhancement are rare. When fluorescence is present a constant correction coefficient is less suitable and considerable error can result, particularly at low concentrations. Figure 1 illustrates the behavior of the iron nickel system. Marked curvature at low concentrations of the iron plot is the result of fluorescence by the nickel radiation.

An extension of the "a" value (or alpha factor) method was suggested by Bolon and Lifshin.[3] These authors proposed using two "a" values, one for low (less than 10 wt. %) and one for high concentrations. This would in effect extend the range of use of the correction coefficient approach to systems where fluorescence is common, such as metal alloys.

Correction coefficients (C/K) for binary systems based on a ZAF method have been published by Toyota Central Research and Development Laboratories.[4] While these may differ slightly from corresponding values computed from the ZAF corrections usually used in MAGIC,[5,6] they will be used here in order to clarify the problem of extending the correction coefficient method to a wider range of specimens. In the Toyota tables C/K values are presented as a function of the concentration of the element of interest in 10 wt. % intervals. We have fitted this data to a simple polynomial, whose coefficients are stored in the computer. The correction coefficients to be used in the subsequent application of equation 1 are then calculated from the first intensity ratio. The same computer performs hardware drive and data gathering tasks.

An Applied Research Laboratories' Scanning Electron Microprobe Quantometer (SEMQ) was used in this study. The electron microprobe was equipped with three scanning monochromators and two fixed channels. Fixed spectrometers are receptive to the radiation of only one element; in this case the elements were silicon and iron. The electron probe was run at 20 kV. Pure element standards were used. All elements present at concentrations greater than 0.1 wt. % and having an atomic number greater than 10 were analyzed. Five material types were examined: Inconel, Monel, stainless steel, low carbon steel and Stellite. For all analyses the SEMQ was operated under computer control.

The histogram shown in Figure 2 exhibits the data resulting from the analyses of 15 samples. About 100 elemental analyses were taken, 29 of which represented amounts present in excess of 10 wt. %. Of these 29 analyses the relative errors in accuracy were as follows:

Percent of Errors Within		
± 1%	± 2%	± 4%
60	74	93

The five alloy groups studied represent varied and complex matrices. The results so far are encouraging. More data will be taken in the future to further evaluate this correction coefficient method.

REFERENCES

1. T. O. Ziebold and R. E. Ogilvie, Analytical Chemistry, 36, No. 2 322-327 (1964).

2. A. E. Bence and A. L. Albee, Journal of Geology, 76, 382-403 (1968).

3. R. B. Bolon and E. Lifshin, Proceedings, Sixth National Conference on Electron Probe Analysis, 26A (1971).

4. Toyota Central R&D Labs, Inc. Diagrams and Tables for Quantitative Electron Probe Microanalysis. DAI Nippon Printing Co., Ltd., Tokyo, (1970)

5. A. L. Albee and L. Ray. Analytical Chemistry, 42, 1408-1414 (1970)

6. J. W. Colby, Advances in X-Ray Analysis, 11, 287-305 (1968).
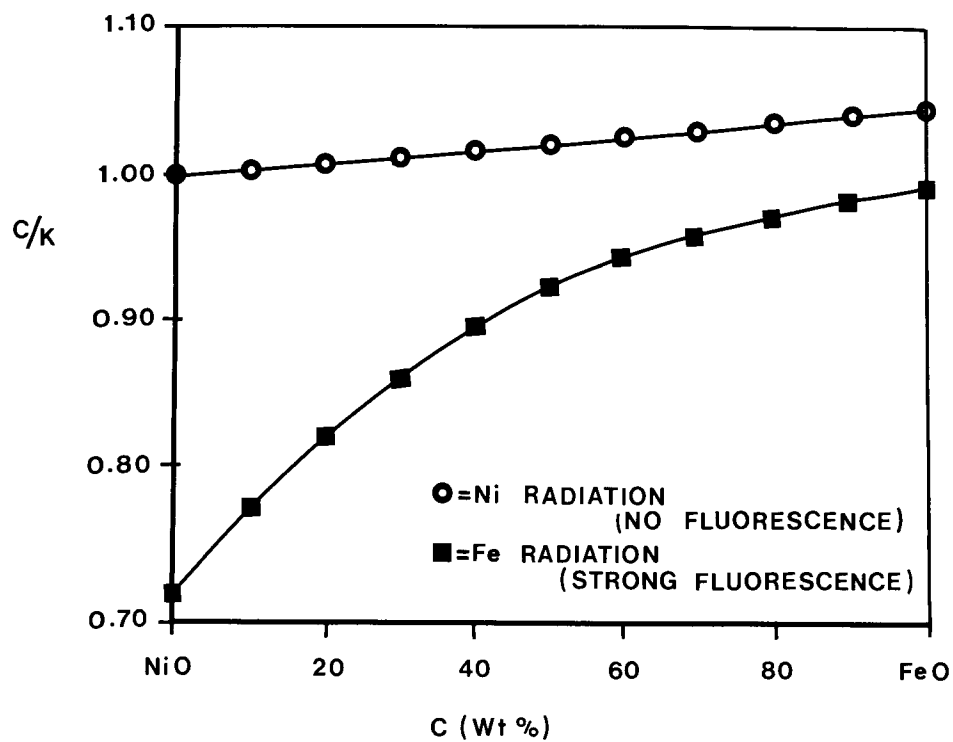
The Concentration/K Ratio Relationship for the FeO-NiO System

Figure 1
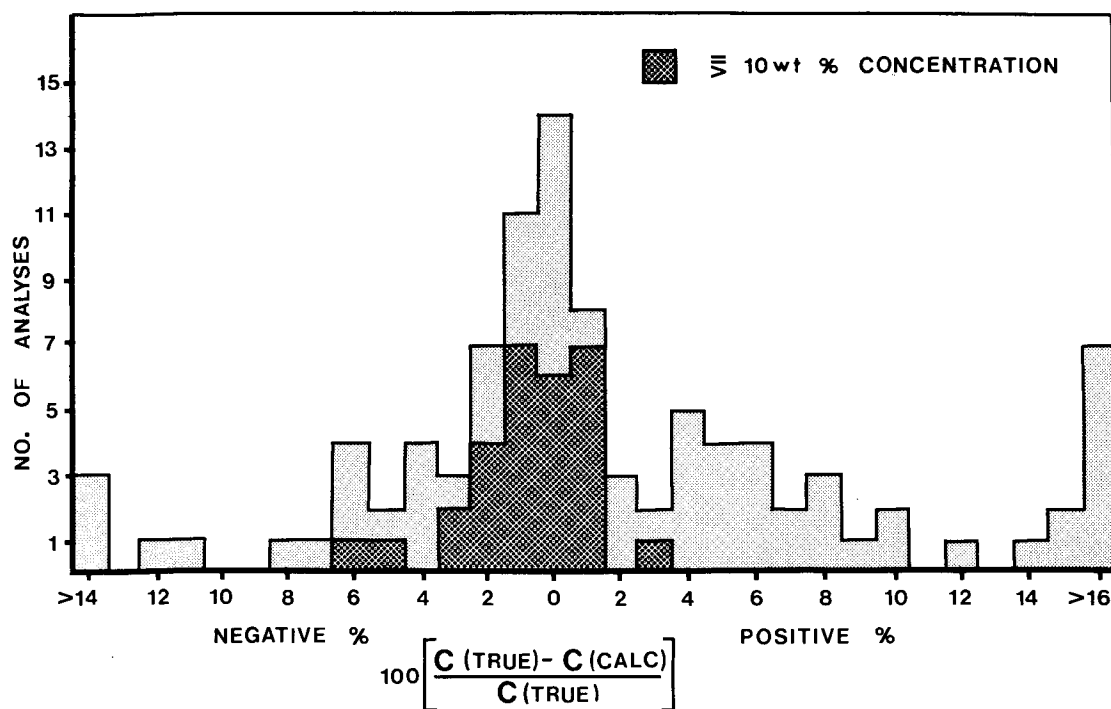
A Histogram of Relative Errors

Figure 2

ANALYSIS OF PHASE SEPARATION IN
Tl-As-Se GLASS

M. J. Mitchell*   S. Narasimhan** M. I. deRojas***
Stanford University

Scanning electron microscopy, microprobe, nondispersive x-ray
analysis, and x-ray diffraction have been used to look at glasses
in the Tl-As-Se system. Phase separation has been suggested for
this system by Markova[1] to account for the electrical properties
when selenium is replaced by sulfur. Narasimhan[2] has also suggested
that phase separation could account for the data from x-ray radial
distribution studies of the glass structure.

The phenomena of phase separation in glass has received considerable
interest in the last ten years. Much of this has been from workers
in the U.S.S.R. but also from Americans interested in glass ceramics
and the fundamental studies of the structure of glass. Since the
regions of heterogeneity are small, transmission electron microscopy
of both replicas and of thin samples or small angle x-ray diffraction
(SAXS) are often used in the study of phase separated materials.
Both of these techniques are time consuming. In addition the data
from SAXS is difficult to interpret. Strong evidence that phase
separation has taken place is usually necessary before these methods
are considered worthwhile.

Liquid-liquid phase separation is possible in organics and chalco-
genide materials as well as oxide systems which form glassy products.
The occurrence of these regions in a glass affect its properties and
may direct the crystallization processes toward the formation of micro-
crystalline products. No evidence of a crystalline phase was found
in the x-ray analysis of the samples used in this study. Samples of
Tl-As $_{.4}$ Se $_{.6}$ of 5, 10, 20, and 30 mol. per cent Tl were prepared in
quartz ampules evacuated to 3×10^{-6} torr, sealed, held for 24 hours
in rocking furnace and water quenched. If phase separated, a thallium
rich phase would be expected to have a higher electron density and

a higher conductivity as well. The electrical properties of a phase separated material would be more affected by the properties of the matrix rather than those of the included phase. Freshly fractured samples showed conchoidal features apparently not disturbed by any non-uniformity in structure. On freshly fractured samples, no evidence of a second phase was observed in the SEM. When samples that had been exposed to air for two to three days were observed in the SEM, the 5% Tl sample showed no new structure whereas the 20% and 30% samples exhibited an increase in surface texture and regions of increased contrast. The results on the 10% samples were inconclusive. On some of the fractured surfaces of the 30% sample the included phase covered more than half the surface but the regions were observed to be very thin irregular shaped platelets distributed throughout the bulk of the sample.

Energy dispersive x-ray and microprobe analysis did not clarify the problem of composition because of the platelet thickness.

As some thallium compounds are hygroscopic, a thallium rich phase may react with moisture in the atmosphere or may oxidize. Similar SEM results were obtained on samples soaked in water for 20 minutes as observed on the sample surfaces exposed to the atmosphere.

---

(1)   Markova, T.P. Electrical Conductivity of Thallium Sulfoselenide Arsenic Glasses in Relation to their Structureochemical characteristics in The Structure of Glass, Vol. 4 O.V. Mazurin, ed. Consultants Bureau, New York, 1965.

(2)   Narasimhan S., The Structural Properties of Amorphous Alloys of Thallium and Arsenic Triselenide, Thesis, Stanford University, 1974.

*   Now with I.B.M. at SP Division, Hopewell Junction, New York.

**   Now with I.B.M. at Research Division, Yorktown Heights, New York.

***   Now with Signetics Corp.

QUANTITATIVE ANALYSIS OF ZEOLITES USING AN ENERGY DISPERSIVE SYSTEM.

Ian M. Steele, J. V. Smith, J. J. Pluth and T. N. Solberg
University of Chicago
5734 S. Ellis Avenue
Chicago, Ill. 60637

Introduction

Zeolites are hydrated aluminosilicate minerals in which the Aℓ,Si and oxygen form an open framework with "cages" on the order of 2-12Å in diameter. These "cages" are occupied by large cations (Ca,Na,K,Ba,Sr) which provide charge balance. Natural zeolites contain loosely bound water molecules and can reversibly dehydrate (see Table 1 for compositional ranges). Synthetic zeolites find wide application in industry and are used for ion exchange (e.g. water softening), catalysis (e.g. petroleum cracking), and molecular sieving (e.g. gas purification). These important properties are affected by changes in the zeolite chemistry and by details of the structure and bonding. Thus accurate chemical analysis of zeolites is important. Because many natural and synthetic zeolites are fine-grained (down to 1μm or less), the electron-microprobe is the most feasible method of analysis. We have used an energy-dispersive system in conjunction with low electron beam currents; this reduces the effects of water and Na-K loss due to electron bombardment and vacuum conditions. We will briefly describe the method, various problems and results of this work. The energy dispersive procedures also apply to a wide range of Ca,Na,K,Aℓ,Si minerals and glasses which commonly occur naturally and as synthetics and are to some extent unstable under electron bombardment.

Analytical procedure

Our analytical system includes an ARL electron-probe in conjunction with a Nuclear-Semiconductor AUTOTRACE energy dispersive system. Probe sample current was set to a value of ~ 0.8 nanoamps on brass with a 15 kv potential and a ~ 30μm beam size. A spectrum was collected for two minutes + live time correction at a count rate of ~ 2000 cps in.

Detector resolution was about 165 ev FWHM @ 5.9 kev. Each spectrum was transferred to an on-line computer for processing, and another spectrum could be obtained during processing. Data reduction followed closely the methods described by Reed and Ware (1973) using computer programs supplied by N. Ware (ZAF matrix corrections). Standards were: Na,Ca,Aℓ,Si-synthetic glass close to average zeolite composition; K,Mg,Fe - natural analyzed minerals. Our system allows quantitative analysis for Na-Zn (the common naturally occurring elements), but zeolites often contain some Ba and Sr. See Table 1 for representative zeolites which we analyzed. Ba presents few problems because the L_α lines fall near Ti and Cr and can be visually recognized; most concentration levels are low enough except for rare Ba-zeolites so as not to affect matrix corrections. However, Sr peaks are masked by the intense SiK_α peak and there is no indication of their presence. Fortunately levels are usually very low (<0.5%); but some apparently incorrect analyses were later correlated with Sr content (see results). Repeat analyses on structurally and compositionally different zeolites showed no significant change in composition after five minutes of exposure to the beam. After one day in vacuum ($\sim 10^{-4}$ torr) some zeolites showed surface effects due probably to partial dehydration. Repeat analysis showed no significant change in chemistry. An advantage was that slight compositional differences were exaggerated by this surface effect and fine intergrowths of two zeolites could be recognized. Two major problems were encountered: 1) the detector acted as a "cold finger" and an oil film was deposited on the Be-window; this attenuated the low energy (<3 kev) signals because of X-ray absorption. This problem was eliminated by placing a small light bulb near the Be-window for heating. 2) Pulse-pile-up of low energy lines (Aℓ-Si) was severe enough to produce an abnormally high argon peak which is used for the background correction. Empirical adjustments were made to the argon peak based on initial Aℓ and Si peak heights and correct backgrounds were then obtained. The limit of detection using the above methods is about 0.15 oxide wt.%.

Results

About 70 natural zeolites comprising 8 different types were analyzed. Most oxide analyses summed to between 75 and 87% as expected from their hydrated nature and the known water content as a function of zeolite type. Two checks can be made on the correctness of a zeolite analysis. When the calculated formulae are considered, the number of Si + Aℓ atoms must be half that of the number of oxygens. Fig. 1 shows this plot (note that each zeolite was analyzed twice, thus about 140 points). Based on 72 framework oxygens, the overall Si + Aℓ average is 36.12 (one σ = 0.22). The slightly high value results in part from the Sr contribution to the Si peak (see later); on the whole this is quite acceptable accuracy. A second check is based on charge balance; the sum of 2Ca + Na + K should equal the number of Aℓ atoms. Figure 2 shows this plot, and several significant departures from a straight line occur. First, points where Aℓ is too great are rather numerous (points below line). These can be attributed to volatilization or substitution by cations not analyzed. The latter is favored because a check of 8 samples (16 points on Fig. 2) showed the presence of Ba or Sr (Sr was checked, using higher beam currents and wavelength dispersion). Indeed, those samples showing Sr also showed the greatest departures from Si + Aℓ = 36.0. More difficult to explain are analyses showing too great a sum for the Aℓ content (see Fig. 2). A sample check showed that all these analyses are from samples from Nova Scotia and are of two types - chabazites and gmelinites. A possible explanation is the occurrence of other molecules in the zeolite structure (e.g. $NaCO_3$, $CaCO_3$, $NaCl$, $NaOH$ etc.) No Cl or S could be detected using wavelength dispersion, but salt occlusion is known to occur in various feldspathoids and synthetic zeolite-salt complexes.

Summary

Zeolites and other unstable minerals can be analyzed accurately with an energy dispersive system. Chemical constraints (Aℓ + Si = $\frac{1}{2}$ Ox and Σ charges) show the accuracy of the data. Deviations from these constraints in zeolites are due to Sr substitution (suggesting a

qualitative method for analyzing for Sr in the presence of Si) and possibly to salt occlusion.

Reference

1) Reed, S. J. B. and N. Ware (1973) Quantitative Electron Microprobe Analysis Using a Lithium Drifted Silicon Detector. <u>X-ray</u> Spectrometry <u>2</u>, p.69-74.

Table 1. Types of zeolites analyzed.[1]

Zeolite	Ideal Formula[2]	Zeolite	Ideal Formula[2]
Natrolite	$Na_2[Al_2Si_3O_{10}] \cdot 2H_2O$	Heulandite	$(Ca,Na_2)[Al_2Si_7O_{18}] \cdot 6H_2O$
Scolecite	$Ca[Al_2Si_3O_{10}] \cdot 3H_2O$	Stilbite	$(Ca,Na_2,K_2)[Al_2Si_7O_{18}] \cdot 7H_2O$
Thomsonite	$NaCa_2[(Al,Si)_5O_{10}]_2 \cdot 6H_2O$	Chabazite	$Ca[Al_2Si_4O_{12}] \cdot 6H_2O$
Mordenite	$(Na_2,K_2,Ca)[Al_2Si_{10}O_{24}] \cdot 7H_2O$	Gmelinite	$(Na_2,Ca)[Al_2Si_4O_{12}] \cdot 6H_2O$
Offretite	$(K,Ca,Mg)[Al_5Si_{13}O_{36}] \cdot 15H_2O$	Phillipsite	$(\frac{1}{2}Ca,Na,K)_3[Al_3Si_5O_{16}] \cdot 6H_2O$
Faujasite	$(Na_2,Ca)_{1.75}[Al_{3.5}Si_{8.5}O_{24}] \cdot 16H_2O$		

[1]Other rare types analyzed include Ba-zeolites, Fe-Mg zeolites and Ba-Sr zeolites.

[2]Some replacement of Ca,Na,K by Ba and Sr commonly occurs.
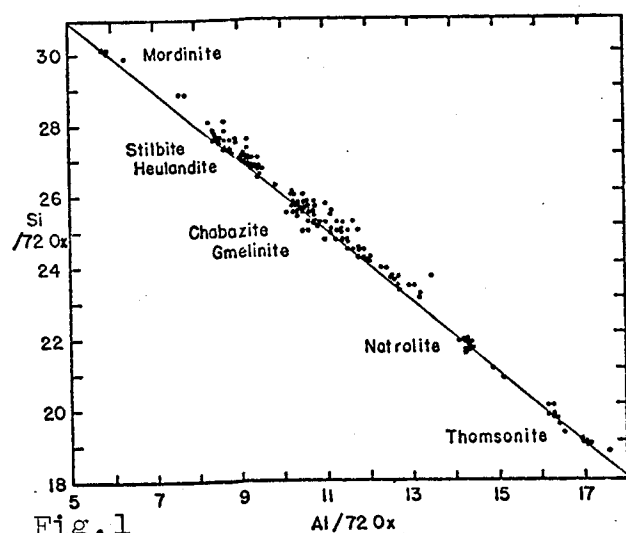
Fig.1
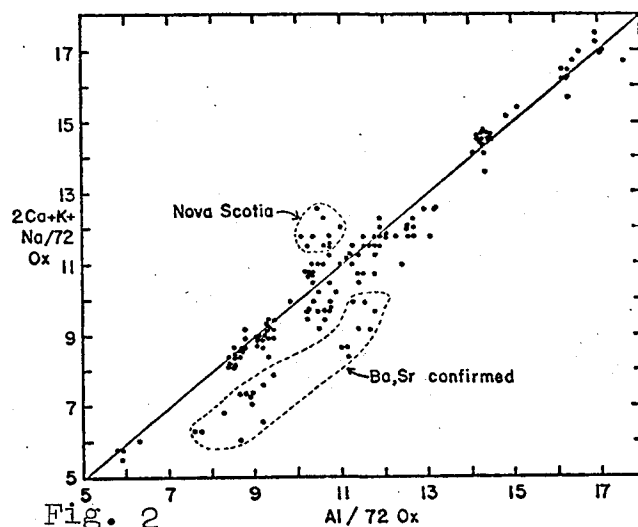
Fig. 2

Fig. 1. Al vs. Si based on 72(ox). Al + Si must equal 36.0 for zeolites (i.e. straight line). Deviations may in part be due to Sr influence on Si peak. Different zeolites have different Si/Al ratios as indicated.

Fig. 2. Plot for charge balance check. 2Ca + Na + K should equal Al (i.e. straight line). Points lying below line as indicated have Ba and/or Sr. Points labeled Nova Scotia may contain molecular species.

ELECTRON MICROPROBE-DERIVED SOFT X-RAY SPECTRAL PARAMETERS; THEIR USE IN CHEMICAL BONDING STUDIES OF IRON MINERALS

Charles G. Dodd[*] and Paul H. Ribbe

Virginia Polytechnic Institute and State University, Blacksburg, Va. 24061

Reports of measurements of soft X-ray spectra using spectrometers in electron microprobes have appeared with increasing frequency in recent years.[1-8] Computations of self-absorption spectra from emission data taken at two E_o values, one with appreciable self absorption and one with a minimal amount, have been reported for L spectra of nickel and other transition metals.[9-12] More recently both electron microprobe spectral data acquisition and self-absorption spectra computation have been automated.[8] We have measured L_{II-III} band emission spectra at 4.0 and 10.0 keV for a series of iron oxides, sulfides, and silicates representative of important rock-forming minerals. The following parameters were derived from the Fe spectra:

1. Fe L_{III} (or $L\alpha$) FWHM, full widths at half maximum intensity, often referred to as, "half widths",
2. Fe L_{II}/L_{III} (or $L\beta/L\alpha$) peak intensity ratios,
3. combinations of the first two, such as plots of L_{II}/L_{III} versus L_{III} FWHM,
4. energies (or wavelengths) of L_{III} and L_{II} absorption edges.

L_{III} peaks of transition metal compounds are particularly rich in spectral structure that can be assigned to transitions from specific molecular orbitals, and there are significant variations from compound to compound.[13-16] An additional feature of L_{III} transition metal emission peaks is the magnitude of emission broadening on the high-energy side of emission edges, that probably is the result of double-vacancy satellites following generation of L_{III} holes by non-radiative Coster-Kronig-type Auger transitions.[10] The extent of edge broadening was found to vary widely for different Fe compounds.

Experimentally measured emission and computed self-absorption Fe L_{II-III} band spectra for specular hematite, Fe_2O_3, are presented in Figure 1. Estimated L_{III} and L_{II} absorption edges are circled. Assignments of spectral

---

features to the respective transition-originating orbitals, based on calculations of Tossell et al.[14], are indicated above the spectra. The 10 keV emission spectrum was used for these assignments because it was considered to be corrected for self absorption.

The weak peak at the low energy end of the absorption spectrum in Figure 1 has been assigned to the excitation of a $1\underline{t}_{2g}\downarrow$ electron by a $K\beta_{1,3}$ photon into an empty $7\underline{t}_{1u}$ orbital.[14] This peak was reproduced clearly on our calculated self-absorption spectra for both Fe_2O_3 and Fe_3O_4, in agreement with the measured absorption spectrum of Bonnelle.[16] It lends confidence to the validity of computed self-absorption spectra, confidence in their capability to reproduce details of absorption spectra measured on thin foil samples in the transmission mode.

Figure 1 shows diagramatically the procedure used for deriving Fe L_{111} FWHM data. Values of this parameter were determined simply by taking the width of the peak at half maximum intensity, expressed in eV. Peak intensity ratios, Fe L_{II}/L_{III}, were determined by making simple measurements of peak heights on spectral plots such as Figure 1, above background, and computing ratios, as per the method of Albee and Chodos.[4] The recommended procedures of Smith and O'Nions[5,6], involving integration under each peak and the application of absorption corrections (as in electron probe microanalysis) were considered to be invalid. Satisfactory integrations of L_{III} and L_{II} peaks could not be performed for three reasons. First, it was difficult to allocate accurately the overlapping peak areas in the L_{II-III} interpeak region. Second, if L_{III} emission edge broadening resulted from Auger-induced double-vacancy LL→MM X-ray transitions it was not appropriate to include these as L_{III} areal contributions because they were initially dependent on an L_I or L_{II} hole. Third, L_{II}/L_{III} peak intensity ratios measured for Fe metal by the soft X-ray appearance potential method were closer to the classical value of 0.5 than were integrated peak ratios, and they varied sharply for different transition metals rather than remain constant at 0.5.[17]

With respect to absorption corrections, there are few spectral regions where absorption coefficients vary more abruptly than in the interpeak parts of L_{II-III} band spectra, which include both absorption edges. The pertinent absorption coefficient values are known only approximately at the peaks, and they vary sharply in the region of interest. Furthermore, the best form of absorption correction to be applied has not been determined.[6,18]

It would seem to be more appropriate to reverse the process and use the spectral data to determine absorption coefficients.

Measured L_{III} FWHM values for Fe metal were found to vary with E_o as shown in Figure 2, which includes data measured at low E_o values, below 2.5 keV, by Hanzely and Liefeld.[12] When E_o was 4 keV, or lower, we found self-absorption effects to be minimal, in agreement with Holliday.[19] Above about 6 to 8 keV the half width became essentially constant. We found 10 keV measurments of half width to be effectively free of emission edge broadening. The difference in half widths measured at 4 and 10 keV can be used as a measure of emission edge broadening.

Spectral parameters for the series of iron minerals studied are shown in Figure 3. Fe L_{II}/L_{III} intensity ratios are plotted against the corresponding L_{III} FWHM values. Half widths measured at 10 kev and at 4 keV are shown by filled circles and crosses, respectively. The 10 keV data are connected by lines to points measured at 4 keV. A similar kind of plot was used by Ribble[7] in his work on copper compounds.

When self absorption effects were eliminated by considering only 10 keV data, distinct areas of the plot were found to be identified with low-spin ferrous compounds, high-spin ferrous compounds, and high-spin ferric compounds, each area distinct and separated from the others. Iron metal was found adjacent to the low-spin ferrous compounds. Among the high-spin ferrous compounds the highest L_{II}/L_{III} ratios were associated with the best insulators, the iron silicates, fayalite and ferrosilite, while the more metallic high-spin ferrous compound, troilite (stoichiometric FeS), had the lowest peak intensity ratio. The still more metal-like iron disulfides such as pyrite and marcasite were characterized by yet lower ratios, lying next to Fe metal.

Absorption edges were determined, as shown in Figure 1, by estimating the mid-point inflection along the edge for each compound studied. Essentially linear relationships were found for ferrous and ferric compounds when formula oxidation states were plotted against L_{III}-edge and L_{II}-edge energies. An essentially linear relation also was found to hold between Fe L_{III} FWHM values and the presumed numbers of electrons in $3\underline{d} - 2\underline{t}_{2g}$ orbitals. It was found that the spectrometer spectral window correction could be estimated by comparing the half width found for pyrite with that measured by Li et al.[15] using electron photoemission spectrometry.

REFERENCES CITED

1. Koffman, D.M. and Moll, S.H., Adv. X-Ray Analysis 9, Mallett, Fay and Mueller, eds. (Plenum Press, New York, 1966) 323-328.

2. White, E.W. and Gibbs, G.V., Amer. Mineral. 52, 985-993 (1967); and 54, 931-936 (1969).

3. Dodd, C. G. and Glen, G.L., J. Appl. Phys. 39, 5377-5384 (1968).

4. Albee, A.L. and Chodos, A.A., Amer. Mineral 55, 491-501 (1970).

5. Smith, D.G.W. and O'Nions, R.K., J. Phys. D: Appl. Phys. 4, 147-159 (1971).

6. O'Nions, R. K. and Smith, D.G.W., Amer. Mineral. 56, 1452-1463 (1971).

7. Ribble, T.J., Phys. Stat. Sol. (a) 6, 473-478 (1971).

8. Romand, M., Solomon, J.S. and Baun, W.L., X-Ray Spectrometry 1, 147-150 (1972); and J. Phys. Chem. Solids 34, 1765-1771 (1973).

9. Liefeld, R.J., Bull. Amer. Phys. Soc. 10, 549 (1965).

10. Liefeld, R.J., in "Soft X-Ray Band Spectra", Fabian, D.J., ed. (Academic Press, New York, 1968) 133-149.

11. Chopra, D., Phys. Rev. A 1, 230-235 (1970).

12. Hanzely, S. and Liefeld, R.J., in "Electronic Density of States", Nat. Bur. Stand. (U.S.), Spec. Publ. 323, Bennett, L.H., ed. (U.S. Gov. Printing Off. Washington, 1971) 319-327.

13. Fischer, D.W., J. Appl. Phys. 41, 3561-3569 (1970); J. Phys. Chem. Solids 32, 2455-2480 (1971); and Phys. Rev. B, Solid State 5, 4219-4226 (1972).

14. Tossell, J.A., Vaughan, D.J. and Johnson, K.H., Nature Physical Science 244, 42-45 (1973); and Amer. Mineral. 59, 319-334 (1974).

15. Li, E.K., Johnson, K.H., Eastman, D.E. and Freeouf, J.L., Phys. Rev. Lett. 32, 470-472 (1974).

16. Bonnelle, C., Ann. Phys. 1, 439 (1966).

17. Park, R.L. and Houston, J.E., Phys. Rev. B, Solid State 6, 1073-1081 (1972).

18. Andersen, C.A. and Wittry, D.B., Brit. J. Appl. Phys. (J. Phys. D), Ser. 2, 1, 529-540 (1968).

19. Holliday, J.E., Adv. X-Ray Analysis 14, Barrett, Newkirk and Ruud, eds. (Plenum Press, New York, 1971) 243-249.
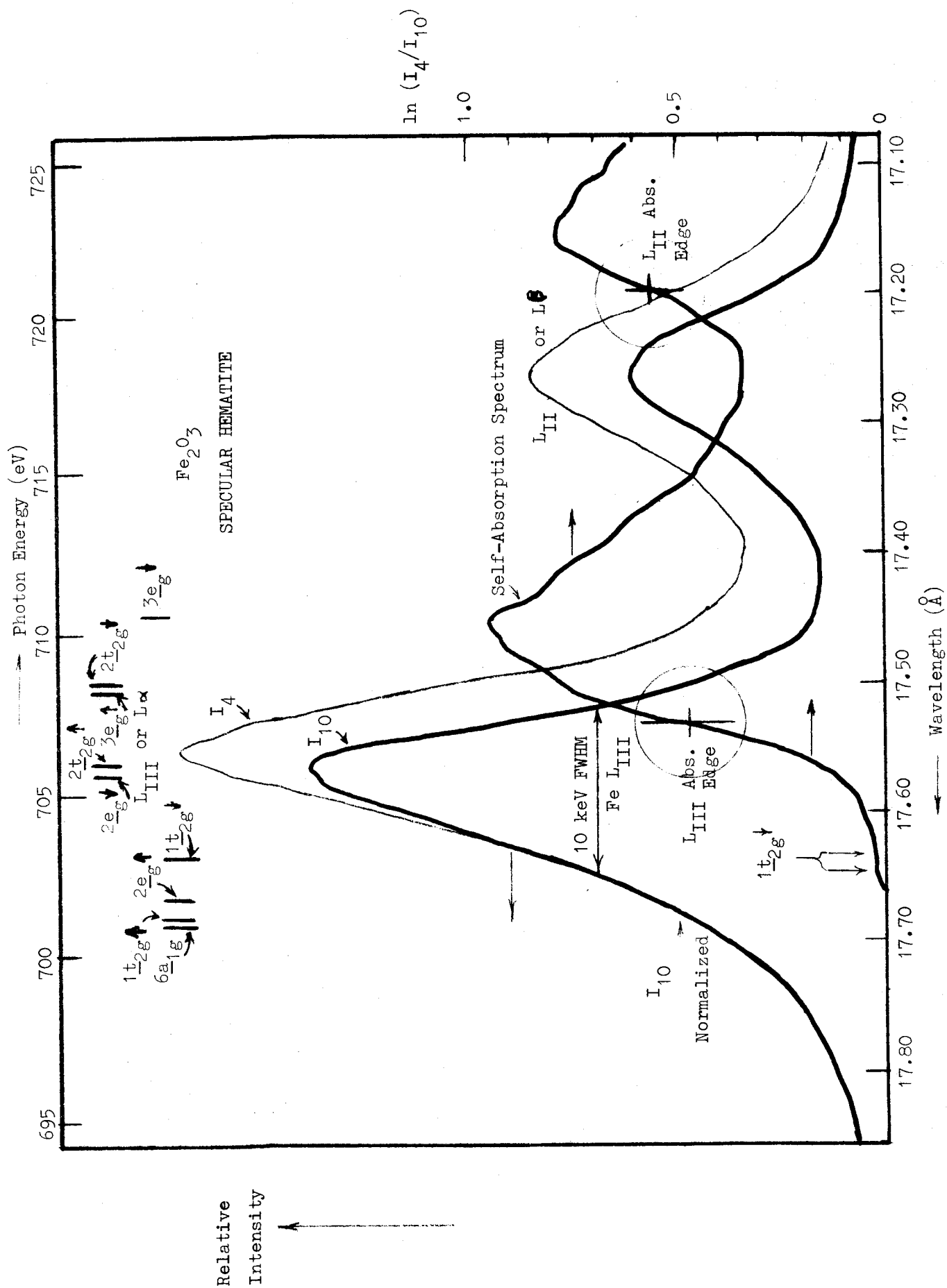
Figure 1. Fe L_{II-III} Band Emission Spectra for Hematite, 4.0 and 10.0 keV, and Computed Self-Absorption Spectrum. Absorption Edges and 10 keV FWHM shown.

Fe L$_{III}$

FWHM

(electron volts)

● This work

✗ Data from Hanzely and
   Liefeld (reference 12)

E$_o$, Electron Beam Accelerating Potential (keV)
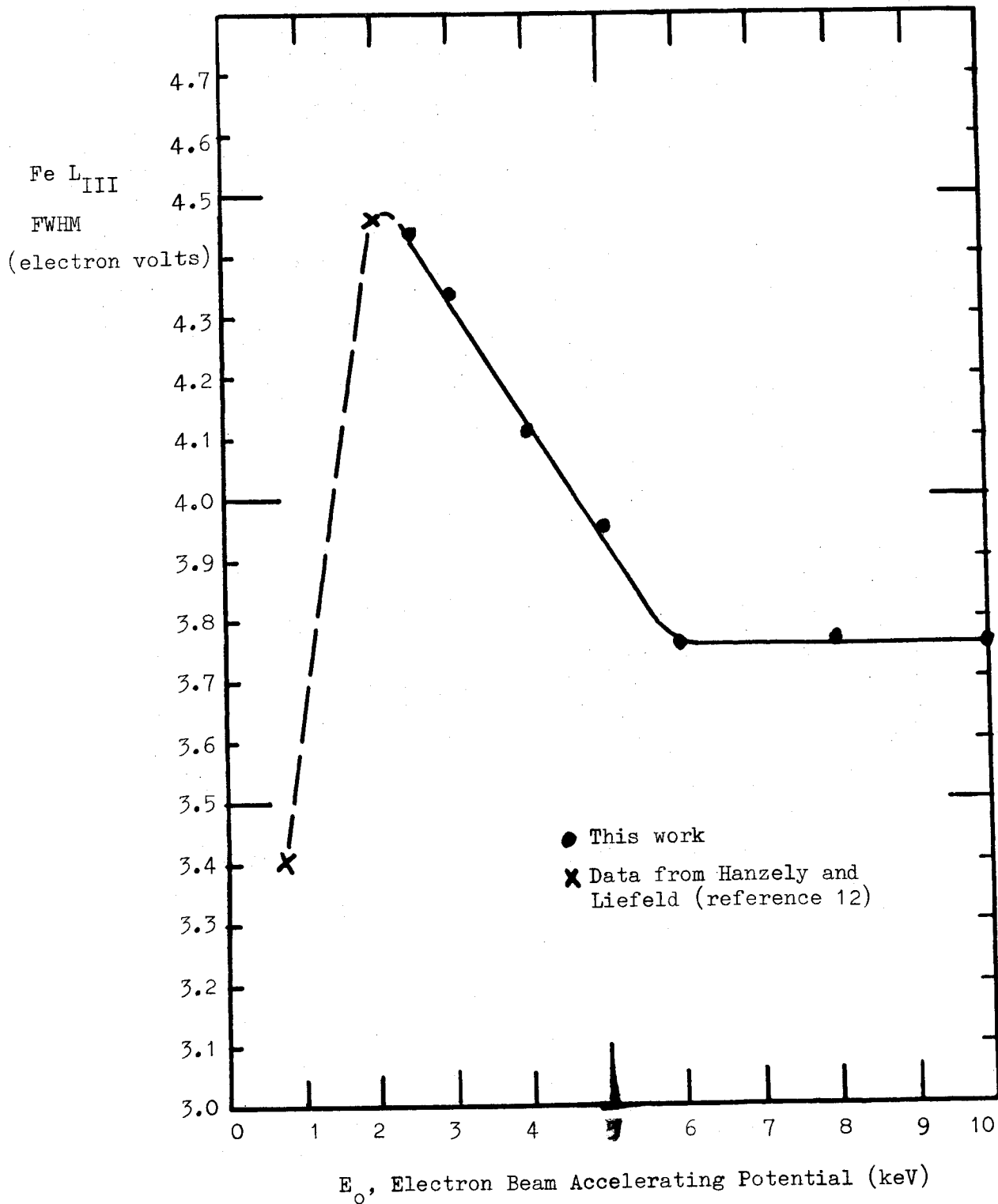
Figure 2. Variation of Fe L$_{III}$ half width with E$_o$
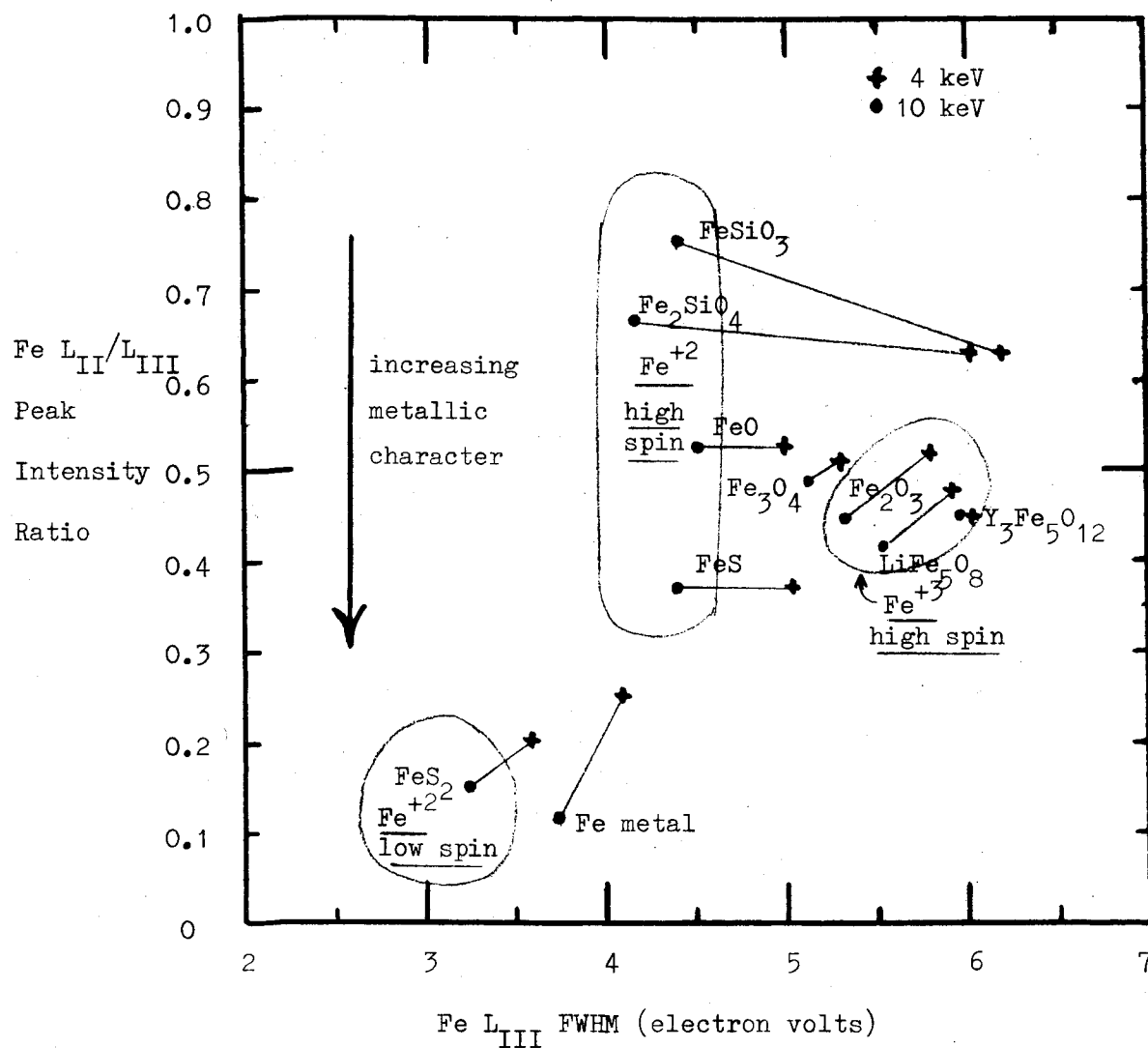
Figure 3. Plot of Fe L_{II}/L_{III} peak intensity ratios versus
Fe L_{III} FWHM half widths for iron minerals,
showing data measured at both 10 and 4 keV.
For the 10 keV data circled areas enclose ferrous
low spin and high spin, and ferric high spin
compounds. Four and ten keV data for each min-
eral are connected by a line.

QUANTITATIVE ANALYSIS AND PHASE IDENTIFICATION OF REFRACTORY INCLUSIONS IN GLASSES BY ENERGY DISPERSIVE X-RAY ANALYSIS

by

Robert F. Craig and John P. Sullivan, Jr.
Technical Assistance Laboratories
GTE Sylvania Incorporated
100 Endicott Street
Danvers, Mass. 01923

The aim of this work is to present a quick and effective method for the identification of refractory inclusions, including phase identification, and where possible, quantitative analysis of these phases. The technique offers a rapid means of evaluating the cause of stone formation (refractory inclusions) without the need of tedious petrographic analysis. (This is especially true if the inclusions are very small and difficult to remove from the host matrix.)

Initial phase identification is made using qualitative microbeam techniques [1,2] after a minimum of sample preparation. Quantitative analysis, using "pure" metal and "pure" crystalline compound standards, is conducted to determine phase composition and final identification. Spectra from both standards and unknown phase areas are collected using identical instrument parameters and are stored on cassette tape for later retrieval and data treatment. The k-ratio values for each element are determined using the multiple least squares fitting program (program ML) described by Shamber[3] and part of the software package of Tracor Northern's NS880 x-ray analysis system. Pure standards for such elements as sodium, potassium, and calcium are generated mathematically and graphically by reversing the matrix correction program to generate k-ratios for the compounds used as standards, adding to these spectra sufficient peak area to yield the computed k-ratios for the compounds used as standards. This is particularly useful when fluoride salts are used for standards. Correction for matrix effects are made using the NS880-system correction program. For comparative purposes two different matrix correction programs are used; first, a modification of the Magic IV program and second, a program fashioned after that of Bence and Albee[4], both of these written for the NS880 system by Tracor Northern. The application of this technique has been centered about the identification of inclusions which may crystallize in conventional soda-lime glass. Samples are prepared by conventional means, encapsulation, polishing and carbon coating; standards used are prepared in like manner. The type and use of standards in energy dispersive analysis has come under much discussion in the recent past, (see for example Russ[5]) and is destined to continue as long as new and more elaborate equipment is made available. It is our contention that meaningful quantitative data cannot be generated without the use of standards at the time the data for correction is collected. This procedure eliminates variations in energy calibration and other instrumental variables as well as other factors which cause havoc with most microbeam

analysts (phase of the moon, temperature at Bankside, or time of high
tide). Experience has shown us significant variation, in k-ratios
and the chi-squared values for goodness of fit, occurs when as little
as a one or two channel difference exists between,unknown and standard,
showing the value of seal time standards. The use and application
of this ML-routine has been dealt with previously[6] and shown to be
very effective and efficient means for data reduction, yielding data
easily transferred to a matrix correction program for final data
manipulation.

The data presented in this work is primarily concerned with refractory
material which can be confined within the SiO_2-Al_2O_3-ZrO_2 ternary,
neglecting for the moment the low concentration elements of the glass.
The source of these inclusions are either the interaction of the glass
melt and the melt tank construction material, or residual undissolved
starting materials. The identification of which is of critical
importance in controlling the operating parameters of a given glass
campaign. The simple ternary system is, however, complicated by a
potantial formation of sodium-zircono-silicates[7], which to this point
have not been found. Results are given which show the complex nature
of these multiphase inclusions which crystallize in the molten glass,
along with the quantitative analysis results of these various phases.
The quantitative data obtained by both NS880 correction programs
are also compared.

REFERENCES

1. Partridge, G., Phillips, S. V., Riley, J. N., Trans, and J. Br.
   Ceram. Soc., 72, 233-267 (1973).

2. Korda, E. J., Pruden, L. H., Williams, J. P., Ceramic Bulletin, 52,
   279-284 (1973).

3. Shamber, F. H., Proceedings of the Eighth Annual Conference of the
   Microbeam Analysis Society, Paper No. 85A (1973).

4. Bence, A. E., Albee, A. L., Journal of Geology, JGEOA, 76, 382 (1968).

5. Russ, J. C., Proceedings of the Ninth Annual Conference of the
   Microbeam Analysis Society, Paper No. 22 (1974).

6. Corlett, M. I., McDonald, M., Proceedings of the Ninth Annual
   Conference of the Microbeam Analysis Society, Paper No. 23 (1974).

7. Toropov, N. A. et al, Phase Diagrams of Silicate Systems:
   Handbook, Third Issue: Ternary Systems, Leningrad (1972)
   Translated by Kanner Associates, NTIS No. AD787517, pp. 405-409.

APPLICATIONS OF ELECTRON PROBE MICROANALYSIS IN PHYSIOLOGY

C. Lechene

Biotechnology Resource in Electron Probe microanalysis
Laboratory of Human Reproduction and Reproductive Biology and
Department of Physiology, Harvard Medical School
Boston, Massachusetts

Electron probe microanalysis has become an extremely powerful analytical tool for the biologist and continues to develop rapidly. It allows for the measurement of many more elements in a much smaller volume than any other analytical method. The biologist now has a tool which could answer elementary and fundamental questions such as: what elements are in the cells, between the cells, and in the fluids bathing the cells? Where are they located and in what amount? Are all the cells in a given tissue of identical composition? Are the different parts of the cells of identical composition? Is one apparently homogeneous compartment of a cell of uniform composition or are certain elements or ions pooled?

Despite its potential power, the use of the electron probe microanalyzer was slow to be introduced in the biological sciences. Although it aroused wide interest in the biological community through the pioneering work of Galles, Tousimis, Ingram and Coleman, for a number of reasons it was not until recently seriously considered as a general method of investigation by the biologists. The apparent complexity of the instrument, its high price, and perhaps most disconcerting, problems of sample preparations slow down the use by physiologists of this uniquely powerful method of analysis. Sample preparation methods must be oriented to the X-ray spectrometric capability of the electron probe. Hevesy had contemplated an X-ray spectrometric method to analyze the elemental composition of a very small volume of material. When Castaing later developed the instrument it took the form of an X-ray spectrometer. The fortunate development of scanning microscopy emphasized the imaging capability of the electron probe and directed it toward electron microscopists. High-image resolution is one of the principal concerns in this area of work, but it had for results to minimize the essential fact that the electron probe is an X-ray spectrometer with the characteristic X-ray lines being emmitted through the excitation of the sample by the electron beam. As in any method of spectrometry, in order to do quantitative analysis it is necessary that the conditions of excitation of the samples be invarient (the electron beam diameter and the electron beam current). The sample is analyzed by being moved under an immobile electron beam and the area to be analyzed is chosen either through light microscope observation, in which case the light microscope is an important component of the instrument, or in some cases direct transmission electron microscopy is used. Under these circumstances the X-ray spectrometry through electron probe excitation can easily provide quantitative analysis by comparing the intensity of signals emitted from unknown samples to those of standards prepared under the same conditions.

Compared to other spectrometric methods, electron probe microanalysis offers invaluable advantages:

1. The sample is not destroyed during the analysis, which means that any element of the periodic table heavier than boron can be analyzed within the same sample.

2. There is no ambiguity, using wavelength dispersive spectrometry, in qualitative analysis since the characteristic X-ray lines are well separated. In quantitative analysis, there is no quenching to affect the signal intensity. Absorbtion and fluorescence are seldom a practical problem for the biologist.

3. The quantity of sample required for analysis is smaller than that which can be used in any other applied analytical method.

4. Femtoliter volumes can be analyzed using the electron probe. Picoliter volumes are routinely manipulated and their elemental content quantitated. For the physiologist the ability to analyze one cubic micron opens entirely new horizons. Determination of all of the elements in the same picoliter sample has never before been possible. Indeed, except for the development of methods to analyze in several nanoliters of samples, Na+ and K+ or with difficulty Ca++ and Mg++, nothing else approaches this capability. Techniques described as ultramicro analytical methods, besides requiring samples of the microliter size, analyze at most only one element. With X-ray spectrometry through electron beam excitation, nearly the whole periodic table can be analyzed in samples one millionth times smaller.

Table I lists the kind of samples which are presently analyzed and the methods which could be used by physiologists for electron probe microanalysis. In general, the methods must avoid any redistribution or translocation of the elements in the volume to be analyzed (1).

The manipulation of picoliter samples (between 10 and 100 pL) is easy, the calibration procedure very accurate, and excellent quantitation and correlation can be obtained for sample sizes impossible to analyze until this method was developed for routine analysis (2,3). Applications of these methods have now spread to many fields of physiology and now permit analyses of the entire elemental content of ultramicrosamples of fluid obtained by micropuncture from the surroundings of living cells.

It should be remembered that X-ray spectrometry does not give the chemical state of the element. For example, sulfur and not sulfate, phosphorus and not phosphate, are quantitated. In order to differentiate between the ionic state and the undissociated form, it is possible to ultramicroprecipitate in drops the ionic form. By measuring before and after precipitation, it is possible to evaluate the total element, both its dissociated and undissociated form. Application of a quantitative precipitation method and a freeze substitution technique to wash the supernatant could permit use of electron probe microanalysis for the study of bio-organic compounds (4).

Samples from 10 pL down to 1 pL could be prepared either by micromelting or by microdissection (5,1).

The analysis of isolated cells has been made by spraying the cells in a nitrogen jet onto a polygraphite carbon support. This simple method allows preparation of a great number of cells, well isolated on their support (6). Even with air drying, by using this method there is practically no ionic redistribution. By using agents which reversibly modify the cell membrane permeability, it is possible to impose a known intracellular content to the isolated cells, making it possible to obtain standard cells for calibration with the electron probe (7).

Tissue analysis offers the ultimate challenge for the full application of electron probe microanalysis. Except for the special case of precipitate analysis, what is to be analyzed are diffusible ions.

In general, physiologists have questions in various situations which correspond to very different levels of resolutions for electron probe microanalysis. In order to recognize the composition between different areas of a tissue the analytical scale is of several hundred microns if not more. In order to analyze and compare the composition of the cell and of the fluids bathing these cells, the analysis has to be made on a scale of 1 to 20 microns; for example, luminal fluid in a canalicule, interstitial or capillary fluid surrounding the cells. The same resolution applies for the study of the distribution of whole cell composition in a given tissue. In order to analyze and compare cells and intercellular fluid, or intracellular organelle components, the resolution needs to be 1 micron or less. It must be emphasized that down to 1 micron resolution, the technological capability is present and the number of physiological questions to be studied are limitless. Thus, although it remains difficult to evaluate the subcellular components of major interest to electronmicroscopists, the available methods offer nearly limitless possibilities to physiologists at all other levels of study.

The major and only problem for use of electron probe microanalysis at the present time is the necessity to avoid ionic translocation in preparation of the samples. In some very special situations, low resolution, homogeneous tissue, freeze drying or freeze drying embedding could be used. But, these methods cannot be used in tissue in which large extra cellular spaces without matrix have a composition very different than that of the cells (8). A general solution seems to be provided by keeping the samples frozen hydrated during the analysis (8).

Table II enumerates some of the applications of X-ray spectrometry through electron probe excitation in physiology. Application of electron probe microanalysis spreads in nearly all fields of physiology where X-ray spectrometry brings original information with absolute or relative quantitation of up to seven elements within the same sample. (Automation of the electron probe and interactive software for data manipulation increases the efficiency of the analysis (9,10)). It is noteworthy that these information, important for a sound understanding of the living organ or of the living cells, would not have been obtainable

by another method. We believe that electron probe microanalysis will have in physiology the same impact that electron microscopy is having in anatomy. If seeing is believing, measuring is understanding and progress. Both are possible by electron probe microanalysis in samples which are several orders of magnitude smaller than those usually manipulated by physiologists.

---

(1)   C. Lechene and R. Warner. Ultramicroanalysis with the electron probe. Annual review of Biophysics and Bioengineering, 5, 1976. (To be Published)

(2)   C. Lechene. The use of the electron microprobe to analyze very minute amounts of liquid samples. Proc. Fifth Nat. Conf. on Electron Probe Analysis (New York) 32A - 32C, 1970.

(3)   C. Lechene. Electron probe microanalysis of picoliter liquid samples. In Microprobe analysis as applied to cells and tissues, edited by Theodore Hall, Patrick Echlin, and Rubolf Kaufmann, pp. 351 -368. Academic Press, London, 1974.

(4)   J. V. Bonventre and C. Lechene. A method for electron probe microanalysis of organic components in picoliter samples. Proceedings of the Microbeam Analysis Society Ninth Annual Conference (Ottawa) 8A - 8D, 1974.

(5)   T. H. Strunk, R. Warner and C. Lechene. Methods for electron probe analysis of tubular fluid and cells deep within the kidney. Abstract, FASEB 59th Annual Meeting, Fed. Proc. 34: 393, 1975.

(6)   C. Lechene, C. Bronner and R. K. Kirk. Electron probe microanalysis of isolated cells: red blood cells. Proceedings of the Microbeam Analysis Society Ninth Annual Conference (Ottawa) 9A - 9E, 1974.

(7)   R. G. Kirk, M. A. Crenshaw and D.C. Tosteson. Potassium Content of single human red cells measured with an electron probe. J. Cell Physiol., 84: 29-36.

(8)   C. Lechene, T. H. Strunk R. Warner and C. Conty. Perspectives in electron probe microanalysis of biological samples kept frozen. These proceedings.

(9)   T. Moher, C. M. Aden, R. Beeuwkes, A. Sanderson and C. Lechene. Automation of an electron probe for biological analyses. Proceedings of the Microbeam Analysis Society Ninth Annual Conference (Ottawa), 34A - 34D, 1974.

(10)   T. Moher, M. Aloisio and C. Lechene. A computer program for the electron probe quantitative analysis of biological samples. Biosciences Communications. (To be Published)

(11) C. Le Grimellec, N. Roinel and F. Morel. Simultaneous Mg, Ca, P, K, Na, and Cl Analysis in Rat Tubular Fluid. Pflugers Arch. 340: 181 - 196, 1973.

(12) C. Lechene, E. Smith and K. Blouch. Site of sulfate reabsorption along the rat nephron. Abstract of the American Society of Nephrology 7th Annual Meeting, Kidney Internat. 6: 64A, 1976.

(13) C. Lechene, E. Abraham and R. Warner. Effect of sulfate loading on ionic distribution along the rat nephron. Abstract, Clinical Investigation Meeting. Clin. Res. 23: 432A, 1975.

(14) N. Roinel and H. Passow. A study of the applicability of the electron microprobe to a quantitative analysis of K and Na in single human red blood cells. FEBS Letters. Vol 41, No. 1: 81 - 84. April 1974.

(15) C. Lechene, C. Bronner and R. G. Kirk. Electron probe microanalysis of chemical element content of single human red cells. J. Cell Comp. Physiol. (submitted)

(16) R. M. Borland, J. D. Biggers and C. Lechene. Electron probe microanalysis of picoliter samples of rabbit and mouse blastocoelic fluids. Kinetic aspects of blastocyst solute accumulation. (In Press) Proc. Nat. Acad. Sci.)

(17) L. Roblero, J. D. Biggers and C. Lechene. Spatial-temporal changes in the oviductal environment during the initial stages of pregnancy. J. Reprod. and Fert. (submitted)

(18) R. M. Borland, J. D. Biggers and C. Lechene. Electron probe microanalysis of uterine oestrus fluid and post-coital uterine fluid in the mouse. Biol. Reprod. (submitted)

(19) R. R. Warner and J. R. Coleman. Electron probe analysis of calcium transport by small intestine. J. Cell. Biol. 64: 54 - 74, 1975.

(20) G. R. Merriam, F. Naftolin and C. Lechene. An electron probe study of elemental distribution in the rat pituitary. These proceedings.

(21) Z. S. Agus, L. B. Gardner, L. H. Beck and M. Goldberg. Effects of parathyroid hormone on renal tubular reabsorption of calcium, sodium, and phosphate. American Journal of Physiology, Vol. 24, No. 5: 1143 - 1148. May 1973.

(22) F. G. Knox and C. Lechene. Distal site of action of parathyroid hormone on phosphate reabsorption in the thyroparathyroidectomized dog. American Journal of Physiology. (In Press)

(23) F. Knox and C. Lechene. Segmental analysis of renal phosphate transport in the presence and absence of carbonic anhydrase inhibitor. International Workship on Phosphate, Paris, June 5-6, 1975. (To be Published)

Table 1

VARIETIES OF SAMPLES AND METHODS OF PREPARATION

Picoliter Samples	Isolated Cells	Tissues
Liquid Droplet	Spray	a) Precipitates:
Organic Compound: Ultramicroprecipitation	Smear By Quick Centrifugation	EM Preparation – Ultrathin Section
Micromelting		Freeze Dryed
Microdissection of Ice		Freeze Dryed Embedded
		b) Diffusible Ions
		1. Special Cases: Low Resolution, Homogeneous Tissue: Freeze Dryed
		2. General: Frozen Hydrated

Table II

APPLICATIONS OF ELECTRON PROBE MICROANALYSIS IN PHYSIOLOGY

<u>Cell and Renal Physiology</u>

Counter Current Mechanism
Ionic Movements Along the Nephron[11]
Sulfate Transport by the Nephron[12]
Perturbation Method for the Study of Ionic
    Equilibrium[13]
Sodium Transport in Toad Bladder

<u>Reproductive Biology</u>

Blastocoelic Fluid[16]
Microenvironment of the Embryo[17]
Uterine Fluid[18]
Epididymal Plasma Composition

<u>Sensory Physiology</u>

Ear: Composition of Labyrinthine Fluid
Eye: Study on Photoreceptors

<u>Digestive Physiology</u>

Intestinal Transport of Ca[19]
Sulfur Content of the Intestinal Glycocalyx
Composition of Isolated Gastric Cells
Comparison Between the Bile Composition in
    Gallbladder and Bile Duct of the Hagfish

<u>Neuroendrocrinology</u>

Study on the Pituitary[20]

<u>Endocrinology</u>

Renal Effect and Mechanism of Action of Parathormone
    21,22,23
Renal Effect and Mechanism of Action of Calcitonin

The numbers refer to the bibliography.

QUANTITATIVE ELECTRON PROBE ANALYSIS OF

ULTRA-THIN BIOLOGICAL SECTIONS

H. Shuman and A. P. Somlyo

Pennsylvania Muscle Institute
Presbyterian-University of Pennsylvania Medical Center
Departments of Physiology and Pathology
University of Pennsylvania

X-ray microanalysis of thin biological sections has developed to the point where elemental assays of organelles are practical[1] and analyses of 500 Å areas are possible.[2] Of the two principal problems: quantitation and reliable specimen preparation, the first has proved most tractable.[3] The method of quantitation presented in this paper has been applied to dried cryosectioned and to resin embedded specimens. The application will be discussed elsewhere (EMSA).

One of the biological problems we are interested in at present is the concentration of calcium at a spatial resolution equal to or better than the size of mitochondria, in approximately 1000 Å thick sections of smooth and striated muscle. The Ca concentration in mitochondria isolated from smooth muscle in the presence of EDTA is approximately 40 mM/Kg dry weight.[4] Assuming that this is also the value _in situ_, the Ca mass in a 1000 Å diameter spot over a 1000 Å thick section, would be about 1.6×10^{-18} gr.

Our microprobe installation consists of a Philips 301 TEM with scanning pole pieces, a Kevex 5100 spectrometer with a 30 mm^2, 162 eV detector and a Tracor Northern NS 880 computer system. For quantitation, we are using a program based on the multiple least squares regression routine (ML) due to F. H. Schamber[5,6], combined with the thin film analysis of Hall.[3] With this method, peaks separated by 30 eV and with FWHM of 162 eV can be deconvoluted. For example the K K_β -Ca K α peaks can be resolved. The fitting routine also produces two types of error estimates: the statistical uncertainty ($\pm \sigma$) for each peak intensity and a "chi-squared" value which gives a measure of systematic errors in the analysis. The method requires collection and storage on tape of pure element spectra, with good statistics, for every experimental condition and for all elements encountered in the unknown. The analyzing system must also be in a previously defined standard condition before each unknown spectrum is taken. The following primary standards have been used: powdered salt crystals embedded in plastic films (i.e. LiCl in formvar), thin evaporated films (Cu, or OsO_4 sublimed on carbon foils), and high concentration solutions of standards in epoxy (500 mM/kg OsO_4 in Spurr's resin).

The unknown spectra are assumed to have the form

$$S_x(E) = B_x(E) + \sum_i k_{xi} P_i(E)$$

where $S_x(E)$ is the total counts per energy channel E in the unknown, $B_x(E)$ is the continuum counts per channel, $P_i(E)$ is the integrated peak count for pure element i, and k_{xi} is the fraction of the pure element peak in the unknown. The pure element spectra are assumed to have the form

$$S_i(E) = B_i(E) + P_i(E)$$

The ML routine ignores the slowly varying, as a function of E, $B_x(E)$ and $B_i(E)$ and determines the values of $k_{xi} \pm \sigma_i$. If it is assumed that $k_{xi} B_i(E)$ is a negligible fraction of $B_x(E)$ as is true for all our pure standards except OsO_4, then subtracting

$$S_x(E) - \sum_i k_{xi} S_i(E) \cong B_x(E)$$

gives the unknown continuum for all energy channels. The continuum is integrated over the region under the peaks, $B = \int B_x(E) dE$, and the concentration is then proportional to: $C_{xi} \alpha\, k_{xi}/B$ The quantitation is completed by determining the constant of proportionality for each element. As in other quantitation schemes this involves performing the same analysis on secondary standards with known composition and similar to the biological unknown. Since it is difficult to produce good secondary standards of all the relevant elements and we have produced standards of K^+ ions dissolved in resin[7], we used the elemental ratio method[8] to derive the proportionality constants of all the light elements from the potassium constant. As other standards are being produced this method will be tested for accuracy.

The minimum detectable levels of mass and concentration for this microprobe were determined using the ML routine applied to the K^+ standards. Standards were made for 25 mM/kg to 600 mM/kg of KSCN carried with crown-6 (duPont) in Spurr's resin.[7] Portions of the castings were dissolved and spectrophometrically analyzed for K^+. Sections of various thickness (1000-4000 Å) taken from the blocks were mounted on bare nylon grids and analyzed in the probe. The standards contain Cl (a component of the resin) and S as well as K. The background was integrated from 1.85 kev to 4.2 kev after the characteristic peaks of these three elements were stripped from the spectra. The X-ray data were taken with a 40 µ spot to minimize the contribution of contamination to the continuum. A graph of the measured concentrations vs peak fraction to background ratio (k_K/B) is shown in Figure 1. The inverse of the slope of the line through the points is the required proportionality constant which we call W_x. The bars shown are $\pm \sigma_i/B$ values from the ML routine. For a real time count of 100 sec at 1000 CPS on a 2000 Å thick section $W_K \sigma/B = 7$ mM/kg. If the minimum concentration is assumed to be twice the standard deviation the MDC = 14 mM/kg K^+. Longer time, higher count rates and thicker specimens will lower the MDC. For

instance a 300 sec count should give an MDC = 8.2 mM/kg, while the experiment gave $W_k\sigma/B$ = 2.3 mM/kg or MDC = 4.6 mM/kg. The minimum detectable mass was estimated from similar data. With the first condensor lens current of the Philips 301 at 1.4 and the C_2 aperture 300 μ, the minimum probe size is approximately 1000 Å. For a 1000 Å section the minimum volume is then $\sim 10^{-15}$ cm^3. For an analysis of a 600 mM/kg K$^+$ section with maximum emission current $W_k\sigma/B = \pm 13.3$ mM/kg, and the MDM = 1.0 x 10^{-18} gr. A 1000 Å spot would produce a thick contamination layer in 100 sec, so the spectra were taken with the second condensor defocused and the actual spot 6μ in diameter. The probe current is unaffected and the MDM unchanged. With first condensor current equal to 2.15 A the minimum spot is 600 Å, $W_k\sigma/B$ = 32 mM/kg K$^+$ and the MDM = 0.9 x 10^{-18} gr.

To derive the W_x values from W_k through the elemental ratio method, the concentration in secondary standards is calculated by the ML routine for element X:

$$C_x = W_x k_x / B_x \text{ and for } K^+, \quad C_K = W_K k_K / B_K$$

where as before k_x is the fraction of pure element peak in the standard spectra, $k_x = P_x / P_{ox}$. From the elemental ratio

$$\frac{C_x}{C_K} = \frac{P_x / B_x \, G_x}{P_k / B_k \, G_k}$$

where $G_x = Q_x \omega_x T_x$,

Q_x is the ionization cross section for element x, ω_x is the fluorescent yield, and T_x is the detector efficiency at the energy corresponding to the emitted x-ray. These three equations reduce to

$$W_x = W_K \frac{P_{ox} / G_x}{P_{ok} / G_k}$$

W_k has been determined, and G_x can be calculated. P_{ox} is the number of counts in the pure element peak, including both α and β lines.

A sample biological spectrum along with the same spectrum with peaks stripped is shown in Figure 2.

Quantitation and detection of MDL of elements using small (500-1000 Å diameter) probes has been limited by contamination. Experimental results of continuum count rate as a function of time for a range of spot sizes and substrates will be presented to indicate the effect of contamination. Preliminary experiments with a liquid N$_2$ cooled specimen stage show that contamination does not appear over cooled specimens under the experimental conditions described. A low background cold stage, therefore, appears

to be essential for limiting both mass loss under the electron beam [9] and mass gain due to contamination.

Acknowledgement

References

1. A. P. Somlyo, A. V. Somlyo, C. E. Devine, P. D. Peters and T. A. Hall, 1974, J. Cell Biol. 61: 723.

2. P. Gambetti, S. E. Erulkar, A. P. Somlyo and N. K. Gonatas, 1975, J. Cell Biol. 64: 322.

3. T. A. Hall and P. R. Werba, 1971, Proc. 25th Anniversary Meeting of EMAG, Inst. Physics.

4. J. Vallieres, A. Scarpa and A. P. Somlyo, in Prep.

5. F. H. Schamber, 1973, Proc. 8th Nat. Conf. on Electron Probe Analysis, 85.

6. D. R. Beaman and L. F. Solosky, 1974, 9th Annual Conf. MAS, 26.

7. A. R. Spurr, 1974, Microprobe Analysis as Applied to Cells and Tissues, (T. Hall et al. ed.), Academic Press, 213.

8. J. C. Russ, 1972, Proc. Symposium on Thin Section Microanalysis, St. Louis.

9. T. A. Hall and B. L. Gupta, 1974, J. of Microscopy, 100: 177.
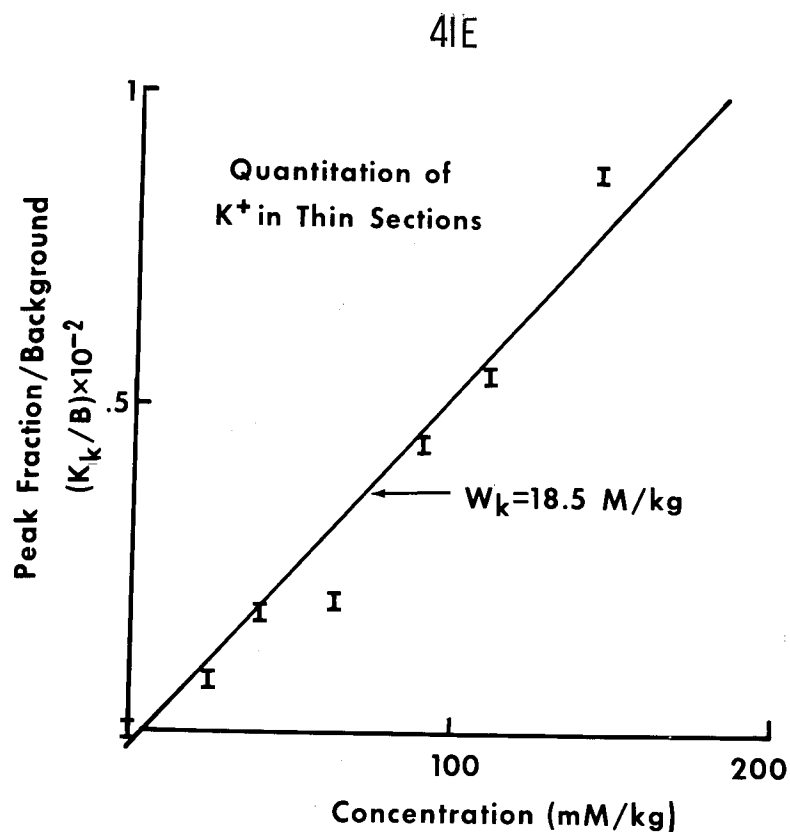
Fig. 1. Calibration of k/B ratio for Potassium. The primary standard has 539 counts/sec in the integrated $K\alpha$, β doublet. W_K is the inverse of the slope of the best fit line.
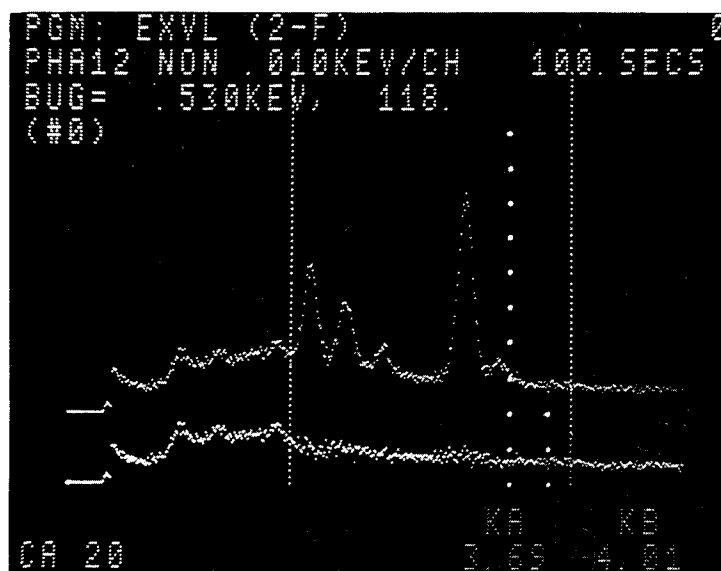
Fig 2. Spectrum of a 1000 Å thick cryosection of frog toe muscle, large spot used for analysis. (data provided by A. V. Somlyo)

AN ELECTRON PROBE STUDY OF ELEMENTAL DISTRIBUTION IN THE RAT PITUITARY

by

George R. Merriam, Frederick Naftolin and Claude Lechene

Biotechnology Resource in Electron Probe Microanalysis, Department of
Physiology, Laboratory of Human Reproduction and Reproductive Biology,
and Department of Obstetrics and Gynecology, Harvard Medical School,
Boston, Mass. 02115

A wide variety of in vitro studies have demonstrated the critical
importance of several cations for endocrine secretion (1,2,3). But lit-
tle is presently known of the optimum levels of these ions and there
are no data on their physiological concentrations in different endocrine
tissues.

These experiments represent the first stage in a study of the ele-
mental distribution in the neuroendocrine system. Because it is made
up of three separate but closely approximated tissues (the glandular
anterior and intermediate lobes and the neural posterior lobe), the
pituitary is a good subject for such preliminary work. These studies
show the kind of information which may be obtained from simply freeze-
dried specimens probed at low resolution.

Materials and Methods

Female Charles River rats weighing 180-220g were killed by cervical
dislocation and the pituitaries were quickly dissected out within one
minute and frozen on dry ice. All rats had 4-day cycles monitored by
vaginal cytology. Frozen 30μ slices were mounted on carbon discs and
dried at -30°C before analysis; alternate slices were stained with hema-
toxylin and eosin for histological confirmation of the tissue and or-
ientation for electron probe analysis. When dry, specimens were stored
under vacuum and then studied in a CAMECA MS 46 electron probe at 11KV
accelerating voltage, 50 nA specimen current, using an electron beam
10μ in diameter. Kα X-ray emission lines of K, S, P, Ca and Cl were
selected with PET crystal; Mg and Na with KAP; and Fe with LIF. Four
elements, or three elements and continuum at 3.50 Å were counted simul-
taneously. Slices containing all three pituitary lobes were counted
for 10-50 seconds at 10-15 points in each lobe. 100-400 points were
studied in each of the 10 pituitaries examined. The coordinates of
points selected were stored in a Hewlett-Packard 2100A on-line computer,
which controlled the operation of the electron probe and collected and
reduced the data, as described previously (4).

Data were pooled for each rat, then pooled again for all animals,
expressed as the ratio of emission line intensity on the specimen to

the background intensity for the same line on the carbon disc[1]. The significance of differences between lobes was tested with Student's t test, using a square root transformation of the data to eliminate inhomogenity of variance.

Results and Discussion

As Table 1 and 2 show, calcium levels were almost three-fold higher in intermediate than in either anterior or posterior lobes. Magnesium was similarly but less strikingly elevated in the intermediate lobe. Given the similar histological appearance and common embryologic origin of the anterior and intermediate lobe, the difference between them is particularly striking, especially considering that tissues as different in appearance as anterior and neural posterior lobe had identical levels of calcium and magnesium. Although chlorine was very slightly lower in intermediate lobe, this was of marginal statistical significance. Potassium, sodium and iron did not vary significantly in the three lobes.

The two primarily non-ionic elements studied, phosphorus and sulfur, were both inhomogeneously distributed, phosphorus higher in anterior than in posterior lobe, sulfur more abundant in the posterior lobe.

Although we believe that these measurements reflect relative physiological values, it might be argued that very mobile ions might have diffused down their concentration gradients before the pituitaries were frozen; dissecting out and freezing the glands required approximately one minute. If so, the even levels for Na and K would be deceptive. Definitive evidence against this possibility will await an in vivo freezing technique similar to that of Lehrer (5) and study of the sample kept frozen in the electron probe. A relative argument against the likelihood of this problem having arisen is the strong contrast between Na and K values for anterior pituitary tissue and for serum in adjacent capillaries in the gland, as shown in Table 3. If significant anoxic damage had occurred before freezing, one could expect diffusion to have eliminated this steep concentration gradient over a very short (40μ) distance before the more gentle gradient over the larger size scale of pituitary lobes. Also, a linear scan across the lobe boundaries for Ca and S, shows sharp gradients at the interfaces between lobes. This is to be expected for a well-fixed structural element such as S but would be less so for a relatively mobile cation like Ca^{++} if anoxic damage were significant.

---

[1] Overall rats studied, continua were not significantly different in the three lobes; net counts from anterior lobe = 9.0 ± 0.4 from intermediate lobe, 9.1 ± 0.9 from posterior lobe, 9.8 ± 0.5.

Although the large calcium and magnesium differences between anterior and intermediate lobes are surprising from a histological point of view, they may reflect the often disassociated evolutionary development of the two lobes; higher vertebrates in general develop larger anterior pituitaries secreting a larger number of hormones, while both the size and importance of the intermediate lobe has diminished (6). Secretory systems evolved at different times could then present different ionic requirements. To elucidate this matter further, a cross-species survey of pituitary elemental concentrations is in progress.

The distribution of sulfur and phosphorus reflect not only inorganic ions but also a larger number of complex organic molecules. The high sulfur levels in the posterior lobe, which as Table 4 shows are higher than in either gray or subjacent white matter of parietal cortex, may reflect stores of the neurohypophyseal hormones oxytocin and vasopressin, both of which are small, sulfur-rich polypeptides. Further study will determine whether these high levels are also characteristic of the supraoptic and paraventricular nuclei of the hypothalamus, where these hormones are produced for transport to the pituitary.

Table 1

Characteristic X-ray Intensities in Pituitary Lobes

(Expressed as signal over background ratios
Mean ± Standard Error, ( ) = no. of rats)

	Anterior			Intermediate			Posterior		
Calcium	2.0	± 0.2	(9)	5.5	± 0.4	(8)	1.8	± 0.2	(9)
Magnesium	5.2	± 0.4	(9)	6.2	± 0.1	(9)	5.0	± 0.1	(9)
Sodium	21.0	± 2.9	(8)	19.4	± 2.9	(8)	19.3	± 3.1	(8)
Potassium	75.5	± 7.9	(8)	70.8	± 3.6	(8)	72.8	± 2.1	(9)
Chlorine	8.0	± 0.9	(8)	6.7	± 0.5	(7)	8.3	± 0.8	(8)
Iron	0.27	± 0.05	(7)	0.29	± 0.06	(7)	0.35	± 0.07	(7)
Sulfur	19.0	± 3.4	(8)	22.7	± 2.7	(8)	30.8	± 3.2	(8)
Phosphorus	110.1	± 13.9	(9)	102.8	± 5.5	(8)	86.3	± 3.0	(8)

Table 2

Significance Levels, P, for Differences in Elemental Concentration Between the Pituitary Lobes

	(Ant.-Int.)	(Ant.-Post.)	(Int.-Post.)
Calcium	<0.01	n.s.	<0.01
Magnesium	<0.01	n.s.	<0.01
Sodium	n.s.	n.s.	n.s.
Potassium	n.s.	n.s.	n.s.
Chlorine	<0.05	n.s.	n.s.
Iron	n.s.	n.s.	n.s.
Sulfur	n.s.	<0.01	<0.01
Phosphorus	n.s.	< 0.01	n.s.

Table 3

Characteristic X-ray Intensities in Anterior Pituitary
and Serum in Pituitary Capillaries
(Signal over background ratios - Mean $\pm$ Standard Error,
( ) = no. of points counted)

	Anterior Pituitary	Serum
Potassium	48.3 $\pm$ 0.4 (60)	11.8 $\pm$ 3.1 (10)
Sodium	13.2 $\pm$ 0.3 (60)	35.9 $\pm$ 4.1 (10)

Table 4

Sulfur X-ray Intensity in Posterior Pituitary and Cerebral
Parietal Lobe
(Signal over background ratio - Mean $\pm$ Standard Error, ( )=
no. of points counted)

Posterior Pituitary	Parietal Cortex	Parietal White Matter
27.4 $\pm$ 0.2 (30)	5.2 $\pm$ 0.3 (10)	3.1 $\pm$ 0.3 (10)

REFERENCES

1. W. W. Douglas, R. P. Rubin. J. Physiol., 159 (1961) 40.

2. N. A. Thorn. Acta Endocrinologica, 50 (1965) 357.

3. A. M. Poisner. In Frontiers in Neuroendocrinology. Eds. W. F. Ganong and L. Martini (1973) 33.

4. T. Moher, C. M. Aden, R. Beeuwkes, A. Sanderson and C. Lechene. Proc. of the Microbeam Analysis Society, Ninth Annual Conference, Ottawa, Canada, 1974, 34A-E.

5. G. M. Lehrer. In Metabolic Compartmentalization in the Brain. Ed. R. Balasz and J. Cremer (1972) 259.

6. K. G. Wingstrand. In The Pituitary Gland. Ed. G. Harris, Berkeley, California (1966) 1: 58.

Scanning, Transmission and Electron Probe Analysis of the Cat Tapetum

C. E. Turnbill

NASA-Ames Research Center
Moffett Field, CA 94035

The tapetum lucidum or "bright carpet" of the cat eye is an adaptation for vision in limited light. The tapetum is of particular interest to our laboratory in that it might be used as a visual maker for cosmic "heavy primary" radiation. Since this marker would be located rear the retina, it would provide close correlation between high energy particle trajectories and related retinal damage. In preparation for this task, the cellular tapetune of adult cats were examined as controls.

Adult cats were perfused with 2% glutaralderhyde, 2% paraformaldehyde and placed in cacodylate buffer. The tapetune was separated from the retina and choroid and processed for either scanning or transmission microscopy.

Material for the transmission microscope was postfixed in 1% osmium tetroxide and examined both stained, with uranyl acetate and lead, and un-stained for microprobe analysis. The stained sections (Fig. 1) cut parallel to the axis of the retinal rods, show layers of cells filled with electron dense rod-like structures approximately 10 microns by .1 micron. As pointed out by Bernstein and Pease (1) the arrangement of the intracellular rods act as an effective reflecting surface with a minimum of light scattering. By reflecting light back into the same area of the retina through which it originally passed, the sensitivity of the eye is increased without blurring vision.

Specimens for the scanning microscope were critical point dried and coated with carbon-gold. The cells are seen to be thin, hexogonal in shape and with rodlets running parallel to the flat surface.

Specimens for probe analysis in the scanning microscope were freeze-dried and coated with a thin layer of carbon followed by aluminum. The crystalline material in the retinal tapetum of fish was identified by Kuhne (2) as guanine. Weitzel et. al. (3) indicated a high concentration of zink in the cellular tapetum of carnivores. Electron microprobe analysis confirmed the presence of zink in the rod-like structures. These structures were also found to contain a high concentration of sulphur. The sulphur was confirmed in both scanning and transmission microprobe analysis. The atomic ratio of sulphur to zink was approximately 2:1 in most cases.

Evidence presented by Bernstein and Pease (1) that the rod-like structure are modified pigment granules, would seem very probable, since comparative probe analysis of the pigment granules and tapetum rods shows a similar relationship between sulphur to zink ratios.

(1) Bernstein, M. H. and Pease, D. C.: J. Biophys. Biochem. Cutol. 5, 1 (1959)

(2) Kuhne, W.: Untersuch. Physiol. Inst. Univ. Heidelberg, 3, 221 (1880)

(3) Weitzel, G., et. al.: Hoppe-Seyler's Z. Physiol. Chem., 299, 19 (1954)

ELECTRON PROBE ANALYSIS AND ULTRASTRUCTURE OF CULTURED, FREEZE DRIED VASCULAR SMOOTH MUSCLE.
R. E. Garfield and A. P. Somlyo

Pennsylvania Muscle Institute, Presbyterian-University of Pennsylvania Medical Center, 51 N. 39th St., Philadelphia, PA 19104

Electron probe x-ray microanalysis at a spatial resolution of 1000 Å or better is now feasible and has been used to demonstrate mitochondrial deposits of divalent cations in ultrathin sections of fixed tissues.(1). Monovalent and unbound ions, however, are lost and/or translocated during chemical fixation (2), necessitating the use of unfixed ultrathin frozen dried sections for electron probe analysis (3,4). The use of whole, frozen-dried cultured cells for electron probe analysis is easier than cryo-ultramicrotomy and presents some advantages such as rapid freezing rates attainable and imaging at conventional (75-80 kV) voltages. Smooth muscle cells from guinea pig aortas were cultured on Formvar-coated nylon grids (Fig 1). Grids with attached cells were blotted on filter paper and plunged into liquid nitrogen and dried frozen in a vacuum evaporator.

In dried whole cells examined at 75 or 80 kV, the cell outline and processes were distinct and the nuclei and mitochondria containing electron opaque granules identifiable (Fig 2,3). The intracellular location of the granules or the extracellular location of crystalline precipitates (NaCl) was readily verified in stereo electron micrographs obtained with the tilt stage of the EM 301. The mitochondrial granules were not seen in every cell, but were occasionally also demonstrable in fixed and embedded sections (Fig 4). Electron probe analysis (5) of the mitochondrial granules identified Ca and P as the dominant components (Fig 5c). Replacement of the Ca in the culture medium with 1 mM Sr for 1 hour prior to freezing lead to the appearance of a prominent Sr signal (Fig 6a,6b) together with the Ca K line, over the mitochondrial granules. Spectra obtained over normal cells in regions other than the mitochondria showed the presence of Na, S, Cl, K and Ca (Fig 5b). The Ca peaks detected over regions of the cell other than the mitochondrial granules were relatively low (Fig 5b), but still greatly in excess of that expected on the basis of normal cytoplasmic concentrations. The low K is compatible with the properties of developing cells, but the contribution in the spectrum of ions (Na,Ca) adsorbed to the surface of cells remains to be established. Counts obtained over the Formvar film were low (Fig 5a). We conclude that, as in some other cells, the mitochondrial granules in freeze dried cultured cells contain primarily calcium and phosphorus.

1. Somlyo, A. P., A. V. Somlyo, C. E. Devine, P. D. Peters and T. A. Hall. J. Cell Biol. 61: 723 (1974)
2. Garfield, R. E., R. M. Henderson and E. E. Daniel, Tissue & Cell.4: 579 (1972)
3. Appleton, T. C. J. Microscopy 100: 49 (1974)
4. Somlyo, A. V. and A. P. Somlyo. This proceedings (1975)
5. Shuman, H. and A. P. Somlyo. Microbeam Analysis Society Proceedings (1975)

44B
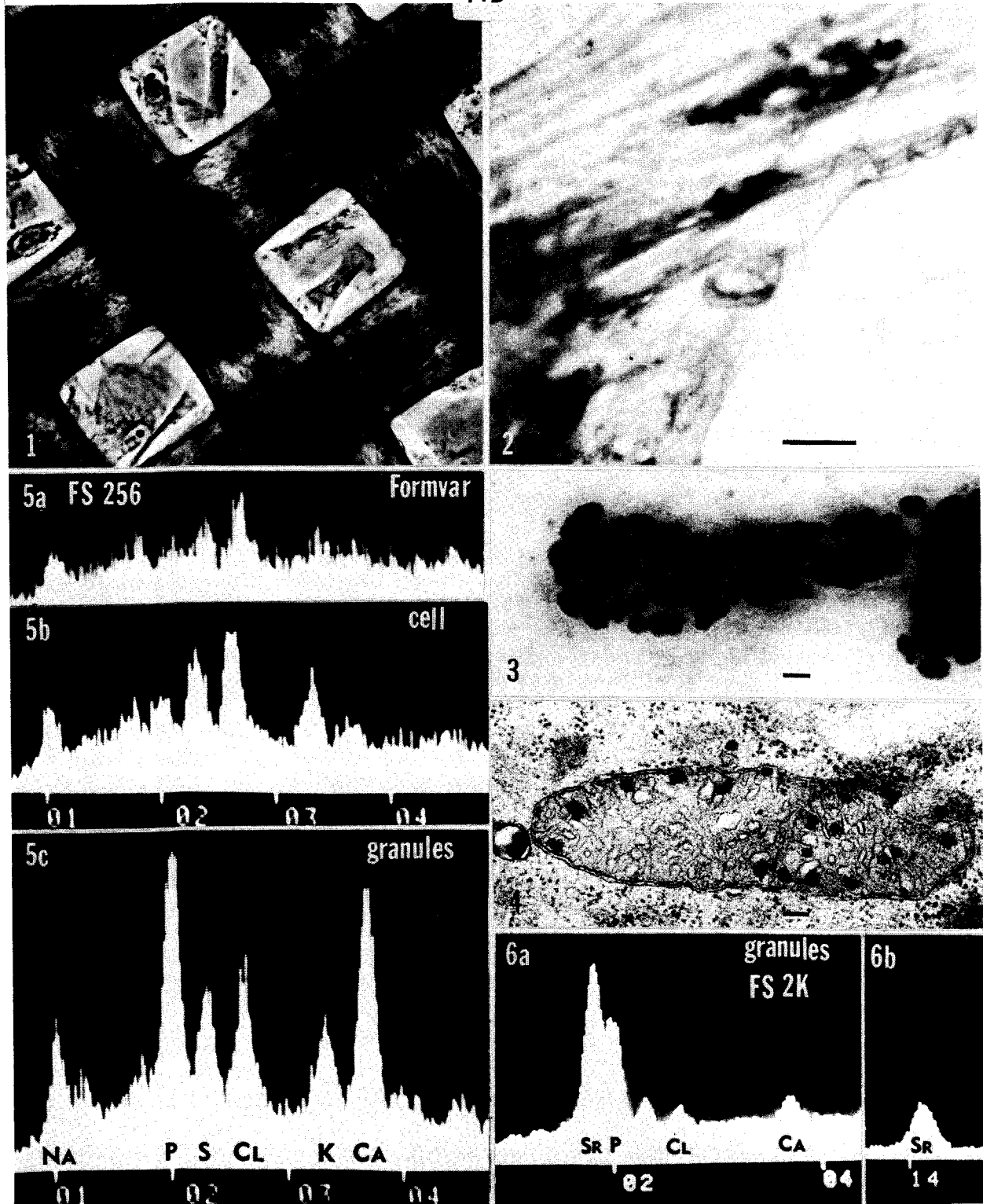
Fig.1. Phase micrograph of cultured smooth muscle cells on nylon grid.
Fig.2. Electron micrograph of freeze-dried cell (marker = 1 μ)
Fig.3. Mitochondrial granules in freeze dried cells (marker = 0.1 μ)
Fig.4. Mitochondrial granules as seen in conventionally fixed cultured
        smooth muscle cells (marker = 0.1 μ)
Fig.5. X-ray spectra obtained over the Formvar film (5a), cell (5b) and
        mitochondrial granules (5c).
Fig.6. Spectrum obtained over mitochondrial granules in cell incubated
        in Ca++ free Krebs-Ringer with 1 mM Sr. Sr L-line (6a) and K-line
        (6b) were prominent.

A SIMPLE TRANSMITTED ELECTRON DETECTOR (TED) FOR THIN BIOLOGICAL SAMPLES

by

James R. Coleman, Scott Davis, Bernard Halloran and Patricia Moran

Department of Radiation Biology and Biophysics

University of Rochester School of Medicine and Dentistry

Rochester, New York 14642

In many biomedical investigations it is important to establish the elemental composition of a structure identified in a thin (80-100 nm) section of tissue during examination by conventional transmission electron microscopy. If one has access to a transmission electron microscope with X-ray analytical capability, the determination of the composition of the structure in the tissue is a relatively straightforward task. However, if one must use a conventional electron probe X-ray microanalyzer, either because of lack of X-ray analytical capability on the transmission electron microscope, or because one wishes to take advantage of the excellent chemical resolution of large, crystal spectrometers, one encounters difficulty in producing a useful image in either sample current, backscattered electron, or secondary electron modes: generally, such images have too little contrast to be useful. We have devised a simple, inexpensive detector for transmitted electrons that produces images with sufficient contrast that the image generated by the electron beam of the probe can be readily correlated with the image seen in the transmission electron microscope. Although designed for use with the ARL EMX-SM (Applied Research Laboratories, Sunland, Calif.) it is easily adapted for other instruments.

An example of the usefulness of this transmitted electron detector is seen in figures 1 and 2. Figure 1, top, shows the transmission electron microscope image of a thin (ca 90 nm) section of lung from a rat which had been exposed to an aerosol of titanium dioxide. Figure 1, middle, shows the scanning transmission image of the same section which is produced by the transmitted electron detector in the electron probe. Although the resolution

in the image is limited by beam diameter (less than 1μ in this case), the
fine structure features seen in the transmission electron microscope image,
are readily identified in the scanning transmission image of the probe.
Figure 1, bottom, shows the titanium K_α X-ray image that corresponds to the
scanning transmission image. It is clear that only one cell inclusion emits
detectable titanium X-rays, and this inclusion is readily identified by
comparing the scanning transmission image with the conventional transmission
electron microscope image.

Figure 2 shows a line scan across the inclusion showing the intensity of
the Ti K_α X-ray over the inclusion. The X-ray intensity at the peak was
32 cps and the background was less than 1 cps. This low background is
characteristic of thin sections mounted either directly on an EM grid or on
carbon films and is a substantial advantage when trying to identify materials
present in small amounts. In addition, samples on EM grids facilitate quanti-
tation using the Hall (1971) technique which requires thin samples on a very
thin substrate.

The transmitted electron detector was derived from a design of Murphy and
Metzger (1968) in which a metal disc 22 mm in diameter, placed 3 cm below the
sample collected transmitted electrons. We found that this arrangement did
not provide sufficient contrast when used with thin sections of epoxy-embedded
tissue. We modified the design so that most of the electrons reaching the
detector would be electrons which had been scattered through small angles.
The device is diagrammed in Figure 2. It uses the 19 pin connector supplied
by ARL as a support for the electron detector which is a polished copper rod,
3 mm in diameter, soldered to a 1 mm diameter lead which serves to support
the detector as well as connect it to two pins of the 19 pin connector. A
brass tube is fitted inside the ARL sample holder. The brass tube contains
an electron shield to absorb backscattered and other electrons. The electron
shield is a circular piece of 0.3 mm aluminum sheet, with a 5 mm circular
hole drilled in the center. The hole is aligned over the upper, polished face
of the electron detector which is about 1 cm from the specimen. A specimen
holder from Phillips EM200 transmission electron microscope is used to hold

the copper grid on which the thin section is mounted. It has been found that after examination with TEM, a thin vacuum evaporated coat of aluminum on the grid will reduce charging by the sample. If the coat is not excessively thick the sample may be examined subsequently by TEM with only minimal loss of contrast and resolution.

It is likely that the usefulness of the detector assembly would be increased if the distance between the sample and detector could be varied. This would permit one to control the solid angle of electrons accepted by the detector, thus changing the proportion of electrons scattered through large and amall angles used for imaging.

References

1. Hall, T.A., 1971, in Physical Techniques in Biological Research (G. Oster, ed.) Vol. I part A, Optical Techniques. Academic Press, New York and London. pp. 158-275.
2. Murphy, A.P. and C.A. Metzger, 1968, Rev. Sci. Instr. 39, 1705.

Acknowledgements

Figure 1. Thin section (ca 90 nm) of lung tissue from rat exposed to
titanium aerosol. Top image is from conventional transmission
electron microscope, magnification 4.500X. Middle image is
scanning transmitted electron image produced by electron probe,
magnification about 4.000 or 2μ/screen division. Bottom image
is titanium K_α of same region, 2μ/screen division.

Figure 2. Transmission electron micrograph of same section seen in Figure
1, is at top, with line scan of Ti K_α X-rays below. The line
in the upper image indicates the path of the beam.

Figure 3. Diagram of transmitted electron detector.

Figure 1

Figure 2

ARL SAMPLE HOLDER

SET SCREW

SPECIMEN
GRID HOLDER

ELECTRON
SHIELD

MODIFIED
ARL SAMPLE
HOLDER

TRANSMITTED
ELECTRON
DETECTOR

TRANSMITTED ELECTRON
DETECTOR
(TED)
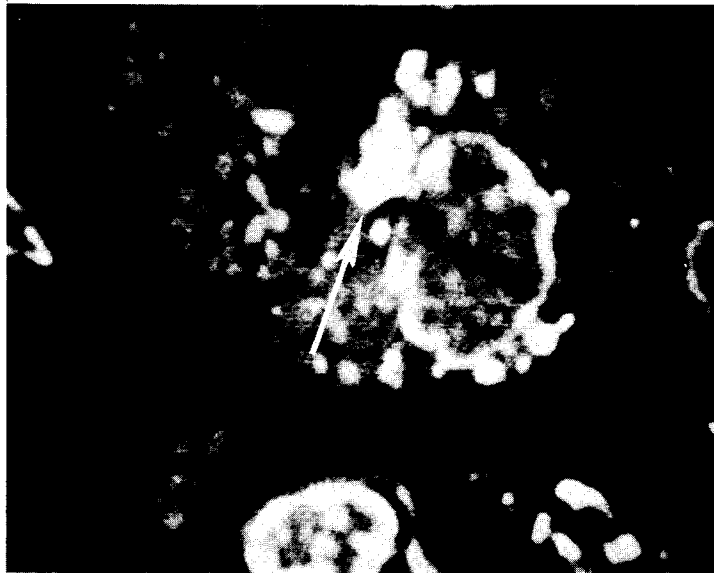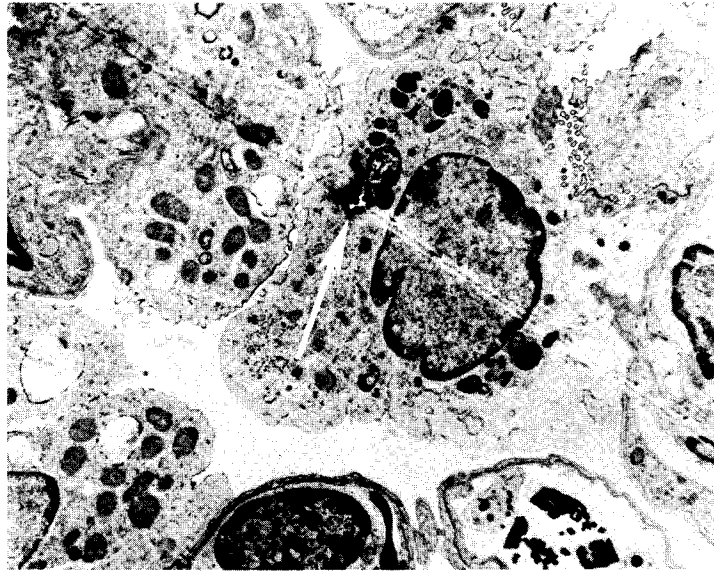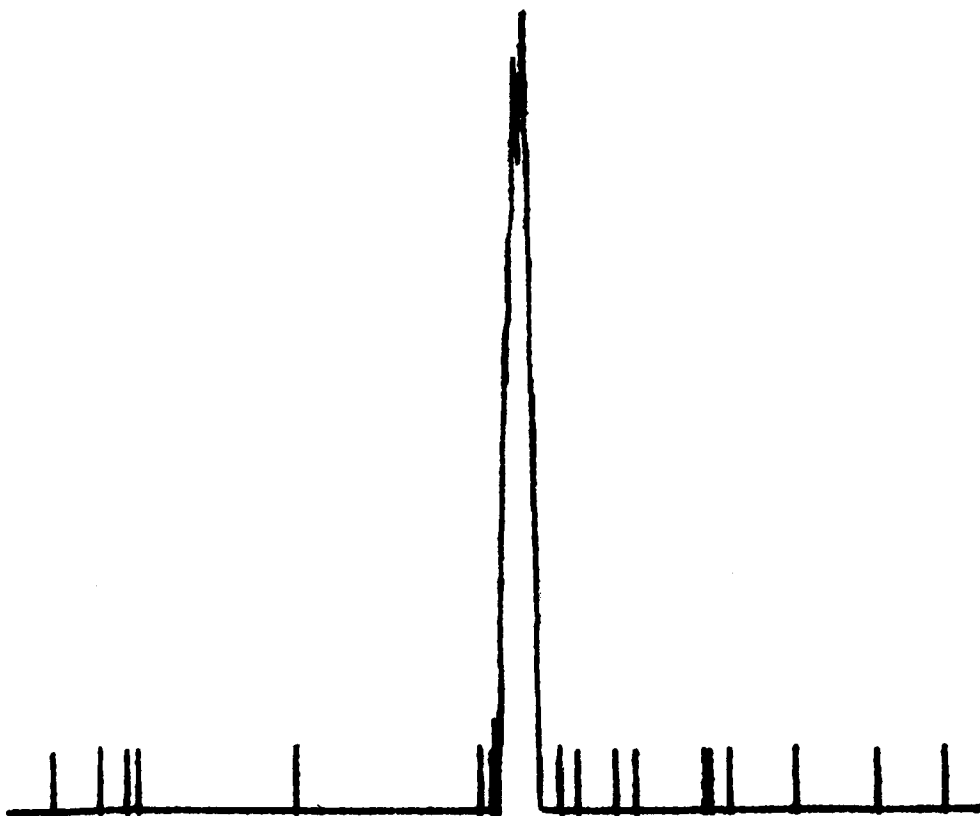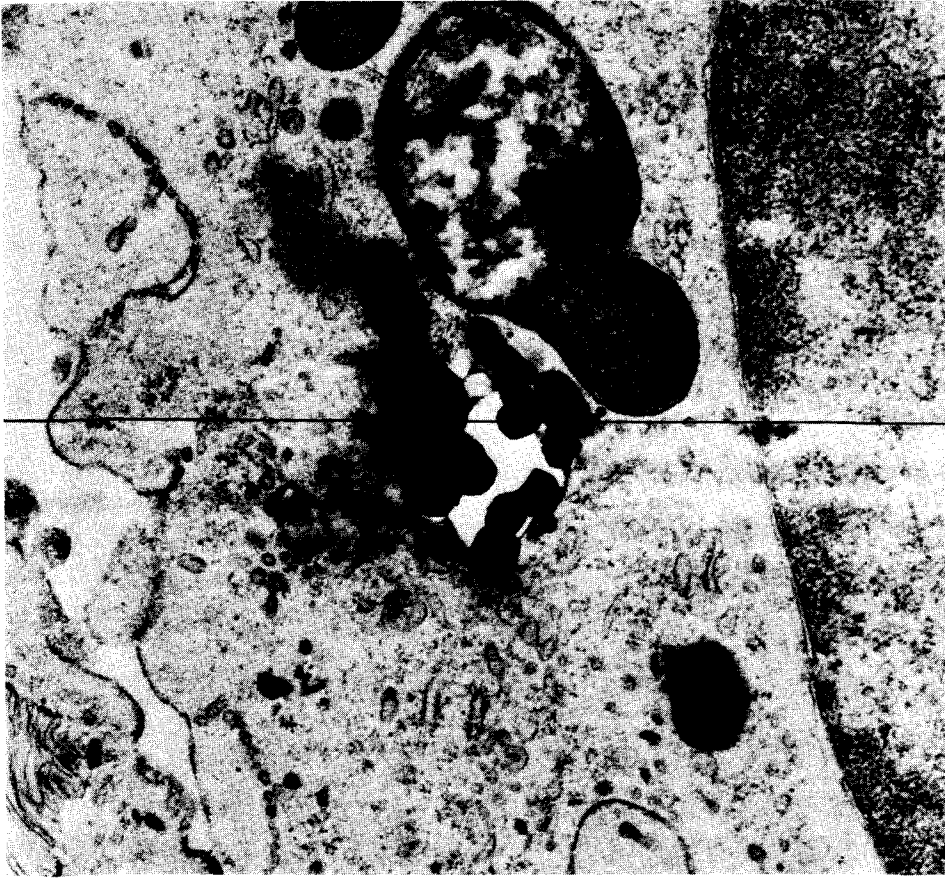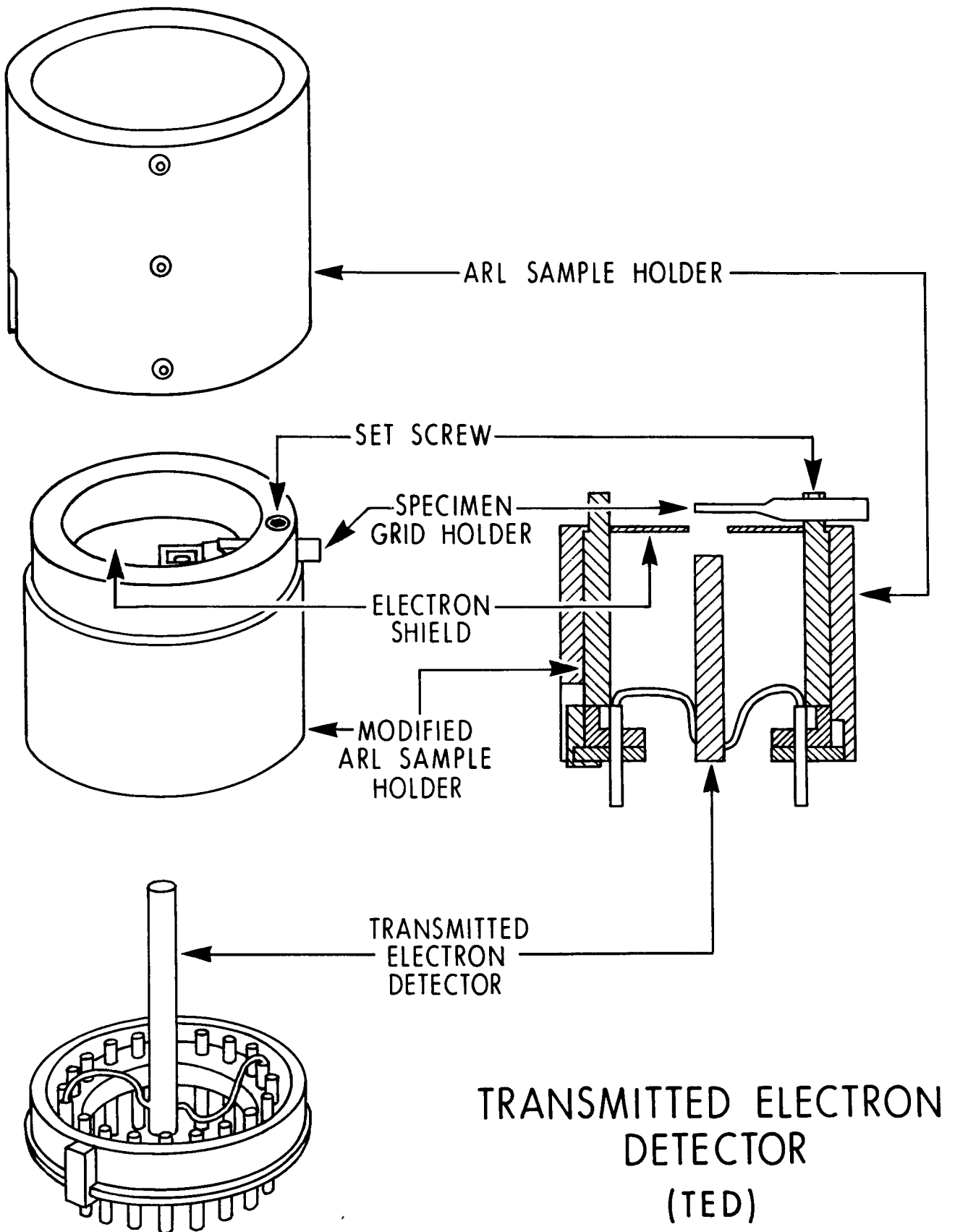
Figure 3

MICROANALYSIS OF ZINC IN INJURED MYOCARDIA

R. Yarom,[*] P.D. Peters,[+] T.A. Hall[+]

*Pathology Department, Hebrew University - Hadassah Medical
School, Jerusalem, Israel. + Electron Microscopy Section,
Cavendish Laboratory, Cambridge, England.

We have used the electron microscopic x-ray microprobe method to analyse the
localization of zinc in hearts of dogs and rats injured in different ways. Zinc
is essential for repair processes and a better understanding of its myocardial
metabolism may have clinical as well as theoretical significance.

Previous work (1,2,3) has shown that the zinc concentration in blood and tissues
undergoes notable changes after all kinds of injuries. Myocardial infarction is
accommpanied by an especially pronounced serum zinc decrease. Although much of the
zinc is taken up by the liver (2), nevertheless an increased local zinc concentration
may occur, its extent being perhaps related to prognostic aspects of the damage.
The heart is a non-homogeneous tissue, and existing methods of chemical analysis
seem to be inadequate for the detection of elemental changes which may be in the
nature of a redistribution of substances between various areas or even various cells
and organelles. The combination of electron microscopy with X-ray microanalysis is
well suited for such an investigation, allowing the detection of very small amounts
of an element under direct subcellular visual monitoring (4).

Our experiments were carried out on dogs in which infarction was produced by
tying a coronary artery and in rats given the cardiotoxic drug isoproterenol. The
animals were sacrificed at progressive intervals after injury, in each case normal
as well as damaged areas of myocardium being taken for examination. The tissues
were processed as for routine electron microscopy but with all the steps rapidly
done. Sections 120 nm thick on formvar and carbon coated grids were examined
unstained. The instrument was an AEI EMMA-4. The voltage was 40KV, the current
200-300 nA, the probe diameter around 250 nm. The analysis time was 20-60 seconds.
The energy dispersive (Si/Li Kevex) analyser was utilized for viewing and photographing
elemental spectra of many areas. The crystal diffractive (LiF as the crystal)
spectrometer was employed for more "in depth" semiquantitative analysis of zinc.
Comparisons of local zinc concentrations in different spots and specimens could
be done.

The results demonstrated that an overall increase in zinc emission occurred in
damaged areas as compared with the normal-appearing parts of the same hearts. This
increase, maximal on the 3rd day after injury, was not uniform, some cells or
organelles taking up more of the metal than others.

In spite of much variability in zinc emission (probably related to specimen preparation) it appeared that nuclei of macrophage-like interstitial cells were the structures showing the highest zinc increase after injury. Within the myofibers, surviving nuclei and mitochondria with electron dense material increased their zinc content while degenerating nuclei, fat droplets, "lysosomes" and oedematous areas had low or decreasing concentrations of the element. Intracellular zinc is a component of several metalloprotein (firm zinc binding) and metalloenzymes (zinc in loose attachment or activator element). A number of these are concerned with biosynthesis of nucleic acids and proteins. It is therefore not surprising that "cells with a future" like undifferentiated interstitial mononuclear cells or surviving myofibers accomulate zinc after injury. The direction and rate of reparative processes may well depend on an adequate supply of zinc-containing enzymes.

The x-ray detection method described here uses zinc as a marker for specific metallo-substances. Further work will show if relative local concentrations of elements can also serve as a measure of the relevant enzyme activity.

References

1. Chvapil, M., Elias, S.L., Ryan, J.N., Zukoski, C.F.
   Pathophysiology of zinc, p.105-125. Neurobiology of the trace metals zinc and copper, Ed. Carl C. Pfeiffer, International Review of Neurobiology, Supplement 1, 1972.

2. Lindeman, R.D., Yunice, A.A., Baxter, D.J., Miller, L.R., Nordquist, J.
   Myocardial zinc metabolism in experimental myocardial infarction.
   Journal of Laboratory and Clinical Medicine, 81; 194-204, 1973.

3. Parisi, A.F., Vallee, B.L.
   Zinc metalloenzymes: characteristics and significance in biology and medicine. The American Journal of Clinical Nutrition, 22; 1222-1239, 1969

4. Hall, T.A., Röckert, H.O.E., Saunders, C.H.
   X-ray Microscopy in Clinical and Experimental Medicine.
   Charles C. Thomas, Springfield, Illinois, 1972, p.139-220
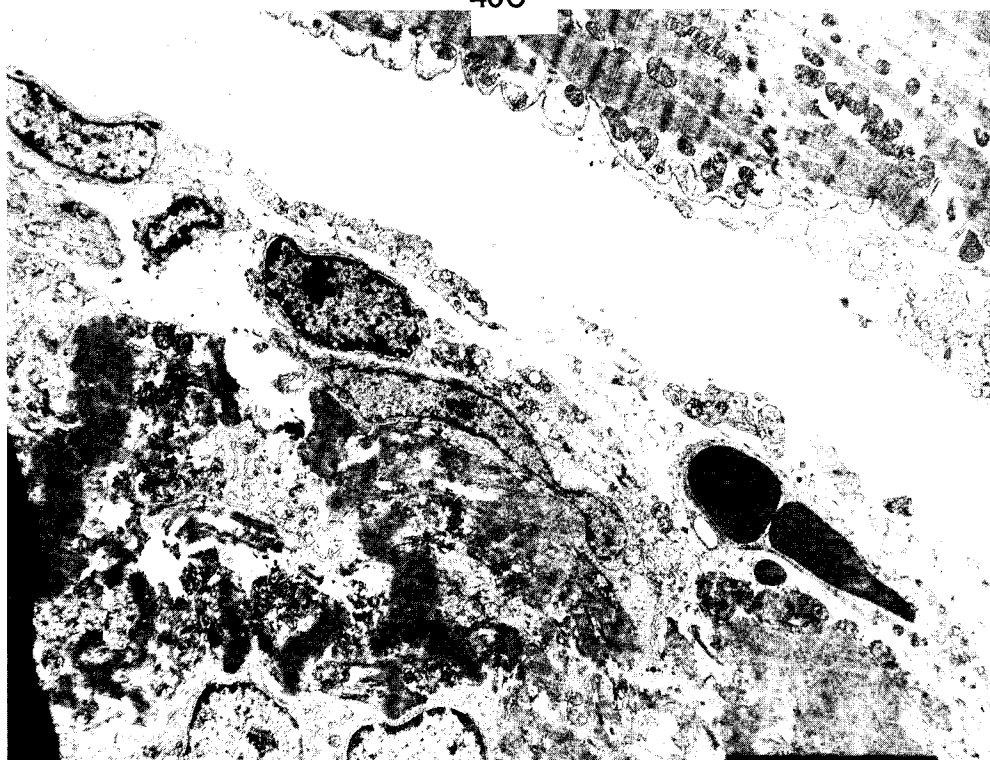
Fig.1. Dog myocardium three days after coronary ligature
       showing the non-homogeneous nature of the specimen.
       At top right there is a well preserved myofiber while
       at lower left there is necrotic material, mononuclear
       cells and capillaries. The mitochondria are clumped and
       contain electron-opaque material.
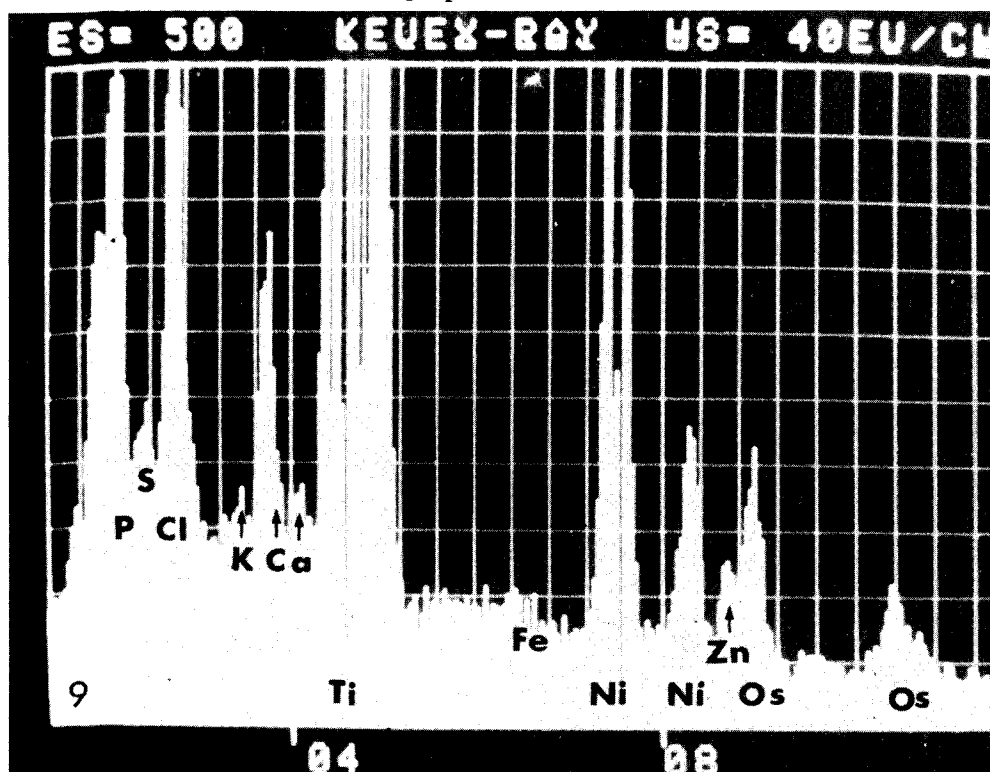
Fig.2. 60 second energy dispersive analysis of a mitochondrion
       in the damaged myofiber.

ELECTRON PROBE ANALYSIS OF THE EFFECT OF PARATHYROID HORMONE ON

INORGANIC IONS IN THE RAT KIDNEY

by

Edward H. Abraham, Ronald R. Warner and Claude P. Lechene

Biotechnology Resource in Electron Probe Microanalysis
Laboratory of Human Reproduction and Reproductive Biology
and Department of Physiology, Harvard Medical School
Boston, Massachusetts, 02115

This study on the renal effects of parathyroid hormone illustrates the considerable advantages electron probe X-ray spectroscopy offers to the study of ion transport in physiology. Classical studies of kidney function have dealt primarily with Na, K and Cl due to the relative ease of measurement of these ions. With new techniques the number of analyzed ions has recently been extended to P, Ca and Mg. However, in any one experiment only two of these ions are generally measured. Some biologically important elements such as sulfur are not measured due to lack of suitable techniques. To determine all of the ion concentrations at one time with conventional techniques would require enormous effort and necessitate large quantities of biological samples. With electron probe analysis it is now feasible to quantitate in a single sample on the order of picoliters all of the chemical elements heavier than carbon and to interrelate them in the same experiment (1,2).

These experiments present the first clearance study of the effect of PTH on seven major biological elements (Na, K, Ca, Mg, Cl, P, and S) measured in the same samples. The experiments were performed on six female Wistar rats anesthetized with inactin. The thyroid and parathyroid glands were removed by surgery followed by local cauterization (TPTX). Catheters were inserted in the right jugular vein for intravenous perfusion, in both ureters for urine collections, and in the right femoral artery for sampling of blood.

Urine and blood collection periods began three hours after TPTX in order to provide adequate time for endogenous parathyroid hormone and calcitonin to fall to very low levels. One hour prior to the first urine and blood collection, tritiated inulin was infused for measurement of glomerular filtration rate (GFR). Sample collection during the hormone deplete period lasted one hour and consisted of two thirty-minute urine samples with blood taken at the midpoint of the urine periods. Parathyroid hormone* was then injected (priming dose, 3.3 units/kg;

---

sustaining dose, 0.1 units PTH/kg/min.). One hour after the start of hormone infusion, a new collection period began for urine and plasma.

The concentrations of the electrolytes in plasma ultrafiltrate and urine were determined by electron probe analysis using the liquid droplet technique (1,2). Analysis was conducted at 11 Kv and 200 nA electron beam current with a CAMECA MS46 electron probe. The $K\alpha$ X-ray lines of Na and Mg were analyzed with a KAP crystal; K, P, S and Cl with a PET crystal. Four elements were analyzed simultaneously. The control of the analysis of the liquid droplets by the electron probe and the data reductions were done as previously described (3) using a Hewlett Packard 2100 A minicomputer and a Tektronix 4012 display terminal. Tritiated inulin was measured with a liquid scintillation counter. Tabulated values were determined by averaging the four urine values (two from each kidney) or two plasma values per collection period. To determine if the hormone had a significant effect, paired values before and after PTH were tested using the Student t test.

In the kidney the arterial pressure causes the formation of an ultrafiltrate of blood. This ultrafiltrate is modified during its passage along the renal tubules by reabsorption of ions and water and possible secretion of ions. The urine is the product of these modifications. Data in this study are expressed in terms of the rate at which an ion is appearing in the urine (U$\dot{V}$ = urine ion concentration x urinary flow rate). To determine the extent of net reabsorption, the data are also expressed in terms of fractional excretion (FE). The FE of any given ion represents the fractional amount of that ion in the ultrafiltrate which ultimately appears in the urine.

$$FE_x = \frac{U_x \dot{V}}{GFR \cdot P_x}$$

where P_x = the concentration of x in plasma

U_x = the concentration of x in urine

$\dot{V}$ = urinary flow rate

and GFR = $\dfrac{U \text{ inulin } \dot{V}}{P \text{ inulin}}$

Table 1 shows the average values for ions in the plasma ultra-
filtrate as determined by the electron probe. These values are in
close agreement with plasma ultrafiltrate values determined by other
techniques. Following administration of PTH there is no significant
change in the plasma levels. Although GFR remains constant there is
a small but significant change in the urinary flow rate.

The effect of PTH on the renal handling of inorganic ions is shown
in Table 2. In the absence of parathyroid hormone, there is nearly
complete reabsorption of phosphate in the kidney (FE=1.88%). With the
addition of PTH there is a more than twenty fold increase in fractional
excretion (FE=41.0%), indicating a dramatic decrease in phosphate re-
absorption. For sulfate and chloride, the addition of parathyroid
hormone has no net effect.

Although less dramatic than the effect on phosphate, the excretion
of several cations (Na, Mg and Ca) is significantly affected by the ad-
dition of parathyroid hormone (Table 2). Sodium fractional excretion
is more than doubled. This is notable in view of the large relative
concentration of sodium, systemically the chief cation. Magnesium FE
decreases by nearly a third following addition of the hormone. There
is a significant slight increase in fractional excretion of calcium.
However, unlike phosphorous, sodium, and magnesium, this change is not
mirrored by a corresponding change in the urinary quantity excreted
(Table 3). This dichotomy may be due to a statistical fluctuation
which will be resolved with further study. Lastly, parathyroid hor-
mone has no significant effect on the excretion of potassium.

Electron probe analysis in these experiments, besides confirming
the important phosphaturic effect of PTH (4,5), allows the study of
the balance of inorganic ion movements in the presence of this hormone
in the same species under the same experimental conditions (increase
in Na and Ca excretion, decrease in Mg excretion and no change in Cl,
S and K Excretion). Such a tabulation was not previosuly possible with-
out taking values from experiments using dissimilar protocols and even
different species of animals; moreover, this tabulation would have been
incomplete due to the lack of data on Cl and S.

This study illustrates one of the unique powers of electron probe
X-ray spectrometry; the ability to quantitate easily the elemental con-
tent of biological fluids in the same sample.

TABLE 1

ELECTRON PROBE VALUES FOR PLASMA ULTRAFILTRATE CONCENTRATIONS

	PTH DEPLETE (mM/L)*	PTH ADDITION (mM/L)*	P Values
SODIUM	140. $\pm$ 3.6	146. $\pm$ 2.9	n.s.**
POTASSIUM	5.29 $\pm$ 0.23	5.42 $\pm$ 0.19	n.s.
CALCIUM	0.88 $\pm$ 0.14	0.91 $\pm$ 0.22	n.s.
MAGNESIUM	0.56 $\pm$ 0.10	0.64 $\pm$ 0.09	n.s.
CHLORINE	124. $\pm$ 4.9	127. $\pm$ 7.1	n.s.
SULFUR	2.75 $\pm$ 0.71	3.31 $\pm$ 0.71	n.s.
PHOSPHOROUS	2.11 $\pm$ 0.32	1.79 $\pm$ 0.31	n.s.
GFR (ml/min.)	1.07 $\pm$ 0.12	1.08 $\pm$ 0.09	n.s.
$\dot{V}$ (μl/min.)	4.26 $\pm$ 1.2	6.25 $\pm$ 1.32	P<.02

* Value $\pm$ Standard Error

** n.s.: Values not statistically significant

TABLE 2

VALUES FOR FRACTIONAL EXCRETION (FE)

	PTH DEPLETE %*	PTH ADDITION %*	Δ%**	P VALUES
PHOSPHOROUS	1.88 ± 0.62	41.0 ± 5.2	3028. ± 646.	< .01
CHLORINE	1.45 ± 0.40	1.61 ± 0.39	19.7 ± 13.1	n.s. ***
SULFUR	10.2 ± 1.8	9.36 ± 1.40	- 2.57 ± 11.8	n.s.
SODIUM	0.44 ± 0.18	0.92 ± 0.28	56.8 ± 5.8	< .02
MAGNESIUM	10.9 ± 2.4	7.66 ± 1.49	-22.8 ± 8.5	< .05
CALCIUM	1.78 ± .43	2.06 ± .40	24.4 ± 8.9	< .05
POTASSIUM	11.8 ± 2.1	17.1 ± 1.6	88.6 ± 53.2	n.s.

TABLE 3

VALUES FOR QUANTITIES EXCRETED (UV)

	PTH DEPLETE μM/min.****	PTH ADDITION μM/min. ****	Δ%**	P VALUES
PHOSPHOROUS	.0393 ± .0136	.794 ± .109	30.7 ± 8.09	<.02
CHLORINE	1.59 ± .51	1.96 ± .44	42.4 ± 19.9	n.s.***
SULFUR	.298 ± .055	.274 ± .033	5.4 ± 17.7	n.s.
SODIUM	.624 ± .269	1.34 ± .38	199. ± 52.	<.02
MAGNESIUM	.0682 ± .0120	.0485 ± .0080	-40.9 ± 7.5	<.02
CALCIUM	.0149 ± .0034	.0168 ± .0021	26.6 ± 13.9	n.s.
POTASSIUM	.704 ± .183	.993 ± .118	100.7 ± 55.4	n.s.

*　　FE in % ± Standard Error

**　　Δ% = mean of [value PTH addition - value PTH deplete]per rat x 100
　　　　　　　　　　[value PTH deplete   ]

*** n.s. values are not statistically significant

**** UV ± Standard Error

REFERENCES

1. Lechene, C., Proceedings of the Fifth National Conference on Electron Probe Analysis (New York) 32A – 32C, 1970.

2. Lechene, C., In Microprobe Analysis as Applied to Cells and Tissues, edited by Theodore Hall, Patrick Echlin and Rudolph Kaufman, pp. 351-368. Academic Press, London, 1974.

3. Moher, T., Aden, C. M., Beeuwkes, R., Sanderson, A. and Lechene, C., Microbeam Analysis Society, Ninth Annual Conference, Ottawa, Canada, 1974: 34A – 34E.

4. Beutner, E. H. and Munson, P. L., Endocrinology 66 (1960) 610-616.

5. Lavender, A. R., Pullman, T. N., Rasmussen, H. and Aho, I., The Para-thyroids, ed. by R. O. Greep and R. V. Talmage, Charles C. Thomas Publ. Springfield, Illinois. pp. 406-412 (1960).

MICROANALYSIS OF CRYSTALS IN BIOLOGICAL TISSUE

S. Siew, R.K. Matta and M. Johnson

Departments of Pathology and Ophthalmology
University of Pittsburgh School of Medicine
and The Montefiore Hospital
Pittsburgh, Pennsylvania 15213

The autopsy tissues of a fatal case of ethylene glycol toxicity were investigated by microanalysis in order to elucidate the structure of the crystals desposited in this condition. About a quart of Prestone II antifreeze was consumed, deliberately, by a young man of 22, who had previously been in good health. Within 6 hours, he was in a state of metabolic acidosis and stupor, which progressed to coma with seizures, 18 hours thereafter. The ethylene glycol level in the blood was 300 mg% and calcium oxalate crystals were noted in the urine. He developed progressive renal shutdown and died following two episodes of cardiac arrest 48 hours after ingestion. The autopsy was performed 9 hours after death. Portions of fresh kidney, brain and liver were submitted for toxicological analysis which showed their ethylene glycol content to be 45 mg%, 107 mg% and 164 mg%, respectively. Routine histology of formalin fixed tissue showed the presence of widespread crystallosis of the viscera. It was most prominent in the kidney within the proximal convoluted tubules in the cortex and the collecting tubules in the papillae. The latter also showed evidence of nephrocalcinosis and focal infiltrates of polymorphonuclear leukocytes. The next heaviest aggregation of crystals was in the brain, where they were found in the walls of the vessels and there was an acute polymorphonuclear leukocyte peri-arteritis.

Polarization microscopy demonstrated well marked birefringence and the brilliant "sheen" of the crystals stood out "like stars on the sea."

Scanning Electron Microscopy. Paraffin sections cut at 10 μ and 1 cm kidney blocks were processed for SEM and examined at 20 KV. Crystalline material was clearly visualized in the tubules (Fig. 1). In the glomeruli, on the parietal layer of Bowman's capsule, there were finer, blade-like, tapering spicules, which measured 2-3 μ. 1 g portions of fixed kidney were digested in 1N NaOH at 100°C in order to separate the crystals from the tissue. SEM of this material showed most of the crystals to have similar morphological features to the ones observed within the tubules. In addition, some prismatic forms were present (Fig. 2).

Energy Dispersive Analysis was performed on all of the above material that had been processed for SEM. The crystalline particles indicated the presence of a strong calcium signal (Fig. 3). This was also present in the areas of nephrocalcinosis in the papillae, but these also had a moderately strong phosphorus signal, which was not present in the crystals.

X-Ray Diffraction was performed on the bulk of the material digested with 1N NaOH. The x-ray diffraction patterns were obtained using a Guinier-De Wolff II, powder diffraction camera (Nonius Corp.). Intensities were measured by scanning the film with a Schoeffel SD3000 (Schoeffel Instrument Corp.).

The x-ray diffraction pattern of the sample contained seven lines corresponding to those of calcite ($CaCO_3$), both as listed in the X-Ray Powder Data File, and as obtained from an authentic sample of calcite run concomitantly. The sample pattern also contained five lines corresponding to those of an authentic sample of calcium oxalate monohydrate ($CaC_2O_4.H_2O$) run concomitantly. In neither case were any major lines from the authentic materials missing from the sample. The sample pattern also contained six lines whose origin could not be identified.

TABLE I

Comparison of Diffraction Patterns

Sample		Calcite[a]		Calcium Oxalate Monohydrate[b]	
d$\overset{o}{A}$	I/I_1	d$\overset{o}{A}$	I/I_1	d$\overset{o}{A}$	I/I_1
5.99	25			5.96	63
4.82	8				
3.83	7	3.86	12		
3.65	9			3.66	100
3.45	11				
3.04	100	3.035	100		
3.02	70				
2.98	16			2.97	63
2.80	27				
2.71	10				
2.50	19	2.495	14	2.50	35
2.36	13			2.36	55
2.29	20	2.285	18		
2.10	21	2.095	18		
1.92	9	1.913	17		
1.87	14	1.875	17		
1.85	11				

[a]X-Ray Powder Data File, American Society For Testing Materials, 1960, O. 644, Card 5-0586

[b]Fisher Scientific Co., Cat. No. C-112, Lot 792311

Conclusion

The sample contains calcite (calcium carbonate) and calcium oxalate monohydrate as major constituents, plus one or more unidentified crystalline compounds.

As a control, 500 mg of the authentic sample of Calcium Oxalate, Monohydrate was processed through all the chemical fixatives and digestion to which the kidney block had been submitted. The x-ray diffraction pattern of the resultant powder was identical in every respect to that of a chemically pure authentic sample of calcium oxalate, monohydrate.

Transmission Electron Microscopy (TEM) of the kidney showed the presence of both electron dense and electron light particulate matter in the tubules and in Bowman's space. A hexagonal pattern was obtained by electron diffraction on the electron dense material.

High Voltage Electron Microscopy (HVEM)

0.5 μ sections were cut from the TEM blocks and were stained with uranyl acetate and lead citrate. They were examined using an accelerating potential of 0.8 MeV and a beam current of 5 microamps. Two reasonably good electron diffraction ring patterns were obtained on electron dense particles, indicating the crystals to be, in fact, aggregates of extremely small crystallites. Hexagonal patterns were also obtained (Fig. 4). Both the hexagonal and ring patterns were compatible with the calcium carbonate (calcite) structure. An occasional tetragonal pattern was observed which was not conclusive, but was considered to be suggestive, of calcium oxalate.

Acknowledgement

Fig. 1 SEM crystals (C) within lumen of proximal tubule (10 μ slide preparation)
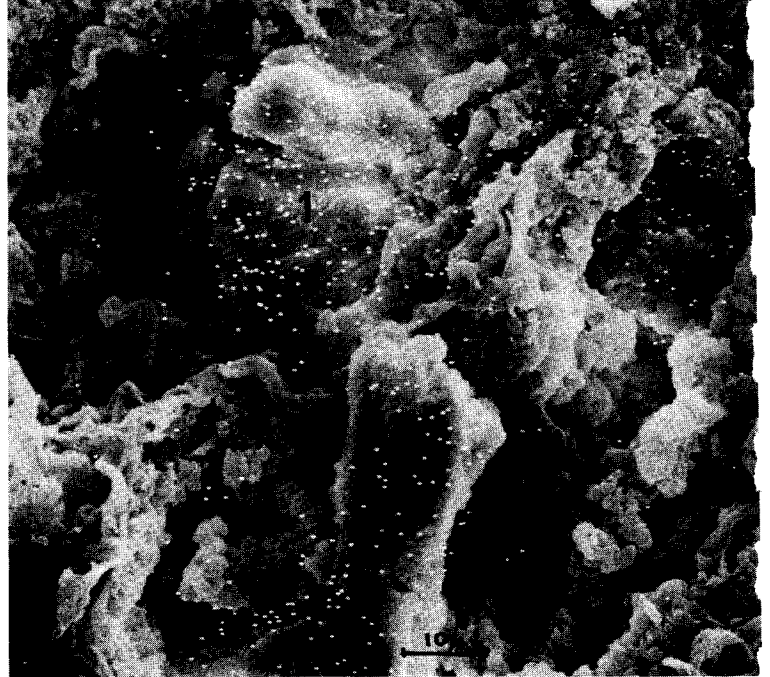
Fig. 3 SEM and X-ray analysis. 3 large crystals (1,2,3) with superimposed Ca K X-ray map

Fig. 2 SEM crystal (C) separated from the kidney. Configuration of a broken prism.

Fig. 4 HVEM Electron diffraction. Hexagonal pattern of CaCO$_3$ (calcite) crystal

PERSPECTIVES IN ELECTRON PROBE MICROANALYSIS

OF BIOLOGICAL SAMPLES KEPT FROZEN

C. Lechene, T. Strunk, R. Warner

Biotechnology Resource in Electron Probe Microanalysis
Laboratory of Human Reproduction and Reproductive Biology
and Department of Physiology, Harvard Medical School
Boston, Massachusetts 02115

and

C. Conty

Cameca, 10.3 Boulevard Saint Denis, 92 Courbevoie, France

The full capability of X-ray spectrometry through electron probe excitation will be expressed when it will be possible to determine and quantitate on the same preparation the elemental content of the cells and of their surrounding fluids; or when it will be possible to evaluate the composition of different cells or of intracellular organelles in a given tissue.

There is not yet a general method of preparation which permits reaching this goal, i.e., which avoids ionic translocation during the sample preparation.

However, the analysis of samples kept frozen hydrated brings very promising perspectives. It is based upon the fact that if the diffusible ions could be analyzed immobilized there will be a minimum likelihood for translocation. And the best way for their immobilization seems to stop them in their matrix by shock freezing the preparation and then by analyzing the preparation kept frozen hydrated.

The problems to be solved are mainly technical. In order to avoid frost, the sample, kept deep frozen, must be introduced in the specimen stage of the electron probe without any contact with ambient air. In order to avoid freeze drying, the sample must be kept at a temperature lower than $-130°C$ to $-150°C$ during the electron probe analysis to maintain the vapor pressure of the specimen ice considerably lower than the vacuum in the column, considering the rewarming of the point being analyzed during the electron beam excitation.

Methods

Two kinds of samples have been analyzed using the cooled sample stage of the Camebax Cameca electron probe.

1. Standard solutions of known composition of sodium chloride were introduced in holes (1mm diameter x 4mm depth) made in a copper block and were shock frozen in liquid nitrogen.

2. Rat kidneys were frozen in isopentane precooled in liquid nitrogen. The kidneys were trimmed with a dental saw in a liquid nitrogen bath. The face to be analyzed was flattened in a cryotome by cutting at $-50°C$.

Then, the entire preparation for both kinds of samples continued in a liquid nitrogen bath. The kidney was put in a special copper holder with the edges of its flat surface applied by pressure on the edges of the copper block. Either of the sample holders was placed within a copper yoke and then within a small teflon container. The sample being still immersed in liquid nitrogen retained in the teflon container was placed in the airlock of the electron probe, isolated from the column. After rough pumping of the nitrogen in the airlock, it is pumped in high vacuum and the teflon holder is lowered exposing the sample which is then introduced in the column with a special tool along a cooled copper slide. The whole operation does not take more than two minutes. In the column, the sample holder is in a shuttle cooled through a copper braid and thermally insulated from the sample displacement mechanism. Slide, copper braid and shuttle are cooled from a Dewar container filled with liquid nitrogen.

The analyses were made at several accelerating voltages and beam currents. Chlorine and potassium were analyzed with a PET crystal and sodium with a TAP.

Discussion and Results

Freeze drying and freeze drying embedding, except in some special applications, have been found unfitted to a general method for preserving ionic distribution. Indeed, during the drying process, "explosions" can be seen within the tissue by microscopic observation. They are likely due to the expansion under vacuum of the gas dissolved and trapped in the tissue and are likely to provoke the sweeping of dry salt crystals by the "wind" of these microcyclones. It should be remembered that profound mechanical distortions are observed by scanning electron microscopy after freeze drying of tissue samples. Moreover, during the drying process, the salt crystal could aggregate and will, by electrostatic attraction or by gravity, move and fall towards the cellular matrix, leaving empty the intercellular, interstitial or intraluminal spaces where the ice has sublimated. For the embedding step it is likely to add mechanical translocation, the salt crystals being swept by the flow of embedding medium filling the cavities of the tissue. These phenomenons are well exemplified in kidneys prepared by such procedures: sodium chloride, although in high concentrations in vivo in the tubular fluid, is practically non-detectable in the nephron lumen after freeze drying or freeze drying embedding (fig. 1 & 2). It was thus extremely important to explore the feasibility of the analysis of samples kept frozen. The following results have been obtained:

i. Shock frozen standard solutions have a homogeneous distribution of the X-ray intensity signals of their elemental content at the micron level of resolution (10 KV, 1 nA). This demonstrates a homogeneous distribution of the salt content immobilized in the ice matrix. This is a necessary condition for the development of a general method for the analysis of diffusible ions in biological tissues.

ii. The X-ray intensity signals from the frozen ice samples are stable and the electron beam does not move, meaning a sufficient electrical and thermal conductivity within the sample. It was noted that even at 2 KV there was apparently no charging effect.

iii. Standard solutions analyzed frozen have provided calibration curves for Na and Cl. It demonstrates the feasibility of quantitative analysis of the elemental content of sample kept frozen hydrated in the $\mu3$ or femto-liter (1.10^{-15}L) range (Fig. 3).

iv. Good scanning secondary electrons picture was observed on the ice standard with a 5 KV accelerating voltage, at 40 pA beam current. In kidney preparations, without any coating, it has been possible to obtain excellent back scattered electrons images from the sample kept frozen (30 KV, 25 nA) (Fig. 4). The localization of the area being analyzed has thus been found surprisingly easy.

v. Intense sodium signals were obtained from the nephron lumen of frozen kidney (Fig. 4). This shows that the sodium content of the sample is preserved by the preparation. However, a lack of homogeneity in the distribution of the sodium signal was observed and was attributed to a possible drying of the sample surface. Such a phenomenon was not observed with the ice standards which had a better thermal contact with the copper holder; it is thus likely due to a deficient thermal conductivity between the tissue sample and the copper holder. This defect could be palliated using special conducting mounting media. It should also be mentioned that whereas the ice standard samples have been prepared just before analysis, the kidneys have been prepared 5 days before analysis and kept in liquid nitrogen where it is possible that they had sublimated on the surface. Also, the kidneys had been rewarmed at -50°C to be flattened by cryocutting, and this step is likely to be avoided.

In any case, it is necessary to ensure that the vapor pressure of the sample ice is always well below the vacuum of the column and that the ice remains below its temperature of transition from the amorphous state (-130°C). To palliate defect in thermal conductivity between the copper sample holder and the specimen and excessive rewarming of the specimen ice by thermal dissipation of the electron beam in the volume being analyzed, the copper specimen holder must thus be maintained well below -150°C. This could be achieved by circulating liquid nitrogen directly in the copper specimen holder.

In conclusion, the analysis of biological samples kept frozen hydrated seems a method of choice; quantitation at the micron level will be relatively easy and imaging has proven not to be a problem. In order to obtain best results, extremely low temperature of the specimen seems to be necessary. Ideally, frozen biological samples could be manipulated and analyzed like alloys or geological samples.
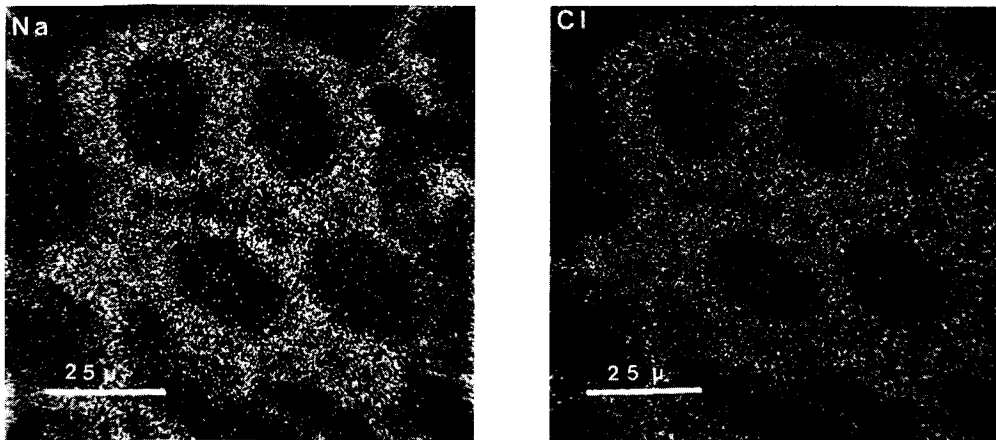
Fig. 1. RAT KIDNEY, FREEZE DRYED SECTION
Frozen section of cortex. .3µ thick. X-ray scan 11KV 25nA
Na: 11,800 count in 103 min. Cl: 10,000 count in 14 min.
No sodium is seen in the lumen and counting rate is six times slower
for sodium compared to chlorine. In vivo, the luminal fluid has
high concentration of sodium, and the whole tissue concentration
is comparable for sodium and chlorine (The counting efficiency
for Cl and for Na was roughly the same).
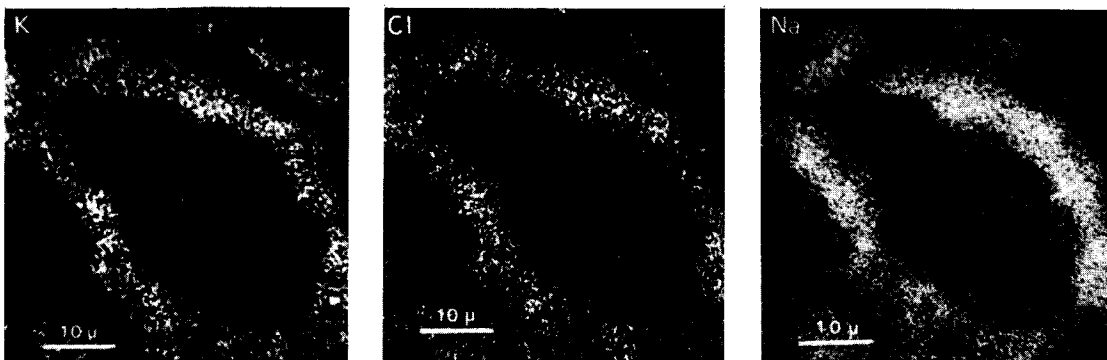
Fig. 2. RAT KIDNEY, FREEZE DRYED EMBEDDED
Cortical tubule. 3µ thick. X-ray scan, 11KV, 100 nA
50,000 counts. K: 6.5 min.; Cl: 22.2 min.; Na: 110 min.
cf legend Fig. 1. Potassium, mainly intracellular, has been
maintained in the cell matrix and gave a high counting rate.
K and Na counting rate should have been relatively the same,
with the K signal detected, as it was in the cells, but a
high Na signal should have been localized in the lumen.
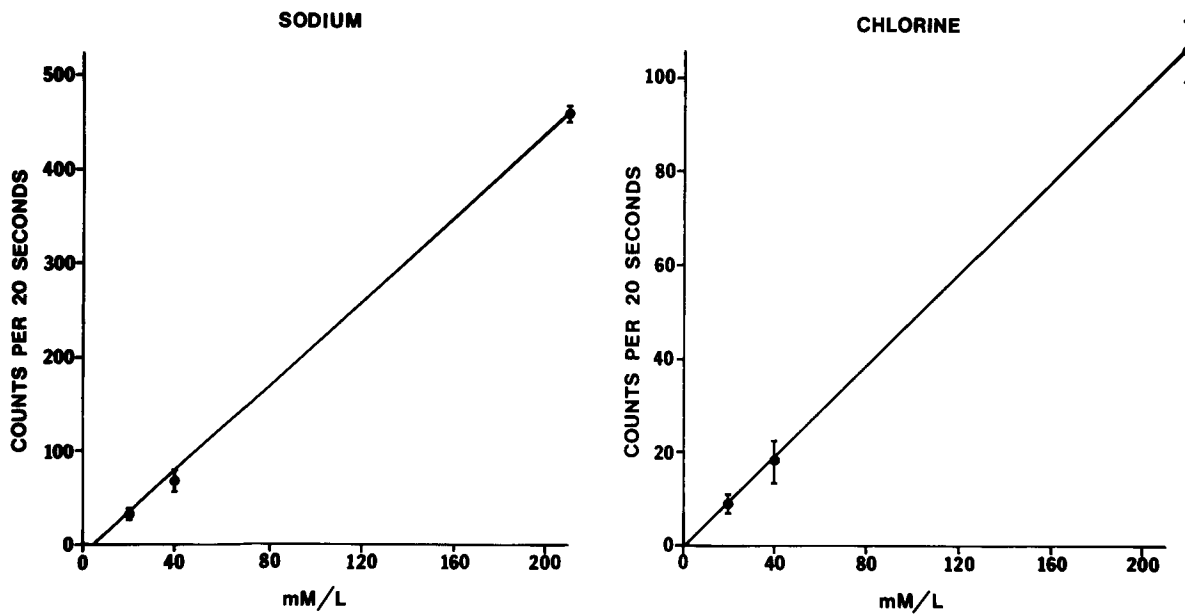
Fig. 3. Calibration curve obtained by electron probe microanalysis. Frozen
solutions containing 20, 40 and 210 mM NaCl. 10 KV, 50µa, <10µ.
The sample was kept frozen at -110°C.
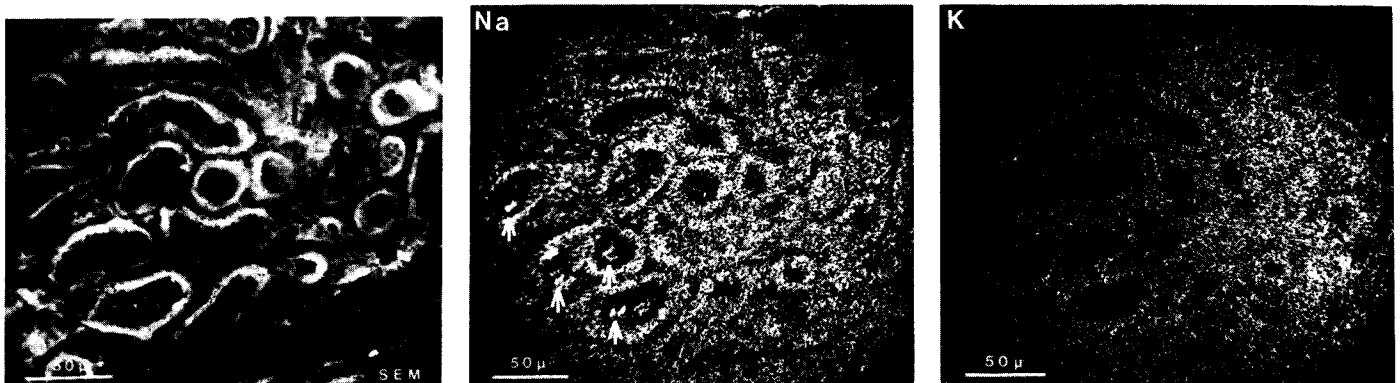
Fig. 4. Backscattered electrons image (30 KV, 25 nA) and X-ray scan of a
frozen hydrated rat kidney (30 KV, 78 nA). Cortex cut flat, Specimen
holder maintained at -110°C. The scanning electrons image shows the
tubule, the lumen well open and the intertubular spaces. The X-ray
scan shows deposits of sodium in the lumen (arrows), but not of potassium.
As should be expected, the count rates were the same for Na and K:
50,000 counts in 10 min.

ENERGY DISPERSIVE X-RAY ANALYSIS OF PICOLITER SAMPLES OF PHYSIOLOGICAL
FLUIDS*

Paul M. Quinton

Department of Physiology, University of California, Los Angeles,
California   90024

Investigations of biological parameters at increasingly refined
levels have sustained interest in methods for analyzing diminishingly
small quantities of biological fluids. This report presents a rapid,
straight forward procedure for elemental analysis of volumes on the
order of 50 picoliters or less using the scanning electron microscope
coupled with energy dispersive X-ray analysis. This technique has
advantages over previously reported methods (1,2,3) in that the pre-
paration is faster, no freeze drying is necessary, and all elements
heavier than flouride can be analized simultaneously.

The analysis is performed by direct reference to a set of standards
prepared simultaneously with unknowns. However, accuracy and repro-
ducibility are critically affected by 1). the geometry of the spot
of residual sample solutes remaining after dessication, and 2). the
crystallization pattern of these solutes.

With respect to controlling the geometry of the sample, consistency
from sample to sample is maximized and X-ray absorption minimized by
causing the sample to spread over a well defined area of constant size
such that the solutes are dispersed in a very thin layer ($< 10^{-9}$ gm/μ^2).
To induce such sample spreading, the area for the spot is prepared
by pipetting, onto a polished berylium (Be) grid under n-decane, a
volume (4) of 40 mM manganese acetate Mn(Ac)$_2$ equal to the volume of
samples to be analyzed. The decane is evaporated, and the droplets
are air dried. The hydroscopic properties of Mn(Ac)$_2$ allow rehydration
of the crystals by moist air which results in the formation of uniform
dome shaped droplets on the Be surface. The rehydrated Mn(Ac)$_2$ droplets
are immersed under mineral oil where an equi-volume sample of an un-
known or standard is added to them.

In order to control cyrstal growth and retain relatively homo-
geneous solute deposits, the samples are flash evaporated: The
mineral oil is washed from the sample grid with 2-3 decane rinses.
Subsequently a vacuum is pulled over the decane bathing the samples
until the decane boiling subsides. The flask is then tilted to
directly expose the droplets to the reduced pressure at which point the
water in the samples vaporizes almost instantly leaving the non-volatile
salts deposited on the grid. The samples are then ready for analysis.
Depending upon the number of samples to be analyzed, the entire procedure
requires less than one hour.

Actual X-ray analysis is accomplished with a Kevex Model 3201
detector and a Kevex 5000 pulse height analyzer attached to a Cambridge
Stereoscan II scanning electron microscope. The beam current,
accelerating voltage (usually 10 KV), raster size (adjusted to surround
sample spot), working distance, and take-off angle (50°) are
maintained constant throughout the analysis. Samples are routinely
counted for 60 seconds at rates of 100,000 - 200,000 CPM including
background.

As may be seen in Fig (1) there is excellent correspondence
(R >.99 for Na , Cl, K) between the total number of characteristic
X-rays and the initial concentration of the element in the sample.
In addition, at least within biological concentration ranges, there
is no significant inter-element interference or absorbance effect.

This approach offers a rapid, accurate means of analyzing
extremely small quantities of fluids for most of the principal
elements present in physiological solutions.
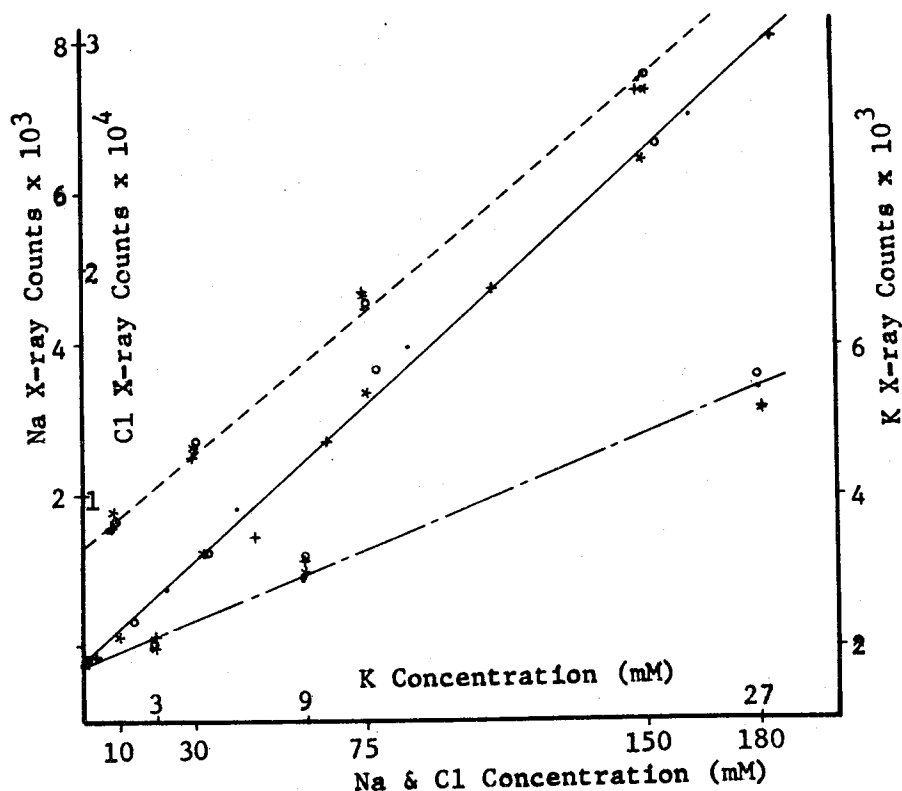
Figure 1. Total Characteristic X-ray Counts vs. Sample Concentration.
Na – – – – – – . Cl ——————. "+" = in presence of 9 mM Ca, 18 mM $MgSO_4$,
27 mM KH_2PO_4; "•" = in presence of 3 mM Ca, 6mM $MgSO_4$, 9 mM KH_2PO_4;
"o" = in presence of 1 mM Ca, 2 mM $MgSO_4$, 3 mM KH_2PO_4; "*" = no other
species present. For K ——————, "+", •, o, and * represent the
presence of 150, 75, 30, and 0 mM NaCl. The excellent correlation (R_{Na} =
.998, R_{Cl} = .997, and R_K = .995) in the presence of varying concentrations
of other elements indicates little, if any, interelement interference. Mg,
P, S, and Ca are not plotted, but all show coeffecients greater than .976.

1. Lechene, C.: Electron Probe Microanalysis of Picoliter Liquid
    Samples, in Microprobe Analysis Applied to Cells and Tissues.
    Academic Press., 351-367 (1974).

2. Garland, H.O., et al. The Application of Quantitative Electron
    Probe Microanalysis to Renal Micropuncture Studies in Amphibians.
    Micron 4: 164-176 (1973).

3. Ingram, Mary Jo, and C.A.M. Hogben. Electrolyte Analysis of
    Biological Fluids with the Electron Microprobe. Analytical
    Biochemistry 18: 54-57 (1967).

4. Quinton, P.M. Construction of Precision Self Filling Microliter
    Volume Pipetts. In Preparation (1975).

SEM Characterization of Respirable Dust in Lung Tissue
Using Ashing and Digestion Techniques

Phillip B. DeNee
Elizebeth R. Walker*
Jerrold L. Abraham

Appalachian Laboratory for Occupational Respiratory Diseases
National Institute for Occupational Safety and Health
Morgantown, West Virginia

*Department of Anatomy, School of Medicine
West Virginia University Medical Center
Morgantown, West Virginia

Inhalation of toxic dust is a common mining and industrial hazard. The identification and characterization of the dust found in samples of human or animal lung tissue is often quite difficult because of the inherent elemental composition of biological tissue. Lung and other tissue contains large amounts of S, K, Ca, P, Na, Cl, Zn, Fe and smaller amounts of other elements such as Cu, Cd, Pb, Ni, Co, etc. Although the inhaled dust particles with an average atomic number 13 (Al) or larger can be easily seen in lung tissue using backscattered electron imaging[1,2,3] they cannot always be adequately analyzed because of the inherent elemental composition of the tissue. This paper evaluates five methods of removing the surrounding tissue to reveal the particles for morphological and X-ray analysis in the SEM. The methods are: 1) low temperature (active oxygen) ashing; 2) high temperature ashing; (3) chemical digestion; 4) chemical digestion followed by low temperature ashing; and 5) low temperature ashing followed by chemical digestion.

Formalin-fixed human lung tissue from a coal miner was paraffin embedded, cut into 5 μm serial sections, mounted on glass slides, and deparaffinized with xylene. Four sections were stained [4] with Hemotoxylin and Eosin, Elastic VanGieson, Reticulum and Trichrome for light microscope histology.

Five sections were air dried and ashed or digested as follows: 1) low temperature ashed in the IPC* Model 101B asher for (24 hours); 2) rinsed in chloroform for 5 minutes, digested in a chlorine bleach (Clorox) for 15 minutes, rinses in 95% ethanol for 1 minute, and rinsed in 100% ethanol for 30 minutes; 3) high temperature ashed in a muffle furnace in air at 750° C. for one hour; 4) digested as in method 2 followed by ashing as in method 1; 5) ashed as in method 1, followed by digestion as method 2.

---

*Mention of specific brand names is for information only and does not imply endorsement by the National Institute for Occupational Safety and Health.

Two sections were neither ashed nor digested to serve as controls. The first was mounted on a glass slide and the second on a carbon planchett. They were critical point dried using CO_2. All seven sections were carbon coated prior to SEM examination.

The sizing of the particles and residual structure and the measurement of the amount of tissue which remained after ashing and/or digestion was done with the aid of an Image Analyzing Computer Model 720.

Figure 1 shows a secondary electron micrograph of the control tissue on a glass slide. The dust particles cannot be distinguished from the cellular material. Although the higher atomic number dust particles can be recognized in the backscattered electron (BSE) image (Fig. 2) the surrounding lung tissue interferes with characterization of the particles. The objective is to eliminate the components of the lung tissue which interfere with X-ray analysis and morphological examination of the dust.

Low temperature ashing was found to remove approximately 75% of the tissue. This technique removes organic material, including coal dust (carbon) particles leaving respirable inorganic dust particles, such as silicas, silicates and pyrites, as well as any other inorganic minerals present in the lung tissue.[5] The mean diameter of 4.5 µm for the residual structure represents inorganic dust particles surrounded by lung tissue residues. The low temperature ashed tissue, Fig. 3, retains the "mineral ghost" of the original lung structure and is valuable for determining the relationship of the inorganic dust to the lung structure.

High temperature ashing was found to remove about 85% of the lung tissue leaving structure which has a mean diameter of 3.5 µm. This technique, like low temperature ashing, removes organic material, leaving the inorganic particles and tissue residue. However, the high temperature (750° C.) causes some changes in chemical structure of the inorganic particles being analyzed. For example, pyrite (FeS) would be oxidized to iron oxide (Fe_2O_3). The method is thus of little use.

Clorox digestion of the lung section (Fig. 4) removes almost all of the tissue. This method digests the organic material, and removes the soluble minerals in the tissue so that the section no longer retains the "mineral ghost" seen with the ashing method. Only respirable dust such as coal and inorganic particles remain. This accounts for the smaller mean diameter (3.1 um) of the residual particles when compared to the ashed sections. BSE imaging (Fig. 5) was especially useful in characterization of the dust particles in the Clorox digested section, since coal particles with a lower atomic number appear darker and inorganic particles such as particles such as silica and iron oxide appear as bright or brighter than the substrate. By this method about half of the particles appeared

to be inorganic and the remainder coal. This method appears best for revealing all the dust for characterization.

One would think that low temperature ashing following Clorox digestion would give the same result as Clorox digestion following low temperature ashing. However, this is not the case.

Low temperature ashing following Clorox digestion (Fig. 6) removes the carbonaceous (coal) particles which remain after the Clorox digestion, resulting in a residue of inorganic particles with a mean diameter of 2 μm. This can be seen in the BSE image (Fig. 7) where all of the particles appear as bright or brighter than the background (glass).

When the low temperature ashing is done prior to Clorox digestion the inherent minerals in the lung tissue appear to be stabilized so that they are not subsequently removed by the Clorox digestion. This leaves a residue of particles with a mean diameter of 2.9 μm. Although this method removes about 90% of the lung tissue, it is not as effective as the prior method for characterization of the inorganic dust particles.

In conclusion, this paper illustrates the selective removal of organic tissue by digestion, ashing or a combination of the two methods. Each technique yields different types of information about the dust particles so that more than one method is essential to the total characterization of respired dust.

References:

1. J. L. Abraham and P. B. DeNee, "Biomedical Applications of Back-scattered Electron Imaging -- One Year's Experience with SEM Histochemistry," in SEM/1974, Proceedings of the Seventh Annual SEM Symposium, IIT Research Institute, Chicago, Illinois, April 1974. P. 251-258.

2. P. B. DeNee, et al., "SEM Identification of Biogenic Silica in Jute: Silica in Human Lung Following Exposure to Burning Jute." Proceedings of the Microbeam Analysis Society of America, Ottawa, Ontario, Canada, Aug. 1974. P. 10A-10G.

3. P. B. DeNee and J. L. Abraham, "SEM Backscattered Electron Imaging -- An Aid To Dust And Particulate Characterization," Proceedings of the Microbeam Analysis Society of America, Ottawa, Ontario, Canada, Aug. 1974. P. 4A-4E.

4. L. G. Luna (ed.), Manual of Histologic Staining Methods of The Armed Forces Institute of Pathology, 3rd ed., McGraw Hill, New York, 1968, 92.

4

5. J. Kruszynski, <u>The microincineration technique and its results</u>,"
    (In English), <u>Handbuch Der Histochemie Band 1/2 Allegmeine
    Methodik,</u> Gustav Fischer Verlag, Stuttgart, Germany 1966, P.
    96-187.

Fig. 1 -- SEM secondary electron image (SE) of 5 μm serial section
         of lung mounted on glass slide. No dust particles can be
         specifically identified.

Figure 1

Figure 2
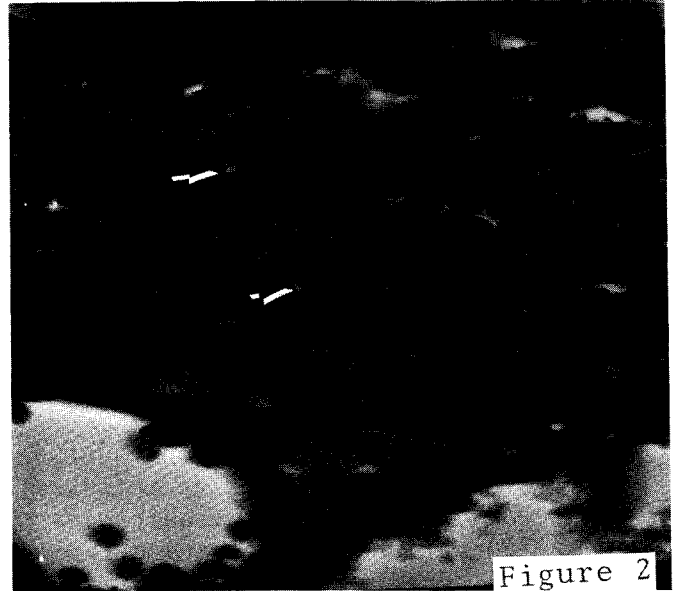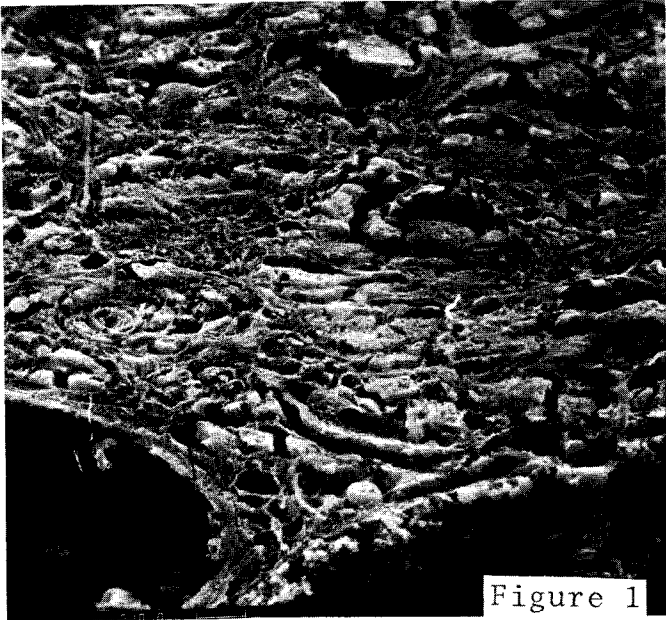
Fig. 2 -- SEM, backscattered electron image (BSE) of identical area
         seen in Fig. 1. Several particles (arrow) appear brighter
         than the surrounding organic tissue, indicating that they
         have a higher backscatter coefficient.

Figure 3
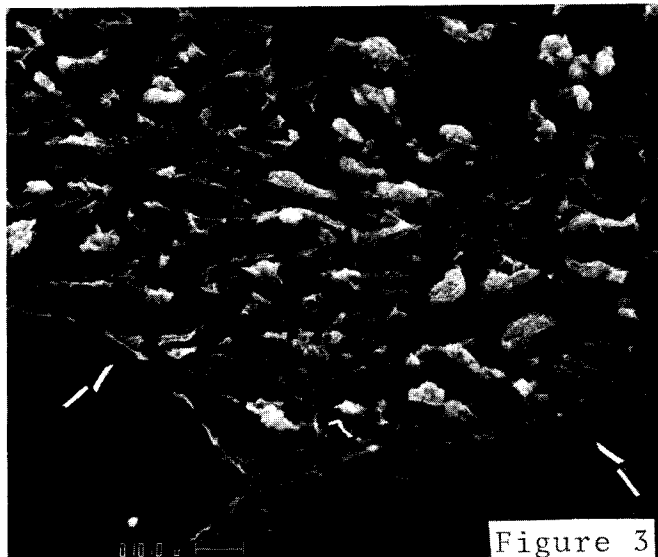
Fig. 3 -- SEM, SE image of 5 μm serial section of lung tissue which
         had been low temperature ashed. Note the "mineral ghost"
         of the lung tissue (arrow).

Note: All micrographs were taken at 20 kV and 45° tilt.

Fig. 4 -- SEM, SE image of 5 μm serial section of lung tissue which
had been Clorox digested. Note some clustering of
particles, presumably ghosts of macrophages.
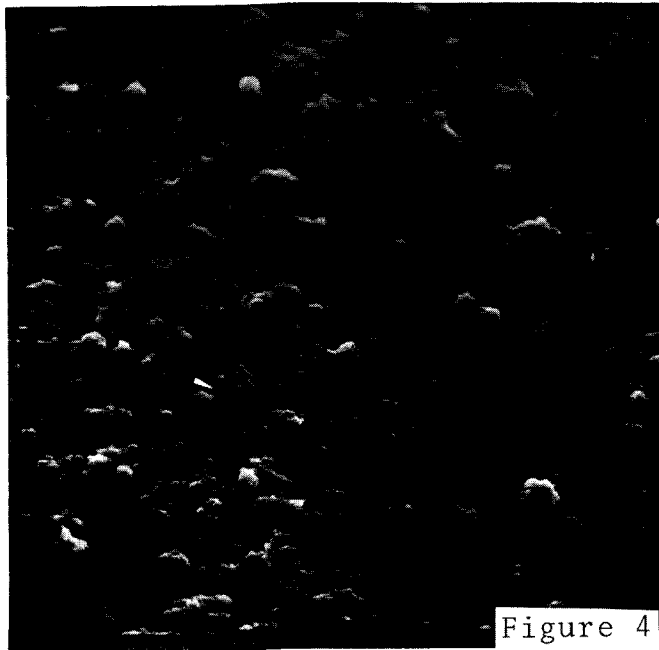
Figure 4
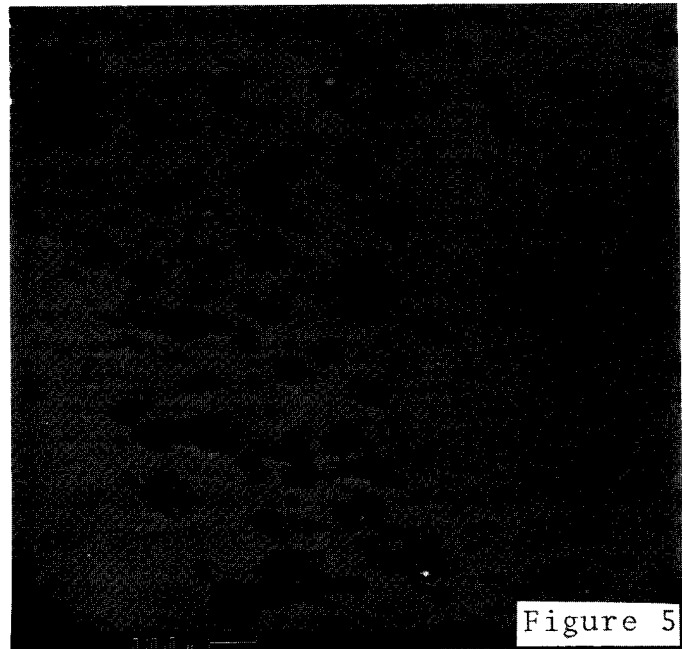
Figure 5

Fig. 5 -- SEM, BSE image of identical area seen in Fig. 4. Approxi-
mately half the particles appear darker than the back-
ground (glass) indicating that they have a lower backscatter
coefficient and are presumed to be coal (carbon). Thus
after digestion, both carbonaceous (coal) and inorganic
particles remain.
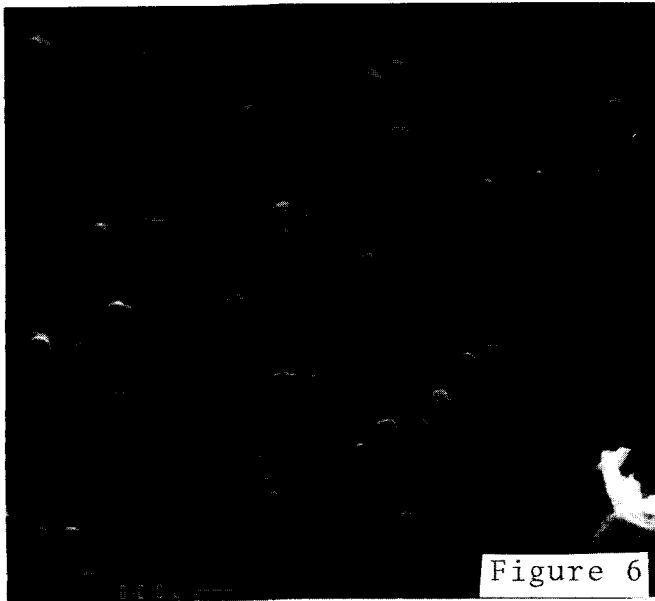
Figure 6
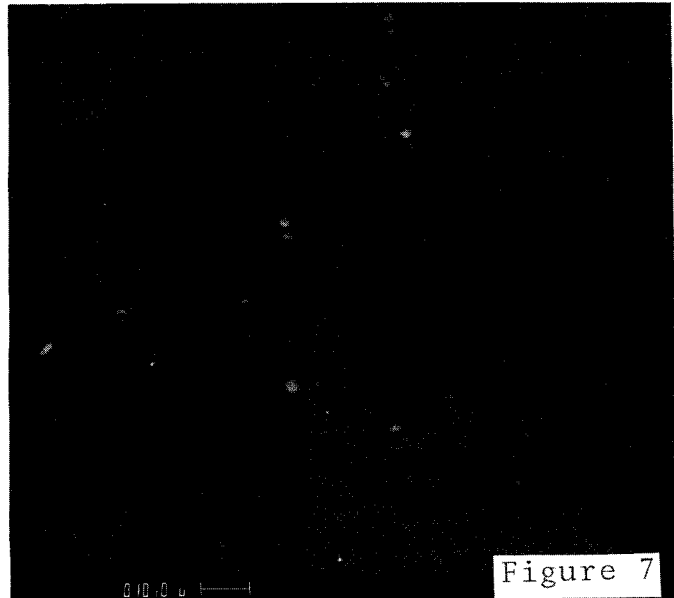
Figure 7

Fig. 6 -- SEM, SE image of 5 μm serial section of lung tissue which
had been Clorox digested prior to low temperature ashing.
Note that there are fewer particles and fewer clusters of
particles.

Fig. 7 -- SEM, BSE image of identical area seen in Fig. 6. None of
the particles appear darker than the background (glass).
This suggests that most or all the carbonaceous particles
which remain after digestion have been removed leaving
only the inorganic particles.

MEASUREMENT OF SURFACE VOLTAGES USING THE VOLTAGE DEPENDENCE OF X-RAY INTENSITIES

C.J. Wu and D.B. Wittry

Department of Materials Science
and Electrical Engineering
University of Southern California
Los Angeles, California 90007

When a semi-insulating specimen is bombarded by a focussed electron beam a surface charging potential will result. Since many of the signals available from the interaction of electron beam with a solid target are voltage dependent, it is important to know how the surface potential changes for a wide variety of materials and different beam currents and voltages. The case of semi-insulating GaAs has been discussed theoretically and experimently in a previous paper by Wittry and Wu[1]. In that paper, it was indicated that the surface charging voltage Vs can be deduced by a shift of the x-ray intensity vs voltage curves for high resistivity material compared with low resistivity material as shown in Fig. 1. For such experiments, either a crystal spectrometer or a gas flow proportional counter could be used. The first case involves the voltage dependence of intensities of characteristic x-ray lines, while the second case involves the voltage dependence of that portion of the x-ray continuum which lies above the absorption edge of the gas used in the counter. From Fig. 1 it appears that the use of the x-ray continuum has important advantages over the use of characteristic lines. These advantages include greater sensitivity due to higher counting rates and steeper $I(E_0)$ curves and also the use of simpler, less expensive instrumentation. The purpose of the present paper is to verify that these results are expected from theory.

In the present work we used a flow proportional counter constructed from $\frac{1}{4}$" O.D. thin wall stainless steel tubing, insulators made from glass tubing, a centeral stainless steel wire of 4 mil dia. and a window of household aluminum foil. Two diametrically opposed slots (1/16" x 3/4") were cut in the tube parallel to the axis by spark machining. The aluminum foil, window, the insulators and the central wire were sealed together with low vapor pressure epoxy. The typical operating voltage was 1500 volts and the maximum theoretical efficiency (for photons of energy $E_\nu = 5.6$ keV) was 13.5%. With the detector located on top of the objective lens in the EMX-SM, the detector to specimen distance was 1.72" and the solid angle subtended by the window was 1.552×10^{-2} steradians. A Hammer pulse height analyzer was used in the integral mode with the threshold set at the minimum in the pulse height distribution (corresponding to photon energy $E_\nu \approx 3.2$ keV).

The expected x-ray continuum intensities (in counts/second) were calculated using the following equation:

$$I = \int_{h\nu_{min}}^{h\nu=E_o} \frac{I_\nu(E_o)}{E_\nu} f(\chi) R \epsilon S (I_B/e) \, d(h\nu) \tag{1}$$

where $I_\nu(E_o)$ is the energy generated per electron for the x-ray continuum having frequency ν, E_ν is the photon energy, E_o is the electron beam energy, $f(\chi)$ is the absorption correction factor, R is the backscattering correction factor, ϵ is the calculated efficiency of the counter, S is the solid angle factor and (I_B/e) is the number of electrons/second striking the specimen. For $I_\nu(E_o)$ we assumed Kramers' equation[2]

$$I_\nu(E_o) = kZ(E_o - E_\nu) \tag{2}$$

where Z is the atomic number of the target and k is a constant. The value of k given by Compton and Allison[3] is $2.2 \cdot 10^{-6}$ if I_ν is expressed in keV/keV energy interval and E_ν, E_o are in keV. This is comparable with experimental values of Dyson[4], and Green[5] and is reasonable agreement with Kirkpatrick and Wiedmann's[6] theoretical value of $2.6 \cdot 10^{-6}$. For $f(\chi)$ we used Philibert equation[7] as modified by Heinrich[8] and mass absorption coefficients given by Heinrich[9]. For R, we used values for the x-ray continuum given by Rao-Sahib and Wittry[10]. The calculation for efficiency took account of window absorption and detector absorption (neglecting absorption of the methane in the P-10 gas used in the counter) also using Heinrich's absorption coefficients. S was calculated from the geometry and I_B was measured on a Faraday cage.

Comparison of theory and experiment is shown in Fig. 2. The agreement is remarkable for voltages less than 10 keV in view of the fact that early work which lead to $k \approx 2.2 \cdot 10^{-6}$ did not include all of the corrections used here. The discrepancy for voltages above 10 keV is due mainly to the K characteristic radiation of Ga and As having critical excitation potentials of 9.24 keV and 10.53 keV respectively. This is demonstrated in Fig. 3 which shows a plot of $(I_{expt} - I_{theo})^{1/1.65}$ vs E_o using $k = 1.94 \cdot 10^{-6}$ in Eq. (2). This figure shows that the excess intensities varies approximately as $I \propto (E_o - E_c)^{1.65}$ which is expected for characteristic lines[11].

In summary, we have demonstrated the usefulness of a technique for measuring surface charging voltage based on detection of the x-ray continuum using a proportional counter with an abrupt discontinuity in detector efficiency. Because the continuum intensity detected increases rapidly as the electron beam voltage increases above the absorption edge this technique can provide greater sensitivity for surface voltage measurements than techniques based on characteristic x-ray lines. We have also verified that the numerical constant in

Kramers' equation (for appropriate units) is $2.2 \cdot 10^{-6}$ to an accuracy of $\pm 10\%$ for photons whose energy is ≥ 3.2 keV and for beam voltages ≤ 10 keV.

References

1. D. B. Wittry and C. J. Wu, "The Charging of Semi-Insulating Specimens in Electron Microprobe Instruments", Proc. 8th Annual Scanning Electron Microscopy Symp., IITRI (1975).

2. H. A. Kramers, Phil. Mag., 46, 836 (1923).

3. A. H. Compton and S. K. Allison, X-rays in Theory and Experiment, (D. Van Nostrand, New York, 1935), p. 90.

4. N. A. Dyson, Proc. Phys. Soc., 73, 924 (1959).

5. M. Green, Ph.D. Thesis (Univ. of Cambridge, 1962), p.63.

6. P. Kirkpatrick and L. Wiedmann, Phys. Rev., 67, 321 (1945).

7. J. Philibert, X-ray Optics and X-ray Microanalysis, (Academic Press, New York, 1963), pp. 379-392.

8. K.F.J. Heinrich, "The Absorption Correction Model for Microprobe Analysis", 2nd Nat. Con. on Electron Microprobe Analysis, p. 7, (1967).

9. K.F.J. Heinrich, "X-ray Absorption Uncertainty", in The Electron Microprobe, Ed. T.D. McKinley, K.F.J. Heinrich and D.B. Wittry, (Wiley, New York, 1966), pp. 296-377.

10. T. S. Rao-Sahib and D. B. Wittry, Proc. of 6th International Conference on X-ray Optics and Microanalysis, pp. 131-137, (1972).

11. A. H. Compton and S. K. Allison, in Ref. 3, p. 81.
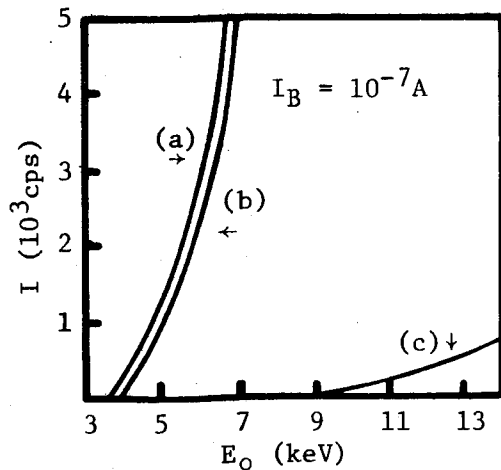
Fig. 1 X-ray intensity vs voltage for GaAs specimens.
(a): prop. counter, low ρ.
(b): prop. counter, high ρ.
(c): crystal spectrometer (GaKα), low ρ.
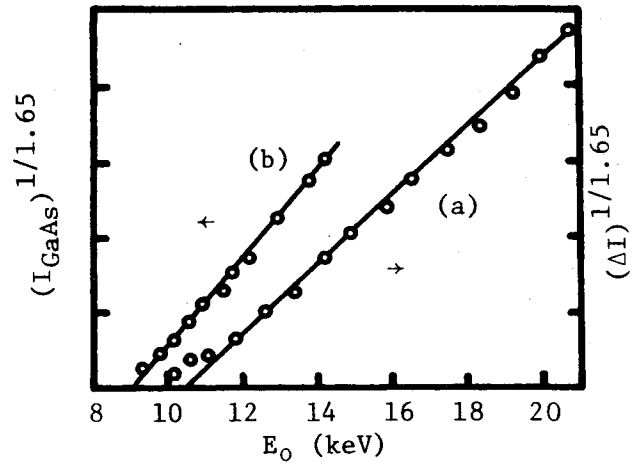
Fig. 3 Difference between theory and experiment for continuum x-ray intensity detected ($\Delta I = I_{exp} - I_{th}$) as a function of beam energy E_0 (a). Intensity of GaKα using crystal spectrometer (b).
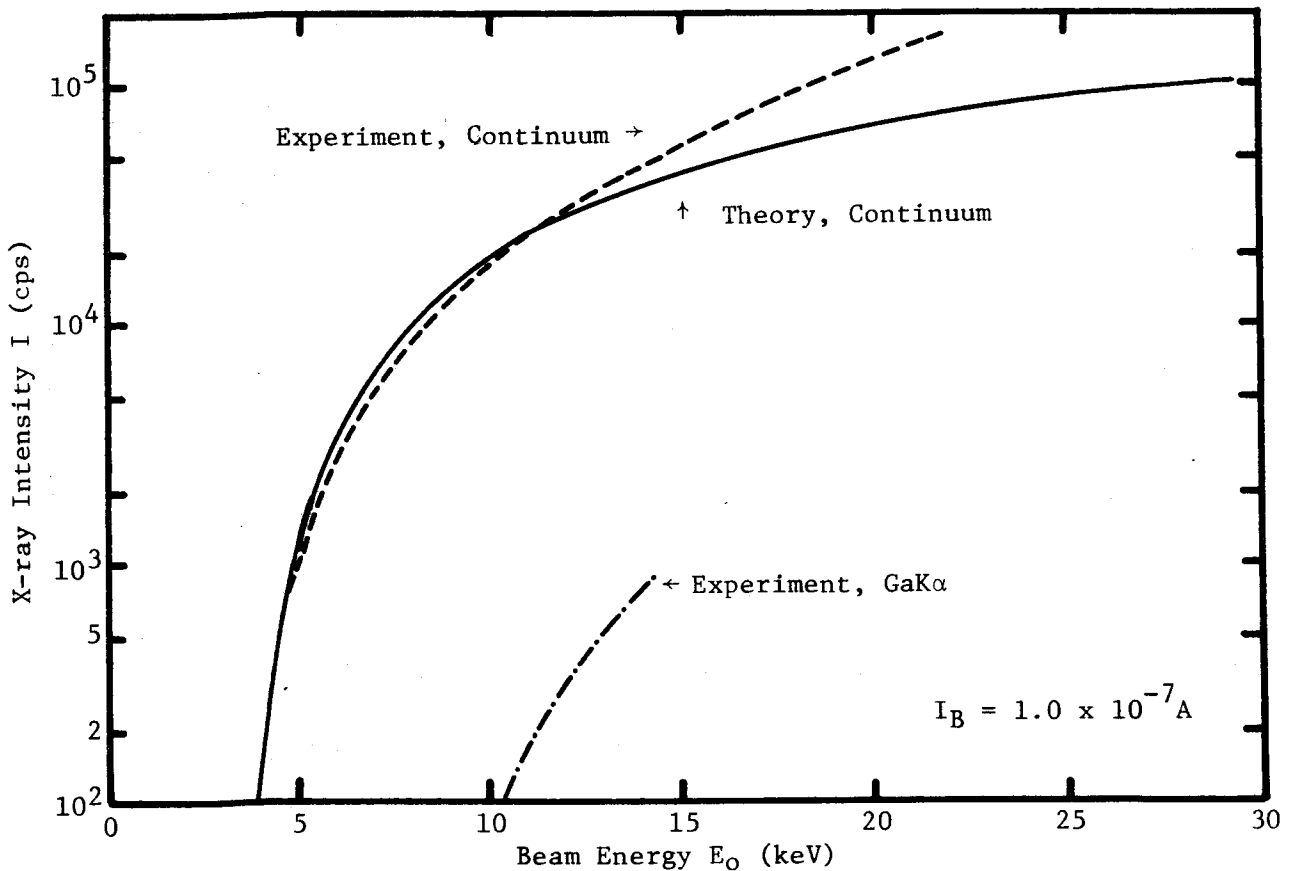
Fig. 2 Comparison of theoretical/observed results for a gas flow proportional counter and observed results for a crystal spectrometer.

PRACTICAL APPLICATIONS OF AUTOMATED MICROPROBE ANALYSIS

W.T. Hatfield, R.B. Bolon and E. Lifshin

General Electric Corporate Research and Development

The microprobe automation system described previously by the authors [1] has been successfully applied to a variety of problems. The computer hardware includes a 64K byte Interdata 70 equipped with tape cassettes, a 1.2 million word disc, high speed paper tape and card readers, a line printer, a plotter and a number of teletypes. Serial asynchronous communication at 1200 baud with Canberra Datanim electronics is used to control a Cameca MS64 electron microprobe and a JEOL JXA50A combination microprobe scanning electron microscope. Energy dispersive data from the latter instrument accumulated in a Northern Scientific model 630 Multichannel Analyzer is read into the computer through a interrupt driven parallel interface.

A real time operating system with appropriate hardware and software drivers for all of the above mentioned peripherals makes it possible to interlace simultaneously operating user programs written in FORTRAN with instrument control and data acquisition functions. On the JEOL JXA50A the computer controls the X,Y,Z sample position coordinates, beam blanking and positioning, scalers and timer, specimen current reading, crystal spectrometer settings, and crystal selection. Control over the multichannel analyzer includes initiating a reading and transfer of spectra into the computer. The controllable features of the Cameca are limited to X and Y sample positioning, crystal tuning and scaler start and readout.

When the JXA50A is run in the automated mode the operator first pre-indexes the points to be analyzed by optically locating them using a remote position control box. The coordinates of each point are automatically recorded by entering a carriage return on a nearby teletype. Input of elemental symbols and other initializing information then results in automatic crystal selection, positioning of standards, spectrometer tuning, and complete data recording. A modified version of the NBS program FRAME[2] is used for conversion of the raw x-ray data into chemical composition.

In cases where sample position reproducibility was considered to be inadequate (<2 microns) for multiple passes with the two spectrometers on the JEOL JXA50A, the solid state detector often proved to be an effective method for collecting entire spectra in a single pass. Figures 1b and 2b illustrate the results obtained from quantitative step scans across Co-Ce diffusion couples formed at 700°C and 650°C respectively. This study[3] provided evidence that the important magnetic Co_5Ce phase which is stable at 700°C, undergoes a eutectoidal decomposition into the non-magnetic $Co_{19}Ce_5$ and $Co_{17}Ce_2$ phases somewhere above 650°C. It is interesting to note that the $Co_{17}Ce_2$ phase in the 700°C sample is about $4\mu m$ wide and was not successfully analyzed using the crystal spectrometers and successive passes. This effect is believed to be due to beam drift rather than mechanical reproducibility.

REFERENCES

1. W.T. Hatfield, M.F. Ciccarelli, R.B. Bolon and E. Lifshin, A Real Time Approach to Laboratory Automation, Ninth Annual Conference of the Microbeam Analysis Society, Ottawa, Canada, 1974

2. H. Yakowitz, R.L. Myklebust and K.F.J. Heinrich, FRAME, NBS Technical Note 796, Oct. (1973), U.S. Dept. of Commerce

3. D.L. Martin, J.G. Smeggil, W.T. Hatfield and R.B. Bolon, Eutectoid Decomposition of Co_5Ce, IEEE Trans. Magnetics, Vol. MAG-11, Sept. 1975 (to be published)
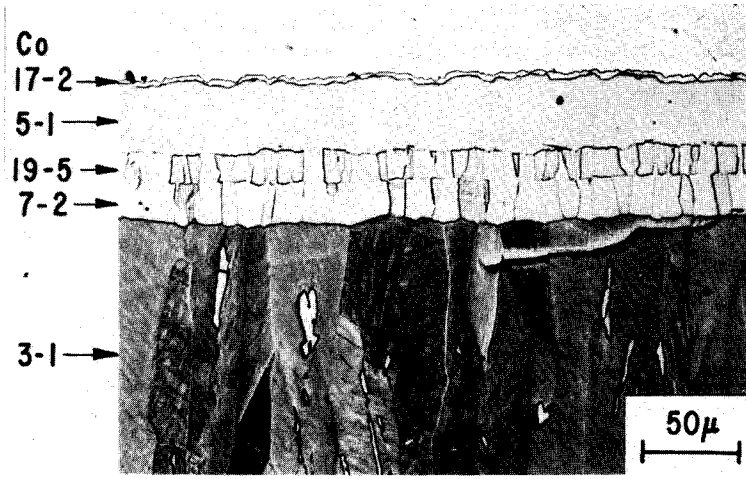
FIGURE la   Optical micrograph of a Co-Ce diffusion couple
formed by heating 620 hours at 700°C. Sample
was etched following analysis to reveal phase
structure
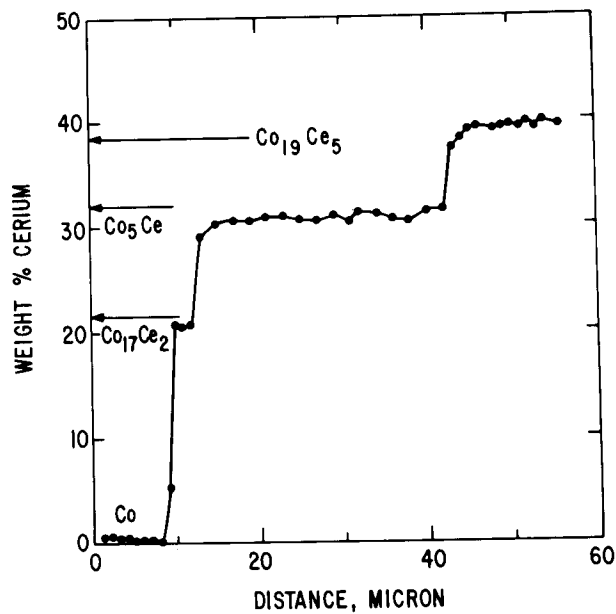
FIGURE lb   Quantitative step scan profile for Ce in the
above diffusion couples obtained with an auto-
mated JXA50A using energy dispersive x-ray data.

Co

17-2 →

19-5 →

7-2 →

3-1 →

20μ
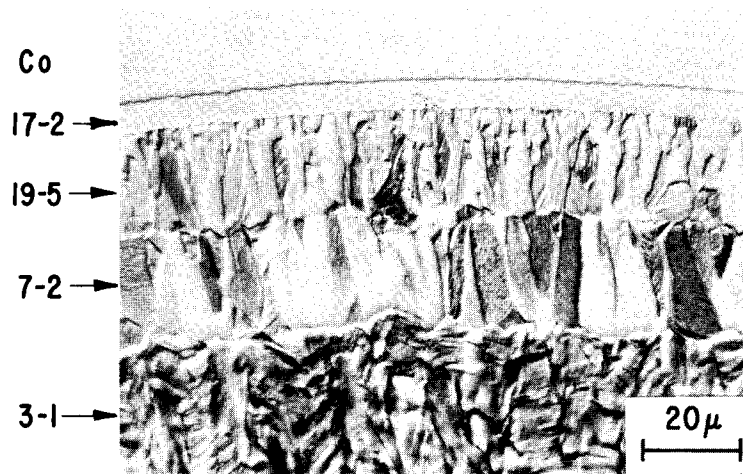
FIGURE 2a   Same as 1a for a diffusion couple formed by heating 1250 hours at 650°C.
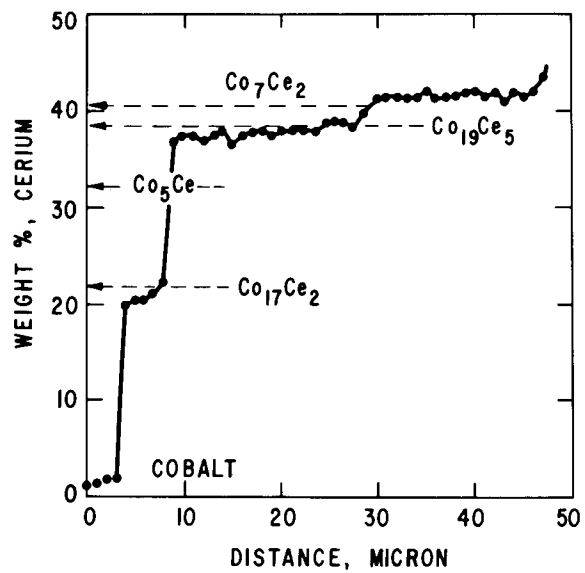
FIGURE 2b   Same as 1b

Automated Characterization
of Particulates and Inclusions
by Computer-Controlled SEM/Probe

M.R. Hoover, E.W. White, J. Lebiedzik, G.G. Johnson

One of the major difficulties with the conventional SEM/probe for characterization of individual features such as dispersed particles or inclusions is the large amount of tedious work required to position the beam on the specimen, collect and reduce the data. Ideally, one should collect data for numerous features in order to obtain statistically meaningful results. It would also be very desirable to have a system which could analyze a wide range of particle sizes and give a quick x-ray analysis of each particle. Our solution to this problem has been the development of an automated SEM/probe interfaced to a PDP 11/20 minicomputer. The mini controls the beam scanning, stop position, x-ray collection, and sampling of the SEM.

A JEOL 50A scanning electron microscope was interfaced to a DEC PDP 11/20 using the DEC DR11-A general purpose interface and a special purpose control and data acquisition system designed for this and similar applications (ref. 2). Both wavelength dispersive and an energy dispersive detector are used. The electron beam is controlled by the computer through a digital scan generator (ref. 3) equipped with all the necessary hardware for random computer beam positioning within a 4096 X 4096 picture point matrix. An analog comparator (ref. 4) serves as a particle or feature detector by the comparison of the brightness of every picture point with a preset threshold level. The threshold level and the video signal are monitored by a dual trace monitor oscilloscope thus allowing easy selection and adjustment of the threshold level.

The software for the system is written in FORTRAN IV with a few assembler language subroutines as device handlers. Essentially, the system consists of a main program which interacts with the user, and a collection of specialized subroutines for performing specific functions. The user may specify the magnification (not controlled by the computer but needed for proper scaling of the results), picture point density, scan rate, x-ray counting time per point, shapes for analysis, and the number of frames to be analyzed. Upon the completion of the data collection, the user can get, if desired, histograms, plots, and tables of his results.

The selected field of view is step scanned at a high scan rate using a coarse picture point grid. As soon as a particle is detected, the picture point density is increased to give a higher on-feature resolution. A process of bisecting successive vertical and horizontal diameters is used to locate the center of the particle. Once the center has been found, a set of eight particle diameters is collected (vertical, horizontal, 22.5°, 45°, 67.5°, 112.5°, 135°, and 157.5°).

The beam is then moved to the center of the particle in order to accumulate a statistically valid x-ray count for up to 16 elements. Taking a preset count at the center of each particle allows one to adjust the dwell time to obtain a statistically meaningful x-ray count.

In conclusion, we have developed an automated SEM/probe system for the characterization of particulates and dispersed inclusions according to size, shape, and chemistry. The system requires a minimum of operator interaction. At present, we have not completed the software for treating a particle as a complete chemical unknown. The system is of course limited by the inherent resolution and uncertainty problems of an electron beam that is susceptible to stray magnetic fields. However, the advantages of this system include 1) a very rapid search for particles using a coarse picture point grid and a high speed scan, 2) a high picture point density for "on field" analysis which in effect gives a high resolution (even at low magnifications), 3) a pre-screening of particle shapes so time is not wasted analyzing particles that are not of interest, 4) rapid characterization of a wide range of particle sizes, 5) maximization of the efficiency of x-ray analysis, and 6) a better x-ray analysis of sub-micron particles which do not normally provide good x-ray counts. This system has been used in the analysis of respirable coal mine dusts, mineral inclusions in polished coal sections, and for the identification and analysis of asbestos fibers.

1. Hoover, M.R., J. Lebiedzik, G.G. Johnson and E.W. White, "Laboratory Automation of SEM Image Analysis Using a PDP 11/20", presented as the DECUS Spring 1973 Symposium.

2. Lebiedzik, J., "Multiple Electron Detector Method for Quantitative Microtopographic Characterization in the SEM." Ph.D. Thesis, The Pennsylvaina State University, 1975.

3. Lebiedzik, J. and White, E.W., "Simple Methods for Automatic Quantative Analysis of SEM and Probe Images." Proceedings of the Sixth National Conference of Electron Probe Analysis. July 27-30, 1971, pittsburgh, pa.

4. Lebiedzik, J. "New methods for Quantitative Particulate and Micro-structural Characterization by SEM." M.S. Thesis, 1972, The Pennsylvania State University.

REPRODUCIBILITY AND OPERATOR BIAS IN A COMPUTER-CONTROLLED
SYSTEM FOR QUANTITATIVE ELECTRON MICROPROBE ANALYSIS

D. E. Champion, A. L. Albee, and A. A. Chodos

Division of Geological and Planetary Sciences
California Institute of Technology*
Pasadena, California 91125

The ULTIMATE program (Chodos et al, 1973) for controlling electron micro-probe analysis was designed with the goal of enabling unskilled operators to perform quantitative analyses as accurately as skilled operators. Statistical analysis of the results obtained on "known samples" by a variety of operators indicate that this goal has been achieved and that the reproducibility is about 1 1/2 to 3 times the counting statistics error for the various elements.

The system consists of a MAC-5 SA3 electron microprobe with a 12K PDP-8L minicomputer and a Tennecomp TP-1371 cartridge tape deck. ULTIMATE is optimized for the quantitative analysis of silicates and oxides and controls essentially all analytical operations. The analysis is performed, corrected, and typed out without operator intervention except for point selection and focusing. Moreover, a single mount of master standards is utilized for all analyses, most of these standards being simple stoichiometric compounds or pure oxides.

Two "known samples", containing the most common elements of natural silicates were analyzed at the beginning of each day of quantitative analysis and typically during the course of long runs (up to 18 hours). These analyses provide a check on the initial setup as well as a running monitor of reproducibility, operator bias, changes in the hardware or software system, etc.

The statistical analysis covers the period from 12/20/73 to 1/21/75, the time interval over which the current version of ULTIMATE has been used without significant software changes. During that time 9 different operators have preformed 333 analyses of the "known samples", 157 of McGetchin garnet and 176 of Leilenkopf sanidine. Five principal operators have performed 279 of these as follows: Operator (A) 65 garnet/60 sanidine; (B) 31/24; (C) 27/35; (D) 10/8; and (E) 7/12. The number of analyses is roughly proportional to their experience;

the operator with the smallest number having had 4 hours of actual instruction before beginning the analyses reported here.

Two operational changes occurred during this time interval. On August 19, 1974 a new master standard was introduced. For the most part it contains the same standards as the previous master standard, but the use of different grains of the standards and of the "known samples" introduced the possibility of bias between the old and new standards. The second change, on April 25, 1974, involved a change in focusing technique, which effectively reduces differences in focusing between individuals. Focusing is accomplished by sharpening the image of the field aperture diaphragm on the surface of the sample, rather than by sharpening the image of the field of view in the usual manner.

The statistical study compared splits of the total group of analyses coinciding with the various changes in the operating system to detect the sources of variance in the analyses. The items examined were: analytical reproducibility, operator bias, differences in composition of standard and "known sample" grains in the old and new mounts, and improvement introduced by the change in focusing technique.

ULTIMATE was written to minimize operator intervention, and to limit operator bias. This bias was tested by comparing each operator's results with the total group of analyses. Figure 1 shows the means and standard deviations for the total group of analyses and for each principal operator. In addition, the variance due to counting statistics for a single analysis is shown by a dashed line on the figure. ULTIMATE specifies counting statistics of 1 percent or better for elements with oxide concentrations in excess of 1 percent in both sample and standard. Hence, the combined variance introduced by counting statistics is about 1 1/2 percent. Figure 1 illustrates that the standard deviations for the entire group of analyses, which we take as our analytical reproducibility, are typically less than twice that introduced by the counting statistics.

The principal operators varied in experience from 65 to 7 analytical days in the 13 month period. Nevertheless, all of these operators have mean values for a given oxide well within the standard deviation of the total group of analyses and commonly within the standard deviation of the counting statistics.

An exception is in the FeO analyses of Leilenkoff sanidine for which operator E has a mean value much in excess of that for the total group of analyses. Inspection showed that these analyses were bimodal with one set in close agreement with the other operators and another much different (See Fig. 1). It was found that in modifying his tape of ULTIMATE to permit analysis for SrO an error had been introduced into the background correction for FeO. Thus, a significant error occurred in those analyses of low FeO samples (such as Leilenkopf sanidine) in which SrO was analyzed.

It was believed that the standardization of the focusing procedure would reduce the size of the standard deviation for a given oxide analysis and better constrain the value of the mean. The effect of changing the focusing procedures was tested by comparing standard deviations for analyses obtained before and after the change for the entire group of analyses and for each of the three principal operators. Since as many standard deviations increased as decreased, there is no clear evidence of improvement for most oxides. Apparently other sources of variance obfuscate any potential improvement. A possible exception is SiO_2, which shows a clear improvement in the size of the standard deviations for the total group of analyses and for all 3 principal operators. The SiO_2 standard (quartz) has a very high polish so that it is rather difficult to focus on its surface. Thus, the focusing procedure using the field aperture diaphragm may significantly reduce the size of the standard deviation for a highly polished sample.

The effect of introducing a new set of grains of the standards and of the "known samples" was also studied. Analyses of the two mounts were statistically analyzed to see if there was any change in the mean values of the analyzed oxides. Results show that 5 of the 8 oxides in McGetchin garnet and 1 of 6 oxides in Leilenkopf sanidine in the new mount have significantly different means at the 99 percent confidence level from the old mount. It should be stressed that while these changes in the means have statistical significance, they are very small and are not of chemical significance. Of the 3 oxides which are analyzed in both the garnet and the sanidine -- SiO_2, Al_2O_3, and FeO -- only those in McGetchin garnet show a significant change. Hence, these statistically-significant changes seem to originate in system-operating conditions or in inhomogenieties in the "known samples", but not in differences between the standards themselves. Chronological splits of 35, 50, and the entire 70 analyses for the period subsequent to the change

of standard mounts typically show a consistent sense of change from the earlier mean value of a given oxide for a given mineral, although the amount of change fluctuates. Thus it seems most likely that we are seeing a slight linear drift somewhere in the operating system. Such statistical analysis provides a means of detecting instrumental problems early.

The results of the statistical study affirm the uniformity and stability of the operating system and ULTIMATE.

REFERENCES

A. A. Chodos, A. L. Albee, A. J. Gancarz and J. Laird (1973) Optimization of computer-controlled quantitative analyses of minerals. Proc. 8th Nat. Conf. on Electron Probe Analyses. New Orleans. La.

McGetchin Garnet

Leilenkopf Sanidine

A B C D E
(60) (24) (35) (8) (12)

Na$_2$O

SiO$_2$

FeO

Al$_2$O$_3$

K$_2$O

BaO

A B   Principal analysts
(60)(24)   Number of analyses

Na$_2$O

Mean & ±1σ for analyst B

Mean & ±1σ for all analysts
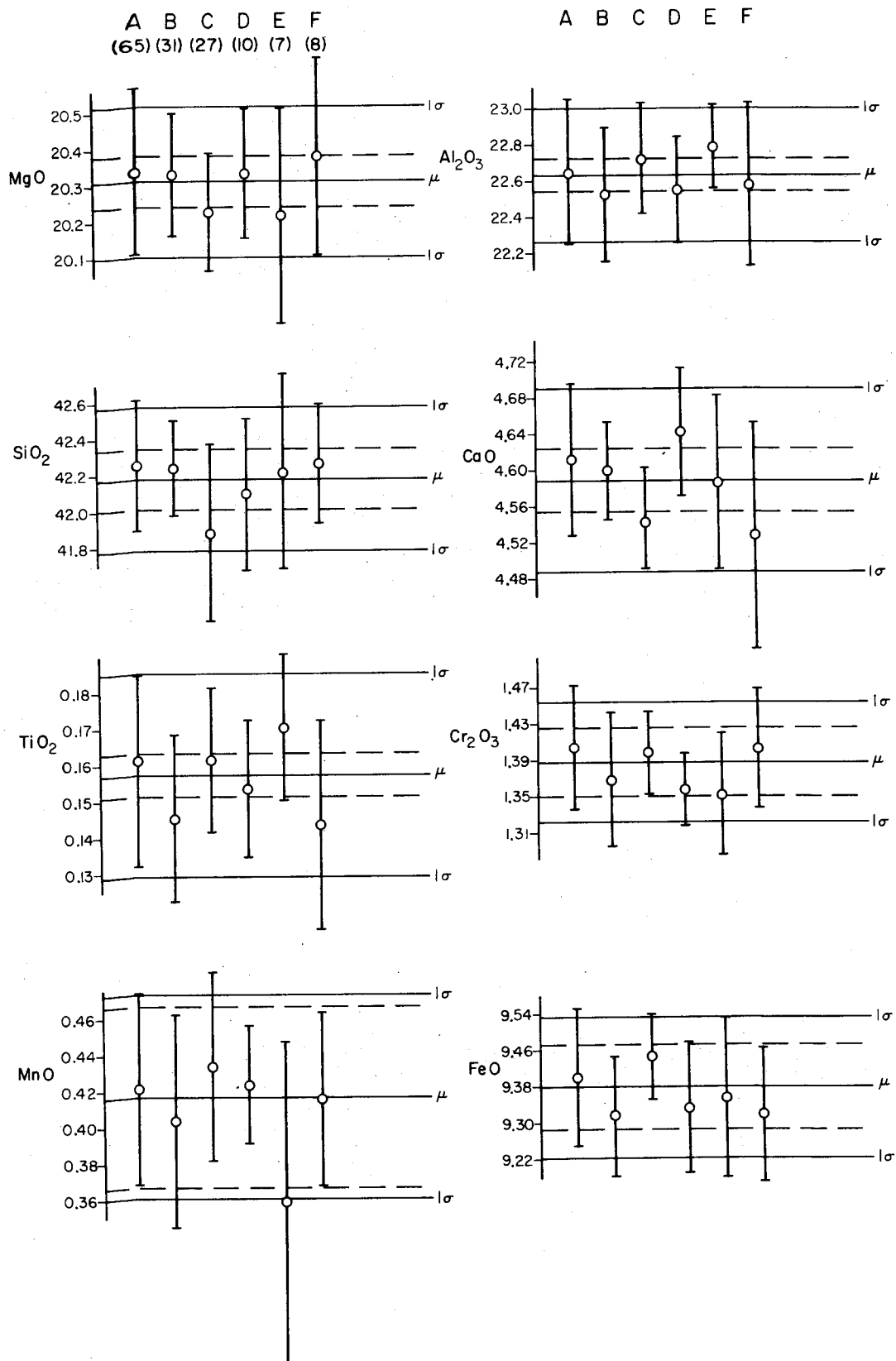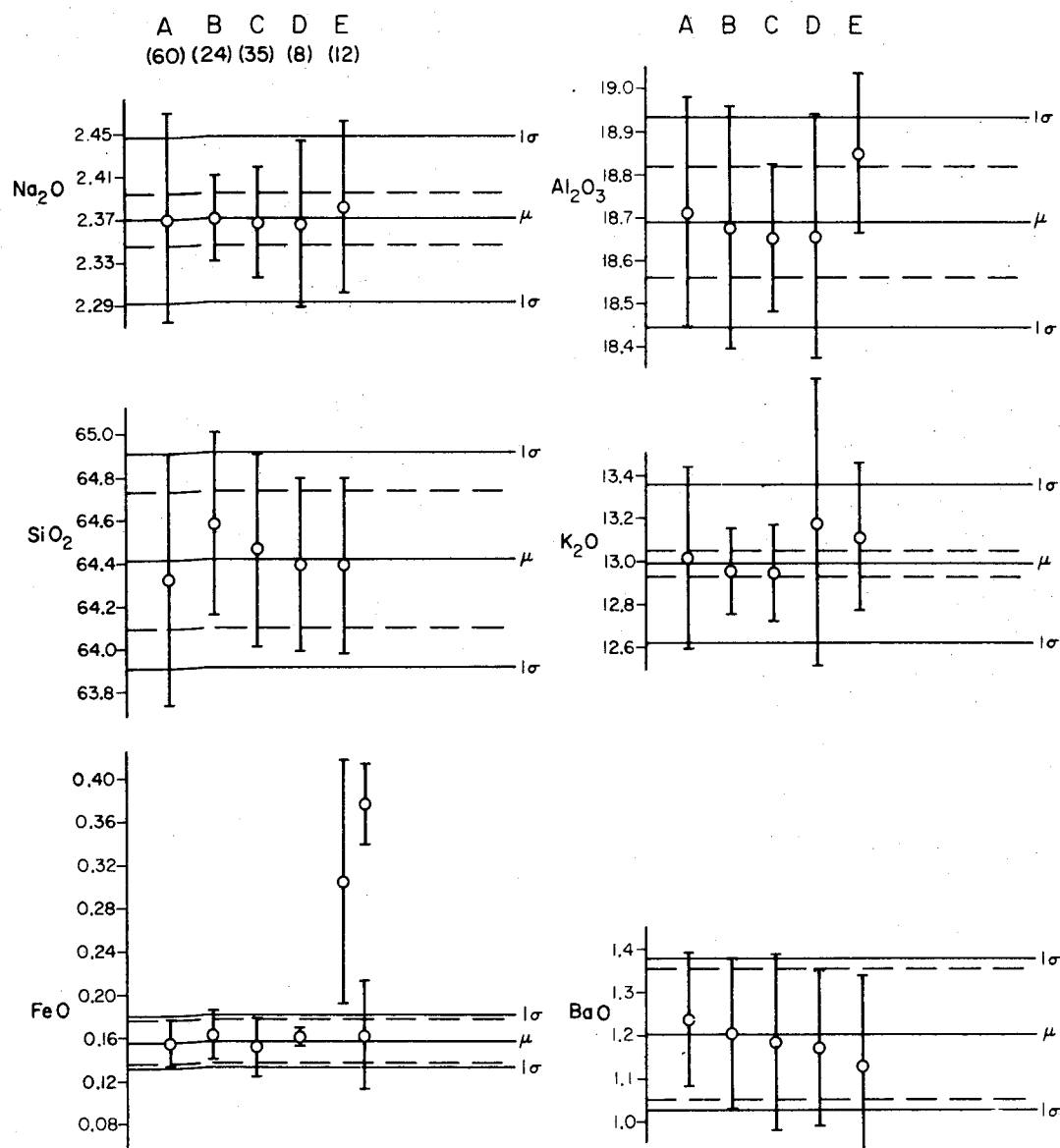
±1σ of counting statistics for individual analysis
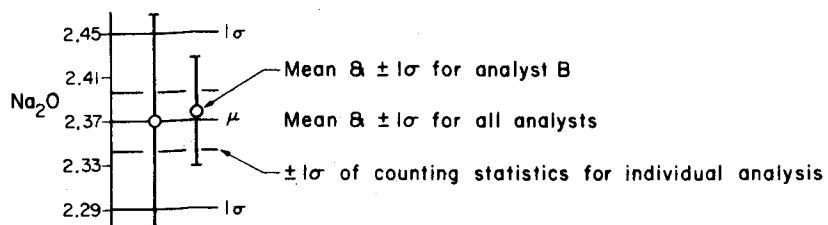
A MINICOMPUTER BASED MULTI-INSTRUMENT AUTOMATION SYSTEM

by

E.M. Butler and A.K. Agrawal

Gould Laboratory for Electrical and Electronic Research
Rolling Meadows, Illinois   60008

INTRODUCTION

The main benefits of analytical laboratory automation are increased sample throughput and overnight operation, which yield broader statistical bases for drawing inferences; and allowing staff to operate at their appropriate technical level. The practical limitations are the states of the arts and economics. The objective in designing a laboratory automation system is to remain on the steeply rising portion of the returns curve defined by these elements.

The basic capabilities required of the system described here are: 1) simultaneous operation of several instruments viz, a scanning electron microscope equipped with nondispersive and wavelength dispersive x-ray analyzers, an x-ray diffractometer, an Auger analysis system, and an ESCA-Auger system; 2) open endedness to allow further expansion in instrumentation; 3) computer control of instrument operation, data acquisition and data reduction; and 4) unattended operation to permit overnight runs.

COMPUTER SYSTEM

Given these desired capabilities it was necessary to choose a computer system and interfacing scheme to implement them. Two choices are available for the computer system: (1) individual minicomputers for each instrument, or (2) one central mini- or midi-computer servicing all of the instruments. The first choice represents considerably less stringent system requirements, but becomes quite expensive if the instruments require much main memory and mass storage for desired data reduction. The second choice is the most cost effective but requires a sophisticated operating system, since it must possess the real-time interrupt capabilities required for instrument control as well as being multiuser or multitasking.

In the recent past, approach (1) was almost mandatory because of declining central processor costs and the commercial unavailability of real-time multitasking operating systems for minicomputers. This situation has also encouraged the proliferation of proprietary languages among vendors of automated analytical equipment.

The current state of the minicomputer art is improved, however, and one can now purchase multitask operating systems with real-time capabilities for minicomputers. Because such systems have general applicability and are available from several minicomputer vendors, the user benefits from competition. These systems can support both Fortran and Basic, thus obviating the need for special vendor languages. This facilitates the use of programs obtained through the open scientific literature. The relatively slow control and data rates characteristic of these analytical instruments is ideally suited for such operating systems, because the computer's resources are handled efficiently in a multitasking environment during time consuming input-output (I/O) operations. A study was performed to compare the computer and system software costs for the two approaches assuming a four instrument system. It showed the multi-computer approach to be approximately 50% more expensive than the shared computer approach.

In particular our computer system (Figure 1) consists of a Digital Equipment Corp. (DEC) PDP-11/40 computer with 32K of main memory, two moving head disks (2.4 million words) for rapid access mass storage, Dectape back-up mass storage and separate operator terminals at each instrument. Our system software is DEC's RSX-11M, which allows up to 10 concurrent tasks in this configuration. Each of these components (hardware and software) is readily expandable to accommodate further growth. Our programming language is Fortran, chosen to eliminate main memory overhead at execution time and improve computer response time in this multitasking environment compared to interpreter based languages.

INTERFACING

The interfacing is a critically important component of an automation system and deserves special attention. Interfacing schemes consist of a controller interfacing module that communicates with the computer; and worker modules (scalers, timers, stepper motor drivers, etc.) that communicate with the controller interface module. The worker modules are configured to meet the requirements of each analytical instrument. Since

the controller interface module is an I/O device to the computer, special software routines called device handlers, are also required. In deciding upon an interfacing scheme one must consider: data transfer rates, the associated software, the flexibility of module configuration and, of course, cost.

At Gould Laboratories we conducted a rather extensive investigation of the current interface market and contacted a great many vendors in the areas of computers, interfacing and instrumentation. We found the vendors to fall generally in one of three categories:

1) primitive interfacing modules consisting primarily of analog to digital (A/D)and digital to analog (D/A) logic cards;
2) automated instruments with proprietary interfacing and relatively inaccessible user software, often utilizing proprietary high level languages;
3) flexible module configurations and uniform interfacing standards applicable to nearly all the analytical instruments of interest and independent of user language choice.

We eliminated category (1) vendors because of the considerable time investment required to design and build worker modules in-house, and category (2) vendors because of software restrictions, a proliferation of interfacing schemes and cost. The number of vendors and systems falling into category (3) is really quite small and a detailed study was made of the advantages and cost of each. The outcome of this study was the selection of the CAMAC interfacing system for our laboratory.

CAMAC is a nonproprietary interfacing specification developed in the field of nuclear physics, the same source as the nuclear instrumentation modules (NIM) with which we are all familiar. The subject of CAMAC was formally introduced to this society last year, and we are aware of several materials oriented analytical laboratories planning its use.[1] Because it is vendor-independent, the user obtains the benefits of competition; and despite the fact that CAMAC interfacing allows data transfer rates considerably higher than our instrumentation requires, we found it to be considerably ($\sim$50%) less expensive than slower interfacing systems in the case of the four instruments considered here.

Space will not permit a full explanation of how CAMAC operates, but the specification and complete vendor information are available elsewhere.[2] Suffice it to say that controller modules (crate controllers), with a device handler routine, directs the operations of sets (crates) of worker modules tailored for each instrument's control and data acquisition requirements.

APPLICATIONS SOFTWARE ARCHITECTURE

The software scheme for each instrument will consist of a main memory resident "instrument executive" and a series of disk resident subroutines. In this approach, main memory is divided into instrument task partitions of various sizes at system generation time (Figure 2). Each instrument executive program resides in its own partition so that they are concurrently core resident. When exercised, an instrument executive will ask the user questions regarding the number and types of analyses required. It then calls the appropriate service routines, overlaying on its own partition, to accomplish the tasks requested, thus making efficient use of main memory.

An example of such a task sequence would be:

1) perform an EDS analysis and determine what elements are present;
2) perform a semiquantitative analysis on the four most abundant elements;
3) determine the instrument conditions best suited to keep corrections near 1;
4) set these conditions on the instrument;
5) call the WDS system routine and perform a quantitative analysis;
6) output the results.

Obviously each of the subroutines is fairly complicated; involving default options, other subroutine calls, and saving intermediate results on disk or Dectape. The routines for the other instruments are similar in structure to the extent that we require the computer to use all of its decision making and control capabilities as well as its rapid calculating capabilities. Since RSX-11M also allows foreground/background operation, program development can be performed concurrently, but in practice we usually perform such development on a separate PDP-11/20 system.

MODES OF OPERATION

Our system is capable of operating in three distinct modes: (1) fully automated, (2) highly operator interactive and (3) manual. The fully automated mode has been described. The operator interactive mode consists essentially in replacing the instrument execution program with an operator, and is

identical to the kind of single instrument automation available from many EDS vendors.

The third mode of operation consists in manual control of the interfacing worker modules either directly, or through the teletype, by means of a local manual control CAMAC module. Provisions for local data display have been made independent of the computer to implement this mode of operation.

Our philosophy of automation regards the computer as an integral component of each of the analytical instruments; and if the computer malfunctions, it must be repaired, just as would the microprobe vacuum system. Moreover, our experience and that of others, supports the contention that the computer is the most reliable component in the analytical system. However, since computer failure in this multitasking environment would cause all instruments to be inoperative, provisions have been made for manual operation.

CONCLUSIONS

The current commerical availability of software and interfacing hardware brings the in-house system engineering effort required for multi-instrument automation within reasonable bounds. In our judgement the combination of minicomputer, multitasking software and CAMAC interfacing result in an effective, economical and viable automation system for medium size analytical laboratories.

ACKNOWLEDGEMENTS

The authors gratefully acknowledge the informative discussions with Mr. W.T. Hatfield of the General Electric Research Laboratory, Syracuse, N.Y. and correspondence with Dr. D. Hammer of the Institut Für Allgemeine Physik, Vienna, Austria.

References

1. W.T. Kane, A CAMAC Automated Electron Microprobe, Proc. Ninth Annual Conf. of the Microbeam Analysis Society, 1974.

2. Available from: Louis Costrell, Chairman U.S. NIM Committee, U.S. Dept. of Commerce, National Bureau of Standards, Wash. D.C. 20234.
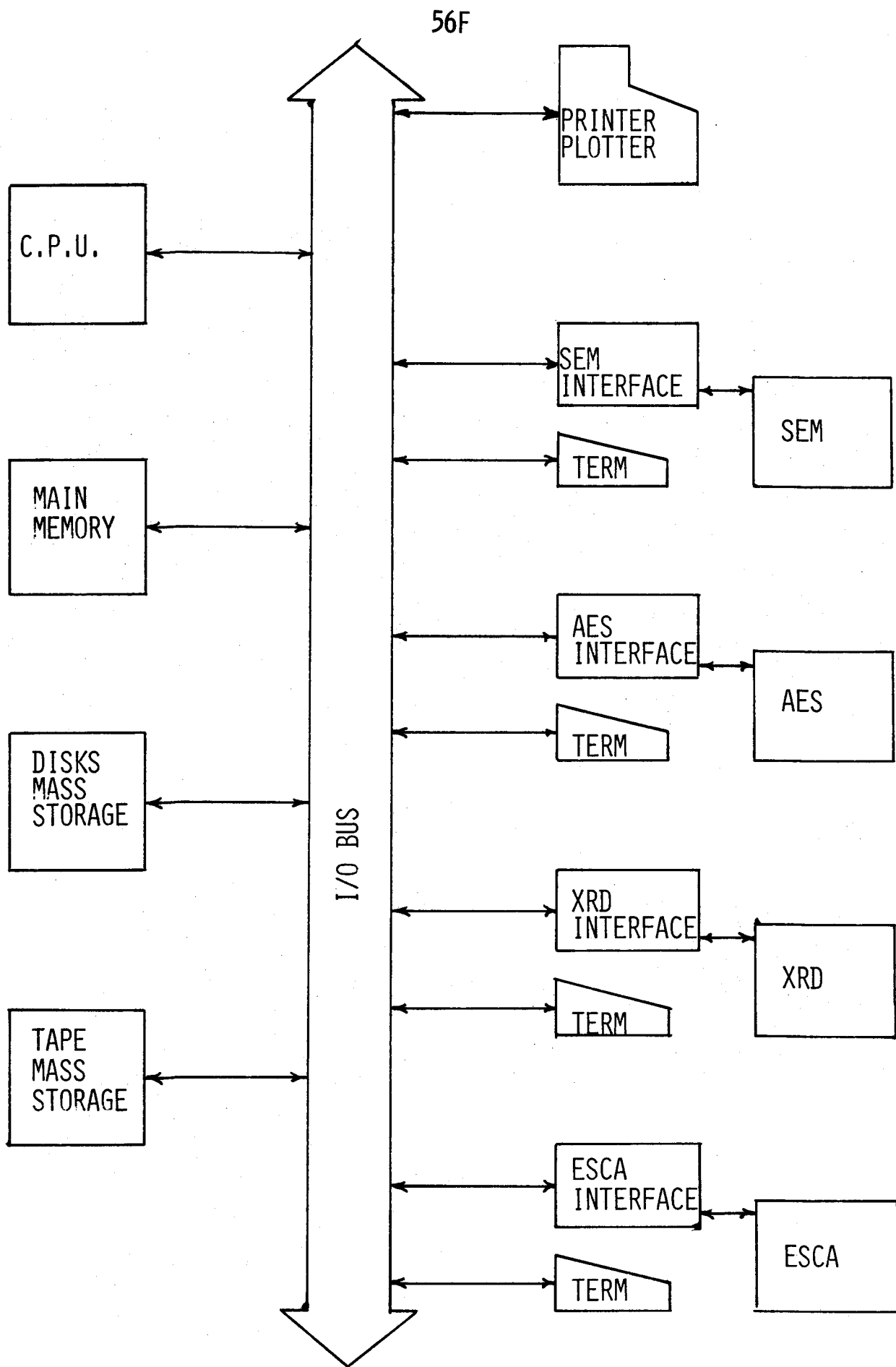
FIGURE 1   HARDWARE CONFIGURATION OF ANALYTICAL INSTRUMENT AUTOMATION

```
        ┌────────────────────────────────┬──────────────┐ ↑
        │ INSTRUMENT #4 EXECUTIVE         │              │
        │                                 │ PARTITION 4  │
        │ OVERLAYS FOR INST #4            │              │
        │    SERVICE ROUTINES*            │              │ ↓
        ├────────────────────────────────┼──────────────┤ ↑
        │ INSTRUMENT #3 EXECUTIVE         │              │
        │                                 │ PARTITION 3  │
        │ OVERLAYS FOR INST #3            │              │
        │    SERVICE ROUTINES*            │              │ ↓
        ├────────────────────────────────┼──────────────┤ ↑
        │ INSTRUMENT #2 EXECUTIVE         │              │
        │                                 │ PARTITION 2  │
        │ OVERLAYS FOR INST #2            │              │
        │    SERVICE ROUTINES*            │              │ ↓
        ├────────────────────────────────┼──────────────┤ ↑
        │ INSTRUMENT #1 EXECUTIVE         │              │
        │                                 │ PARTITION 1  │
        │ OVERLAYS FOR INST #1            │              │
        │    SERVICE ROUTINES*            │              │ ↓
   8K   ├────────────────────────────────┴──────────────┤
        │                                                │
        │         SYSTEM EXECUTIVE                        │
        │                                                │
    0   └────────────────────────────────────────────────┘
```
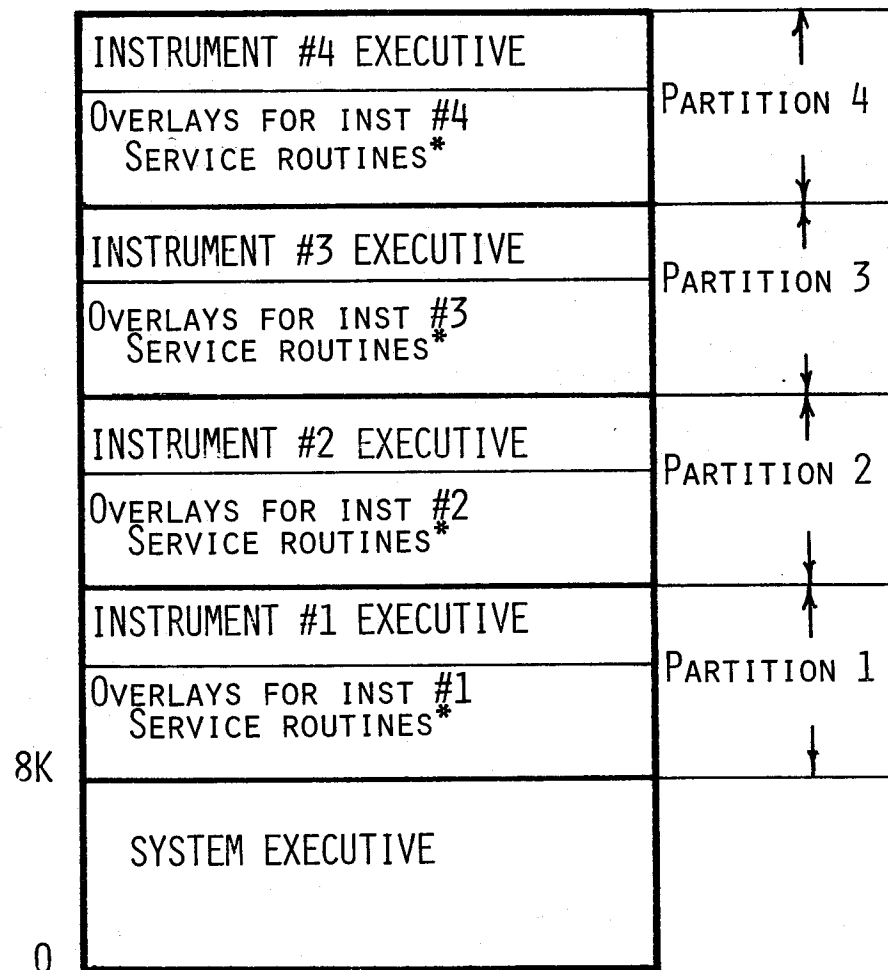
* ALL THESE ROUTINES NORMALLY RESIDE ON THE DISK AND ARE
   CALLED WHENEVER NECESSARY

FIGURE 2: MAIN MEMORY ORGANIZATION DURING SIMULTANEOUS
           MULTI-INSTRUMENT OPERATION

Experimental APL Programming for Quantitative

Electron Microprobe Analysis

H. R. MacQueen*

R. Lasky**

This paper describes programming in APL for quantitative electron microprobe analysis. Some of the programming deals with corrections by standard ZAF procedures, plus the Gaussian and fixed f(χ) absorption corrections suggested by Kyser.[1] In another part of the programming, for use in research, known weight percents can be input to calculate the corresponding relative intensities. The programming was done in the conversational mode; that is, the user is requested to enter appropriate input parameters and data.

The correction procedures, patterned after Colby's MAGIC IV,[2] are as follows:

Correction procedure	Authors	Input parameter
A. Absorption (these three can be used in any combination)		
1. Standard	Philibert[3]- Heinrich[4]	Mass absorption coefficient
2. Gaussian f(χ) (critical excitation potential < 1.5 keV with large over-voltage)	Kyser[1]	Mass absorption coefficient
3. Fixed f(χ) from experimental data[1,5,6]		
B. Atomic number		
1. Ionization-penetration	Philibert- Tixier[7]	Closed form using Berger- Seltzer[8] mean ionization potential
2. Backscatter loss factor	Duncomb-Reed[9]	Polynomial fit
C. Fluorescence	Reed[10]	Jump ratios[11] Fluorescence yields[12]
D. Continuum fluorescence (correction available as subprogram)	Springer[13]	

*IBM Corporation, System Products Division, East Fishkill Facility, Hopewell Junction, New York 12533.
**IBM Corporation, System Products Division, P. O. Box 6, Endicott, New York 13760.

The iteration scheme of Birks and Criss[14] (as modified by Colby[2]), dead-time correction, the compound-standard option, and the element-by-difference option are used. The outputs are relative intensity, weight and atomic percents for each data point, mean weight and atomic percents for the summed data points, peak-to-background, and minimum detectability limits. In addition, a summary of the input data and correction parameters can be listed.

The major advantage of these procedures is that the user can control the correction procedures and the input parameters. This control is gained at the expense of having to enter correction parameters and raw data manually. With appropriate interfacing, however, the raw data can be entered directly into the user's workspace. The methods of changing and listing have been kept simple so that the user can readily fit the procedures to a specific application.

By use of the same choice of ZAF corrections, relative intensities can be calculated from known weight fractions. For two elements, this involves setting a starting point, an increment, and a number of data points. The resulting data can be easily plotted to make calibration curves or comparisons[15] of the results obtained by different correction procedures. For three or more elements, the weight fraction values must be predetermined and entered manually.

Results obtained by these procedures and by our on-line MAGIC calculations will be compared. Both procedures are intended not to replace on-line corrections, but to offer the user hands-on control of an analysis when such control would provide insight into a problem.

References
1. D. F. Kyser and H. R. MacQueen, "New Absorption Correction for Soft X-rays in Quantitative Electron Probe Microanalysis," 7th National Meeting, Electron Probe Analysis Society of America, paper 10, San Francisco, 1972.

2. J. W. Colby, "Data Collection and Reduction - MAGIC IV Computer Program," paper B, Tutorial Session, 7th National Meeting, Electron Probe Analysis Society of America, San Francisco, 1972.

3. J. Philibert, "A Method for Calculating the Absorption Correction in Electron Probe Microanalysis," X-ray Optics and X-ray Microanalysis, Academic Press, New York, 1963, pp. 379-392.

4. K. F. J. Heinrich, "The Absorption Correction Model for Microprobe Analysis," 2nd National Conference on Electron Microprobe Analysis, Extended Abstracts (1967).

5. D. F. Kyser, "Indirect Determination of Mass Absorption Coefficients, for Soft X-rays," 5th National Meeting, Electron Probe Analysis Society of America, Paper 12, New York City, 1970.

6. D. F. Kyser and D. E. Horne, "High Voltage Sweep and Controlled Magnetic Lens Current Supplies for the Electron Microprobe," The Review of Scientific Instruments, Vol. 43, No. 9, August 1972, pp. 1334-1338.

7. J. Philibert and R. Tixier, "Electron Penetration and the Atomic Number Correction in Electron Probe Analysis," Brit. J. Appl. Phys., Vol. 1, 1968, pp. 685-694.

8. M. J. Berger and S. M. Seltzer, "Tables of Energy Losses and Ranges of Electrons and Positions," NASA Report N65-12506 (1964).

9. P. Duncum and S. J. B. Reed, "The Calculation of Stopping Power and Backscatter Effects in Electron Probe Microanalysis," Quantitative Electron Probe Microanalysis, K. F. J. Heinrich, ed., National Bureau of Standards, Special Publication 298, Washington, D. C., 1968, p. 133.

10. S. J. B. Reed, "Characteristic Fluorescence Corrections in Electron Probe Microanalysis," Brit. J. Appl. Phys., Vol. 16, 1965, p. 913.

11. K. F. J. Heinrich, "X-ray Absorption Uncertainty," The Electron Microprobe, ed. T. D. McKinley, K. F. J. Heinrich, and D. B. Wittry, Wiley, New York, 1966, pp. 296-377.

12. J. W. Colby, "Quantitative Microprobe Analysis of Thin Insulating Films," Advances in X-ray Analysis, Vol. 11, ed. J. Newkirk, G. Mollett, and H. Pfeiffer, Plenum Press, New York, 1968, p. 287.

13. G. Springer, "Fluorescence by Continuum Radiation in Multielement Targets," VIth International Congress on X-ray Optics and Microanalysis, Osaka, Japan, 1971.

14. L. S. Birks and J. W. Criss, "Intensity Formulae for Computer Solution of Multicomponent Electron Probe Specimens," The Electron Microprobe, ed. T. D. McKinley, K. F. J. Heinrich, and D. B. Wittry, Wiley, New York, 1966, pp. 217-236.

15. R. M. Ingersoll, H. R. MacQueen, and J. L. Solomon, "An Investigation of the Atomic Number Effect in Cu-Ni Alloys," 4th National Meeting, Electron Probe Analysis Society of America, paper 17, Pasadena, California, 1969.

COMPARATIVE PERFORMANCE OF THE X-RAY PROBE AND FRIEDA*

P. S. Ong and H. L. Cox, Jr.
The University of Texas System Cancer Center
M. D. Anderson Hospital and Tumor Institute
Houston, Texas 77025

INTRODUCTION

Scattering phenomena form one of the major limitations in the use of an energy dispersive x-ray analyzer for trace elements analysis. This is particularly so if the matrix consists of light elements. Under the appropriate conditions, however, these scatterings may be used to an advantage for mass determinations. This subject will be explored in another paper presented at this meeting (H. L. Cox and P. S. Ong).

Because of scattering, the continium and impurities of the x-ray target contribute to the background. For this reason, and also for accurate mass determinations, it is important to assure that the incident beam is highly monochromatic.

The most efficient method of producing a monochromatic beam is by the use of secondary fluorescence in combination with a β filter. Such an arrangement was proposed by Hall (1) in 1957 using a gas proportional counter. Less frequently used for fluorescence excitation are the crystal monochromators because of their associated high intensity loss. In our Laboratory for Bioanalytical Physics, we are using analyzers with both the secondary fluorescence (2) and the crystal monochromator (3) as excitation sources for trace elements analysis in biomedical samples; each of the instruments fulfills a specific need. The comparative merits of these two instruments are discussed here.

CHARACTERISTICS OF THE SECONDARY FLUORESCENCE MONOCHROMATOR

The major feature of the secondary fluorescence monochromator is its versatility. One x-ray tube may be used to excite a number of secondary fluorescers. It also permits the use of emission lines from elements unsuited for use as an x-ray target. This is an important feature since two interfering elements may be separated by the use of an appropriate fluorescer. The element As ($K\alpha$ = 10.530 KeV), for example, which interferes with Pb $L\alpha$ (10.49 KeV), can be selectively excited by the Br $K\alpha$ line (11.907 KeV) (see Table I). Also, when a wide range of elements must be measured, it is desirable to use several exciting radiations. The major shortcoming is that the fluorescence radiation is diffused onto a large sample area and for good sensitivity, a close optical coupling is necessary. The sample chamber and any part obstructing the beam should be made of the same material as the secondary fluorescer.

*Acronym for fluorescence radiation induced energy dispersive x-ray analyzer.

TABLE I.

ELEMENT	Z	ENERGY KeV ABSORPTION EDGE	EMISSION
As	33	K - 11.862	$K\alpha$ - 10.530
Br	35	K - 13.468	$K\alpha$ - 11.907
Pb	82	L_3 - 13.038	$L\alpha_1$ - 10.448
			$L\alpha_2$ - 10.550

CHARACTERISTICS OF THE CRYSTAL MONOCHROMATOR

The crystal monochromator does not have flexibility in the choice of radiation, that is, unless a multitargeted x-ray tube is used. Moreover, targets are restricted to materials which have a high melting point and a good electrical and thermal conductivity. If flat x-ray optics are applied, most of the radiation is unused and thus results in poor efficiency. However, in cases where beam collimation or focusing is required, it proves to be superior to the secondary fluorescence monochromator. Focusing permits the analysis of a small sample with a low power x-ray tube, and therefore results in highly efficient utilization of the radiation and a high sensitivity of the system.

THE EQUIPMENT

The two types of instruments used for the comparative study are shown schematically in Fig. 1 and Fig. 2. Figure 1 shows the arrangement of our FRIEDA system which has a beam diameter of 13.4 mm. The sample enters the beam at a 45° angle, total analysis area is 200 mm^2. Figure 2 shows the x-ray probe (3), which presently provides a line focus 0.5 mm wide and 40 mm long.

Both instruments use a commercial sealed-off Mo tube. The x-ray probe uses the MoK line (17.441 KeV), while FRIEDA is normally operated with a Zr fluorescer (15.744 KeV) without β filter. For certain measurements, an Mo fluorescer is used, excited by the high energy bremstrahlung of the Mo tube.

PARAMETERS OF INTEREST

The measurements of interest are related to sensitivity, peak to background ratio, limit of detectability (absolute and in weight fraction), total amount of sample for a required precision, and to inherent and practical limitations. The samples used for these comparisons are all of biomedical importance such as body fluids, tissues from needle biopsies, and hair (single strand, bulk and beard shavings). The present measurements indicate that both instruments perform equally well for the type of samples mentioned above but the sensitivity of the focusing x-ray probe is improved by an amount comparable to the inverse ratio of the analytical areas. A further reduction of the line focus into a circular spot (0.5 mm diameter) will further improve the sensitivity of the x-ray probe. Detailed quantitative data will be presented and discussed.

FRIEDA
Fluorescence Radiation Induced Energy Dispersive Analyser
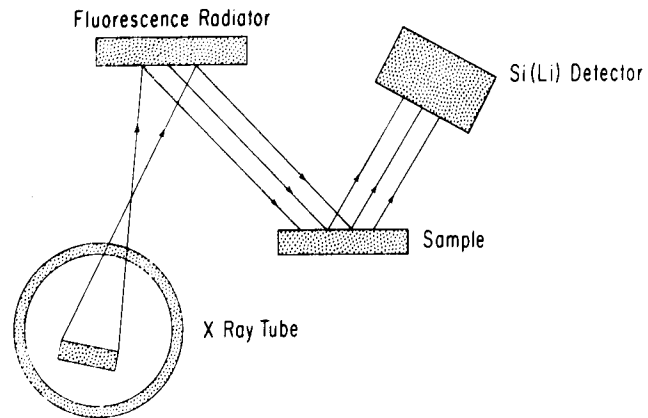
.Fig. 1. Schematic presentation of FRIEDA using
secondary fluorescence.
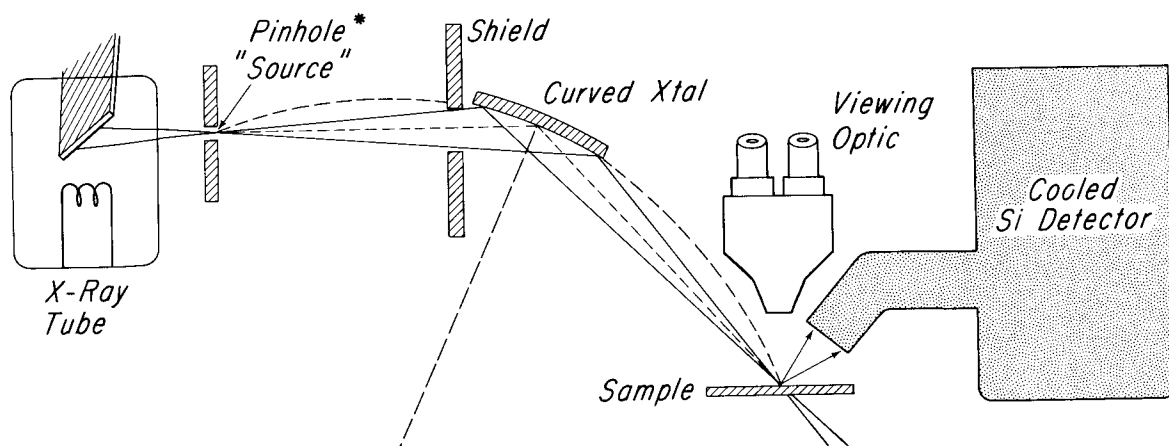
Fig. 2. Schematic presentation of the x-ray probe using a line
focusing crystal monochromator.

REFERENCES

1. Hall, T.: In Advances in X-ray Analysis, 1:297, W. M. Mueller, Ed., Plenum Press, New York, 1957.

2. Ong, P.S., P. K. Lund, C. E. Litton, and B. A. Mitchell: An energy dispersive system for the analysis of trace elements in human blood serum. In Advances in X-ray Analysis, Vol 16, pp124, Plenum Press, New York, 1973.

3. Ong, P.S. and H. L. Cox, Jr.: A monochromatic x-ray probe for the analysis of trace elements. Proc 9th Ann Conf Microbeam Analysis Soc, Ottawa, Canada, July 22-26, 1974.

SEM + SIMS: A UNIQUE COMBINATION FOR SURFACE CHARACTERIZATION

J.A. Leys   Central Research Laboratories
J.T. McKinney New Business Ventures Division

3M Company, P.O. Box 33221, St. Paul MN 55133

The scanning electron microscope/microprobe in conjunction with energy and/or cyrstal dispersive X-ray analysis systems has proven to be an extremely useful analytical tool. However, the practicing analyst is often confronted with problems where the depth of analysis, or poor sensitivity to low mass elements, may preclude the use of the X-ray emission technique. This paper will show illustrations where the combination of the SEM and secondary ion mass spectrometry (SIMS) provides the necessary information required to solve surface analysis problems not amenable to X-ray analysis.

Figure 1 shows a diagram of the SIMS apparatus. A leak valve admits suitable gas into the ion source region where ions are produced and accelerated at voltages up to 5KV. Lens assemblies permit focusing of the ion beam from less than 100μ to a few millimeters in a diameter on the specimen surface. Deflection plates allow scanning of the ion beam for imaging or depth profile[1] purposes. Low energy sputtered ions from the specimen surface are admitted to a quadropole mass analyzer through an energy prefilter that eliminates the high back ground and peak broadening caused by higher energy sputtered or scattered particles. To prevent contamination from diffusion pump oils depositing on the specimen surface, a liquid nitrogen cold trap is used either surrounding the specimen, or at the outlet to the diffusion pump. A gas capillary jet directed at the specimen surface may also be used to reduce surface

SEM SIMS APPARATUS

FIGURE 1

contamination from hydrocarbon pump oils. In addition, if an "inert" gas is used for the primary ion beam, then the use of oxygen in the capillary jet provides an "active gas" surface to maintain high secondary ion yields.
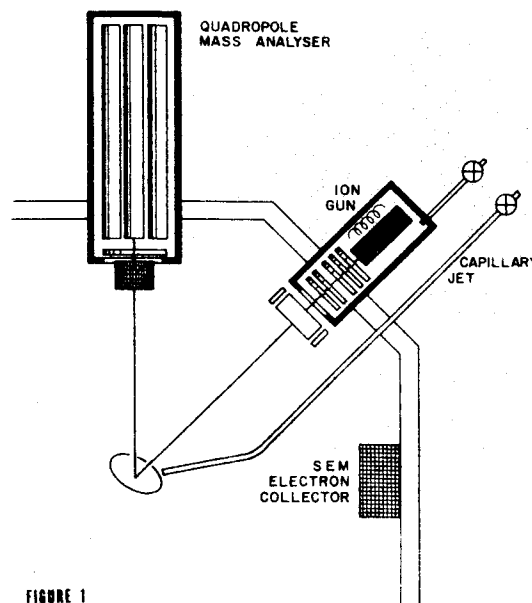
Figure 2a shows scanning electron micrographs of two areas of a high purity fine grained aluminum oxide ceramic. The area on the right showed an unexplained grain growth X-ray analysis using both energy and wavelength dispersive methods failed to detect any difference between the two areas. However, differences were clearly seen in the SIMS spectra. Figure 2b shows that the coarse grained area is contaminated with sodium, silicon, and magnesium. Further sutdies showed that sodium was responsible for the grain growth.

Metal surfaces are often given chemical surface treatments which impart desired physical or chemical characteristics such as corrosion resistance, improved paint or resin bonding, modified electrical properties, and desired lubrication or friction properties. The analytical chemist is often called upon to measure or monitor this coating thickness or composition. One example of this is shown in Figure 3. The scanning micrograph shows an aluminum alloy surface which has been chemically cleaned, treated in a solution of sodium silicate and subsequently washed with de-ionized water. This treatment renders the aluminum surface hydrophobic as well as providing corrosion and wear resistance for certain applications. The coating cannot be detected by X-ray analysis because the silicon signal from the very thin silicate coating is masked by the silicon signal originating "in depth" from the aluminum which contains 0.7% silicon as an alloying element.

The mass spectrometer was set to scan mass numbers 27 (aluminum) and 28 (silicon) repeatedly while sputtering slowly with a He^+3 ion probe. The resultant depth profile is shown in Figure 3b. The existence of a silicate layer is clearly established and the concentration of the aluminum in this layer can also be determined.

Organic surfaces or coatings are often amenable to useful analyses by SIMS. In many cases it is possible to observe the negative sputtered ion fragmentation pattern of these surfaces and identify the type or classification of compound present. Figure 4a shows a scanning electron micrograph of glass microspheres. The energy dispersive X-ray spectrum shows that the glass is of the soda-lime type. The negative SIMS spectrum of the glass surface, Figure 4b, shows that it is coated with a fluorocarbon which has been applied to modify the surface tension of the glass.

These illustrations indicate that the strengths of SIMS are often corresponding weaknesses of SEM X-ray methods, and that the combination of the two techniques can often provide comprehensive analyses.

REFERENCES

1. T.W. Rusch, J.T. McKinney, J.A. Leys, J. Vac. Sci. Technol. Vol. 12, No. 1 Jan/Feb 1975.

2. C.A. Andersen, Int. J. Mass Spect. & Ion Physics 2 (1969).

ALUMINA CERAMIC

SIMS ANALYSIS
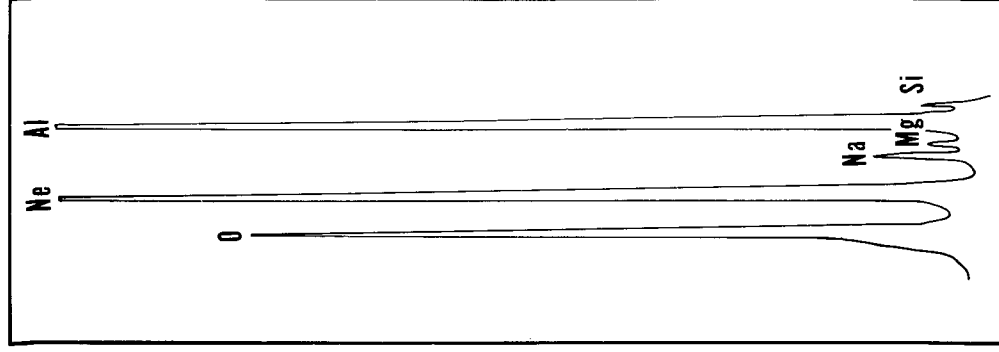
normal area   grain growth area
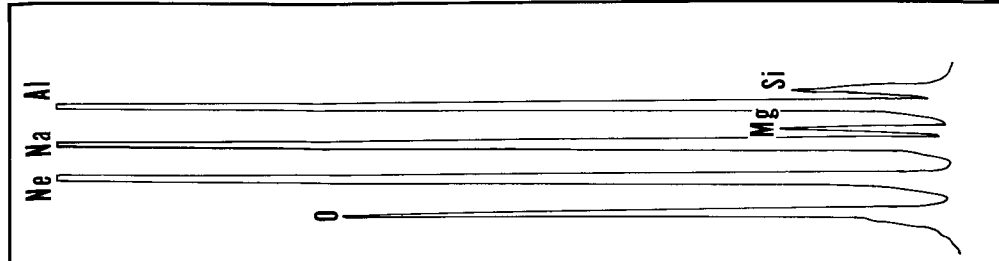
POSITIVE SIMS, Ne+ IONS

FIGURE 2b

SEM ANALYSIS

grain growth area

3000 X

normal fine grained area

3000 X

energy dispersive X-ray analysis

Al Kα

Al Kα

FIGURE 2a

Aluminum Surface Treated with Na$_2$SiO$_3$ Solution

SIMS DEPTH PROFILE

POSITIVE SIMS, ^{3}He
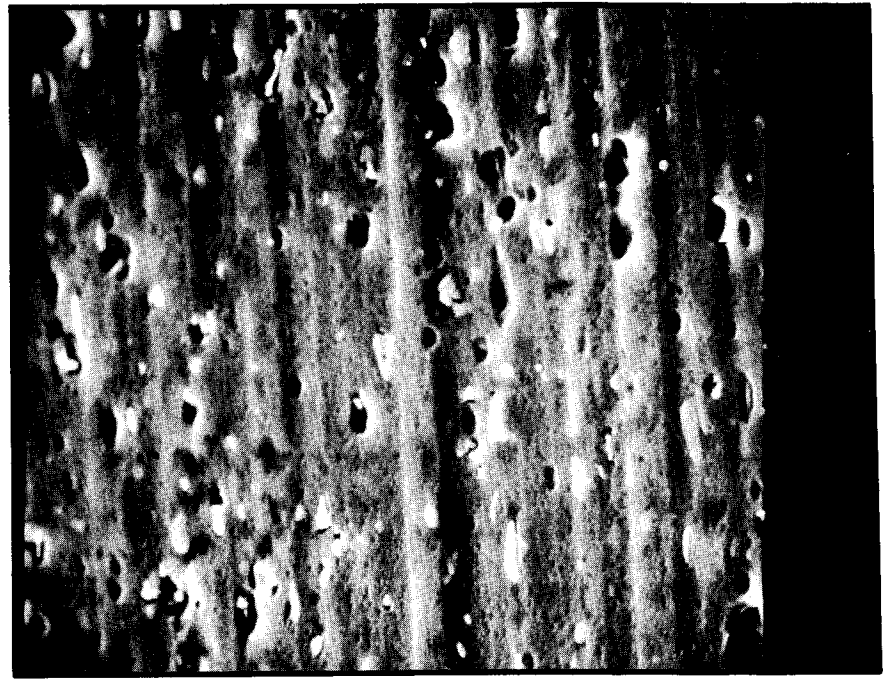
FIGURE 3b

SEM ANALYSIS

1000 x

FIGURE 3a
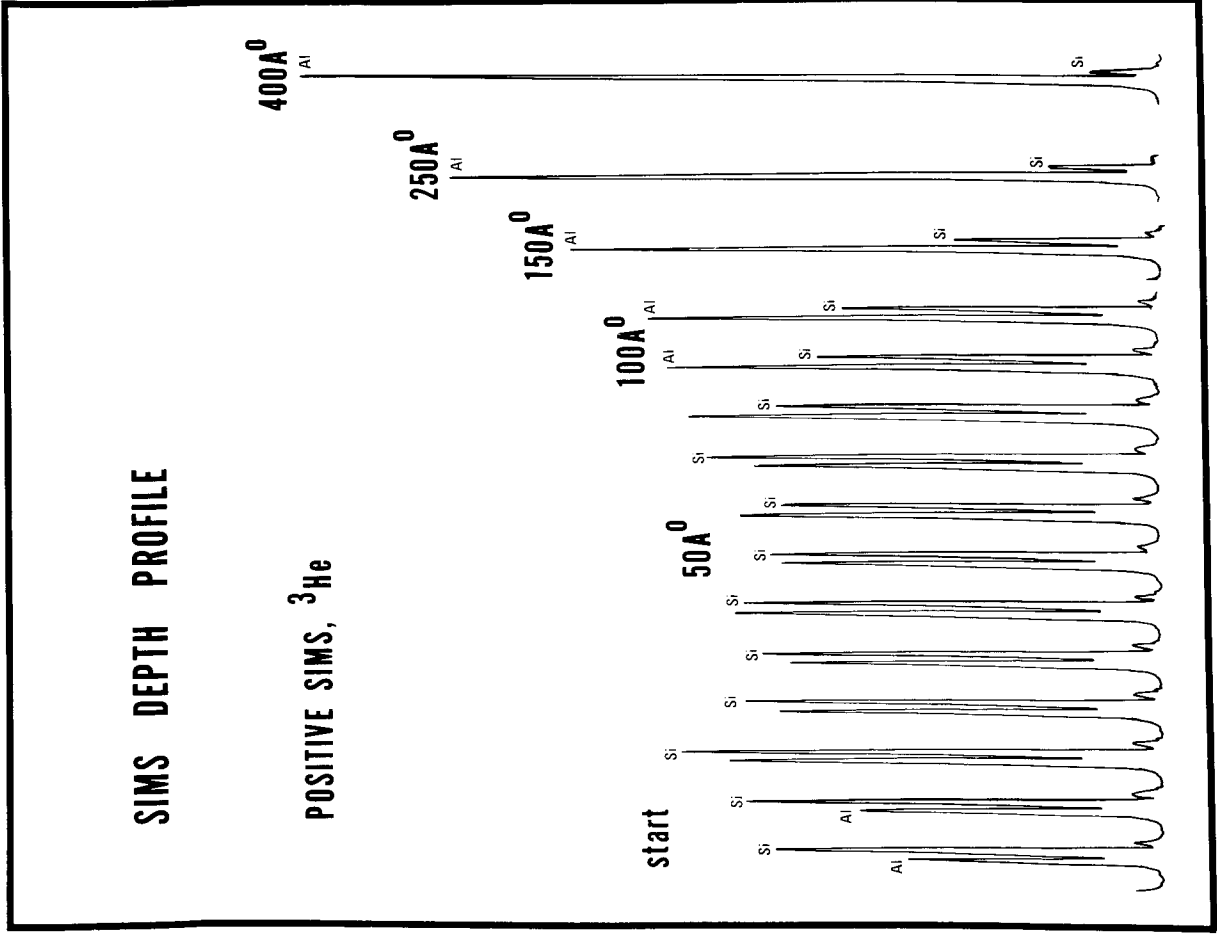
GLASS MICROSPHERES CONTAINING FLUOROCHEMICAL SURFACE TREATMENT

SIMS ANALYSIS

NEGATIVE SIMS, $^3He^+$ IONS

FIGURE 4b

SEM ANALYSIS

200 X

energy dispersive X-ray spectrum

Na Si   Ca

FIGURE 4a

A PRETREATMENT METHOD FOR SEM·EPMA SPECIMEN SURFACE

A INSTRUMENT COMBINING ION-PLATING, ION-ETCHING AND VACUUM EVAPORA-TION, AND ITS APPLICATIONS

by

Hiroyoshi SOEZIMA and Takeshi ARAKI

Shimadzu Seisakusho Ltd.

Nishioji Sanjo, Nakagyoku, Kyoto, JAPAN

In the preparation of specimens for the scanning electron microscope or electron probe microanalyzer, the vacuum evaporation treatment with various kinds of materials such as Be, C, Aℓ, Cr, Pd, Au, Pt, their mixtures or alloys, is sometimes made for the following purposes:

(1)　To give a good electric conductivity to the specimen surface.

(2)　To increase the production efficiency of secondary electrons.

(3)　To make a shadowing to emphasizing the detail contrast.

(4)　To protect the specimen surface against electron beam bombardment and resulting heat.

The advantages of vacuum evaporation treatment are as follows:

(a)　The microstructure of specimen surface is not spoiled; because, the evaporated material rains softly on the specimen surface to coat it, without collision and bombardment.

(b)　The detail of the specimen surface to be coated is regenerated on the coating.　In general, the specimen surface is coated as shown in Fig. 1, and so irregularities as high as 100 Å, is regenerated on a coating as high as 100 Å.

(c)　The shadowing effect can be produced.　For a specimen with so slight irregularities and variations in the structure that its contrast can hardly obtained on the electron beam image, the vacuum evaporation treatment offers a good contrast nearly corresponding to the micro-structure by coating the specimen surface with oblique incidence so as to emphasize the irregu-larities.　Furthermore, it is possible to discriminate between concaveness and convexness on the surface by observing the shadowing pattern.

On the contrary, the vacuum evaporation treatment has the following disadvantages:

(d)　For a specimen with great irregularities, it is difficult to obtain a good conductivity over the entire surface; because, the vacuum evaporation treatment does not offer a good uniformity of coating.　For example as shown in Fig. 3, coating can be made only on the convex parts not on the concave parts, and thus the part (3) becomes to be electrically floating apart from the other parts.　As a result, a correct electron beam image cannot be obtained.

(e)　The specimen surface may be spoiled by thermal radiation from the evaporation source and the heater.

As mentioned above, the vacuum evaporation treatment has many advantages, but it has dis-advantages sometimes not negligible in observation and analysis.

On the other hand, the recently developed ion plating can compensate the disadvantages of vacuum evaporation treatment by the following features:

(a)　The ion plating offers a good uniformity.　The reason is as follows:　A large number of

ions go round easily to the rear surface (viewed from the anode) of the cathode loaded with specimen; because, the mean free path of ions is considerably short in the relatively high surrounding pressure, and thus the collision between ions and gaseous molecules is very frequent. Moreover, ions go along the electric lines of force formed in the electric field, then being accelerated in a strong field of the dark space surrounding the cathode, and coming to the cathode. Consequently, a uniform coating can be made not only on the cathode surface facing the anode but also on its rear surface. And in general, this method provides a uniform and chargingless coating on the whole of a topographic and complicated specimen surface, including its side and rear surfaces.

(b) Furthermore, it is not necessary to face the ion source directly to the specimen, and thus a thermal radiation shutter can be installed between them. On the contrary, the method has the following disadcantages:

(c) In ion plating generally, the ion sputtering phenomenon namely ion etching or sputter etching, occurs at the same time, causing some probability of spoiling the microstructure.

(d) Shadowing effect cannot be expected.

Therefore, it is possible to make a better coating by combining both methods of the vacuum evaporation and ion plating, and making the best of their advantages selectively according to the specimen to be analyzed.

The ion sputtering provides etching and cleaning of the specimen surface by bombarding it. Especially, the etching effect can produce an interesting etching pattern related to the constitution, structure and crystallity of specimen surface, and offers such a microsubstructure pattern of a biological specimen that cannot be obtained by ordinary fracture observation, thus attracting a special attention in many fields.

We devised an instrument as a combination of these three methods vacuum evaporation, ion plating and ion etching, to make the best of their advantages and also compensate their disadvantages. Fig. 4 shows a schematic view of the instrument. In this figure, part (1) is a heater, and part (2) is a material to be evaporated which is, for example, wound on the he heater. Part (3) is a power supply for the heater, and part (4) is a heater power switch. The part (5) is a specimen table to be loaded with a specimen (6), which can be rotated and tilted as shown by the arrow-heads. Part (7) is a power supply for applying a voltage across the heater (1) and the specimen table (5), and part (8) is its power switch. The part (9) is an anode located near the heater (1), and the part (10) is a power switch for connecting the anode (9) and power supply (7). The part (11) is a shutter located between the heater (1) and specimen table, which can be inserted as shown by the arrow-head. These parts are con- tained ina bell jar (12) which is connected to a cacuum pump not shown in the figure. The parts (13) and (14) are respectively inlet cocks and nozzles for introducing inert gases such as Ar, or air into the bell jar.

The operation of this system is as follows:

1. Vacuum Evaporation

After the specimen (6) is mounted on the specimen table (5), the power switch (4) is turned on to energize the heater (1) and thus evaporate the material (2). At this time, the power switches (8) and (10) should be off, and also the shutter (11) should be out. Then the specimen surface can be coated evenly or with shadowing effect by controlling the specimen table motion rotation or precession according to the purpose. And a slight amount of gas can

be introduced through the nozzles (14) to improve the uniformity by virtue of a decrease in the degree of vacuum, and/or to prevent a crack in the coating film. Though omitted in the figure, a carbon coating electrode is independently provided to coat the specimen surface with carbon or carbon/metal mixtures. In addition, the shutter (11) should be out ordinarily, but it may be inserted temporarily during the transient process of evaporation and coating in the initial stage of heating, to prevent contaminations on the heater and the material from sputtering the specimen surface. And it is pulled out after the stationary state is recognized.

2. Ion Plating

First, the specimen (6) is mounted on the specimen table (5), the material to be evaporated is installed on or near the heater (1), and then the inert gas is leaked in through the nozzles (14) after evacuating the bell jar (12) to a high degree of vacuum. Next, the power switch (8) is turned on to connect the power supply (7) between the heater (1) and the specimen table (5). Then, by the voltage thus applied, a glow discharge occurs across the heater (1) positive and the specimen table negative. While the glow discharge is kept, the material (2) is evaporated by heating, and the metallic gas thus produced is ionized in the plasma atmosphere, and then attracted strongly to the cathode (specimen) by the force resultant from a kinetic energy increased by heating, and from an accelerating force of electric field. The ions coming to the specimen (cathode), get electrons there, being neutralized, and thus forming a coating film on the specimen surface. Furthermore, ionized material and non-ionized one are both scattered by the inert gas and ionized inert gas, thereby coming to the specimen from all directions with the result of much better uniformity in coating.

When the specimen may be spoiled by radiation heat from the heater (1), the shutter (11) is inserted between the heater and specimen as shown by the arrow-head. In this case also, the specimen can be coated sufficiently and uniformly. The specimen table (5) can be rotated or moved in precession mode, to coat the specimen more widely and uniformly, and thus to prevent an etching pattern from occurring due to some degree of ion sputtering involved in the ion plating. The reason is as follows, though it will be mentioned later. In glow discharge, an etching pattern tends to occur if the specimen is placed at rest in the flow of ionized inert gas. Whereas, if the specimen is rotating and changing its direction, an etching pattern is less probable to occur.

In addition, the anode (9) is not used in the ordinary ion plating; because, if the anode (9) is on, the ion etching effect is intensified, thus damaging the coating film immediately after its formation.

3. Ion Etching

First the specimen (6) is mounted on the specimen table (5), and the inert gas is leaked in through the nozzles after evacuating the bell jar (12) to a high degree of vacuum. Next, the power switch (10) is turned on to connect the power supply (7) to the anode (9), thus producing a glow discharge across the anode (9) and the specimen table (5). Then the inert gas is ionized, attracted by electric field, and bombards the specimen, thus ion-etching the specimen. In this case, the case of ion etching, the difference of anode (9) from the heater (1) used as an anode in ion plating, exists in its shape suitable to increase the density of ion bombardment in order to intensify the etching effect. Of course, ion etching occurs also when turning on the power switches (8) and/or (10) with the power switch (4) turned off, that is, with the heater (1) not energized.

In addition, when making an etching while rotating the specimen table (5) or moving it in precession mode, ions will bombard the specimen surface from various directions, thus producing the following effects:

(a) Cleaning the specimen surface.

(b) Etching the specimen surface and thus exposing the substructure.

(c) Thinning the specimen and preparing a very thin foil for transmission electron microscopy.

Furthermore, when etching the specimen surface with an oblique incidence and with the specimen (6) at rest, an etching pattern will occur which is peculiar to the structure, constitution and crystallity of the specimen surface. Thereby it offers new data for structural study of the specimen.

There are two nozzles (14) located respectively near the anode and near the specimen. The former is for leaking in the inert gas near the anode to increase the ionization density in ion etching. And the latter is for leaking in the inert gas near the specimen to increase the uniformity of scattering in vacuum evaporation and ion plating.

Many modes of treatments can be made by variously combining the above-mentioned three methods the cacuum evaporation, ion plating and ion etching (or cleaning effect occurring in some cases); that is, they can be made independently, successively or at the same time. For example,

(a) After cleaning, vacuum evaporation treatment or ion plating.

(b) After ion etching, shadowing for emphasis of contrast.

(c) After thin ion plating, shadowing for contrast.

(d) After ion-plating the surface thinly with a light element for a good conductivity to such an extent as not to hide the microstructure, making a vacuum evaporation with a heavy . element without rotation and precession of specimen and without gas leakage as shown in Fig. 1, thus increasing the production efficiency of secondary electrons.

Photos 1 through 9 show some examples of applications of the present methods, and their SEM images.

Fig. 1   Fig. 2   Fig. 3

(4) Heater power switch

(3) Heater power supply

(1) Heater

(2) Material to be evaporated

(8) High tension power switch for plating

(10) High tension power switch for etching

(9) Anode

(11) Shutter

(7) High tension power supply for plating and etching

(13) Gas inlet cocks

(14) Nozzles

(6) Specimen

Specimen table (5)

(12) Bell jar
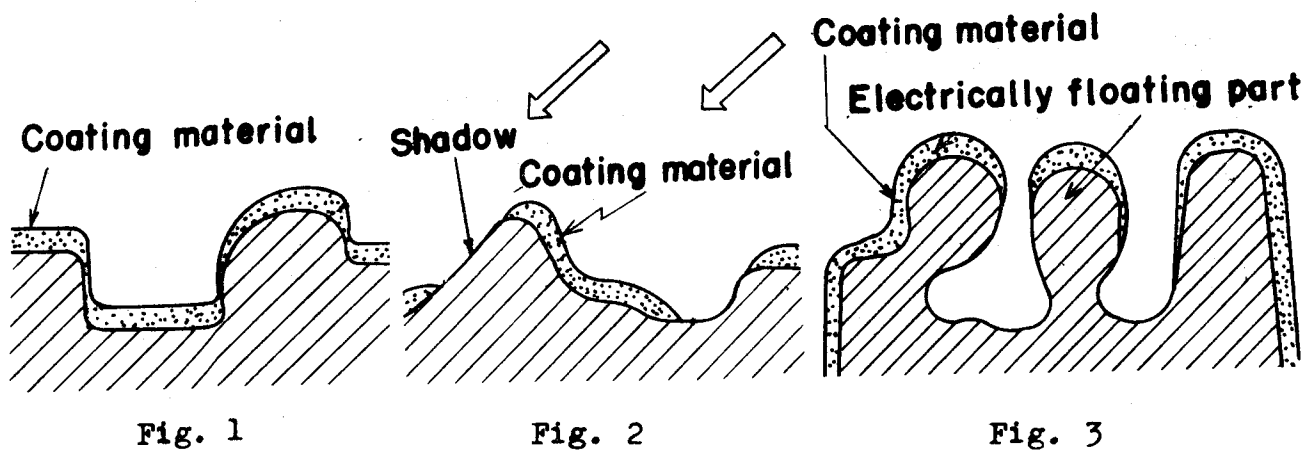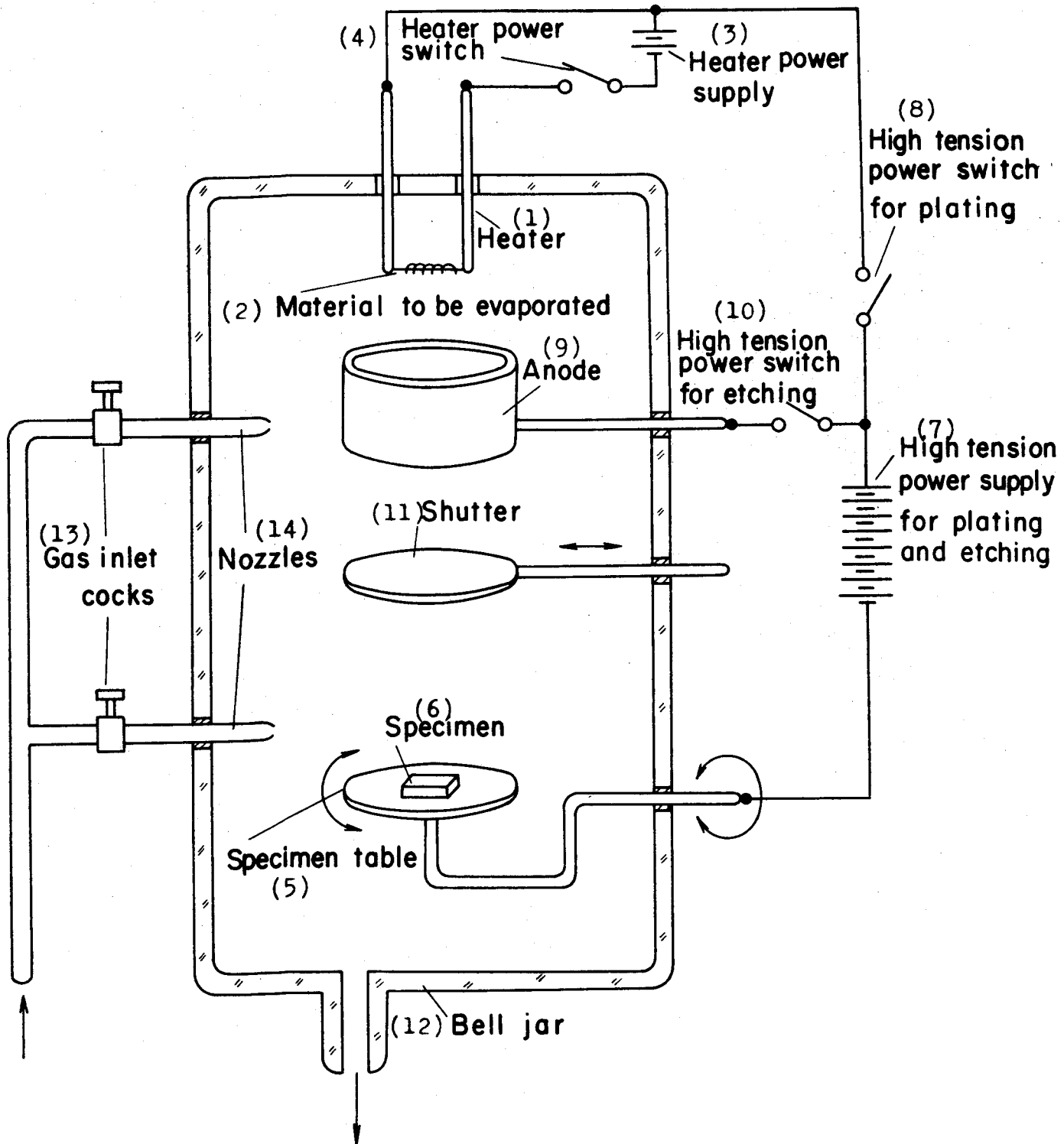
Fig. 4
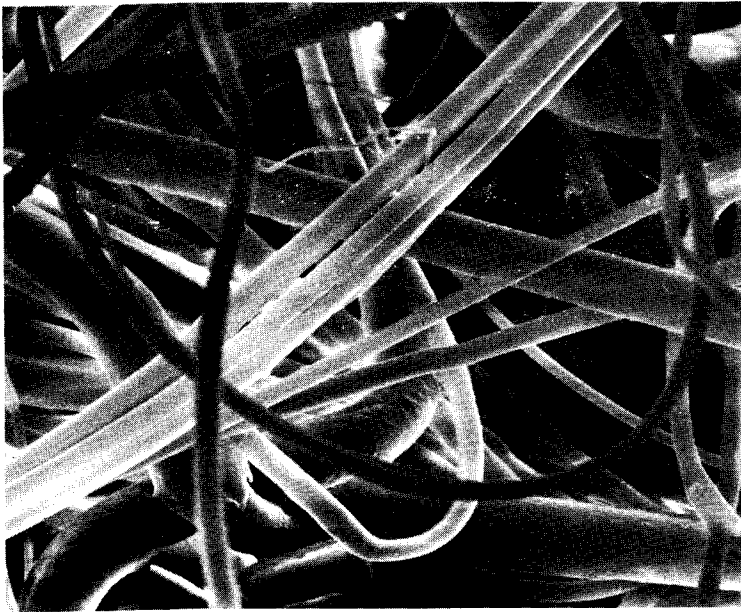
Photo 1

Specimen: Fleecy polypropylene

Treatment: Vacuum evaporation with Au at 100 Å. The specimen precession.

Exposure: At 25 KV, 2×10^{-11} A for 150 sec.

Remarks: Coating film shows some discontinuity with electrically floating parts, due to its fleecy and airy form. And so, local charging-up occurs with abnormal contrast.

5 μ
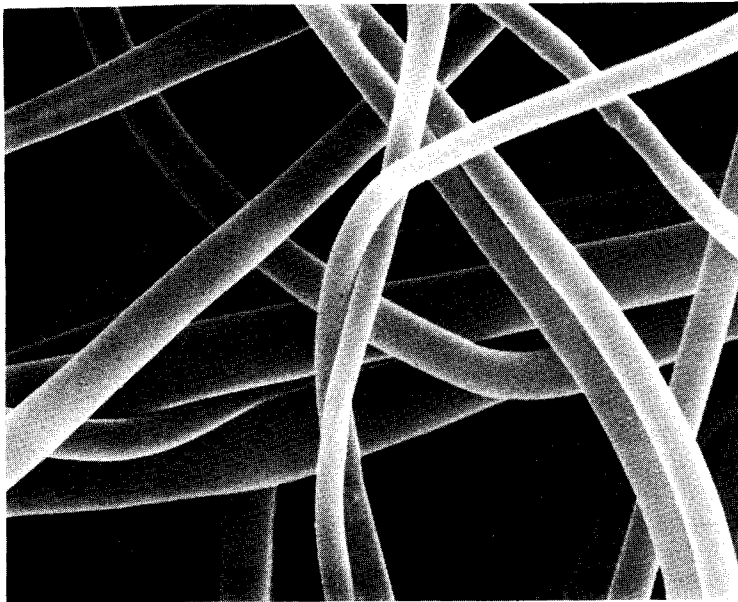
Photo 2

Specimen: The same as in Photo 1.

Treatment: Ion plating with Au at 100 Å, gas leakage Ar 3×10^{-2} Torr, ionization voltage 500 V. The specimen in horizontal rotation.

Exposure: At 25 KV, 2×10^{-11} A for 150 sec.

Remarks: The photo shows a chargingless and clear image without abnormal contrast, produced by ion plating.

5 μ
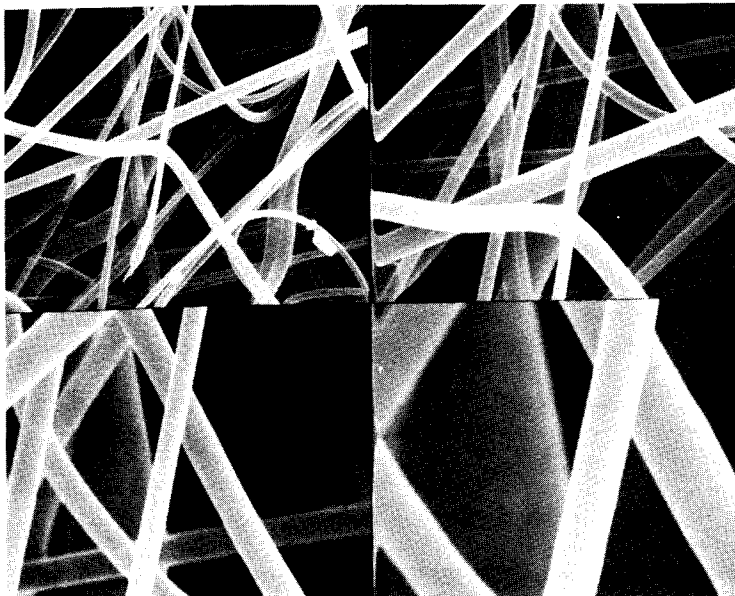
Photo 3

The specimen, treatment and exposure are the same as those in Photo 2, except to use an image composer.

Note: The image composer is a device for displaying two or four kinds of images (with different magnification factors and signals) on a CRT at the same time.

20μ	10μ
5 μ	2.5μ
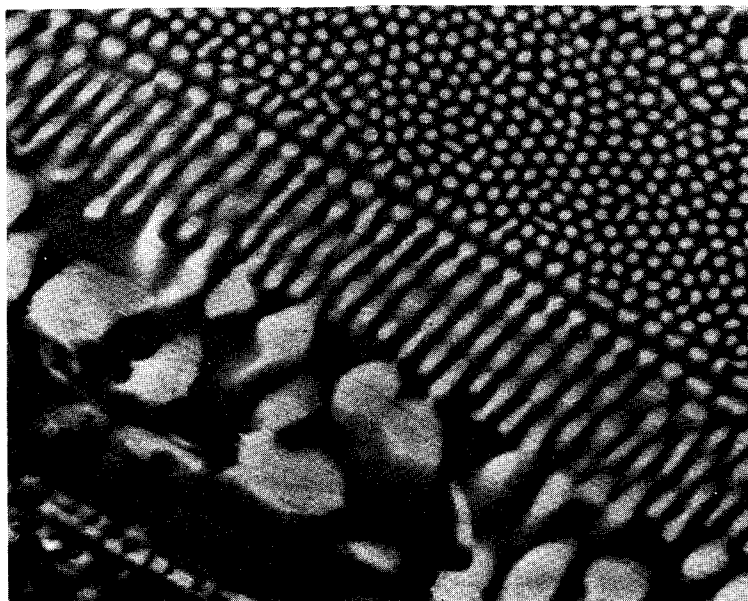
Photo 4

Specimen: Ag-Cu-Aℓ alloy

Treatment: Only buffing

Exposure: At 25 KV, 2×10^{-11} A for 150 sec., tilt angle of 40 deg.

Remarks: The photo shows some contrast attributed to structure, and slight buffing flaws. Relatively bright areas show high concentrations of Ag, and relatively dark areas show high concentrations of Cu and Aℓ.

3 μ
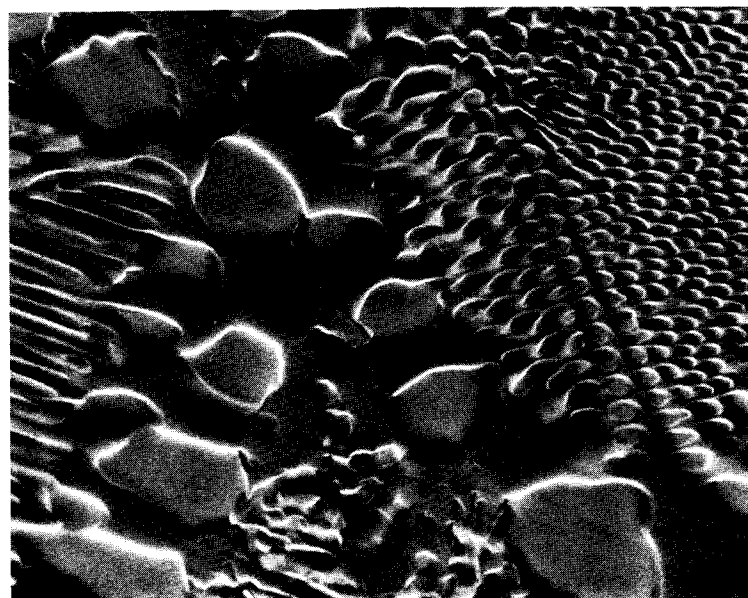
Photo 5

Specimen: The same as in Photo 4.

Treatment: After buffing, ion etching with gas leakage Ar 5×10^{-2} Torr, at 1500 V for 20 min. The etching with normal incidence and with the specimen at rest.

Exposure: The same as in Photo 4.

Remarks: The higher the concentration of Cu and Aℓ, the deeper the surface is etched.

3 μ
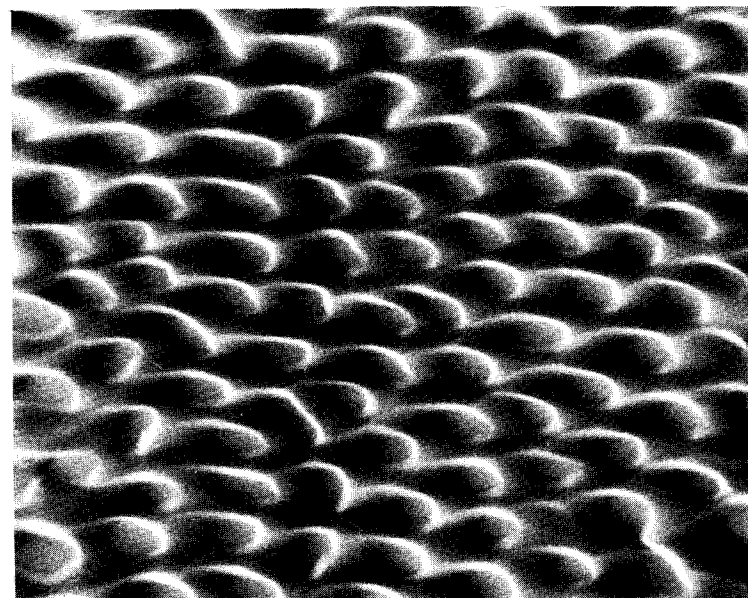
Photo 6

The specimen, treatment and exposure are the same as those in Photo 5.

Remarks: The photo shows a close-up view of the upper right-hand side of Photo 5 where a granulated structure is recognized with high concentrations of Ag.   The granules are of rod-shape and oblique to the normal direction; this allows the etching pattern to appear to flow.

1 μ
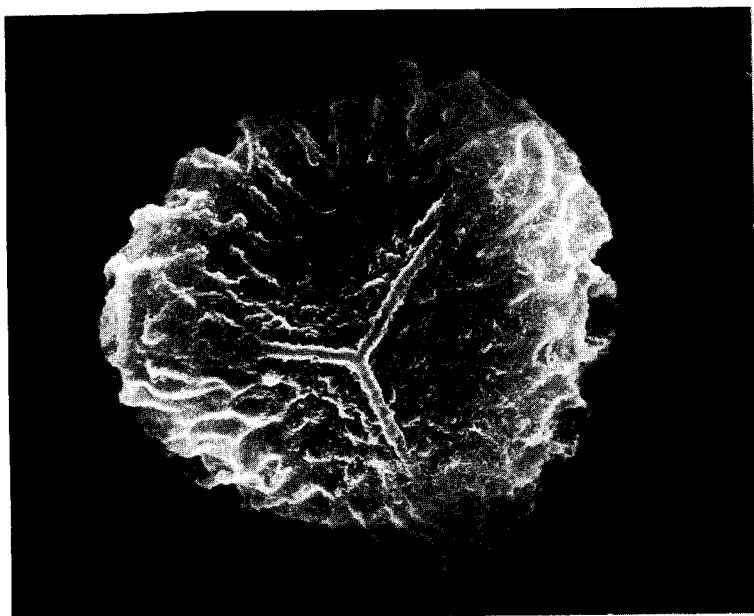
Photo 7

Specimen: Spore of a fern

Treatment: Only vacuum evaporation
  with Au-Pd. The specimen in
  precession.

Exposure: At 25 KV, 2×10^{-11} A for
  150 sec.

Remarks: The spore is as small as
  20 μ dia., and similar in shape with
  a seed-case. When it is split, a large
  number of granules of nearly 1 μ
  dia. come out.

  $\underline{5\ \mu}$
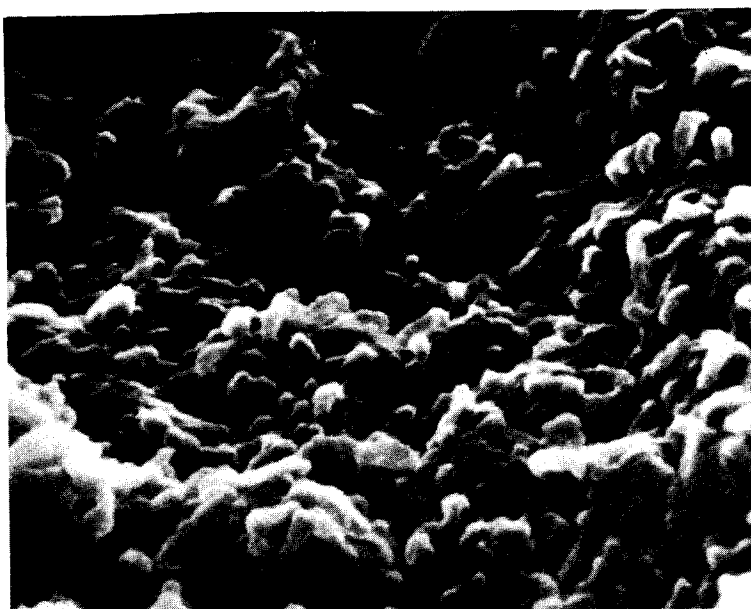
Photo 8

The specimen, treatment and exposure
are the same as those in Photo 7.

Remarks: The photo shows a close-
  up view of Photo 7.

  $\underline{0.5\ \mu}$

Photo 9

Specimen: The same as in Photo 7.

Treatment: After ion etching, ion
  plating. The ion etching with Ar
  3×10^{-2} Torr at 1500 V for 20 min.
  and with the specimen at rest. The
  ion plating with Ar 3×10^{-2} Torr,
  Au 100 Å, at 500 V and with the
  specimen in horizontal rotation.

  $\underline{0.5\ \mu}$

"Content map" and "Content profile" as applications of

automated electron probe microanalyzer.

K. Okumura, T. Soya* and H. Ohyi**

* Geological Survey of Japan

Hisamoto 135, Takatsu-ku, Kawasaki

** JEOL LTD.

Nakagami 1418, Akishima-shi, Tokyo

Because of the point character of the electron beam, electron probe microanalyzer is in wide use for the mineralogical and petrological studies of fine-grained minerals, zoned minerals, exsolution lamellae and others. The major difficulties in analyzing these minerals are due to their complex texture and chemical complexity. A slight shift of the irradiating position seriously affects the accuracy in quantitative analysis. Computer automation which can measure all elements to the measure without any stage movement reduces the above difficulties appreciably (Chodos et al.; 1972, Finger et al.; 1971) but leaves an error which may be attributable to electron beam drift during measurement.

The distribution and the contact relation of each phase in analyzing the sample are in themselves a very interesting; moreover, they show us the appropriate position to be analyzed. Before making quantitative analyses, we may or may not carry out linear or areal, qualitative analyses. Conventional linear or areal analyses by beam scanning or by moving the sample under a fixed beam, however, have the disadvantages of poor resolution of the scanning image and the difficulty of estimating quantitatively the concentration of each element.

Our automation system consists of the JEOL JXA-5A electron probe microanalyzer interfaced with a DEC PDP8/e minicomputer having a 12K word memory, and a typewriter. This system uses a high level conversational language, "JECASS" modified from "FOCAL*", and can provide all the instrument control and data reduction as simple commands. (Okudera et al.; 1974)

Two application programs of the automated electron probe microanalyzer, "Content map" and "Content profile", provide means to connect the quantitative character of point analyses with the continuous nature of qualitative linear or areal analysis. The sample stage is moved by micron-sized steps under the fixed electron beam and the measurement is carried out at each step. Three elements are measured simultaneously in each program. Analytical results are expressed in the content map as a two dimensional array of characters, in which each character represents the atomic ratio of three elements at each point. In the content profile, the results are shown by concentrations and three strings of characters which represent the variation of the respective elements along a measuring line.

* FOCAL is a language provided by DEC.

The standard procedure for constructing the content map is as follows.
(1) Designation of the three elements to be measured.
(2) Designation of the counting time for one point.
(3) Designation of "Composition areas" to be distinguished in the map.
    Composition areas are arbitrarily designated in a ternary system
according to the atomic ratio of the respective elements in compliance
with the mineral.
(4) Designation of the starting point of mapping, the number of counting
    points and the interval between each counting point.
(5) The standard sample is then automatically set under the electron beam,
    the X-ray peak is searched and the count rate is measured.
(6) The stage then moves to the starting point of mapping and the count
    rates of the three elements are measured simultaneously. The con-
    centrations in weight percentage given in comparison with standards,
    are divided by atomic weight and converted into the atomic ratios of
    the three elements. Each atomic ratio is compared with the composition
    areas designated in (3), and the character corresponding to the compo-
    sition area is printed. After typing the character, the stage moves
    to the next point and the process is repeated until all the points have
    been measured.
(7) Finally, the numbers of the counted points for each composition area
    and their proportions with respect to the total counts are printed.
    The procedure for constructing the "Content profile", is similar to
    that of the "Content map".

An example of the map is given in figure 1 which shows a part of a
pyroxene microphenocryst in basalt from Oshima volcano, Japan. Ca, Mg and
Fe are selected as measured elements since most pyroxenes are chemically
approximated by the ratio of the three end components, VIZ., wollastonite
$CaSiO_3$, enstatite $MgSiO_3$ and ferrosilite $FeSiO_3$.
The map shows the complex pattern of five distinctive areas, which are
indistinct under an optical microscope except for the orthpyroxene grains
scattered near the central part of the clinopyroxene prism. These five
phases are identified as augite (1), two subcalcic augites (4) and (5),
hypersthene (8) and pigeonite (9) by the nomenclature of pyroxene. Figure
2 shows the composite map and a sketch covering almost the whole part of
the same grain.

An example of the content profile along line a-b in figure 2 is shown
in figure 3. This profile presents the following information,
(1) The atomic ratio of Fe, Ca and Mg is shown as three strings of char-
    acters, 1, 2 and 4 respectively and four phases are clearly distin-
    guishable. Each phase corresponds to the respective composition area
    in the map and the boundaries agree with those in the map.
(2) Each phase is relatively homogeneous except for a little substitution
    between Fe and Mg near the marginal part of the phase and each phase
    contacts the adjacent phase at the sharp boundary.
(3) The ratio of the end components of pyroxene is directly estimated from
    the profile. For example, the phase expressed as pigeonite in the
    figure has a ratio of wollastonite 12, enstatite 56 and ferrosilite 32.
(4) It may be realized that the simultaneous fluctuation of the X-ray intencity
    caused by beam current drift and the surface topography or the differ-
    ence in the thickness of the conducting film is minimized by proportional
    expression. This is a common advantage in both the "Content map" and
    "Content profile" programs and enables us to make stable analysis over
    a prolonged period regardless of beam current drift and topographical
    conditions.

X= 15510   15540   15570   15600

(Content map of a pyroxene grain — ASCII character map with hand-drawn mineral-phase boundaries and an inset Ca–Mg–Fe composition triangle. Triangle regions labeled A, 1, 3, 25, 4, 5, 6, B, 7, 8, 9, C, with axis marks 45, 25, 28, 40 and X= scale 15630, 15660, 15690.)

Legend (upper table):

	count	%
A	0	0.00 %
B	0	0.00 %
C	84	14.46 %
1	119	20.48 %
2	0	0.00 %
3	16	2.75 %
4	5	0.86 %
5	77	13.25 %
6	9	1.55 %
7	0	0.00 %
8	0	0.00 %
9	267	45.96 %
X	4	0.69 %
-	293	
SP	87	

Legend (lower table):

	count	%
A	0	0.00 %
B	0	0.00 %
C	27	3.70 %
1	137	18.77 %
2	0	0.00 %
3	16	2.19 %
4	214	29.32 %
5	88	12.06 %
6	3	0.41 %
7	4	0.55 %
8	31	4.25 %
9	210	28.77 %
X	0	0.00 %
-	145	
SP	86	

Fig. 1. This shows an example of "content map" of a pyroxene grain in basalt, Oshima volcano. The measured elements are Ca, Mg and Fe. The characters on the map correspond to the specific "composition area" labeled as the same character on the inset triangle expressed in atomic ratio. The dots in the triangle represent the results of quantitative analyses on each mineral phase showing good agreement with the mapping. The total concentration of the above three elements in pyroxene mineral is between 20 and 50 weight percentage in oxide form. A point out of this range, over or under, is printed as "X" or "-" respectively. This figure was composed of two maps and the boundary between the mineral phases were written by hand.
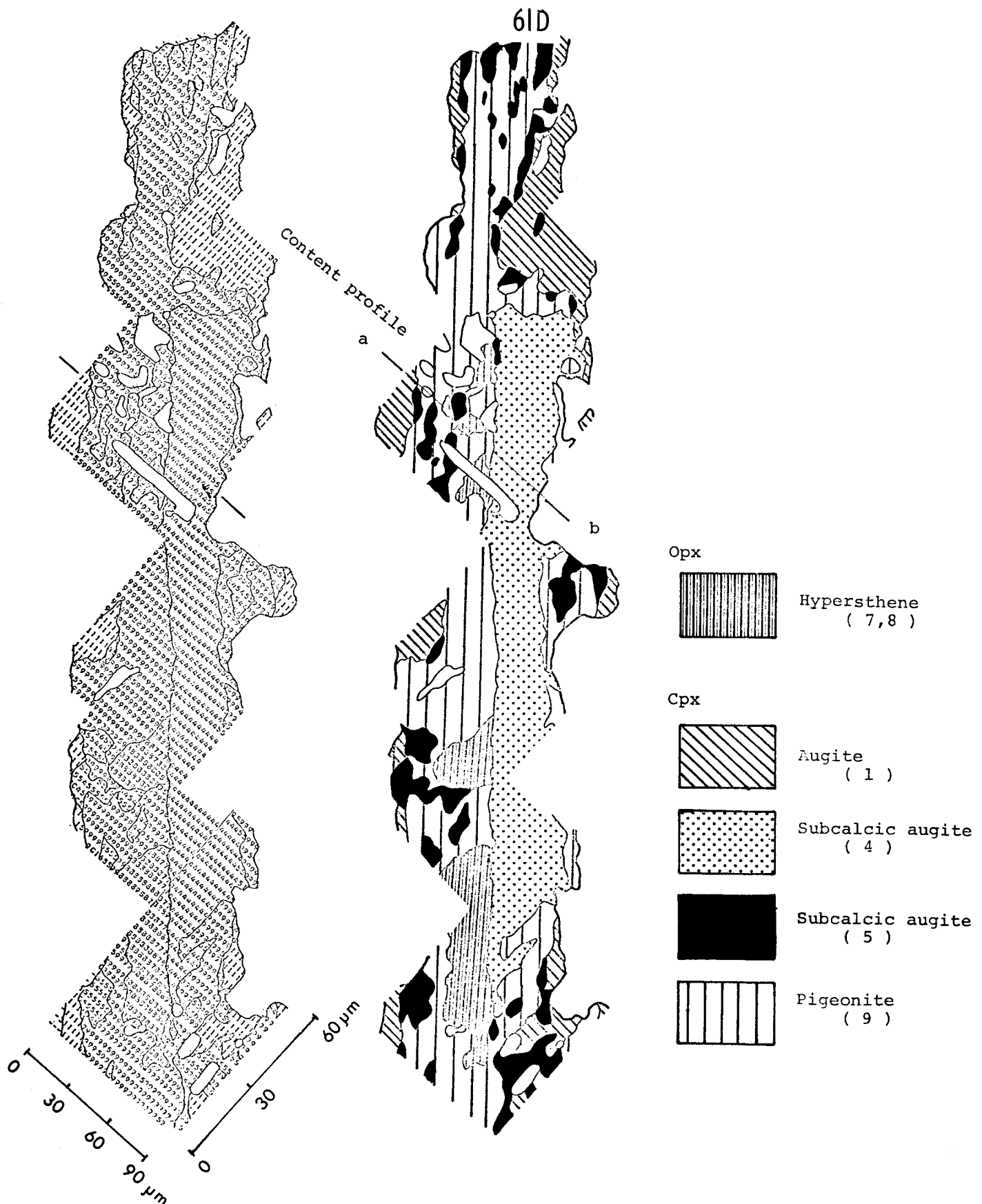
Fig. 2. This shows a composite content map and a sketch of a pyroxene grain showing the distribution of each phase. Line a-b shows the location of the "content profile" shown in Fig. 3. Hypersthene is rather easily located under an optical microscope matching with the pattern in the map but to distinguish each phase of clinopyroxene appearing in the map is difficult without the aid of an electron microprobe.

6lE

STARTING POS.* X: 16462 Y: 14299 Z: 1194
STEP RANGE: 40
INTERVAL * X: 3 Y: 0

MEAS ELEMENT 7 8 6

Content profile

1: Fe

2: Ca

4: Mg

```
ATM.RATIO        0.00    20.00    40.00    60.20    80.20   100.00
  X      Y    1 2 3*****0*****0*****0*****0*****0*****0*****0*****0*****0
16462 14299 161511*              1  6       a
16465 14299 131512*              1  6
16468 14299 131512*              1  2 4
16471 14299 141512*              1  2  4
16474 14299 141413*              1  2  4
16477 14299 141413*              1  2   4
16480 14299 131513*              1  2  4      Augite (1)
16483 14299 161214*                 3 4 4
16486 14299 180616*            2     3  1   4
16489 14299 170515*           2         1  4
16492 14299 170517*           2         1   4
16495 14299 170517*           2        1    4
16498 14299 160617*            2       1    4   Pigeonite (9)
16501 14299 160617*            2       1    4
16504 14299 160515*            2       1   4
16507 14299 160516*            2       1    1
16510 14299 170517*            2       1   4
16513 14299 150515*            2       1   4
16516 14299 180419*           2        1    4  4
16519 14299 170221*        2            1     4
16522 14299 180219*        2            1    4   Hypersthene (7,8)
16525 14299 180418*          2          1   4
16528 14299 180517*            2        1   4
16531 14299 180517*           2         1   4
16534 14299 180517*           2         1   4   Pigeonite (9)
16537 14299 160518*           2        1    1
16540 14299 150917*             2   1       4
16543 14299 140916*              2  1       4
16546 14299 140916*              2  1       4
16549 14299 150916*             2   1       4
16552 14299 140316*             2   1        4
16555 14299 150816*             2   1       4
16558 14299 150916*             2   1       4   Subcalcic
16561 14299 150816*.            2   1       4     augite (4)
16564 14299 160916*             2   1       4
16567 14299 170815*           2    1        4
16570 14299 130911*                   2 1      4
16573 14299 21400*4  1                              2
16576 14299 21400*4  1                              2
16579 14299 21500*4  1            b        Plageoclase (c) 2
16582 14299 11500*4  1                              2
  X      Y    1 2 3****0****0****0****0****0****0****0****0****0****0
```

SAMPLE: NI59021201 MINERAL: PX LINE: 5
DATE: MARCH5.75

Fig. 3. This shows the "content profile" along line a-b in Fig. 2. The first and second columns represent the stage position of the measured point and the third column shows the concentration of FeO, CaO and MgO, without correction, as a six digit number. For example, 161511 means FeO 16%, CaO 15% and MgO 11% (wt). Three curves show the compositional change in the atomic ratio of the measured elements. The character string "1" represents the Fe ratio, "2" the Ca ratio and "4" Mg ratio. When two strings meet at the same position, the sum of the two characters is printed as "6" for "2" and "4".

References

Chodos A. A. and Albee A. L. (1972): Automated microprobe analysis and applications to analysis of exotic lunar phases, Proc. 6th International Conference on X-ray Optics and Microanalysis, 779-784

Finger L. W. and Hadidiacos C. G. (1971): Aspects of computer automation of an electron microprobe, Annual Rep. Geophy. Lab., 1970-1971, 269-275

Okudera, S., Ohyi, H., Harada, Y. (1974): Applications with a computer controlled electron probe microanalyzer system, 9th Annual Conference on Microbeam Analysis, 33A-33C,

INTEGRATED MICROANALYSIS SYSTEM FOR THE MODERN LABORATORY

B. Kenessey and J. Leitner

Applied Research Laboratories
Sunland, California

Electron microprobe automation has gained momentum considerably over the past few years. Several individual laboratories accomplished automation very successfully. Typically, first and second generation instruments were fitted with a digital control system to control crystal spectrometers, sample stage movements, and other hardware functions. Very often the interfacing, which provides means for communication between the computer and the microprobe, presented a great deal of inconvenience for the users because the various system interface components lacked compatibility.

With a clearly established trend towards automation, integrated micro-analysis systems have been developed to greatly extend the electron probe's capability. Such systems consist of a digitally controlled electron microprobe, with the associated hardware and software required to control the instrument and handle the analytical data.

A truly automated and versatile microprobe required that new hardware be designed for digital control. In particular the dynamic components such as the wavelength dispersive scanning spectrometers and sample handling devices need to be precise and durable to accommodate the increased demands. In the design of an instrument incorporating such improved components, it was also logical to develop fixed wavelength monochromators to provide rapid simultaneous analysis of a selected array of elements and to complement the scanning spectrometers which have the ability to perform sequential qualitative as well as precise quantitative determinations.[1] The instrument's versatility is further enchanced by a clean vacuum system and electron optical system that provides high spatial resolution and versatility for signal detection. A full complement of easy to operate controls are provided for the electron beam scanning system, along with a large 1000 lines/frame visual display CRT and a high resolution 2500 lines/frame photographic CRT.

The system manipulation and data exchange is accomplished with a dedicated PDP 11/05 minicomputer via standard NIM modular instrumentation controlling the following functions:

1. Up to five scanning spectrometer motors

2. X, Y, and Z sample stage motors

3. Sample stage joystick

4. Electron beam deflection in X and Y axis

5. Base line and window width settings for PHA's

6. Timer - scalers

7. Beam blanking

Alternatively, the instrument has been interfaced with the internationally recognized standard for digitally controlled instruments, the modular CAMAC system.[2] In this particular instance additional instrument functions, such as high voltage supply, filament current, bias voltage and magnetic lens controls were automated.

The heart of the software system is a set of some 20 assembly language coded subfunctions which allow the operator to communicate with the electron microprobe hardware. Using BASIC, a high level conversational computer language, the subfunctions are programmed to do meaningful hardware manipulation and data gathering tasks.

The computer program developed to do quantitative analysis using the correction coefficient method of converting K ratios to weight percent has the following salient features:

1. Spectrometers seek peak on standards also on unknown if desired.

2. Intensity data are corrected for background, drift, and dead time.

3. Variable count termination capability: Operator can specify minimum count requirement and also maximum time allowed to achieve this count.

4. Multiple unknown data point X/Y/Z coordinates are conveniently input to the computer via the joystick control pushbutton. Once the analysis at the first data point begins it proceeds uninterrupted.

5. Fixed channels are always observing the x-ray peak intensity. On the unknown sample the fixed channels collect data along with the scanners, and the data gathering is cumulative, i.e. each time a scanner count integration occurs fixed channel counts are collected, thus effecting a speed and precision improvement.

6. The correction coefficient used in the data correction procedure can either be assumed to be a constant, independent of concentration, or can optionally be calculated from the first intensity ratio, using a simple polynomial fit to binary calibration curves.

7. Hard copy output is Wt %, K Ratio, standard counting error, and atomic proportion if applicable.

Because of the underlying programming philosophy, new programs are created with relative ease as various needs arise. Other programs include: Qualitative analysis, parallel stepper motor driver, step scan, matrix generation, spectrum analysis, statistical studies and carbon contamination investigation. Specific examples of these programs and appropriate evaluation data will be presented.

In summary, a complete integrated microanalysis system for practical and flexible operation has become a reality. An automated electron microprobe with durable dynamic components, versatile signal detection, and good SEM

imaging capability can contribute significantly to the efficiency of data gathering. Its usefulness is further enhanced by the simultaneous x-ray detection capability for the determination of multiple elements and the computer software programs for quantitative analysis which have been developed to minimize the required interaction between the analyst and the system.

References:

1. E. Davidson and B. Kenessey, "The Quantometer Principle Applied to Microanalysis". Seventh International Conference on X-Ray Optics and Microanalysis 1974

2. W. T. Kane, "A CAMAC Automated Electron Microprobe". Microbeam Analysis Society, Ninth Annual Conference

A New Transmission Electron Microscope Accessory

for a Combination SEM/Electron Probe Microanalyzer

C. Conty and D. Colliaux

A transmission electron microscope (TEM) has been developed for the Cameca MBX combination scanning electron microscope/electron probe microanalyzer. With this accessory, a direct transmission electron image can be obtained as in the conventional transmission electron microscope.

In certain particular applications the scanning electron microscope is used to examine thin electron transparent specimens such as thin metal films, extraction replicas of metallurgical or geological interest and biological specimens. With these types of specimens it can be very useful to observe them using the classical techniques of transmission electron microscopy and provide the researcher with the type of images with which he is more familiar. This TEM observation should be possible without abandoning the electrical imaging and x-ray microanalysis capability of the SEM/electron probe.

The technique of combining TEM imaging with electron probe x-ray microanalysis capabilities was first described by P. Duncomb in 1962.[1] The acronym coined for this instrument was EMMA – electron microscope microanalyzer. This instrument and subsequent versions of this instrument have firmly established the unique advantages of a combination electron probe TEM instrument.

A simpler version of EMMA was developed by Cameca in 1966 for their second generation electron probe, the MS46 developed in 1964. The accessory being described here is a more sophisticated version containing an additional electromagnetic lens. The other technique for observing electron transparent specimens in electron probe microanalysis is scanning electron transmission microscopy (STEM). However, using this technique severely limits detection sensitivity when simultaneous electron imaging and wavelength dispersive x-ray analysis is required. This results from the much lower illumination conditions imposed by STEM compared to TEM electron imaging.

The MBX TEM accessory is shown schematically in Figure 1 and Figure 2. It consists of the following principle elements:

- A supporting housing
- A vertical column containing three electromagnetic lenses
- A specimen stage with three orthogonal motions
- A viewing chamber with a large window for viewing the fluorescent screen
- A 70 mm film cassette
- An electronic control and measuring chassis

Characteristics

The accessory has the following operational characteristics:

- High voltage range (continuously adjustable): 1 to 50 KV
- Magnification range (continuously adjustable): 2,000 to 50,000
- Typical resolution: 20 Å
- Specimen displacement: 20 mm in X , 6 mm in Y, 1 mm in Z

Up to five 3 mm diameter specimens may be accomodated on a transmission type holder which is introduced through an air lock.

Electron Optics

The electron optics consists of the following lenses:

- An objective lens located directly below the specimen with a focal distance of 4 mm and containing a three position aperture control.
- An intermediate low distortion lens that permits the magnification to be adjusted continuously by a factor greater than 10 in each range setting.
- A projection lens with a 1.6 mm focal distance and containing a 750 micron fixed aperture.

Alignment controls are provided for the lenses and apertures. These controls are operable from outside the vacuum with the beam on. The lens coils are freon cooled. The illumination conditions are such that switching from TEM mode to the conventional microanalysis mode can be done conveniently and rapidly.

With the TEM in operation it is possible to utilize this accessory in conjunction with most of the standard MBX accessories, in particular:

- inclined and vertically mounted wavelength dispersive spectrometers
- an energy dispersive spectrometer
- specimen anticontamination device
- light optical viewing

The mounting of the accessory on the MBX does not interfere with normal SEM and electron probe operation. When the standard specimen chamber is to be used, the accessory is stored conveniently in the base of the console.

Notes:
1. Duncumb, P. ,"Fifth International Conference on Electron Microscopy", Academic Press (1962).

ADAPTATION OF A COMBINATION SEM/ELECTRON PROBE
FOR BIOLOGICAL INVESTIGATIONS

By

C. Conty, CAMECA, Courbevoie, France

R. Lewis, Cameca Instruments, Inc., Elmsford, N. Y.

Biological studies with the electron probe are placing new requirements on electron probe instrumentation. These requirements stem mostly from the different techniques encountered in specimen preparation and handling together with the need for high x-ray spatial resolution. This paper describes the objectives of an accessory development program being carried out at Cameca to tailor the MBX combination SEM electron probe to the study of biological specimens.

One of the more critical problems encountered with biological specimens is the need to manipulate and analyze the specimen in a frozen state. This has been solved on the MBX with a special specimen stage that permits:

1. Freeze fracturing the specimen in the MBX,
2. Coating the specimen with a conductive material if necessary, and
3. Analyzing the specimen at temperatures below -140°C.

A standard MBX accessory which compliments the new cold stage is the cold plate decontamination system. The cold plate minimizes carbon buildup greatly improving light element analysis. In addition, an automated stage with a joystick control has been developed as a part of this program. Programmed control of X, Y and Z is possible using appropriate computer software.

For viewing biological specimens in modes more familiar to the biologists, two types of imaging systems have been developed; namely scanning transmission electron microscopy (STEM) and transmission electron microscopy (TEM). The latter, the more sophisticated system, provides spatial resolution down to 20 Å. TEM provides the ability to view the specimen under high illumination conditions which is particularly important in x-ray analysis.

This biological version of the MBX can be equipped with an energy dispersive spectrometer (EDS) and/or wavelength dispersive spectrometers (WDS). The latter can be mounted vertically and/or inclined. The inclined configuration is important for examining the freeze fracture type of specimen because it is the least sensitive to specimen height variation.

Electron Spectroscopy for Chemical Analysis

D. A. Shirley, Department of Chemistry
University of California, Berkeley, CA.

As an analytical method, electron spectroscopy has advantages and disadvantages relative to conventional techniques. We shall focus on a particular aspect of electron spectroscopy for chemical analysis; namely, the characterization of surfaces by x-ray photoelectron spectroscopy (XPS). Auger lines also appear in these spectra, induced by x-rays rather than by electron excitation. Since the surface sensitivity is determined primarily by the outgoing electrons, most of the comments made below apply equally well to photoelectron and Auger spectra, and they will be treated together.

The essential XPS experiment involves the ejection of photoelectrons by characteristic x-rays of energy $h\nu$. A photoelectron from an orbital of binding energy E_B leaves the sample with kinetic energy

$$K = h\nu - E_B.$$

The photoelectrons are energy-analyzed in a high-resolution electron spectrometer. They are counted individually, with each electron producing a digital pulse, and the spectrum is stored in a memory as in-intensity versus binding energy.

Individual electronic orbitals appear as peaks in the spectrum. This is advantageous relative to the usual "derivative" mode of obtaining Auger spectra, because peak shapes and intensities can be interpreted readily (Auger lines in XPS spectra appear as peaks). However, the very fact that single-electron counting is necessary (and feasble) is indicative of the relative insensitivity of XPS. Even with an intense x-ray source and a concentrated sample, a line of average cross-section will yield only 10-100 counts per second. This is the figure for a large sample, of 10 mm^2 area. While some improvements are surely feasible, the prospects for an XPS microprobe of general utility are very poor.

The XPS method has the advantage of being able to detect all elements except hydrogen; i.e., all elements that possess core electron orbitals. Because it is a high resolution technique, there is little danger of assigning an XPS peak to the wrong element.

Thus the 1s electron binding energies in the adjacent elements carbon and nitrogen are 290 eV and 410 eV, respectively, while the peak widths are 1-2 eV.

Another advantage of XPS is that the exact value of the core-level binding energy is determined by the chemical state (roughly speaking, by the oxidation state). Thus, for example oxygen in adsorbed CO, adsorbed O_2, or surface oxide will all give distinctive chemical shifts in the oxygen 1s binding energy. This allows very detailed studies of surface oxidation to be performed, using XPS to monitor the chemical state of the oxygen as it is adsorbed, reduced, diffused into the bulk, etc.

Surface sensitivity is a strong point of XPS. The mean free path of a monoenergetic 1000 eV electron through typical metals is 15 - 20 Angstroms. This is the distance travelled between two events that involve energy loss. The energy loss is quantized, however (usually by plasmon creation), and the quanta are large enough to remove electrons completely from the main (zero-loss) line. Thus the main line is made up of electrons photoemitted from atoms at a mean depth of 15 - 20 Angstroms from the surface, if the experiment is designed to detect electrons that leave normal to the surface. Tilting the sample, so that electrons leaving at an angle θ from the surface are detected, increases the effective thickness through which an electron must travel, by a factor of $1/\sin\theta$. For $\theta = 6°$, this reduces the effective sample depth from 15 - 20 Angstroms to 2 Angstroms, thereby greatly enhancing the surface sensitivity of XPS. In some respects this tunability of surface sensitivity is a distinct advantage. For example, a given spectral feature may be positively identified as arising from surface-layer atoms or not, depending on whether or not its relative intensity increases on reducing the electron takeoff angle θ.

Aluminum metal can be used to illustrate the application of XPS as a surface technique. If a sample of aluminum is introduced into the spectrometer without treatment, the 50 Angstrom oxide layer will completely mask the metal spectrum. A strong oxygen 1s line will be observed, and all the core-level lines of the element aluminum will appear in the oxide positions.

Mechanical cleaning of the aluminum surface in air before intro-

duction into the spectrometer will reduce the oxygen line intensity. The metal peaks will appear with intensities comparable to the oxide peaks.

If the sample is evaporated in high vacuum (10^{-8} torr), a well-developed bulk plasmon satellite structure appears. The aluminum lines are in the metal positions, and only a slight asymmetry toward higher binding energies betrays the presence of a sub-monolayer oxide layer. A weak oxygen 1s signal is visible. Tilting this sample to a low takeoff angle alters its appearance dramatically. An oxide peak appears beside the metal peak and of equal intensity, and the oxygen 1s peak grows. This illustrates the power of surface-sensitivity "tuning".

A sample prepared and studied in ultra-high vacuum (10^{-10} torr) shows new features: Surface plasmons. These establish the presence of a clean aluminum surface. In this case tilting the sample enhances the surface-plasmon intensity.

Adsorption can also be studied by XPS. In particular, detailed spectra of CO adsorbed on various metals show several bonding sites and appear to establish from the molecular-orbital XPS spectrum of CO alone that the alpha form involves CO "standing up" with the carbon bonded directly to the metal.

W. Reuter
IBM Research Center
Yorktown Heights, N.Y. 10598

ION INDUCED X-RAY SPECTROSCOPY

The generation of vacancies in atomic core levels by irradiation with photons or electrons followed by the emission of x-radiation is widely applied in materials characterization today (electron microprobe (EMP), X-ray fluorescence spectroscopy). Alternatively such vacancies can be produced by ion impact and the emitted x-radiation can be analyzed by a silicon or crystal dispersive spectrometer similar to well established procedures in electron probe microanalysis. Recently we have seen much research activity in this rapidly expanding field of ion induced X-ray spectroscopy (IIXS). One reason for this renewed interest in a phenomenon known for four decades is the increased availability of particle accelerators in the MeV region at reasonable cost. While research in nuclear physics, ion implantation and charged particle backscatter analysis are still the primary motive in the acquisition of an accelerator, the relatively small added cost for an X-ray analysis system can be easily justified in view of the increased flexibility. The proper choice of the projectile mass and energy allows in some cases the highly selective excitation of a particular element in a composite target, not possible in the other modes of X-ray spectroscopy. The intensity of the background radiation is much smaller in IIXS as compared to EMP leading to inherently better detection sensitivities in the former method, assuming operation at the same beam current and for energies yielding similar ionization cross sections. The most serious disadvantage of IIXS is its inability to generate X-rays efficiently with a micron size beam without a prohibitive temperature rise of the specimen, i.e. IIXS is not a microprobe technique.

Very little attention so far has been given to the potential of IIXS as a quantitative analytical technique. We developed a correction scheme (to be published J. App. Phys. in 1975) that can be applied to the quantitative analysis of any multi-element target assuming a homogeneous distribution of all constituents over the projectile range. Thin films may also be analyzed in respect to thickness or composition provided that one of these two parameters is known. The direct X-ray production is calculated from the binary encounter approximation, thus restricting the applicability of this model to pure Coulomb excitation. The charge state of the projectile is assumed to remain unchanged over the effective excitation range in the target. This assumption is theoretically valid for protons independent of the energy. The incident ion can always transfer some of its kinetic energy to a target atom. Target – target collisons leading to ionization have been assumed to be neglible for the proton energies used in this experiment (<3 MeV). The second part of our program accounts for the enhancement of the X-ray production of an element A by the radiation of an element B in the target. This secondary X-ray production process can only occur provided the energy of the exciting radiation of element B is higher than the absorption edge energy of the particular core level of element A. Up to 40% of the total X-ray production may be due to this process under the favorable condition of K → K excitation with the energy of the exciting radiation slightly above the absorption edge energy of the excited core level. Usually, however, the effect is small and can be neglected. We have performed several sample calculations so that the reader may estimate the magnitude of this correction for a particular radiation combination and elemental concentration.

A general review of ion induced X-ray spectroscopy will be given with special emphasise on the quantitative aspects of this technique.

NUCLEAR BACKSCATTERING TECHNIQUES

James W. Mayer
California Institute of Technology
Pasadena, California 91125

Backscattering spectrometry is basically a nuclear technique that has been utilized recently to a large extent for analysis of the near surface region of solids. Applications of backscattering spectrometry as an analytical technique have primarily focused on depth microscopy - the ability to determine composition variation or impurity distribution as a function of depth below the surface of the sample. The technique is capable of providing analysis with depth resolution of a few hundred angstroms over depths of thousands of angstroms without recourse to sample erosion or layer removal. In addition, it provides quantitative analysis without recourse to standards of similar composition.

We compare in Fig. 1, techniques which utilize sputtering and those which rely on energy loss to obtain depth profiles. Techniques (such as AES and SIMS) which provide analysis of the composition at the outermost layers of the sample must be combined with target sputtering or some other means of layer removal to allow means to obtain depth profiles. Depth profiles generated by energy loss of energetic particles is the subject of this review; particular emphasis is placed on backscattering analysis because of its versatility in the determination of composition profiles. Ion beam generated x-rays can give modest depth information due to the strong energy dependence of the excitation cross-section and nuclear reactions, particularly those with sharp resonances, can be utilized to obtain depth profiles.

One of the major advantages of backscattering spectrometry is that it gives depth profiles in a fast, simple and direct fashion. To a first approximation, there is a linear conversion from the energy scale to the depth scale. The technique is quantitative and can be used to give absolute numbers

for the number of impurities per cm^2 or layer thicknesses in terms of atoms per cm^2. On the other side, there are limitations to backscattering spectrometry: the sample depth that can be analyzed with MeV He ions is about one micron. Beyond this depth the total energy lost along the inward and outward paths becomes large and there is a loss, then, in the simplicity of the technique. Greater analysis depths (up to about 10 microns) can be achieved with MeV protons with a concomitant loss in mass and depth resolution and hence loss in quantitative ability. The sensitivity to low atomic number elements is poor and nuclear reactions or resonance techniques must be introduced to obtain quantitative data on trace amounts of these elements. Of course, if large concentrations (greater than a few atomic percent) of a small atomic number element are present, the concentration can be determined from its influence on the back-scattering yield from high mass elements.

The basic concepts underlying backscattering analysis will also be discussed in this review. Mass identification is provided by the kinematics of elastic collisions between the energetic projectiles and target atoms and depth scales are provided by the energy loss of the projectiles along their inward and outward paths. Quantitative analysis rests upon the well-established behavior of the scattering cross sections. Details are given in (1) to (4) and references cited therein.

References

1. M-A. Nicolet, J.W. Mayer and I.V. Mitchell, Science <u>177</u>, 841 (1972).

2. W. K. Chu, J. W. Mayer, M-A. Nicolet, T. M. Buck, G. Amsel and F. Eisen, Thin Solid Films <u>17</u>, 1 (1973).

3. W. K. Chu, M-A. Nicolet, J. W. Mayer and C. A. Evans, Jr., Anal. Chem. <u>46</u>, 2136 (1974).

4. J. W. Mayer and A. Turos, Thin Solid Films <u>19</u>, 1 (1973).

Depth Concepts

A. Layer Removal by Sputtering

• Auger electrons ⎫
electron beam   ⎬ Auger Electron Spectroscopy

ion beam   ⎫
• sputtered ions ⎬ Secondary Ion Mass Spectrometry (SIMS)
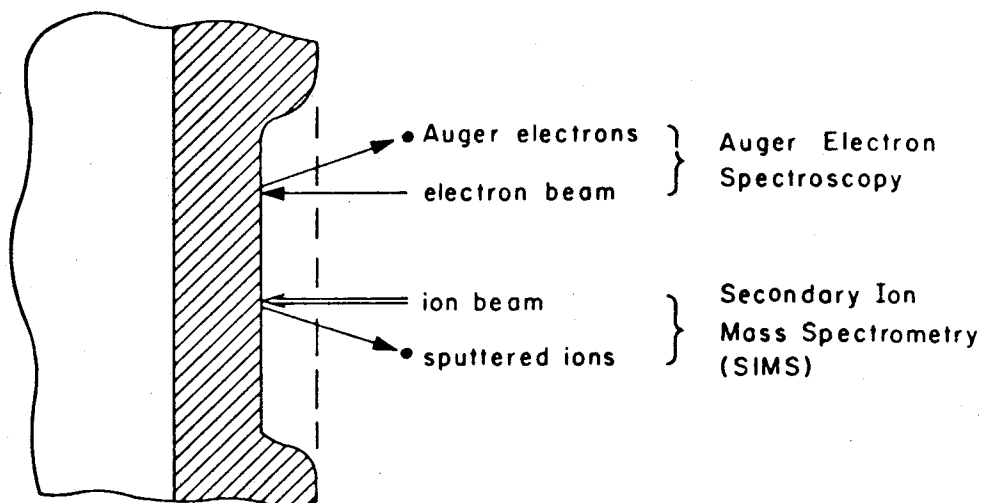
B Layer Thickness by Energy Loss

x-rays   Ion Induced x-rays

Reaction products   Nuclear Reactions

○ MeV He^+ or H^+

He ions   Backscattering Spectrometry
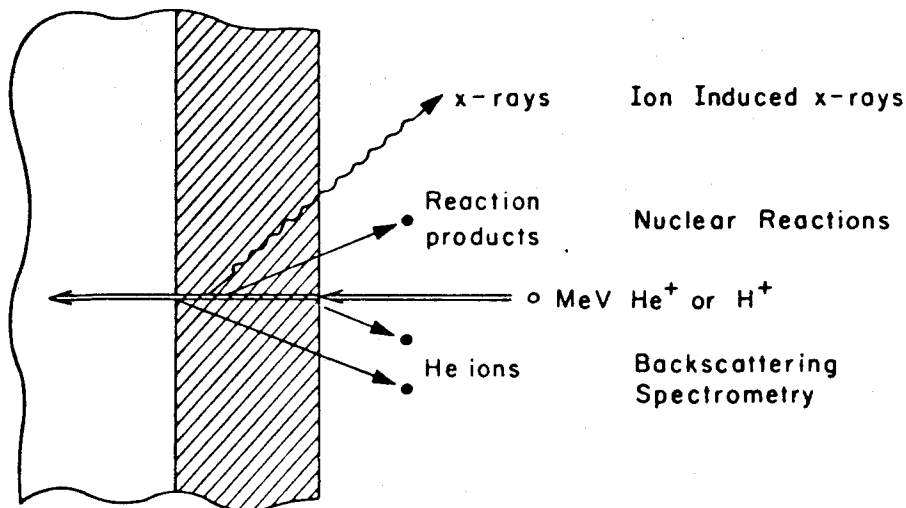
Figure 1. Schematic representation of the two primary methods by which composition in depth has been obtained. In A, surface sensitive techniques, AES and SIMS, are used to analyze the outermost layers of the surface. Layer erosion by sputtering is used to expose deeper regions. In B, energetic particles penetrate the layer of interest. Depth profiles are determined from energy loss of particles on their inward and/or outward trajectories.

Surface Characterization
of Heteroepitaxial (0001) CdS Films

H. Edward Mishmash
3M Company, Saint Paul, Minnesota

With the increasing application of cadmium sulfide as a
photoconductor and possible use for solar energy cells, the
conditions related to the growth of CdS films have become
more important. Growth conditions favoring a particular
morphology have been determined by several investigators,
with a few hypothesizing growth mechanisms. This paper
involves the use of microscopy (light, transmission electron,
and scanning electron), x-ray topography, low temperature
(4.2°K) uv excited edge emission, and electron probe cathod-
oluminescence to correlate the growth conditions necessary
to produce a flat surface, a surface dominated by flat tops,
or a surface predominately populated by pyramids.

Single crystal CdS films were grown epitaxially on the (111)
SrF_2 cleavage face by vacuum vapor deposition. Film thickness
was determined and optical and scanning electron micrographs
taken of the surface. Also, some TEM photographs were made
of very thin (<1000Å) films to determine the dislocation
structure. After studying the morphology of a film, it was
examined with the above mentioned techniques to experimentally
prove the hypothesized growth mechanisms.

The surface morphology and structure of the CdS films were found
to be very dependent upon the degree of supersaturation and the
surface roughness of the substrate. The smoothest films were
grown at the lowest level of supersaturation. At a medium
supersaturation, the flat tops become the dominant morphological
structure, as shown in Figure 1a (optical micrograph) at 150X
and the scanning electron photomicrograph (Figure 1b) at 6000X.
As the supersaturation is maximized, the hexagonal pyramid is
the primary surface structure. Figure 2 represents a typical
area on these films. The same type of micrographs are obtained
for a system of minimum supersaturation, but with a pitted
substrate surface.

It was believed that the formation of the pyramids was by growth
around a "precipitate" and that in this case the precipitate was
a cadmium droplet. The droplet forms on the substrate when the

cadmium atoms cluster at a nucleation site faster than they can diffuse away, this condition occurring at high supersaturation.

Observations of the low temperature (4.2°K) uv excited edge emission spectra support the hypothesis. They show that there are definite relationships between the various surface structure types and cadmium sulfide crystals doped with excess cadmium. X-ray topographic studies show that the hexagonal pyramids have a different crystallographic orientation than the film and that they are probably twins. The twins could be formed by short-ranged diffusion at stacking faults generated by a lattice mismatch when the film grows around the cadmium droplet.

A significant part of the characterization of the morphology-growth mechanism hypothesis was the cathodoluminescence observations. The little used fact that cathodoluminescence can be used as an indicator of minor impurities which may be present in concentrations less than may be otherwise detected by the microprobe was applied in this case. Photos were generated by scanning the sample and monitoring the photon emission with a photomultiplier tube attached to the optical microscope of a MAC 400 microprobe. The generated signal was used to modulate the face of the cathode ray tube from which the photos were taken. No attempt was made to determine the wavelength(s) of the emitted radiation, but it was noted that it was in the green region of the spectrum. The photos obtained show that the films with a preponderance of hexagonal pyramids were grossly inhomo-geneous. It can be discerned from Figure 3 that the dark non-fluorescing areas correspond to the areas occupied by pyramids. This observation is consistent with the hypothesis that the pyramids are cadmium rich, because a cadmium droplet should not fluoresce.

Films in which the dominant feature was the hexagonal flat top were also examined and the results shown in Figures 4a & 4b. The flat tops fluoresce uniformly like the surrounding film, indicating similar structure. This is what would be expected if they were formed by two dimensional nucleation. X-ray topographic results further support this by the fact that they indicated that the flat tops have the same crystallographic orientation as the film, not a defect induced growth.

Acknowledgements
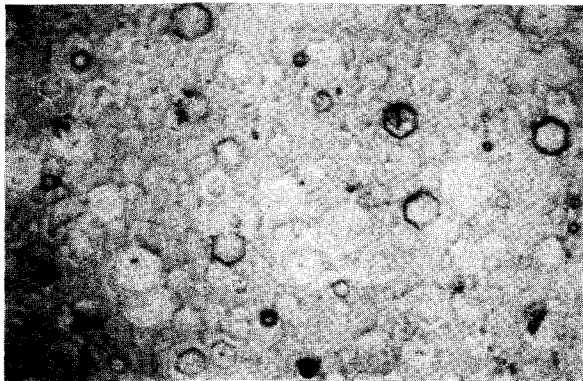
Fig. 1a Optical micrograph of CdS film grown at medium supersaturation on SrF_2. 150X
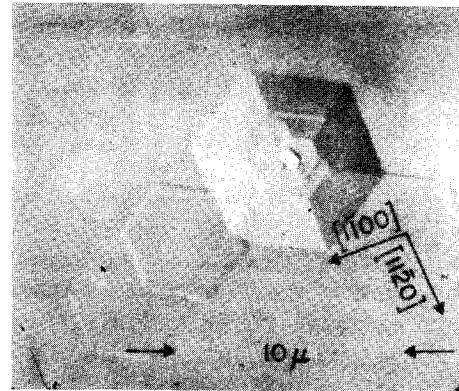
Fig. 1b Scanning micrograph of the film showing hexagonal flat tops at 6000X.
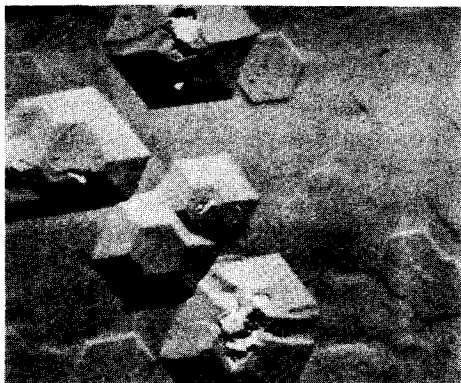
Fig. 2 SEM photo of CdS film grown at maximum supersaturation showing pyramids. 6000X
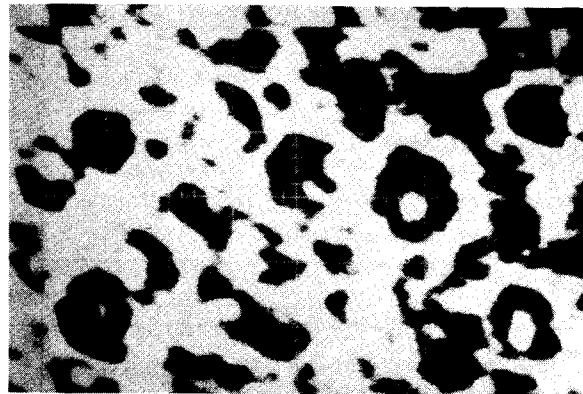
Fig. 3 Cathodoluminescence photo of CdS film with pyramid surface. 500X
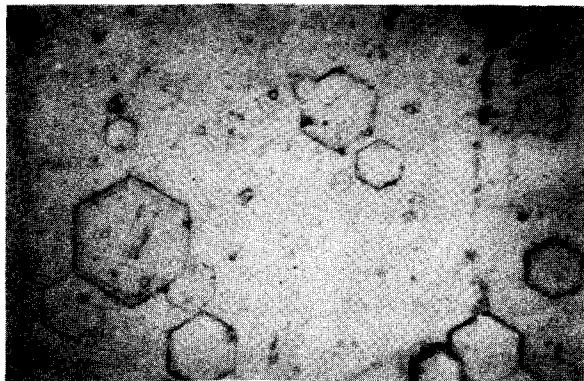
Fig. 4a Optical micrograph of flat top CdS film. 500X

Fig. 4b Cathodoluminescence photo of area on 4a. 500X

DIGITAL PROCESSING OF AUGER DATA

J. B. Bindell and J. W. Colby
Bell Laboratories
555 Union Boulevard
Allentown, Pa. 18103

Since Auger spectra are superimposed on a very high secondary electron background, it has become common practice to obtain Auger spectra by differentiating the detected secondary and Auger signals.[1] The derivative spectra obtained in this way from a cylindrical mirror analyzer (CMA) is the usual mode of Auger spectra presentation. It has become quite common for workers in this field to use the lower extrema of the spectra for elemental identification and the peak-to-peak excursions as a measure of the amplitudes of particular Auger peaks.

Both the modulation technique used to obtain the derivative spectra and the CMA introduce distortions into the data, the former usually being referred to as modulation distortion while the latter is the result of the detector geometry. Since any theoretical quantitative Auger analysis technique must, of necessity, be based upon the true $N(E)$ data, it is clear that computer interfacing to Auger spectrometers and subsequent data processing is a logical development. Toward this end, a PDP-8E computer has been interfaced to a Physical Electronics Inc. Scanning Auger Microprobe system and the collected data have been analyzed

on a larger PDP-11 computer system; the latter was required
due to core limitations of the PDP-8. In this paper, we
shall outline some of our preliminary observations con-
cerning data analysis and present some initial results
of our digital approach to Auger Spectroscopy.

In the process of developing data reduction programs,
a number of interesting computations were made concerning
the use of derivative spectra. In particular, if $N(E)$ is
the actual electron energy distribution emitted from a
sample, then the CMA is known to produce an output signal
$I(E)$ given by $E \, N(E)$ where the constant of integration has
been taken to be unity.[2] The output of the lock-in
amplifier is then given by the Fourier component of this
equation at the modulating frequency. This results in
the well known expression:

$$I(E_0) = \sum_{n=1}^{\infty} b_n K^n \frac{d^n I}{dE^n}\bigg|_{E_0} , \qquad (1)$$

where K is the modulation amplitude,

and
$$b_n = \frac{2n}{\pi(n+1)} \int_0^{\pi} \sin^{n-1} x \, dx \quad (n \text{ odd}) . \qquad (2)$$

It is usually assumed for E less than 100 eV,

$$I (E_O) = E_O N' (E_O) \quad , \tag{3}$$

that is, all but the leading terms may be neglected. By assuming a Gaussian form for $N(E)$ whose standard deviation is 2 eV and which is centered at $E = 100$ eV it is easy to demonstrate the inadequacies of equation (3). Figure 1 shows just this case where a modulation voltage of twice the standard deviation of the line is used and the output is evaluated at various levels of approximation to equation (3). In this case it is clear that the series does not really converge to a fixed signal until at least 11 derivatives are included in the summation. For further increases in the modulation voltage, still more terms are required while at the same time, the position of the signal's negative extrema continually increases with modulation voltage. This is shown in Figure (2) for the theoretical case mentioned above; it has also demonstrated for the real experimental situation.

Although the Taylor series approach to the analysis of CMA data is useful for identifying certain difficulties associated with the data collection, deconvolution techniques by means of the Fourier Transform is far more rewarding in that it allows us to actually correct the data via the inverse transformation. The mathematics of

this approach has been documented by Houston and his co-workers.[3,4,5] In his approach it is recognized that the Auger spectra is distorted by both the dynamic and the static properties of the analyzer. Houston's approach is to use a double integration technique to enhance sensitivities, but this approach suffers from the limitation that it only applies to well separated peaks where the Auger signals from constituent elements of the sample do not overlap.

Mularie and Peria[6] on the other hand, have assumed that the elastically reflected beam is a representation of BOTH distortion functions and has the advantage of separating out plasmon loss peaks as well. Spectra comparable to ESCA were obtained in this way.

In the present case, signal averaged data (multiple passes over the same energy interval) were directly collected by the computer system and the results were deconvoluted with the modulation distortion function derived by Houston and Park. Fourier methods were then used to filter out the noise and the resulting spectrum could be integrated directly to produce $N(E)$. This is shown in Figures 3 and 4. By assuming a static distortion function in the form of a Gaussian, it is now possible to sharpen the spectra to enhance the resolution of the $N(E)$ curves. Subsequent integration or peak intensities may then be employed for quantitation procedures, which are independent of recording conditions.

REFERENCES

(1) L. A. Harris, J. Appl. Phys. 39, 1419 (1968).

(2) N. J. Taylor, Rev. Sci. Instr. 40, 792 (1969).

(3) J. E. Houston and R. L. Park, Rev. Sci. Instr. 43, 1437 (1972).

(4) J. E. Houston, Surface Science, 38, 283 (1973).

(5) J. T. Grant, T. W. Haas and J. E. Houston, Surface Science 42, 1 (1974).

(6) W. M. Mularie and W. T. Peria, Surface Science 26, 125 (1971).

Figure 1. Graphical representation of various levels of summation of the Taylor series expansion. The modulation amplitude is twice the standard deviation of the assumed gaussian form for N(E). (a) First derivative only; (b) sum of first and third derivatives; (c) sum of first, third and fifth derivatives; and (d) sum of first through eleventh derivatives. Considerable broadening and a shift may be noted by comparing (a) and (d).
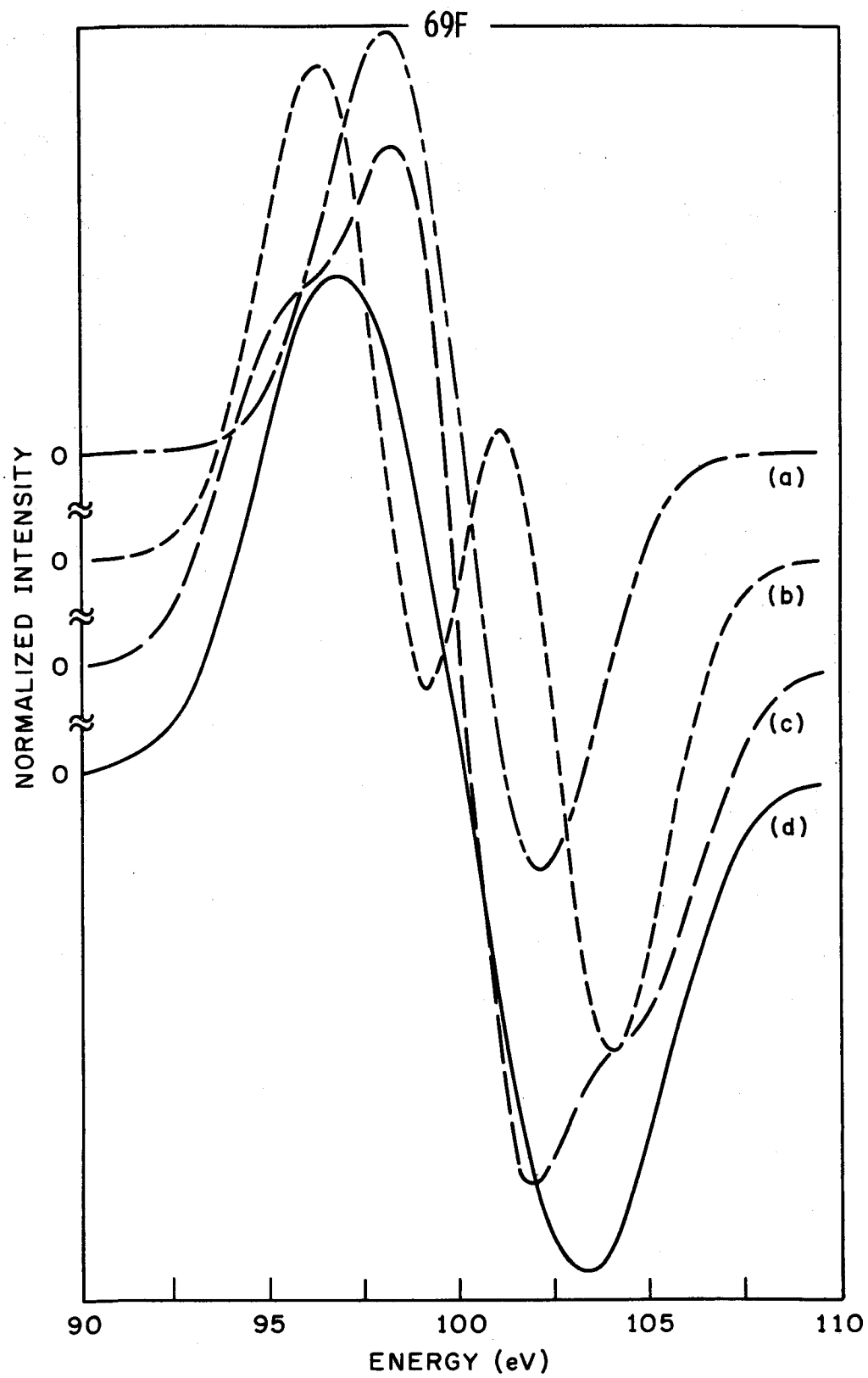
Figure 1
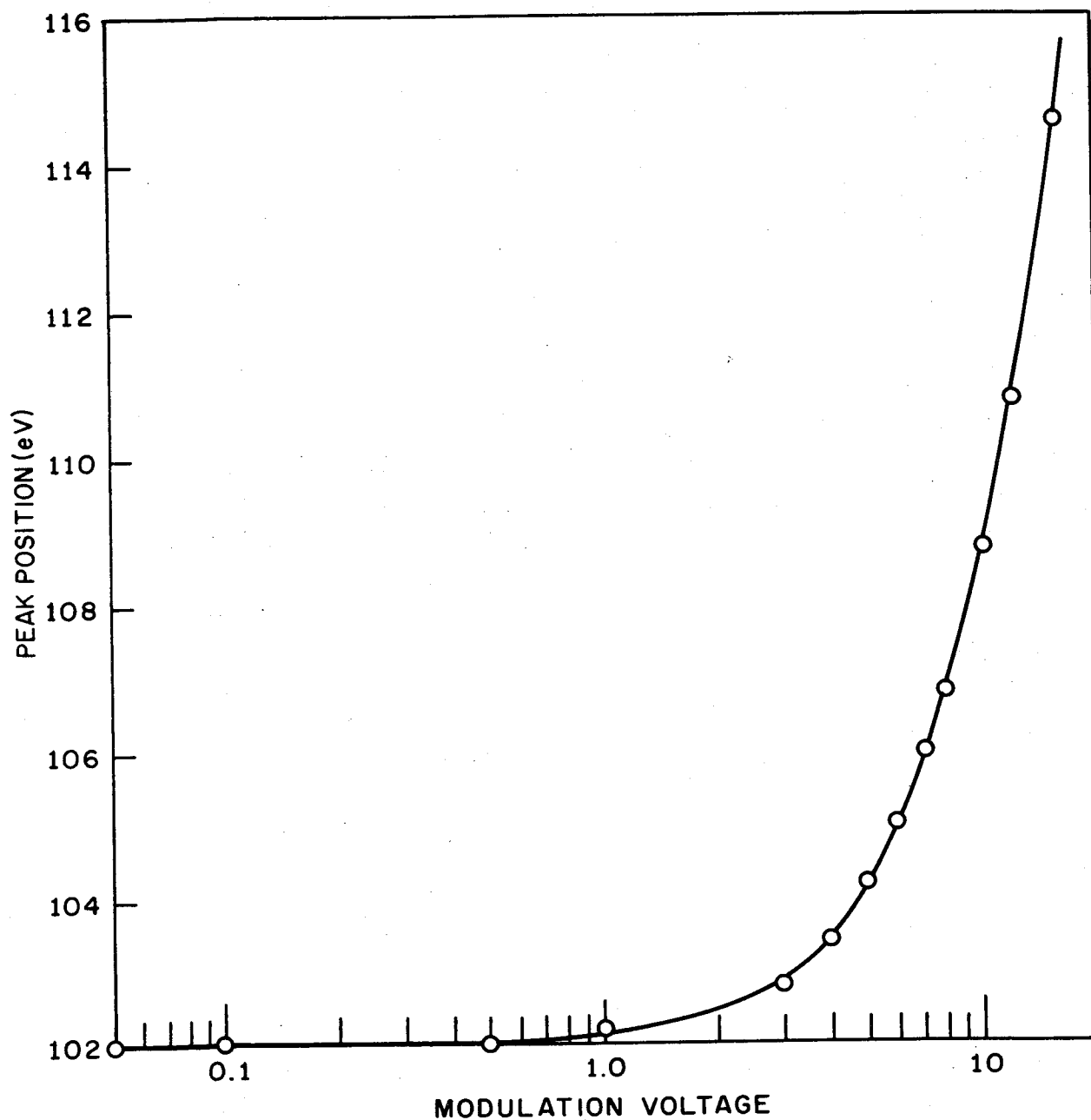
Figure 2. Variation in position of negative extrema with modulation voltage, for the same assumed gaussian as in Figure 1.
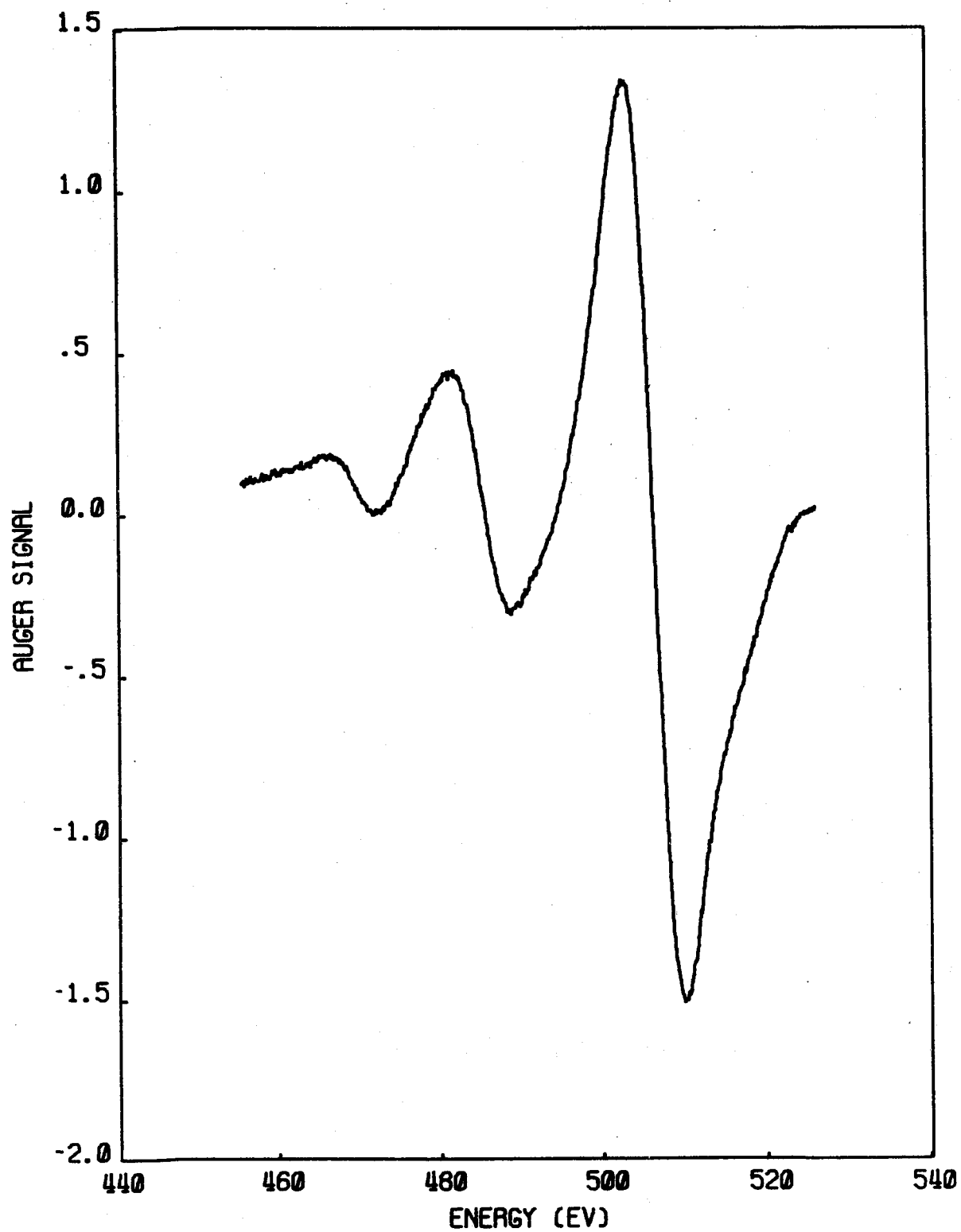
Figure 3. Raw oxygen KLL derivative spectrum collected
by CMA.
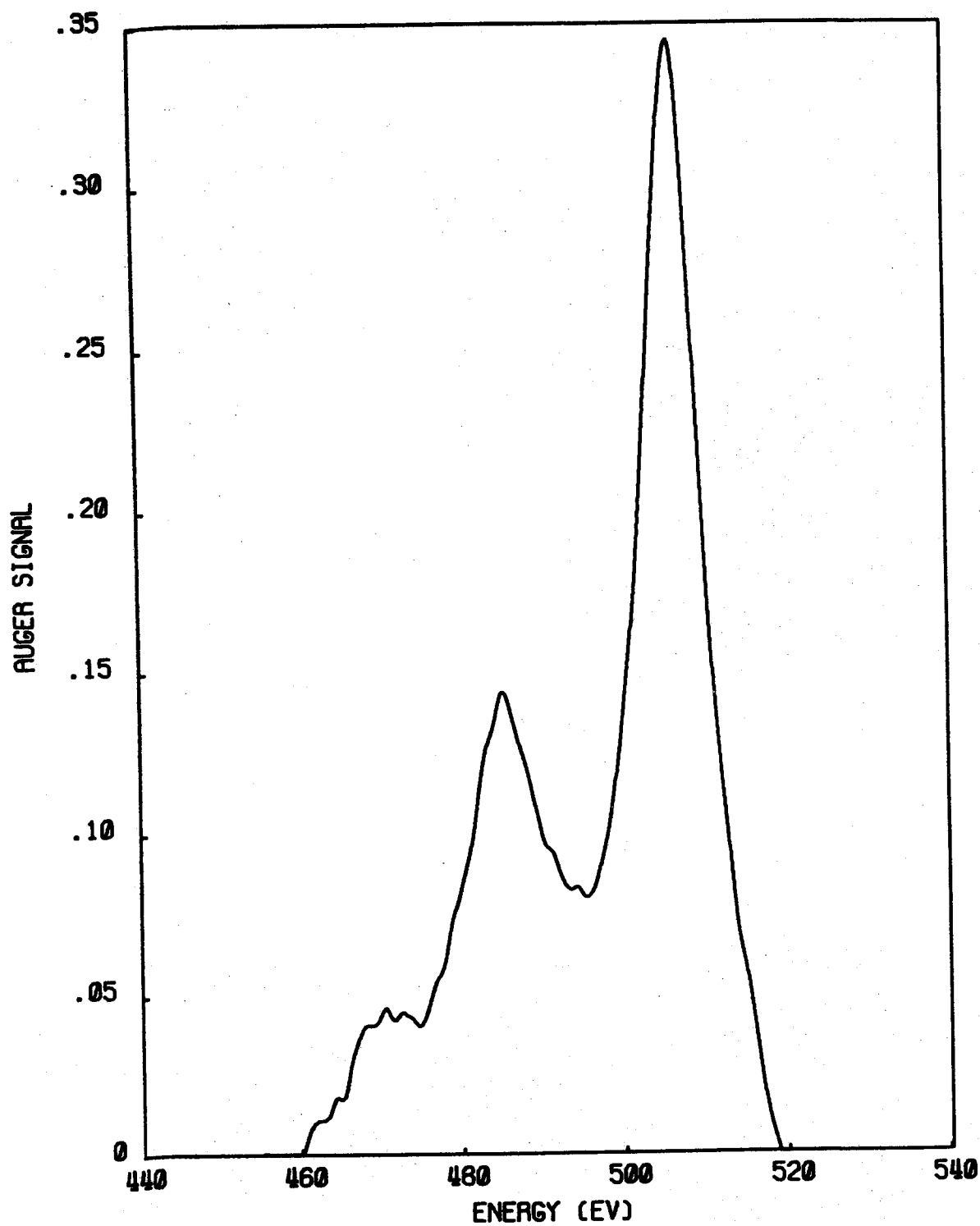
Figure 4. Result of deconvolution and integration of data shown in Figure 3.

Combined X-ray Photoelectron (XPS) and Auger Electron (AES) Spectroscopic Studies.

Principles and Applications

by

A. Barrie, F.J. Street and P. Swift

AEI Scientific Apparatus Ltd., Manchester, England

and

W. A. Wolstenholme

AEI Scientific Apparatus Inc., Elmsford, New York

A flexible ESCA spectrometer has been used for study of a wide variety of materials, each representing an analytical problem where information concerning elements present at or near a surface is of great importance. When used in conjunction with an ion etching gun, elemental depth profiles and "Chemical" depth profiles have been recorded for materials such as oil additives, glasses, and semiconductors. The dependence of surface sensitivity with electron "take-off" angle has also been investigated in relation to the CO/Mo chemisorption system. More recently, the use of electron beam excitation of Auger spectra has been used in conjunction with X-ray Excitation.

The principles relating to photo-ionization and Auger electron emission processes are discussed with emphasis on parameters which govern the quality of the spectra. (E.g. the dependence of the ionization cross-section upon the incident photon or electron energy). This is illustrated by using spectra obtained from a spectrometer in which the same electron energy analyzer is used to record both the X-ray and electron excited spectra.

A comparison of chemical shifts observed in XPS and AES is made with particular reference to metal-metal oxide systems (e.g. Al/Al_2O_3, see Figure 1, and Na/Na_2O).

The advantages of a high resolution energy analyzer which can be used for both XPS and AES are summarized and its application to both solid and gaseous samples is discussed.

Factors affecting the natural energy distribution of an Auger electron are discussed. For example, the contribution from the atomic energy levels involved in the radiationless transition. This is illustrated by reference to spectra where the peaks arise from transitions in which (a) valence or conduction band levels are involved, usually resulting in broad peaks (e.g. $C_{KLL} \sim 10eV$) and (b) only core levels are involved, which can produce quite narrow energy spreads (e.g. $Na_{KLL} \sim 0.8eV$). The initial vacancy of the Na_{KLL} transition is created in the 1s electron orbital, which, by XPS, using monochromatized $AlK\alpha$ radiation is observed to have a width of less than 0.8eV.

Auger electrons can display even narrower energy distribution if ejected from materials in the gaseous state, since line broadening as a consequence of solid state effects is eliminated. This is illustrated by reference to the Auger spectra obtained from neon, where the width of the Ne_{KLL} peak is approximately 0.6eV.

A further illustration of peak broadening as a result of solid state effects is given by comparing the Auger spectra obtained from carbon monoxide adsorbed on a metal (e.g. Mo) with that obtained from the molecule (CO) in the gaseous state. Carbon Auger spectra showing (a) the 4 broad, partially resolved C_{KLL} peaks of the adsorbed species and (b) a very narrow (0.2eV) C_{KLL} peak of the gaseous molecules (Figure 2) are discussed. Reference is made to the several bands showing resolved vibrational structure which can be clearly seen in the gas phase spectrum of carbon monoxide.

Advantages and disadvantages of X-ray and electron excitations of samples is discussed. For example, the comparison of the possible change in composition at the surface of solid materials or adsorption systems, as a consequence of electron bombardment, with the generally less damaging effects of X-ray excitation. This is contrasted with the electron and X-ray excitation of gaseous materials, where the gas flow continuously presents fresh sample for analysis, therefore overcoming specimen decomposition.

Al$_{2p}$

Oxide   Metal

Excitation Mg K$_\alpha$

2·5eV

1170   1175   1180   1185   1190

E$_{kin}$ (eV)
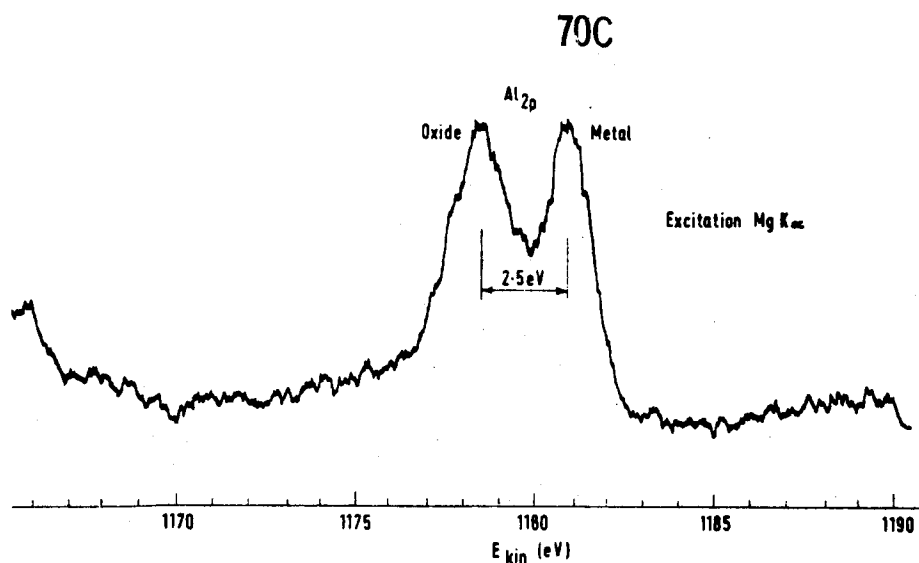
X-Ray photoelectron spectrum of oxidised aluminium

Al KL$_{2,3}$L$_{2,3}$(^{1}D)

Oxide   Metal

Excitation energy 5keV

7·0 eV

1380   1385   1390   1395   1400

E$_{kin}$ (eV)
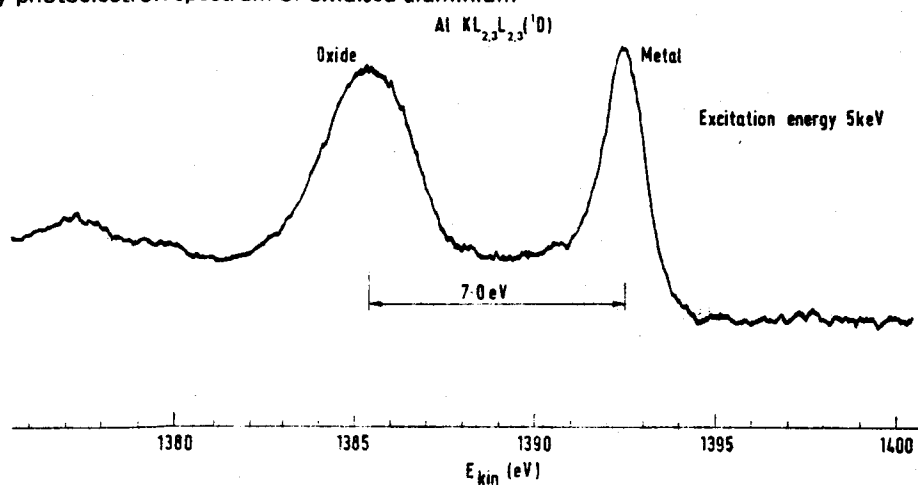
Electron excited Auger spectrum of oxidised aluminium

FIGURE 1.   Comparison of metal/oxide chemical shifts in X-ray excited
photoelectron and electron excited Auger spectra of aluminum.
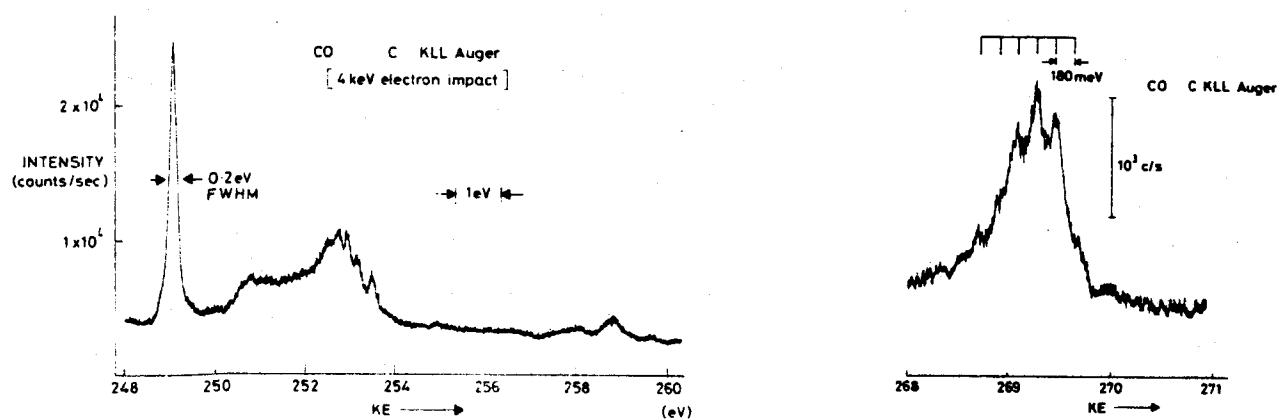
FIGURE 2. Gas Phase electron excited KLL Auger spectra of CO.

MONTE CARLO CALCULATIONS APPLIED TO ION PROBE MICROANALYZER

R. Shimizu

Department of Applied Physics, Faculty of Engineering
Osaka University, Suita, Osaka, Japan

Ion probe microanalysis has received increasing interest partly due to the continuing developement of ion implantation technology that requires exact knowledge of in-depth profiles of implanted ions in wafers, because the ion probe micro analyzer permits an in-depth analysis with high sensitivity for chemical analysis. Although the ion probe microanalyzer has already widely been used for the chemical and in-depth analysies, fundamentals of the analyses, e.g. ionization and knock on processes have not been well clarified.

However, so far as elementary scattering processes are concerned the physical principles of interaction of an incident ion with solid were set down in some detail by Lindhard et al (1) (LSS theory) more than ten years ago. Hence the question how accurately we can perform the in-depth analysis may be attainable to some extent with help of theory, especially by using Monte Carlo technique which is mainly based on (i) elastic scattering in atomic binary collision approxi mation governed by atomic potentials of Thomas -Fermi type or others and (ii) inelastic scattering due to electronic stopping described by LSS theory or Firsov's theory(2).

In view point of theory on the hand, the ion implantation provides an element tary subject for theoretical approaches to examine the validity before going to such a more complicated phenomen on as atomic mixing effect which is one of the most fundamental problem for a micro beam analysis based on ion bombardment technique.

Applying the LSS theory on assumption that the in-depth profile is represented by Gaussian distribution the projection range $\langle R_p \rangle$, the peak position, and the projected standard deviation $\langle \Delta R_p \rangle$ have usually been obtained by solving the first order differential equation(3) or higher order ones (4, 5) converted from the general integro-differential equation. However, the experimental investigations have recently pointed out that the in-depth profiles of boron in amorphous silicon (6) and silicon oxide (7) are considerably skewed for higher primary energies though those of Gaussian distribution are found in many cases. The conventional analytical approaches have not so well described these asymmetric distributions even by using the higher moments of range(8).

Another problem of practical importance for micro beam analysis is atomic mixing effect caused by ion bombardment. Secondary ion mass sepctrometry and Auger electron spectroscopy have been applied to the in-depth as well as surface face analyses with considerable success. In these techniques the ion sputtering has usually been applied to sputter away the outer atomic layers of the target layer

by layer during the ion bombardment.   These primary ions, however, cause successive nuclear collisions which results in atomic displacement cascade or knock on cascade, and this results in the changes of atomic composition in surface layers in the surface chemical analysis(9) and considerable deterioration in the in-depth analysis(10).

To describe this theoretically the conventional analytical approach seems to be less useful for this atomic displacement cascade phenomenon than the in -depth profile of the ion implantation just mentioned above.

Monte Carlo technique is probably the most basic approach to these questions in which individual incident ion trajectories are simulated in computer (as seen in Fig. 1-(a)) as a series of random scattering acts.   This permits the calculations of basic data; three dimensional spatial distribution (as a typical example in-depth profiles of boron in an amorphous silicon are shown in Fig. 2 with experimental results of Hofker et al(6) for the comparison), backscattering of incident ions, energy deposition, atomic displacement (Fig. 1-(b)) or atomic mixing effect on which Monte Carlo studies have recently been published (11, 12).

Application of Monte Carlocalculations to the fundamental phenomena of ion bombardment will be presented.

References

(1)   J. Lindhard, M. Scharff and H. E. Schiott; K. Danske Vidensk. Selsk. mat. -fys. Medd. 33, 1(1963).

(2)   O. B. Firsov; Sov. Phys. -JETP 36, 1076(1959).

(3)   W. S. Johnson and J. E. Gibbons; Projected Range Statistics in Semiconductors (Stanford University Bookstore, 1969).

(4)   D. K. Brice; Proc. 1st Intern. Conf. on Implantation in Semiconductors edited by F. H. Eisen and L. T. Chadderton (Gordon and Breach, New York, 1971) p. 101.

(5)   S. Myroie and J. F. Gibbons; Proc. 3rd Intern. Conf. On Ion Implantation in Semiconductors and Other Materials edited by B. L. Crowder (Plenum Press, New York, 1973) p. 23.

(6)   W. K. Hofker, D. P. Oosthoek, N. J. Koeman and H. A. M. De Grefte; Radiation Effects(in press).

(7)   K. Wittmaack, F. Schulz and B. Hietel; Proc. Intern. Conf. on Ion Implantation in Semiconductors and Other Materials (in press) p. 175.

(8)   K. B. Winterbon, P. Sigmund and J. B. Sanders; K. Danske Vidensk. Sesk. mat. -fys., Medd. 37, No. 14(1970).

(9)   P. Staib; Radiation Effects 18, 217(1973).

(10)   J. A. McHugh; Radiation Effects 21, 209(1974).

(11)   M. T. Robinson and I. M. Torrens; Phys. Rev. 9, 5008(1974).

(12)   T. Ishitani and R. Shimizu; Applied Physics 6, 241(1975).
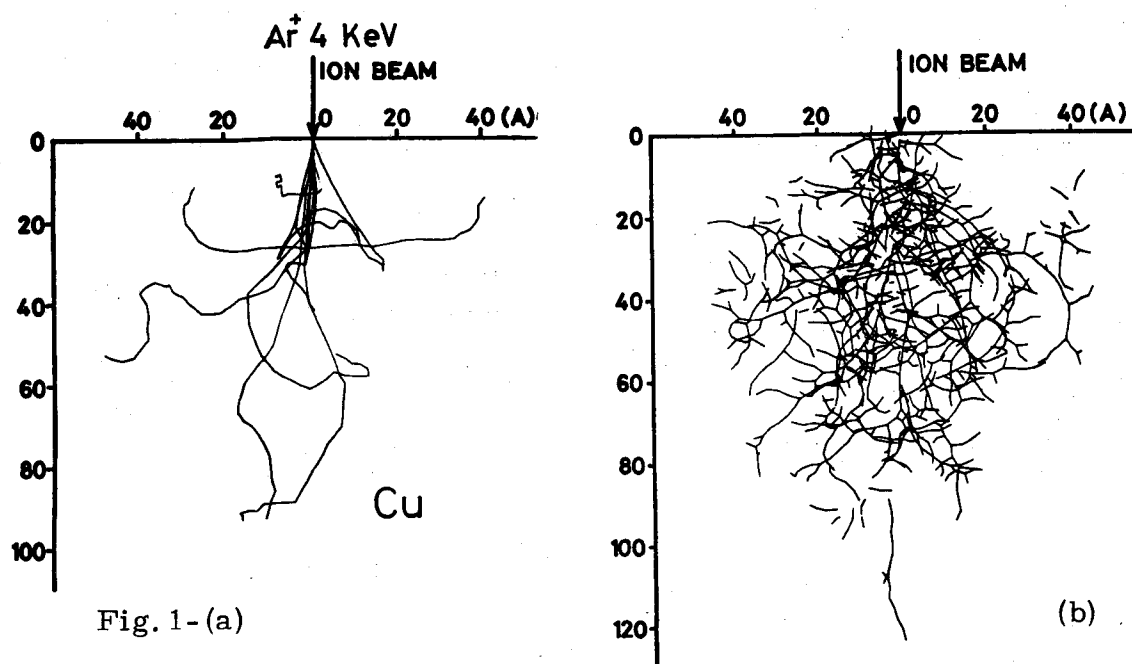
Fig. 1-(a)

(b)

Fig. 2
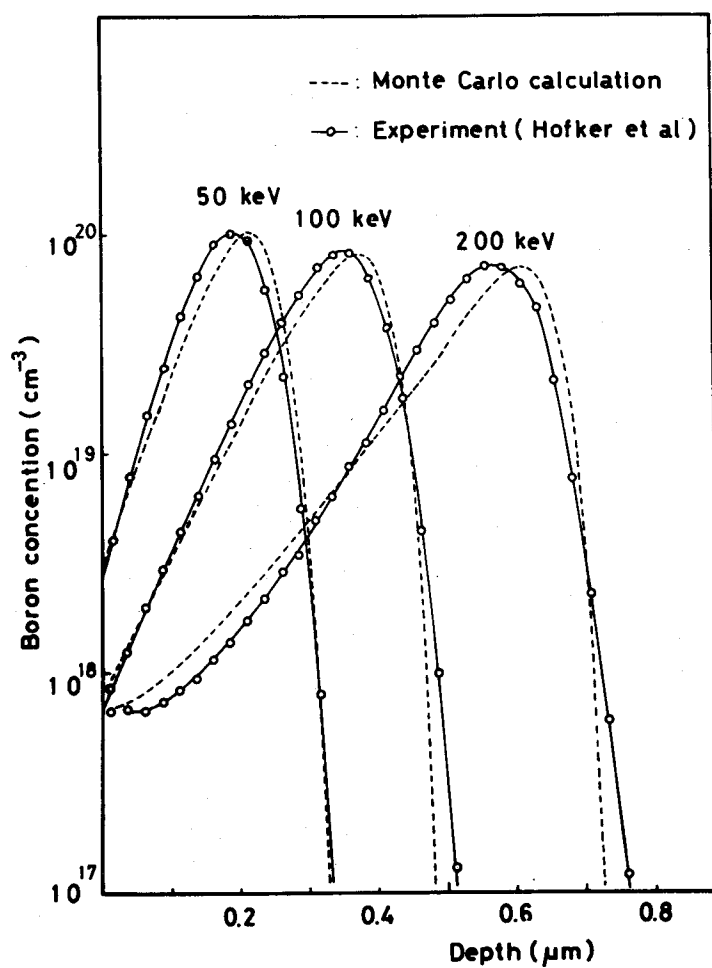
QUANTITATIVE IMPURITY ANALYSIS BY SECONDARY ION MASS SPECTROMETRY —
PRINCIPLES; MEASUREMENTS IN GaP.

M.-J. Lim, Western Electric Company, Engineering Research Center,
P. O. Box 900, Princeton, N. J. 08540

Examination of the equations for quantitative impurity analysis

in a matrix by the secondary ion mass spectrometry (SIMS) commonly used

in the literature[1-6] reveals that the secondary ion yield is not well

defined, and the quantitative analysis often leads to incorrect results.

New equations are derived from the hypothesis that the first derivative

of secondary ion yield with respect to the atomic fraction of the elements

in solid is constant in the infinitely dilute solution range.

From this model, the tatal secondary ion current of isotope $X_i^{\pm z}$

detected at the exit of the mass spectrometer, $I_s\{X_i^{\pm z}\}$, is shown to be

$$I_s\{X_i^{\pm z}\} = I_p Y_2^0\{X_i^{\pm z}\} x_i n_t,\qquad (1)$$

where the braces indicate a functional relationship, $X_i^{\pm z}$ is an atomic

or molecular specie containing an impurity element i with electron

charge +z or -z, x_i is the atom fraction of impurity i in solid, I_p is

the primary beam current, and n_t is the mass spectrometer transmission

coefficient. The constant Y_2^0 is the <u>solute standard state secondary ion</u>

<u>yield</u>, the superscript ^{0} designating the standard state. It is not

the secondary ion yield of the pure impurity itself, designated by Y_1^0,

or the yield for a completely covered surface for surface impurity

analysis, as commonly used in the literature. The subscript j of 1 and 2

in Y_j refers to the secondary ion from the solute and solvent component

of solid, respctively. It is shown that Y_2^0 is the secondary ion yield

of a hypothetical pure impurity state, and is similar in concept to the

Henry's law constant in solution theory.

If one makes the drastic assumption that the fraction of secondary ion of the total sputtered atoms remain constant at all impurity concentration, one obtains

$$I_s\{X_i^{\pm z}\} = I_p Y_1^0\{X_i^{\pm z}\}\frac{S_{1,m}^0}{S_{1,i}^0}x_i n_t \tag{2}$$

where $S_{1,m}^0$ and $S_{1,i}^0$ are sputtering yields of pure matrix and pure impurity element respectively. Equation (2) is still different from equations commonly used in literature, which does not have the sputtering yield ratio. From the assumptions used in deriving (2), one can show that

$$Y_2^0\{X_i^{\pm z}\} = \frac{S_{1,m}^0}{S_{1,i}^0}Y_1^0\{X_i^{\pm z}\}. \tag{3}$$

The validity of (3) is tested with measured Y_1^0, Y_2^0, and calculated S_1^0's by sputtering theory of Sigmund[7]. As shown in Table 1, (3) is not valid, thus (2) is not valid. The equations in literature even neglecting $S_{1,m}^0/S_{1,i}^0$ term in (2) thus cannot be valid.

Based on (1), various equations including conversion of secondary ion current to photon counts are derived for quantitative impurity analysis, and Y_2^0 of several impurities in GaP is calculated by comparison of SIMS data with spark source mass spectrometry (SSMS) data. The results are shown in Table 2 for a given primary beam density, Jp.

Experimental measurements by Cameca IMS 300 Secondary Ion Analyzer show that secondary ion yield of $^{31}P^+$ and $^{47}PO^+$ in GaP decreases as the primary beam density increases. See Figs. 1 and 2. Due to the different chemical nature of surfaces prepared differently, the surface data has

considerable scatter, indicating the importance of chemical mechanism[8] of secondary ion generation.

In spite of the variation of the secondary ion yield as primary beam density changes, even for the surface impurities, the secondary ion output of impurity as count rates normalized to the output of a specie from the matrix remain constant as shown in Table 3. The symbols N_j's are count rate corresponding to Y_j's. Thus different experimental results can be normalized for impurities to a matrix specie. However, one specie from a matrix cannot be normalized to the other specie from the same matrix due to the complex dependence of these two secondary ion yields.

It is concluded that in quantitative impurity analysis by SIMS, the secondary ion yield of the pure impurity plays no role, contrary to what has been used in the literature. More research should be directed to samples with infinitely dilute impurities, to obtain the solute standard state secondary ion yield.

REFERENCES

1 H. W. Werner and H.A.M. de Grefte, Vakuum-Tech., 17 (1967) 37.

2 H. W. Werner, E. L. Grove and A. J. Perkins (Eds.), Develop. Appl. Spectroscopy, Vol. 7A, Plenum, New York, 1969, p. 239.

3 A. Benninghoven, Surface Sci., 35 (1973) 427.

4 H. W. Werner and H.A.M. de Grefte, Surface Sci., 35 (1973) 458.

5 J. M. Morabito and R. K. Lewis, Anal. Chem., 45 (1973) 869.

6 J. M. Morabito and R. K. Lewis, in S. P. Wolsky and A. W. Czanderna (Eds.), A Method of Surface Analysis, Elsvier, Amsterdam, 1975.

7 P. Sigmund, Phys. Rev., 184 (1969) 383.

8 A. Slodzian and J.-F. Hennequin, C. r. hebd. Séanc. Acad. Sci. (Paris), 263 (1966) B1246.

Table 1. Test of Eq. (3) in GaP for O_2^+ Beam at 10 KeV, $J_p = 0.9$ A/m^2.

Element i	$Y_2^0\{X_i\}/Y_1^0\{X_i\}$	$S_{1,m}^0/S_{1,i}^0$
C	119	6.87
Al	68	1.69
Si	48	2.21

Table 2. Quantitative Impurity Analysis in GaP

Impurity	B	C	Al	Si	K	Ca
$Y_2^0\{X_i\}$ at J_p=9.6A/m^2	3.75×10^{-5}	3.73×10^{-4}	3.42×10^{-1}	1.15×10^{-2}	6.06×10^{-2}	5.40×10^{-3}

Table 3. $N_2^0\{X_i\}/N_1^0\{^{31}P^+\}$ at Two Different J_p Values in GaP Surface.

X_i	J_p=1.7(A/m^2)	J_p=9.6(A/m^2)
Li	9.10×10^{-3}	9.21×10^{-3}
B	9.42×10^{-4}	7.46×10^{-4}
C	2.77×10^{-3}	3.92×10^{-3}
F	5.23×10^{-3}	8.56×10^{-3}
Al	5.39	6.48
Si	1.06	1.01
$N_1^0\{^{31}P^+\}$	19113	72410

Fig. 2. Secondary Ion Yield of $^{47}PO^+$ of GaP.
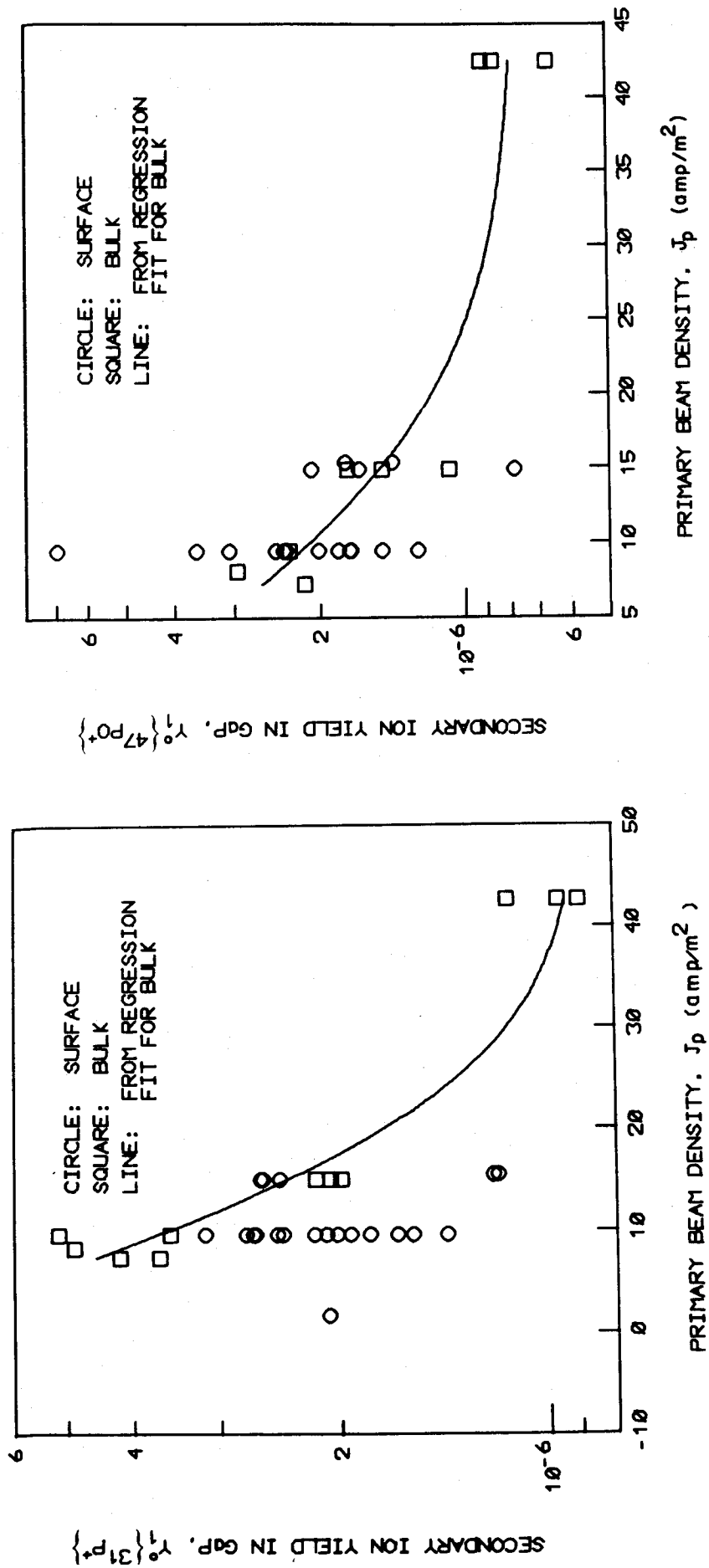
Fig. 1. Secondary Ion Yield of $^{31}P^+$ of GaP.

EFFECTS OF SAMPLE SURFACE ON ION MICROPROBE
ANALYSIS OF PtRhW ALLOYS[*]

by

E. A. Hakkila, J. M. Hansel, and W. B. Hutchinson
University of California
Los Alamos Scientific Laboratory
Los Alamos, NM 87544

The ion microprobe, a relatively new tool for analysis of micrometer areas of surfaces, does not provide the spatial resolution of the electron microprobe, but it can provide information on elemental distribution as a function of depth, often with better sensitivities than obtained with the electron microprobe. For these reasons, the ion microprobe was used in studying the distribution of various impurities, primarily boron, silicon, and phosphorus, in Pt-30 Rh-8 W alloys.

Study of the surface of the as-rolled alloy indicated the presence of significant amounts of sodium, magnesium, aluminum, potassium, and calcium as well as boron and silicon, even after severe ion cleaning of the sample surface. Also, apparent segregation of the platinum, rhodium, and tungsten was indicated.

The sample was reexamined after polishing with 0.3 μm Al_2O_3 and ultrasonic cleaning with 190 proof ethanol. Again, the sample was ion etched for 1 h with a 15 nA beam of 0^{+32}. The sample surface after ion cleaning is shown in the SEM, Fig. 1a. Aluminum ion intensity distribution (Fig. 1b) showed that the aluminum had been removed from the ion-etched area, but the surface around the etched area was severely contaminated, particularly in polishing scratches. Rhodium ion intensity distribution (Fig. 1c) indicated that rhodium was heterogeneously distributed in the ion-etched areas, but was not in the unetched areas.

Two areas of investigation were suggested by these studies: (1) Would a polishing agent other than Al_2O_3 result in lower surface

contamination? (2) Were the anomolous rhodium intensities real or artifacts of surface preparation?

Diamond, CeO_2, and CrO_2, all obtained from Buehler, were investigated as polishing agents for these alloys. In addition to aluminum, other serious contaminants found on the metal surface after polishing with these materials were sodium, magnesium, silicon, and calcium. These contaminants probably are extenders added to the materials. Numerous hydrocarbon peaks also were observed from the diamond as a result of the oil lubricant. The Al_2O_3 contaminated the surface less than the other polishing agents tried.

To study the possible segregation of platinum, rhodium, and tungsten in these alloys, the rhodium/platinum, rhodium/tungsten, and platinum/tungsten ion intensity ratios were measured from three areas of high rhodium intensity and from three areas of low rhodium intensity. Although ion intensity yields between the two types of areas varied by as much as a factor of two, significant variations in intensity ratios were not observed. The variations in ion yields probably resulted from measurements on different crystal faces, as observed by Castaing for binary CrNi alloys (1). Electron microprobe analyses also failed to show segregation of platinum, rhodium, and tungsten in these areas, with intensities of the rhodium and platinum x-rays being constant to within approximately 1%.

Microscopic and SEM examinations of the areas examined with the ion probe showed that the grains having high rhodium, platinum, and tungsten ion yields were etched deeper than those with low sputter yields.

Boron and silicon, generally occurring together, were detected in inclusions in the ion-cleaned areas. These elements could not be detected using the electron microprobe and aluminum could not be detected on the uncleaned surface, even with electron beam currents of 100 nA on the sample.

Several conclusions can be drawn from these studies. (1) Polishing agents seriously contaminate the sample surface and this contamination

cannot be removed effectively by ultrasonic cleaning. (2) Al_2O_3 polishing results in less surface contamination than diamond, CeO_2, or CrO_2. (3) Contaminated surfaces do not provide the same matrix ion intensities as do ion-cleaned surfaces. (4) Rate of ion etching is a function of crystal orientation. (5) Caution should be exercised in using evaporated films of known measured thickness to measure rates of ion etching in unknowns for obtaining depth profiles. (6) The ion probe can detect impurities in inclusions and on surfaces that cannot be observed with the electron microprobe.

---

(1) R. Castaing, "Secondary Ion Microanalysis - Crystalline and Temperature Effects," Proceedings Eighth National Conference on Electron Probe Analysis, New Orleans, La., 1973.
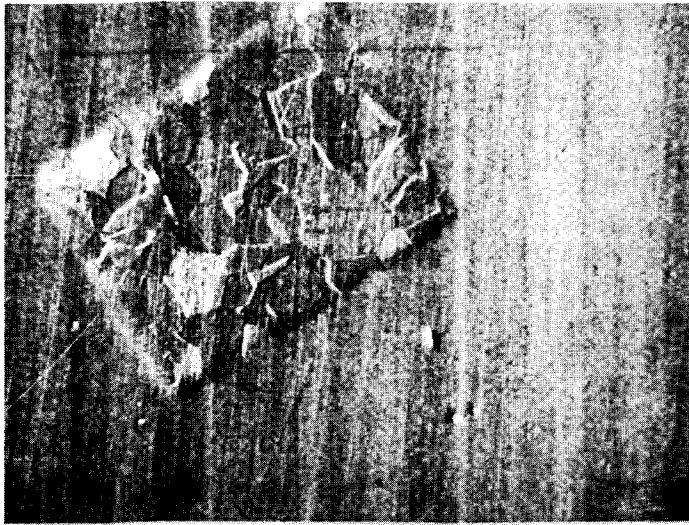
FIG. 1A. SEM OF PTRHW ALLOY SURFACE AFTER ION PROBE ANALYSIS (250X).
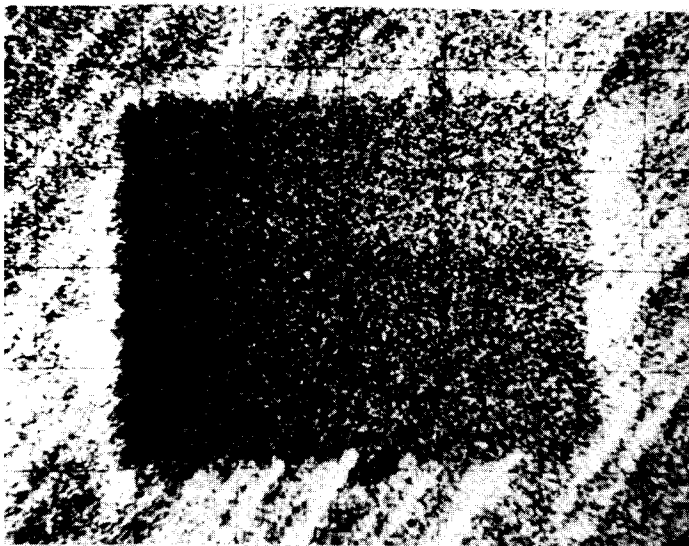
FIG. 1B. AL ION DISTRIBUTION (400X).

FIG. 1C. RH ION DISTRIBUTION (400X).

THE APPLICATION OF PEAK STRIPPING TO PROBLEMS
IN ION PROBE MICROANALYSIS

J. R. Hinthorne and R. L. Conrad
Hasler Research Center, Applied Research Laboratories
95 La Patera Lane, Goleta, California 93017

INTRODUCTION

The mass spectra usually obtained from sputtered secondary ion emission mass spectrometers are typically less cluttered with interferences from molecular ions or multiply-charged ions than other types of mass spectrometry. Even so, there sometimes are significant interferences of these types, as well as the direct isobaric interferences such as ^{54}Cr-^{54}Fe or ^{87}Rb-^{87}Sr, at some of the masses which need to be measured.

The relative frequency of elements needing correction is highly variable, but a practical analytical problem will illustrate a typical case. On the analysis of glass formed by the fusion of rocks, 25 elements can be routinely determined (see Table VI in [1]). Only three elements have significant interferences and all three can be easily corrected with peak stripping.

GENERAL APPROACHES

There are three general approaches to the solution of the interference problem in sputtered ion mass spectrometry. None of the three techniques alone (or, even all three together) will provide solutions to all possible interferences. Each can be used in certain cases and each has certain fundamental limitations.

(1) Control the components (except, of course, the sample) present in a given analytical situation. Examples include such techniques as a clean vacuum system, a cold plate near the sample to trap condensible vacuum system components, bombarding the sample with a primary beam containing none of the isotope to be analyzed, or bombarding with a reactive gas species to minimize the abundance of metal-metal molecular ions. It is apparent that control of the system components cannot greatly affect the multiply-charged or isobaric interferences.

(2) The use of higher mass resolution is a valid technique for the separation of some interferences. The main difficulty with this approach is that it is not applicable to low signal levels (microanalysis and trace analysis) because large fractions of the signal (90-99.9%) must be discarded to achieve the desired high resolution. Usually the lost intensity is not recoverable by extended integration time because of the limited amount of material available to microanalysis. Electronic background also does not decrease at higher mass resolutions so peak/background is generally degraded.

Another problem is that the ratios of secondary ion species are a function of instrument parameters, such as effective energy bandpass, and these ratios can change with resolution changes. The problems in practical instrument operation and data interpretation these changes can create are numerous. For example, in the glass sample mentioned above some trace elements must be measured at low resolution (where a signal is detectable) and compared with some major and minor elements measured at high resolution (to separate interferences).

(3) The use of peak stripping generally will be applicable to the correction for interferences except where the raw data is not statistically significant or where a second isotope is not available on which to base a correction.

PEAK STRIPPING METHOD

Peak stripping is accomplished by predicting the amount of an interference and subtracting it from the total intensity of the peak of interest. The predictions can be made from several kinds of information. We will consider here only the correction which can be made directly from the measured intensities in the spectrum of interest (without reference to standard samples).

Consider two mass peaks with an isotope of each of two components on each peak. Then the total intensities of each peak are:

$$^{A}\text{Total} = I_1 \cdot {}^{A}C_1 + I_2 \cdot {}^{A}C_2$$

$$\text{and} \quad {}^{B}\text{Total} = I_1 \cdot {}^{B}C_1 + I_2 \cdot {}^{B}C_2$$

where I = intensity of an isotope (assuming 100% abundance) and C = the actual isotopic abundance; the superscripts indicate mass number, and the subscripts are component or element designations. The unknowns in these equations are I_1 and I_2 and they can be solved as a system of two simultaneous linear equations in two unknowns.

Calculations of this type are commonly employed in isotope dilution mass spectrometry for highly accurate concentration determinations.

The use of peak stripping requires four conditions to be met:

(1) The components comprising the observed peaks can be identified.

(2) The components add linearly to produce each peak.

(3) The isotopic abundances are known.

(4) The system of simultaneous equations has a unique solution.

This last condition requires that there be at least as many measured peaks as unknown components and that no two components are monoisotopic at the same mass.

A convenient method for solving the simultaneous equations is by matrix algebra. The solution to the simultaneous equations is given by:

$$[I] = [R]^{-1} \cdot [Y]$$

where I = vector of total intensities (i.e., each component, isotope corrected),
R = matrix of isotopic abundances,
and Y = vector of measured intensities.

It is apparent that when using this method of interference correction, only the minimum mass resolution necessary to adequately separate the integral masses is required. Thus, sensitivity is not sacrificed and instrument operating parameters can be identical for the measurement of major and trace elements.

APPLICATIONS

In studying the genesis of some copper ore deposits in Arizona it was desirable to determine the abundance of copper in the primary silicate and oxide minerals of the host rocks and in the alteration minerals (2). Electron probe studies showed that copper was below the detection limit ($\sim$.03 wt.%) of that instrument in all the primary minerals. Most of the silicates contain titanium (up to 5 wt.%) and the mass spectra contain peaks of the TiO molecule at masses 62-66. In addition many of the phases are hydrous so that the TiOH molecule is also present (m/e 63-67). These two molecular ion components plus copper (m/e 63 and 65) and zinc (m/e 64,66,67) were considered in the corrections. The five mass peaks 62-66 were accumulated simultaneously with a multichannel scaler using 10-15 minutes of integration. After solving the five simultaneous equations in four unknowns (with a matrix algebra computer stripping program written by J. Colby) the components intensities are printed and a statistical precision assigned to each. The determined copper concentrations on samples of biotite (mica) with 3-5% Ti range from 0±2.8 ppmw to 278±11.5 ppmw. Three repeat integrations on the same sample gave 40.3±7.8, 44.2±16 and 47.3±12 ppmw; the ratios ^{63}Cu/^{63}TiO/^{63}TiOH = 1.0/5.75/.08 for the components comprising mass 63. Thus it is possible to precisely separate the TiO, TiOH, Cu and Zn by peak stripping.

In a preliminary application of the ion microprobe to age determinations of old rock samples using the rubidium strontium system in calcium-rich feldspars it was found to be necessary to subtract CaAlO and CaSiO molecules from the Rb and Sr isotopes and to subtract ^{87}Rb from ^{87}Sr. In this system ^{87}Sr is a monoisotopic independent variable because it is a decay product of ^{87}Rb. A system of five equations in five unknowns is used to solve for the Rb, Sr, ^{87}Sr, CaAlO and CaSiO components. The intensities of masses 83-87 are used as the raw data. The results on a well documented sample for the ^{87}Sr/^{86}Sr ratio is 0.70305 which differs by .065% from the average for this ratio obtained in two independent laboratories (0.7035) using conventional filament mass spectrometry.

In a similar study on potassium-rich feldspars, where the molecular components are KAlO and KSiO, a Rb-Sr isochron was determined with an age of 2505 million years, which compares favorably with ages of 2550 and 2590 m.y. obtained by conventional techniques (3).

It is important to note that a mass resolution of 300,000 would have been required in order to separate ^{87}Rb from ^{87}Sr--an impossible condition to achieve with any present secondary ion mass spectrometer.

The ion microprobe has recently been used to determine the relative abundance of the light rare earth elements (REE) in lunar minerals. In phases such as phosphates, zircon, and ZrO_2 the REE isotopes are abundant enough to measure directly without correcting for interferences, but in the calcium-feldspars the REE are 0.1 to 5 ppm and significant interferences (such as BaO) must be corrected for. Some of the elements (e.g., Eu) have more than 50% interference on all isotopes, but peak stripping allows the appropriate corrections to be made. By measuring the isotope intensities from mass 139 to 154, and stripping the identified interferences the REE's La-Gd have been determined and the results compare favorably with conventional isotope dilution analysis of the same sample (4).

It should be pointed out that long integration times (up to 2 hours) at maximum sensitivity (low mass resolution) are sometimes necessary to accumulate a significant number of counts for these REE determinations. If high resolution were employed to separate the interferences, at least 20 hours of integration would be required for each point analyzed.

CONCLUSION

Peak stripping is the logical solution to most interference problems in ion probe microanalysis because good detection limits are maintained and analysis time is not extended significantly.

REFERENCES

1. Andersen, C.A. and Hinthorne, J.R.(1973), Anal. Chem, 45, 1421.

2. Study suggested by Dr. Norman Banks, U.S. Geological Survey.

3. Tilton, G.R. and Steiger, R.H. (1969) J. Geophys. Res., 74, 2118.

4. Haskins et al (1974) Lunar Science V, The Lunar Science Institute, 313-315.

Ion Microprobe Analysis for Niobium Hydride
in Hydrogen-Embrittled Niobium

Peter Williams and Charles A. Evans, Jr.

Materials Research Laboratory

and

Martin L. Grossbeck and Howard K. Birnbaum

Department of Metallurgy and Mining Engineering

and Materials Research Laboratory

University of Illinois, Urbana, Illinois   61801

INTRODUCTION

The problem of hydrogen embrittlement in niobium has come under
intensive study in recent years. Niobium is a refractory metal with
nuclear properties which make it well suited for use as a first wall
material in proposed fusion reactors. In such an environment, the
metal must withstand exposure to isotopes of hydrogen in addition to
intense radiation. It has been known for many years that the solution
of hydrogen in niobium can lead to catastrophic embrittlement[1] even
in concentrations as low as 0.1 at.%.[2] The mechanism of the process
has long been the subject of speculation. Although niobium can form
a hydride, NbH, which is itself brittle, embrittlement can occur at
hydrogen concentrations too low for hydride to be formed. Two of the
most plausible mechanisms depend upon the extremely rapid diffusion
rate of hydrogen in solution in niobium. It can be shown thermodynam-
ically that hydrogen will diffuse toward a region of tensile stress.[3]
In one proposed mechanism it is postulated that the increased concen-
tration of hydrogen in solution in the high stress region reduces the
lattice cohesion.[4,5] In the other mechanism precipitation of niobium
hydride is presumed to occur due to the reduction in the free energy
of transformation by the stress field.[6,7] Fracture then occurs in the
brittle hydride. In either case, once a crack has begun, the region of
high stress moves with the crack tip and the process of diffusion and
fracture reoccurs, propagating the crack through the metal.

Extensive metallographic and scanning electron microscope (SEM) studies at the University of Illinois[8] have produced strong evidence for the second mechanism. Chemical evidence of niobium hydride in the fracture region of an embrittled sample would provide final confirmation of the mechanism, since an increased solution concentration would rehomogenize when fracture relieved the stress. SEM evidence indicated hydride-like layers in fractured samples with dimensions of the order of microns. The ion microprobe is the only instrument capable of hydrogen analysis on the micron scale.

ANALYSIS

The AEI-IM20 ion microprobe[9,10] at the University of Illinois was used to study a niobium − 2 at.% hydrogen sample fractured at 4°C in the SEM. Hydride precipitated at low temperature in such a sample is stable at room temperature due to a pronounced hysteresis associated with the phase transformation. Several comparison samples of solid solution and bulk niobium hydride were also studied. Figures 1 and 2 show the results of the studies on two sites of the fractured, embrittled sample. The area imaged was a small secondary crack in a sample that had previously been fractured in the SEM. SEM images of the sample taken _after_ the ion images show the details of the crack and also the ion-etched crater produced during imaging. Most of the images, of which Figure 1 is typical, were taken using the NbH^+ and Nb^+ ions and show clearly an enhanced NbH^+ signal from the region of the crack. The lateral resolution is limited by the primary beam spot size which, here, was about 5 x 10 μm. The primary ions were O_2^+.

Figure 2 shows images taken with NbO^+ and H^+ ions in addition to Nb^+ and NbH^+. No enrichment in oxygen is seen (one would expect oxide formation to enhance the Nb^+ signal even when using an oxygen primary beam). The H^+ image confirms the hydrogen enrichment in the crack region.

Figure 3 shows the result of line scans taken across the crack of Figure 1 between the points marked by the arrows. The ratio NbH^+/Nb^+ is plotted as a function of distance across the frame. The maximum

value of the ratio (NbH^+/Nb^+) on crack ÷ (NbH^+/Nb^+) off crack is 10:1. This
ratio will be referred to hereafter as the "chemical contrast" between
the hydrogen-rich and hydrogen-poor regions.

While the presence of a residual enhanced hydrogen concentration is
alone sufficient to eliminate the concentrated solution mechanism—the
solution should rehomogenize in the absence of stress—it remains to be
demonstrated that the NbH^+/Nb^+ ratios observed are typical of hydride.
In particular, the high NbH^+/Nb^+ ratio away from the crack is anomalous.
One would expect, on the basis of hydrogen concentration alone, a "chemical
contrast" of the order of 25:1.

No a priori relationship between molecular ion intensities and
surface composition exists. It was therefore necessary to examine
standard samples to establish empirical relationships. It was found
that homogeneous samples of bulk niobium hydride were difficult to make,
confirming the experience of other investigators.[11/] The samples examined,
while showing a higher NbH^+/Nb^+ ratio than Nb - 2 at.% H by a factor
of about 3, nevertheless gave NbH^+/Nb^+ ratios about a factor of three
lower than the crack region. Possibly nucleation of the hydride occurred
deep within the bulk of such samples leaving the surface, which the ion
probe samples, somewhat depleted. Only in samples in which visible
precipitates of hydride coexisted with solid solution at the surface
was the chemical contrast comparable with that of the fractured sample.
Figure 4 shows crude depth profiles on hydride and non-hydride regions
of such a sample. The hydride apparently precipitated in layers inter-
leaved with solid solution. Such layers have also been observed in the
transmission electron microscope (TEM). The spacing of the layers— 3-4 μm —
agrees quite well with TEM observations. The maximum chemical contrast
in Figure 4 is again 10:1, although in this case the solution concentration
was 5.5 at.%.

To eliminate the possibility that hydrogen from background gas species
was contaminating the surface, samples of Nb - 2 at.% D and NbD were
examined. The NbH^+ signal observed from these samples could have contri-
buted no more than about 10% to the NbH^+ signal from the hydrogen
containing samples.

The proposed explanation of the anomalously high NbH^+/Nb^+ ratios from dilute solutions again involves the rapid diffusion of hydrogen in solution in niobium. It has been shown that the heat of adsorption of hydrogen on niobium is greater than the heat of solution, so that monolayer coverage has to be achieved before bulk solution begins.[12/] Sputtering is a process which continuously generates clean surface. It seems likely then that regeneration of a monolayer of hydrogen by diffusion out of the bulk solution is energetically favored.

To test this hypothesis a sample of Nb - 1 at.% D was cooled in the ion probe to about -100°C to reduce the diffusion rate of deuterium. The NbD^+/Nb^+ ratio from bulk NbD was typically about 0.032 while the Nb - 2 at.% D solution gave 0.018 at room temperature, a chemical contrast of less than 2. On cooling, the solid solution produced star-shaped precipitates of NbD, visible both in the optical microscope and in NbD^+ images in the ion probe. The NbD^+/Nb^+ ratio on such a precipitate at -100°C was still 0.031%, but now, away from the precipitate, the ratio was 2×10^{-4} although the phase diagram of the system shows that the equilibrium concentration of the solution at this temperature was still about 0.13 %. This experiment supports the hypothesis of a diffusion-replenished surface layer.

CONCLUSION

Ion microprobe studies of fractured, hydrogen-embrittled niobium have demonstrated enhanced hydrogen concentrations in the immediate vicinity of the fracture. The NbH^+/Nb^+ ion ratios on, and away from, the crack have been shown to be typical of precipitated niobium hydride and solid solution, respectively. The anomalously high NbH^+/Nb^+ ratios from dilute solid solutions appear to be due to surface monolayer replenishment during sputtering via diffusion of hydrogen from the bulk.

ACKNOWLEDGEMENT

REFERENCES

1. D. P. Smith, Hydrogen in Metals (Univ. of Chicago, Chicago, 1948).

2. S. Gahr and H. K. Birnbaum (to be published).

3. J. C. M. Li, R. A. Oriani, and L. S. Dorben, Z. Phys. Chem. New Folge 49, 271 (1966).

4. A. R. Troiano, Trans ASM 52, 54 (1960).

5. R. A. Oriani and P. H. Josephic, Scripta Met. 6, 681 (1972).

6. D. G. Westlake, Trans AIME 245, 1969 (1969).

7. T. W. Wood and R. D. Daniels, Trans. AIME 233, 898 (1965).

8. M. L. Grossbeck, Ph.D. thesis, 1975.

9. D. K. Bakale, B. N. Colby and C. A. Evans, Jr., Analytical Chemistry (to be published).

10. A. E. Banner and B. P. Stimpson, Vacuum (in press).

11. G. C. Libowitz, The Chemistry of Fusion Technology, edited by D. M. Gruen (Plenum, New York, 1972), p. 321.

12. D. I. Hagen and E. E. Donaldson, Surface Science 45, 61 (1974).

FIGURE CAPTIONS

Fig. 1   Ion and SEM images of fracture. Site 1.

Fig. 2   Ion and SEM images of fracture. Site 2

Fig. 3 NbH^+/Nb^+ ratio. Variation along line scan on site 1.

Fig. 4 NbH^+/Nb^+ ratio. Depth profile through NbH precipitate.

128 μm
SEM

MASS 93
Nb⁺

MASS 94
NbH⁺

Fig. 1

SEM   MASS 93
                 Nb⁺

MASS 94   MASS 1   MASS 109
NbH⁺   H⁺   NbO⁺

|← 128 μm →|
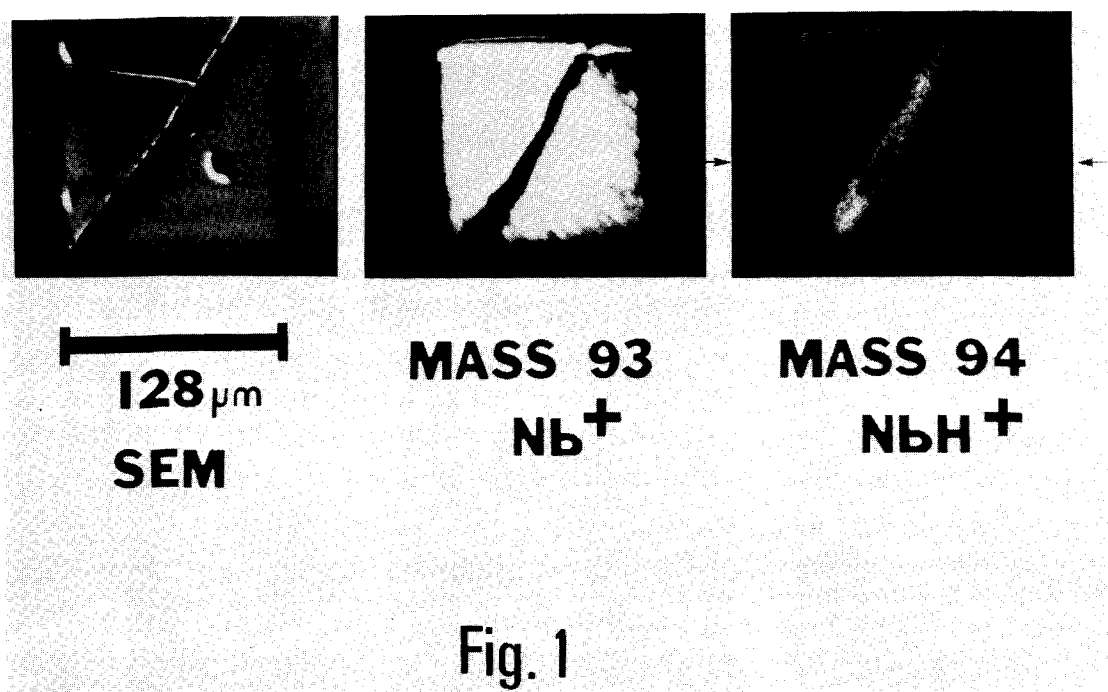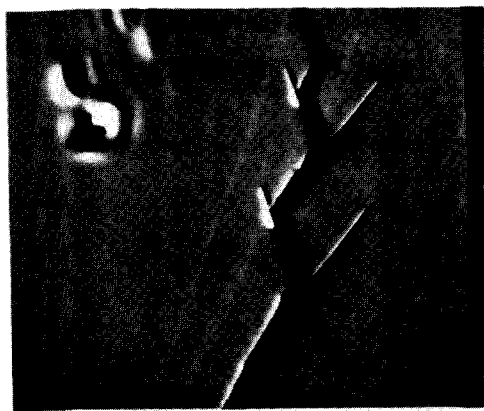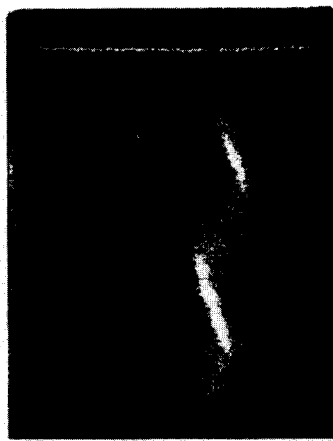
Fig. 2
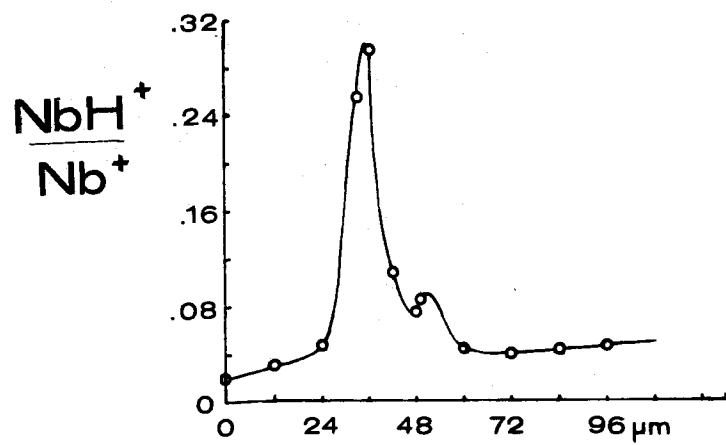
Fig. 3
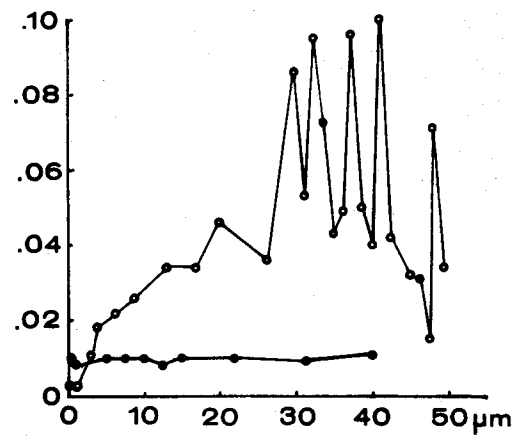
Fig. 4

A QUADRUPOLE INSTRUMENT FOR INVESTIGATIONS OF ELECTRON AND ION BEAM INTERACTIONS WITH SOLIDS

J.C. Potosky and D.B. Wittry

Department of Materials Science
and Electrical Engineering
University of Southern California
Los Angeles, California 90007

An instrument to study interactions of energetic charged particle beams with solids has been under construction. It will provide for the capability of bombarding solid surfaces with a focussed beam of ions or electrons with energy up to 20 keV and detecting subsequently emitted secondary particles.

Of primary interest is the determination of the chemical composition of the surface and immediate subsurface regions of a solid by Sputtered Ion Mass Spectroscopy (SIMS)[1]. Quantitative chemical analysis using this method is complicated by the limited basic understanding at present of the secondary ionization process and the role of residual gases in this process. The instrument described here was developed primarily to investigate these effects. An electron source was also incorporated to provide for the capability to investigate electron beam induced desorption[2] effects.

The instrument consists of interchangeable ion and electron sources, electrostatic lens column, specimen stage, quadrupole mass filter and associated electronics, and two independent vacuum systems. The ion source is a cold cathode duoplasmatron capable of producing ions with any source gas or ion polarity[3]. The electron source is a conventional triode electron gun. The primary beam column was adapted from a MIKROS electrostatic electron microscope and consists of three electrostatic lenses separately controlled from high voltage potentiometers. The lenses of this system were relocated for more suitable performance in a demagnifying optical system. The final lens working distance is approximately 3.5 cm. Electrostatic deflection plates for electronic beam positioning and scanning, hexapole electrostatic stigmator and electrostatic chopper plates comprise the remainder of the column. The lens column is provided with a separate vacuum system with the final lens serving as a differential pumping aperture isolating it from the specimen chamber.

The specimen stage positions the specimen so the beam incidence angle with respect to the specimen's surface is 30° in order to maximize the sputtered particle yield and the coupling of sputtered particles into the detection system. Three-axis motion of specimen and optical viewing have been provided for positioning the specimen under the beam. A specimen change airlock and leak valve for introducing gas are also included in the specimen chamber.

The specimen is surrounded by a LN_2 cooled cold dome which
is part of the electrostatic secondary particle optical system.
The lenses formed by these electrodes will accelerate secondary
particles and focus them into the quadrupole mass filter. The
chromatic aberration of this system provides energy discrimi-
nation of the secondary charged particles in order to enhance
the mass resolution of the quadrupole mass filter for sputtered
ions. The quadrupole mass filter is an Extranuclear Labora-
tories model 210. It is mounted in a gold coated glass tee to
reduce electrical noise and is preceeded by an electron bombard-
ment ionizer and three electrostatic lenses. The ionizer
may be activated to analyze the residual gas in the system or
to investigate sputtered neutral particles.

The particle detection system is a Daly[4] type detector consis-
ting of an aluminum converter electrode with subsequent detec-
tion of secondary electrons by a plastic scintillator and
photomultiplier tube. This detector system provides for count-
ing single particles in addition to analog detection with high
gain and decoupled output signal. The output signals are amp-
lified and can be displayed in various modes. The primary ion
beam can be positioned at a selected point on the specimen
surface and a mass spectra of the point obtained by sweeping
the mass control of the quadrupole. The beam can be elec-
tronically deflected and the quadrupole mass control main-
tained constant to yield a line profile or scanning ion micro-
graph of the specimen's chemical distribution. When the spec-
men is being bombarded by electrons, the secondary electrons
produced may be focussed by the secondary particle optics
through the inactive quadrupole filter and detected by the
Daly detector in order to form an image similar to a scanning
electron microscope. Also, with the quadrupole and ionizer
operating as a residual gas analyzer, electron beam induced
desorption can be investigated.

The two vacuum systems employ 2" oil diffusion pumps with LN_2
traps. The total system volume is approximately 4 liters. An
ULTEK partial pressure analyzer is connected in close proximity
to the specimen so that the residual gas in the system can
be monitored during sputtering investigations. The figure shown
is a schematic representation of the instrument. Its operation
and performance will be reported in future papers.

Acknowledgements

References

1. H. W. Werner, "Secondary Ion Mass Spectrometry and Its Application in Thin Film and Surface Layer Research", Invited paper -- Sixth International Vacuum Congress, Kyoto, Japan, March 1974.

2. D. Lichtman and McQuistan, Progress in Nuclear Physics, Series IX, 4, (Pergamon Press, London, 1965) pp. 95-136.

3. J. C. Potosky and D. B. Wittry, "Study of a Duoplasmatron Ion Source with a Quadrupole Mass Spectrometer", Proc. 8th Natl. Conf. on Electron Probe Analysis, New Orleans, 1973, pp. 2A-F.

4. N. R. Daly, Review of Scientific Instruments, Vol. 31, No. 3, March 1960, pp. 264-267.
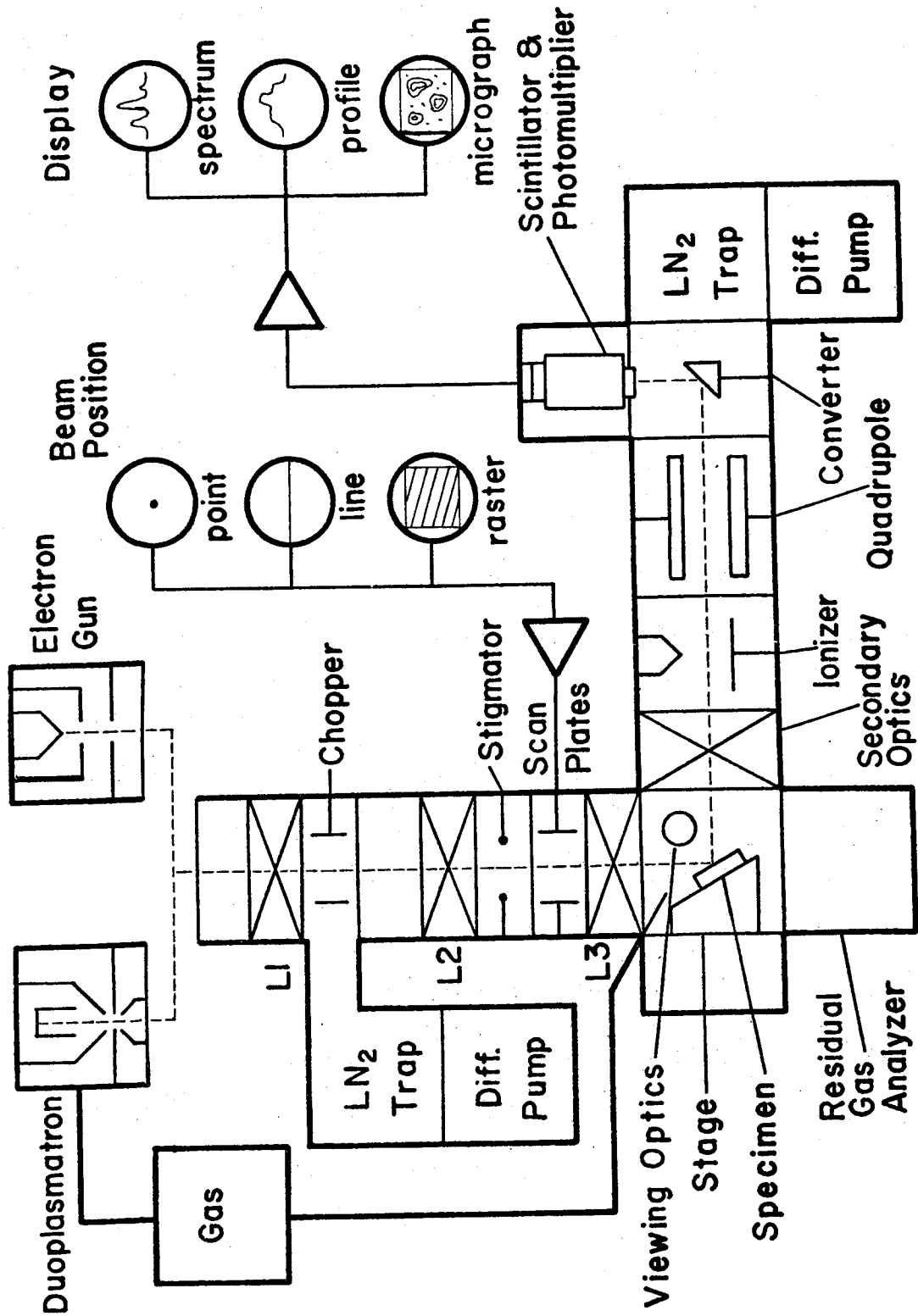
Schematic of Quadrupole Instrument

PERFORMANCE EVALUATION OF A CESIUM POSITIVE ION SOURCE FOR SECONDARY ION MASS SPECTROMETRY*

H. A. Storms, K. F. Brown and J. D. Stein

Vallecitos Nuclear Center
General Electric Company
Pleasanton, California

An experimental Cs^+ ion source is being evaluated for secondary ion mass spectrometry (SIMS) applications. This thermal ionization source was designed and fabricated by Hughes Research Laboratories and has been attached to an Applied Research Laboratories (ARL) Ion Microprobe. It consists of a heated reservoir containing cesium metal supplying vapor to the back of a hot porous tungsten ionizer. Accelerating electrodes extract a beam of positive cesium ions from the front of the ionizer. The brightness, maximum current density delivered to the sample and minimum beam diameter of the Cs^+ source is comparable to that achieved with O_2^+ from the duoplasmatron ion source originally supplied with the instrument.

Cesium has distinct advantages over oxygen, nitrogen and argon ion sources for certain SIMS applications. Implanted cesium provides an electron rich surface resulting in enhanced negative secondary ion emission for elements with modest electron affinities. Especially promising elements are the Groups V (except nitrogen), VI and VII elements, the noble metals, hydrogen and carbon. The negative ion emission of these elements is markedly enhanced relative to the ion emission obtained using the common primary ions. In addition, emission is enhanced for certain elements (e.g., Zn and Cd) by the formation of relatively stable molecular ions of the type MCs^+. The presence of oxygen appears to inhibit formation of the MCs^+ ion. Oxygen apparently also plays a role in the negative ion yield of some elements.

Qualitative data will be presented on a number of special samples.

SURFACE ASSOCIATIONS OF TOXIC ELEMENTS IN AIRBORNE PARTICULATES: AN ION MICROPROBE STUDY

Richard W. Linton and David F. S. Natusch
School of Chemical Sciences

and

Peter Williams and Charles A. Evans, Jr.
Materials Research Laboratory

University of Illinois
Urbana, Illinois 61801

Recent investigations of airborne particulate matter have indicated that a number of potentially toxic trace elements are more concentrated in the smallest particles in urban aerosols and in particulate emissions from high temperature combustion sources.[1,2,3] In general, such evidence has been accumulated by fractionation of particles on the basis of size and subsequent analysis with bulk techniques such as spark source mass spectrometry (SSMS) and atomic absorption spectroscopy.

The results are of considerable environmental import for several reasons. The specific concentrations ($\mu g/g$) of many trace elements are highest in particles which preferentially deposit in the pulmonary regions of the lung where the extraction of particulate components into the blood stream is most efficient. In addition, existing emission control devices are least efficient in collecting the smallest and apparently the most toxic particles. Thus estimates of toxic element emissions using samples taken from particle precipitators will be lower than the actual emissions. In the case of particles produced in the combustion of coal, this inverse dependence of trace element concentration on particle size suggests that an element (present either in elemental or compound form) is volatilized in the high temperature combustion zone and subsequently deposited or condensed on the particulate surfaces.[4] Such preferential concentration of trace elements on particle surfaces is of potential environmental significance because it is the particle surface which is in the most immediate contact with body fluids and tissues.

In summary, bulk analytical techniques have provided only indirect evidence for the adsorption of toxic elements on the surfaces of airborne particulates. To obtain direct substantiation for this hypothesis, analytical techniques with both surface and in-depth elemental analysis capabilities must be employed. In our research to date, some typical particulate fly ash emissions from coal-burning power plants have been analyzed by MeV ion backscattering, ESCA, and scanning Auger microscopy. Results of

the backscattering experiments employing 2 MeV ^{4}He$^+$ bombardment of the fly ash particulates were inconclusive. The backscattering technique suffers from poor sensitivity at low masses and poor spectral resolution for high mass elements. In addition, surface roughness effects introduced by the non-planar geometry of the particles hinder the analysis. The microbeam capability of the scanning Auger microprobe offers the advantage of single particle analysis. However, it suffers due to the lack of sensitivity to trace constituents, spectral interferences arising from the chemical complexity of the particulate samples, and charging effects resulting from the insulating nature of the particles. In addition to the matrix constituents (Fe, Al, and Si), K, Na, C, S, and Ca were detected. The latter group of elements showed an initial Auger signal significantly more intense than that observed after removing approximately 10-20 Å from the particle surface by argon ion sputtering. The ESCA technique does not suffer from sample charging problems, but it lacks the microbeam capabilities necessary for single particle analysis. In addition, ESCA detection limits are generally no better than those of Auger electron spectrometry. The elements Al, Fe, Si, Na, C, S, and Ca were detected in the ESCA surface spectra.

Since elemental detection limits for the above techniques appear to be the major limitations in substantiating the surface deposition hypothesis, the use of secondary ion mass spectrometry (SIMS) is indicated. In this technique, a beam of 10-35 keV ions impact on the sample surface causing sputtering of the outer atomic layers. A small fraction of the ejected species are ionized and can be analyzed mass spectrometrically. In-depth profiles are obtained by monitoring one or more specific ion species as the sputtering process removes successive atomic layers. For this investigation, an ion microprobe (AEI Scientific Apparatus, Ltd. IM-20) was employed to examine in-depth elemental distributions of fly ash particles. Particles of greater than 75 µm diameter were pressed into indium foil and mounted in the ion microprobe specimen chamber. If the surface deposition of trace elements takes place as postulated, then the surface concentration of any deposited element should be essentially independent of particle size. Consequently, the choice of large, easily handled particles for ion microprobe analysis is legitimate. A 35 keV negative oxygen ion primary beam was employed. An 80 nA beam of about 16 µm diameter was rastered over an area 100 µm by 100 µm. Sputtering rates were estimated to within about a factor of two by using rates measured on silicon samples at similar current densities. As a result of the relatively large rastered area and the lack of rapid peak-switching capabilities, only one element was depth profiled per particle in the electrical detection mode.

Typical experimental results obtained to date are shown in Figures 1 through 3. These depth profiles confirm the surface enhancement hypothesis suggested by the earlier bulk analytical studies. Figure 1 shows the concentration enhancement of the toxic trace elements Tl, Pb, and Cr near the particle surface. Other trace elements showing similar surface correlations include Be, Mn, V, and P. Although present at high levels in the bulk, the alkali metals (Li, Na, K) and Ca show considerable surface concentration enhancements agreeing well with the trends observed in the Auger data. Figure 2 shows that the levels of the matrix

elements Al and Si remain reasonably constant as a function of depth. Mg shows a similar trend. Figure 3 demonstrates the "monolayer" nature of the adsorbed organic species. $C_4H_7^+$ is easily resolved from $^{55}Mn^+$ ($M/\Delta M = 580$). The depth profile of $C_4H_7^+$ only shows a significant ion intensity over an estimated depth of 3 Å into the particle.

As pointed out above, only one element was profiled per particle using the electrical detection mode. Simultaneous multi-elemental depth profiling on the same particle may be carried out by use of photographic detection of the ions as dispersed by the double-focusing Mattuch-Herzog analyzer. A series of successive short exposures corroborated the trends observed using single element electrical detection. The intensities of the matrix element lines remained fairly constant (e.g. Si, Al), while trace elements and hydrocarbons which showed high surface concentration enhancements in the electrical mode appeared only in the first few exposures. Each successive exposure corresponded to an additional depth of approximately 100 Å. The major limitation in photographic detection is its relative insensitivity compared to electrical detection methods. Thus, some of the trace elements which showed surface concentration enhancements in the electrical detection mode produced an insufficient number of ions to be detected during the duration used for these photographic exposures. Longer exposures could not be employed because the depth consumed per exposure would increase and hence the depth resolution would decrease.

In conclusion, the surface analysis capabilities of the ion microprobe allow the acquisition of direct evidence supporting the enhancement of toxic trace element concentrations on the surface of airborne particles. Quantitating depth scales and elemental concentrations directly is even more difficult than in more conventional ion probe applications. This is a direct result of the irregularities, inhomogeneities, and complexity of particulate samples. However, most elements show a reasonably constant "bulk" level at a depth of only 1000-2000 Å. Consequently, bulk techniques such as SSMS may be used to quantitate the secondary ion intensity in the bulk. The ratio of the surface ion intensity to that observed for the bulk can then be used to give a semi-quantitative value for the concentration levels of toxic trace elements near the particle surface.

References

1. Natusch, D. F. S., Wallace, J. R., Science 186, 695(1974).
2. Davison, R. L., Natusch, D. F. S., Wallace, J. R., Evans, C. A., Environ. Sci. Technol. 8(13), 1107(1974).
3. Lee, R. E., Goranson, S. S., Enrione, R. E., Morgan, G. B., Environ. Sci. Technol. 6(12), 1025(1972).
4. Wallace, J. R., Ph.D. Thesis, University of Illinois, 1974.

78D

ESTIMATED DEPTH(Å)

$^{203}Tl^+$

$^{208}Pb^+$

RELATIVE INTENSITY

$^{52}Cr^+$

x3

x1

TIME (SEC.)
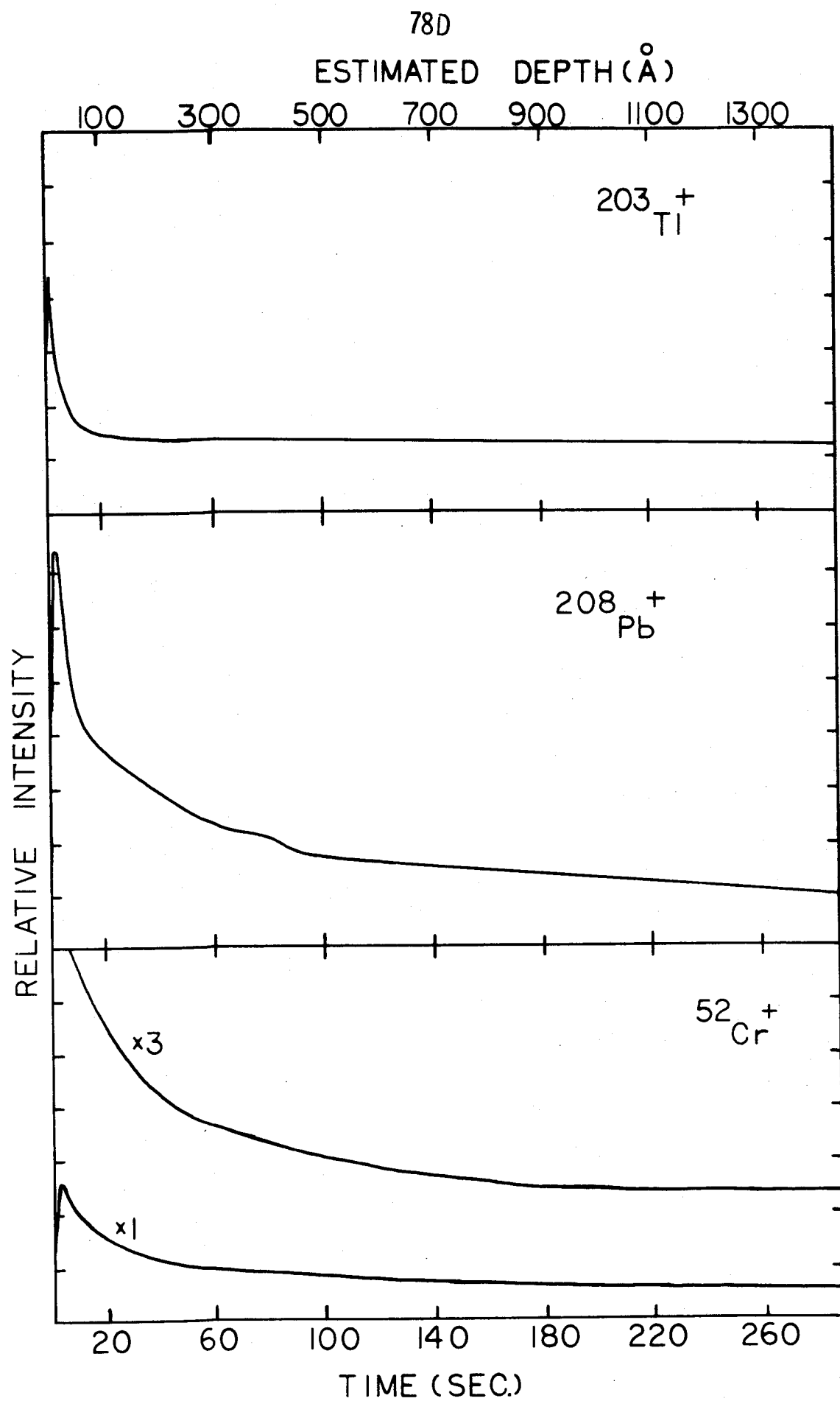
FIGURE 1: Pb, Tl, Cr DEPTH PROFILES

ESTIMATED DEPTH (Å)
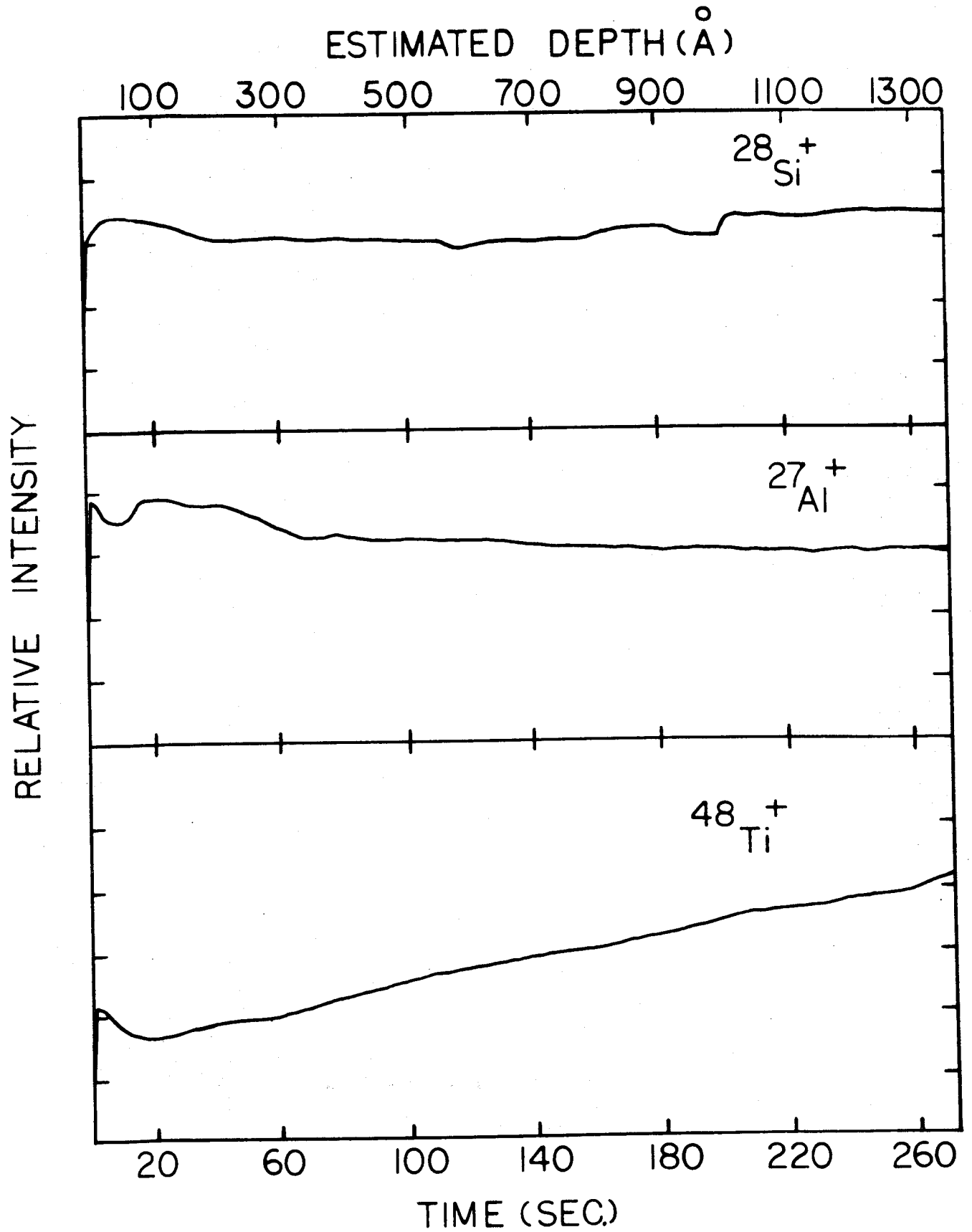
FIGURE 2: DEPTH PROFILES OF MATRIX ELEMENTS Al, Ti, Si
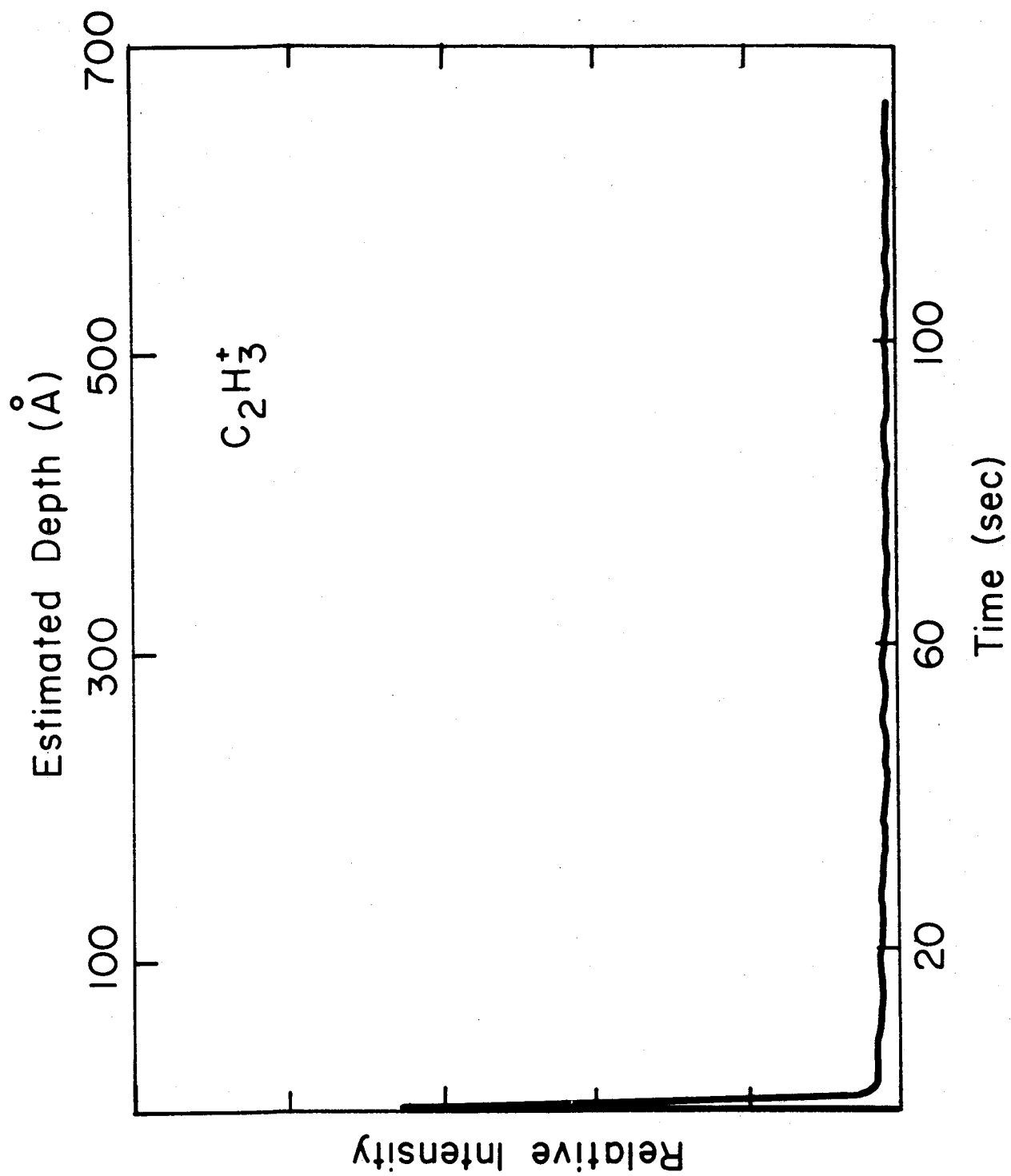
FIGURE 3a: DEPTH PROFILE OF $C_2H_3^+$
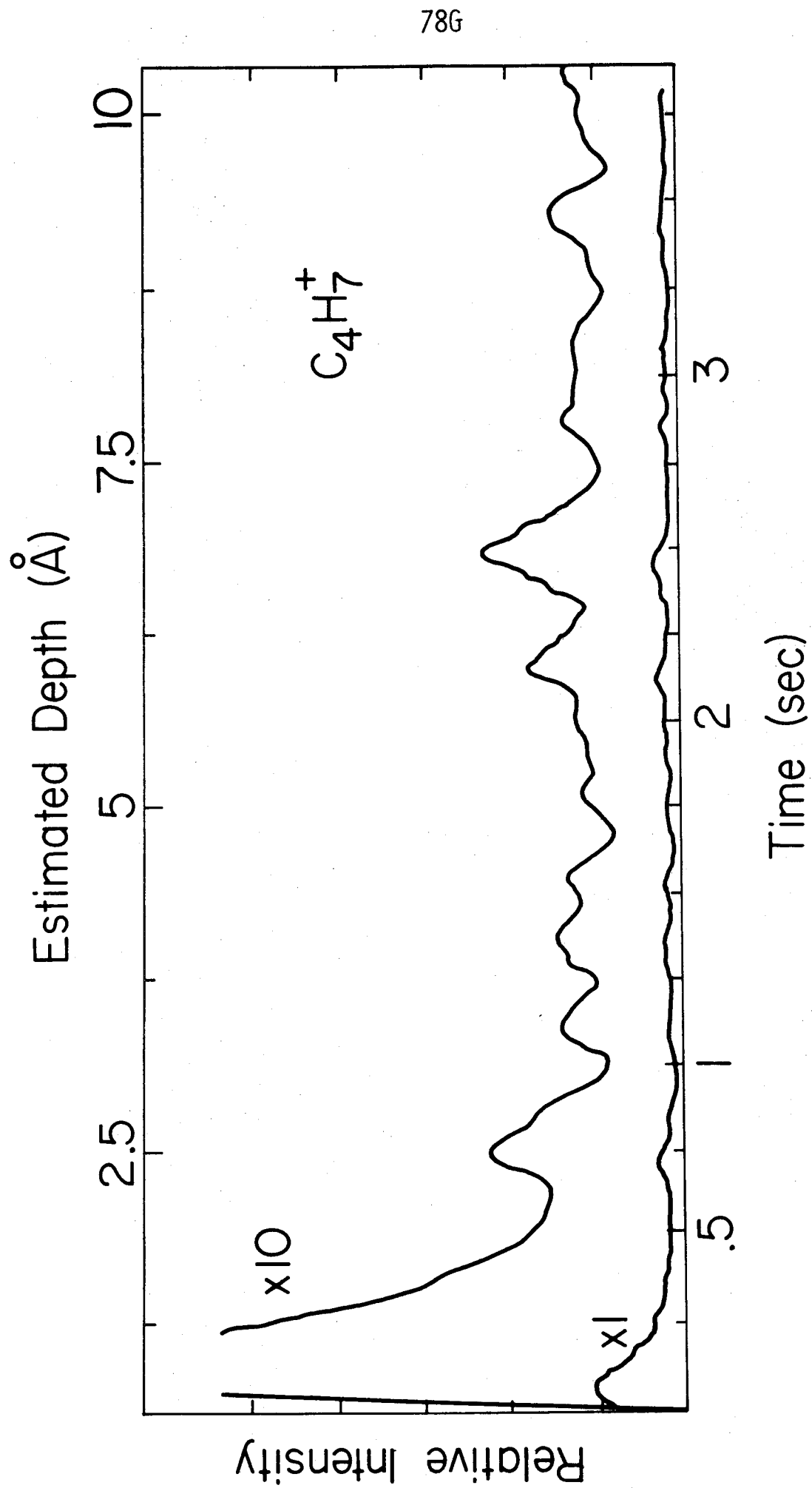
FIGURE 3b: DEPTH PROFILE OF $C_4H_7^+$

Qualitative Depth Profile Analysis of Metal Hydride

Films, Using an Ion Microprobe Mass Analyzer*

W. G. Perkins and J. A. Foesch

Sandia Laboratories, Albuquerque, New Mexico 87115

ABSTRACT

The macroscopic chemical and physical properties of bulk quantities of
the common metal hydrides (e.g., TiH_2) have been well documented. However,
the microchemistry of metal hydride films ($\sim$ 1 μm thickness) on various
substrates is far less well known. In this paper, we present our initial
results of depth profile analyses performed on erbium deuterotritide thin
films, done with an ion microprobe mass analyzer. The data indicate the
presence of significant ($\sim$ 0.1 μm) surface oxide layers and the existence
of some degree of film-substrate interaction, depending on substrate
material and on film deposition and hydride formation processes. The use
of deuterotritides permits elimination of the effects of residual hydrogen
or water vapor on the apparent hydrogen isotope depth profiles. Relative
deuterium and tritium depth distributions are compared to the results of
film outgassing analysis for deuterotritides of several deuterium-tritium
compositions. The effects of foreign particle inclusions on the apparent
materials depth profiles are illustrated by means of the ion imaging
technique.

PROGRAM FOR PREPARATION OF HIGH PURITY MINERALS
FOR USE AS ELECTRON MICROPROBE STANDARDS[*]

by

E. A. Hakkila and C. C. Herrick

Los Alamos Scientific Laboratory
Los Alamos, NM 87545

ABSTRACT

A program to prepare and characterize high purity minerals has been initiated at the Los Alamos Scientific Laboratory.

Anhydrous minerals are prepared using presses with capacities to 5×10^6 psi and choosing the appropriate assembly from a selection which includes a Boyd-England, piston-cylinder, set of a NBS, cubic anvils, a Tracy Hall, belt or conventional hot pressing-dies. Internal heating provides temperatures in the 2000°C range. Occasionally, explosive pressing in metal dies is used. Hydrous minerals are prepared using hot isostatic presses capable of 30,000 psi and 1600°C. Conventional small capacity autoclaves are used if higher gas pressures are required.

Mineral characterization includes x-ray diffraction to measure phases present, electron microprobe to determine homogeneity of major phases and to identify minor phases, ion microprobe and emission spectroscopy to measure minor constituents, and wet chemical analysis to determine concentrations of major constituents.

The purpose of the program is to prepare high purity minerals for use in various geosciences experiments, and suggestions of minerals that would be of interest to be used as electron microprobe standards are solicited. It is anticipated that those minerals that can be prepared in suitable purity would be made available to interested laboratories.

Correspondence should be addressed to:

Dr. Claude Herrick, Chairman
Mineral Synthesis Laboratory
Group CMB-8, MS 734
Los Alamos Scientific Laboratory
Los Alamos, NM 87545

ELECTRON SPECTROSCOPY: Chemical Information From Spatial Information and Energy Analysis

N. C. MacDonald
Physical Electronics Industries, Inc.
Eden Prairie, Minnesota 55343

In electron spectroscopy, chemical information is usually determined by measuring an energy shift of a peak or a change in the peak shape. For spatially homogenous, conducting specimens such information derived from electron spectra usually provides unambiguous information about the chemical state of the atoms. However, for spatially inhomogenous, nonconducting samples, changes in the energy position of the peak or changes in the shape of a peak must be carefully analyzed to unequivocally identify the chemical state of an atom.

This paper discusses various analysis situations on spatially inhomogenous samples where the combination of ESCA (X-ray excitation), Auger spectroscopy (electron excitation) and scanning Auger microanalysis is used to perform a three dimensional elemental and chemical analysis.

Simple geometrical models for the surface and in-depth distribution of atoms are derived and experimental results obtained on model samples are presented to illustrate the use of the model atomic distributions for the interpretation of electron spectra. Auger and ESCA spectra and scanning Auger micrographs obtained from catalysts are analyzed to illustrate how the ESCA and Auger data are used to identify the three dimensional elemental and chemical composition of the catalysts. Interpretation of electron spectra obtained on metallurgical and corrosion samples are also discussed to illustrate the main points of the paper.

INDEX OF AUTHORS AND THEIR AFFILIATIONS

INDEX OF AUTHORS AND THEIR AFFILIATIONS

INDEX OF AUTHORS AND THEIR AFFILIATIONS

INDEX OF AUTHORS AND THEIR AFFILIATIONS

INDEX OF AUTHORS AND THEIR AFFILIATIONS

INDEX OF AUTHORS AND THEIR AFFILIATIONS

INDEX OF AUTHORS AND THEIR AFFILIATIONS

INDEX OF AUTHORS AND THEIR AFFILIATIONS

INDEX OF AUTHORS AND THEIR AFFILIATIONS

INDEX OF AUTHORS AND THEIR AFFILIATIONS

INDEX OF AUTHORS AND THEIR AFFILIATIONS

INDEX OF AUTHORS AND THEIR AFFILIATIONS